Novel Layered Double Hydroxide Chemistry for Application in Cement and Other Building Materials

Anchalee Wongariyakawee

A thesis submitted in part fulfilment of the requirements for the degree of Doctor of Philosophy at the University of Oxford

Balliol College
Oxford
May 2013

The work described in this thesis was carried out in the Chemistry Research Laboratory, 12 Mansfield Road, Oxford from October 2009 to May 2013 under the supervision of Professor Dermot O'Hare. All the work described is my own unless stated to the contrary, and has not been submitted for any degree at this or any other university.

Anchalee Wongariyakawee

May 2013

Abstract

Novel Layered Double Hydroxide Chemistry for Application in Cement and Other Building Materials

Anchalee Wongariyakawee Balliol College

D.Phil. Thesis Trinity 2013

The investigation into the syntheses and the intercalations of LDHs is the focus of the work described in this thesis. An introduction to Layered Double Hydroxide (LDH) materials with an emphasis on the possible host lattices and to their applications is given in **Chapter 1**. The application of LDHs in cement including; history of cement, cement production process, and cement hydration is detailed.

The synthesis of the Ga-doped $Ca_2Al(OH)_6Cl{\bullet}nH_2O$ LDHs ($Ca_2Ga_xAl_{(1-x)}$-Cl; where $0 < x < 1$) *via* the co-precipitation method is reported in **Chapter 2**. The effect of doping Ga^{3+} on *a* parameter of $Ca_2Ga_xAl_{(1-x)}$-Cl was determined by using Vegard's law and the correlation between *a* parameter and *x* value was derived. The intercalation of organic anions including; sodium styrene sulfonate, sodium butene dicarboxylate, sodium fumarate and ammonium poly(styrene sulfonate), in Ca_2Ga-Cl structure is described.

The intercalation of lignosulfonate, naphthalene sulfonate and polycarboxylate into $Ca_2Al(OH)_6NO_3{\cdot}6H_2O$ (Ca_2Al-NO_3) is detailed in **Chapter 3**. The release behaviour for the LDHs and the kinetic modelling of the release are reported. The effects of these LDHs on cement hydration studied by using the *in situ* X-ray diffraction and the ultrasound shear-wave reflection are discussed.

In **Chapter 4**, the synthesis of $Ca_2Al(OH)_6NO_3{\cdot}nH_2O$ *via* a non-ionic surfactant reverse microemulsion is reported. The effects of the amount and the solubility [Hydrophile-Lipophile Balance (HLB)] of non-ionic surfactant on the morphology and the size distribution of the LDHs are discussed.

Two new nitrite intercalated Ca_2Al-LDHs [$Ca_2Al(OH)_6NO_2{\cdot}nH_2O$] synthesised *via* both the co-precipitation and the reverse micro-emulsion method are detailed in **Chapter 5**. The hydration of Portland cement samples with additive nitrate- and nitrite-intercalated Ca_2Al-LDH made using co-precipitation is discussed.

The synthesis of dispersed, uniform nanoplatelet $[Ca_2Al(OH)_6DDS]{\bullet}H_2O$ LDHs is reported in **Chapter 6**. The effects of the amount of the surfactant on the morphology and size distribution of the LDHs are described.

The experimental procedures and characterising techniques employed in this study are listed in **Chapter 7**. Additional data are provided in the **Appendices**.

Acknowledgements

This thesis would never have been possible without the help of several individuals, who in one way or another, contributed and extended their invaluable assistance allowing this study to be seen through to completion.

First and foremost, I would like to express my deepest gratitude towards my supervisor, Professor Dermot O'Hare for all the support and guidance. I would also like to thank you for the opportunity that has enabled me to pursue an academic area in the fields of my interest. I owe particular thank to Dr. Gareth Williams for his LDH knowledge, Dr. Andrew Jupe for the ultrasound shear-wave equipment he built and the experience on cement hydration and XRD refinement, Dr. Jamie H. Warner and Dr. Franziska Schäeffel for TEM training, Dr. Robert M. J. Jacobs for AFM advice, Dr. Phillip J. Wiseman for helping me solve XRD problems, Dr. Andrew Allan for his assistance on EM facilities at Harwell Research Complex, and Fabio Denis Romero for his TGA access, as well as his GSAS knowledge.

At Diamond Light Source, I got a great experience from wonderful people there, the I12 Beamline Scientist team: Dr. Michael Drakopoulos, Dr. Thomas Connolley, and Dr. Michael Hart. I would like to thank them all for their sacrifice and excellent support.

I would like to thank to the Siam Cement Group (SCG) for giving me the opportunity to carry on with higher level studies, but most importantly, for being my second family. Not enough words would be sufficient to express my gratitude for everything that has been possible. To my bosses, Kan Trakulhoon, Pramote Techasupatkul, Cholanat Yanaranop, Santi Lorlowhakarn, Prinya Sainamthip, Somchai Chitwarodom, Manasit Sarigaphuti, Sakprayut Sinthupinyo, Nitithep Chaichuay, and my colleagues. I truly thank you for your support.

I would like to extend my appreciation to all the friends who have stood by me both mentally and physically, without which this journey would have been impossible. Your friendship and love have given me strength to withstand all obstacles and hardships in life. I would like to thank to Charlie Griffiths, Rutairat Rubporn, Wilai Siriwatcharapiboon, Thutchai Puengsupa, Chanchanok Poolvoralaks, Hasna Zaher, Chengle Joyce Wang, Saul Moorhouse, Charles Markland, Samantha Binding, Henry Fisher, Hannah Buckley, Tom Arnold, Mark Chadwick, Robert Cooper, DOH group members, and members of the Thai society for all the memories.

Last but not least, I would like to express my undying love towards my family.

Contents

Chapter 1: Introduction

1.1 Structure of Layered Double Hydroxides

Layered double hydroxides (LDHs) are a class of synthetic anionic clays whose structures are based on brucite-like layers. The brucite structure consists of magnesium cations coordinated with six hydroxide ions.[1] The magnesium cations occupy the octahedral holes between oxygen atoms of the hydroxyl group. The octahedral units connect to form infinite layers by edge-sharing. These layers stack on top of one another to form the 3D structure.

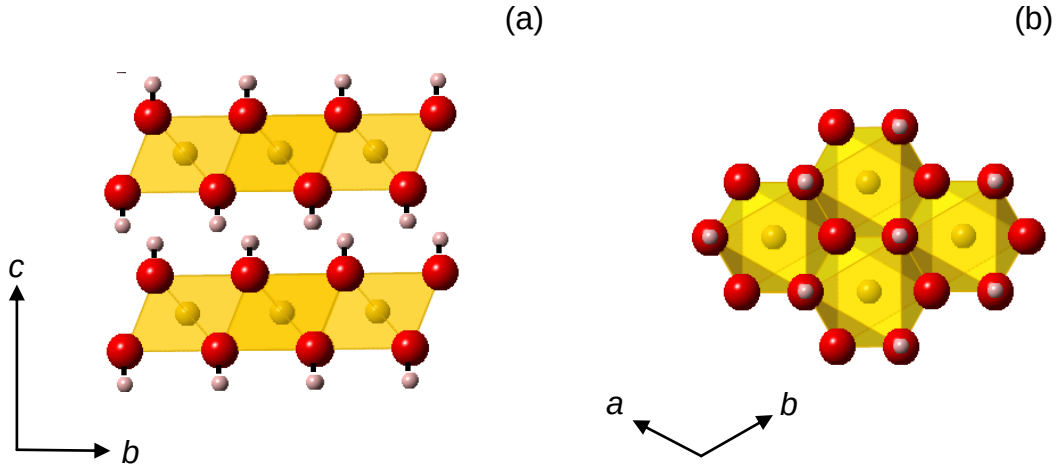

Figure 1.1. Views of brucite [$Mg(OH)_2$] along (a) the *a*- axis and (b) the *c*-axis. Magnesium cations shown in yellow coordinate with oxygen atoms (in red) from a hydroxyl group. Hydrogen atoms are shown in pink.[1]

The main structural features of LDHs were first studied by Allmann[2] and Taylor[3]. The LDH structure is derived by the substitution of trivalent cations on some of the divalent cations sites in a brucite structure, creating positively-changed sheets. The intercalation of anions in the interlayer region balances the total charge in order to retain overall electroneutrality of the structure. To show the diversity of LDH materials synthesised using different cations and anions, a general formula may be written as $[M^{II}_{1-x}M^{III}_{x}(OH)_2]^{x+}[A^{n-}]_{x/n} \bullet yH_2O$, where M^{II} *and* M^{III} represent divalent and trivalent cations, (e.g. Ca^{2+}, Mg^{2+}, Fe^{2+}, Mn^{2+}, Zn^{2+}, Cu^{2+}, Ni^{2+} or Co^{2+} for M^{II}, and Al^{3+}, Cr^{3+}, Mn^{3+}, Fe^{3+}, Ga^{3+}, Co^{3+}, Ni^{3+}, V^{3+} or Sc^{3+} for M^{III}) and A^{n-} is the intercalated anion.[4] It was initially thought that LDH structures can typically form within *x* values ranging between

0.20 and 0.33.[5-7] However, a more recent investigation suggested that LDHs can be formed over the greater range between 0.07 and 0.5.[8] Furthermore, many ternary LDHs involving mixtures of different M^{II} and/ or M^{III} cations have been successfully synthesised, for example, sulfate intercalated $Mg^{II}Cu^{II}Al^{III}$-LDH[9], carbonate intercalated $Mg^{II}Fe^{II}Fe^{III}$-LDH[10], and carbonate intercalated $Mg^{II}Al^{III}Fe^{III}$-LDH.[11, 12] Tetravalent cations (M^{IV}) have been incorporated into LDH layers such as carbonate intercalated $Mg^{II}Al^{III}Zr^{IV}$-LDH[13, 14], carbonate intercalated $Mg^{II}Al^{III}Sn^{IV}$-LDH[15], carbonate intercalated $Zn^{II}Al^{III}Zr^{IV}$-LDH[16]. The synthesis of quaternary LDHs have also been investigated such as $[(Cu,Co,Zn)_6Al_2(OH)_{16}CO_3 \bullet H_2O]$.[17] The thermal stabilities of the LDH structures varies from one another in the following order: Mg < Mn < Co ≈ Ni < Zn for M^{II} and Al < Fe for M^{III}.[18] Furthermore, it was found that LiX can react with $Al(OH)_3$ to form $LiAl_2(OH)_6X \bullet nH_2O$, where X = Cl^-, Br^- and NO_3^- ($LiAl_2$-LDH).[19, 20] The Li^+ cations locate in the octahedral holes within the $Al(OH)_3$ layers which are not occupied by Al^{3+} ions. Further studies reported the synthesis of $[MAl_4(OH)_{12}](NO_3)_2 \bullet yH_2O$ (where M = Co, Ni, Cu or Zn) by incorporating small divalent cations into activated $Al(OH)_3$ using the hydrothermal method.[21, 22]

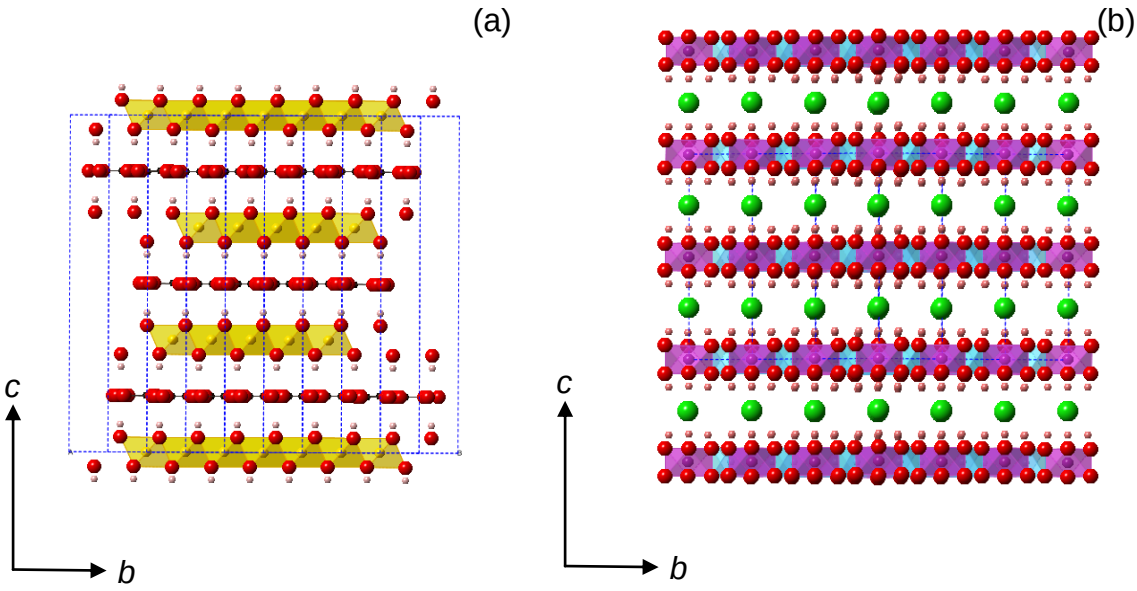

Figure 1.2. The structures of (a) hydrotalcite $[(Mg_4Al_2(OH)_{12}(CO_3) \bullet 3H_2O$, Mg_4Al_2-$CO_3]$[23] (Mg^{2+} and Al^{3+} cations in a octahedral hydroxyl coordination (with oxygen atoms in red) are shown in yellow and hydrogen atoms are shown in pink, while CO_3^{2-} anions are located between the LDH layers in red.), and (b) $LiAl_2(OH)_6Cl$ ($LiAl_2$-Cl)[24] (Li^+ cations (in light blue) and Al^{3+} cations (in pink) coordinate with oxygen atoms (in red) from the LDH layers, while Cl^- anions and H atoms are shown in green and pink, respectively.

There are two main types of LDH stacking arrangements. The positively charged layers may be stacked with hexagonal symmetry [e.g. $LiAl_2(OH)_6Cl•nH_2O$] with an *aba* two-layer sequence[16], or with rhombohedral symmetry [e.g. $[Mg_4Al_2(OH)_{12}]CO_3•nH_2O$] giving an *abca* three-layer sequence. These polytypes are classified based on the number of LDH layers stacked along the *c*-axis of the unit cell. Rhombohedral and hexagonal structures can be distinguished by the systematic absences in the XRD. Bragg reflections are systematically absent unless $-h + k + l = 3n$ for rhombohedral structures; where *h, k, l* are the Miller indices, and *n* is an integer. For hexagonal unit cell structures, the reflections are present when $-h + k + l \neq 3n$. The d-spacing of the Bragg reflections along the *c*-axis can be indexed to either a tri-layer 3R polytype with rhombohedral symmetry, or a bi-layer 2H polytype with hexagonal symmetry. Simulated X-ray diffraction patterns showing the different reflections of hydrotalcite allowed for the 3R polytype compared to the 2H polytype is illustrated in Figure 1.4.

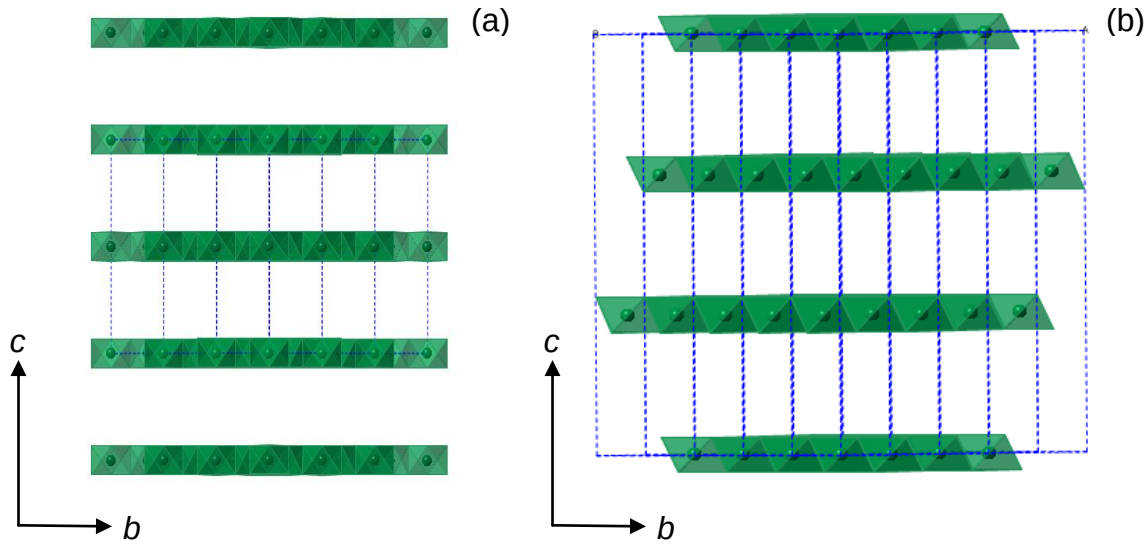

Figure 1.3. The generalised structure of an LDH, showing (a) hexagonal and (b) rhombohedral stacking sequences. MO_6 octahedra are shown in green. H atoms and interlayer anions are omitted for clarity. Dotted lines correspond to unit cells of the structure.

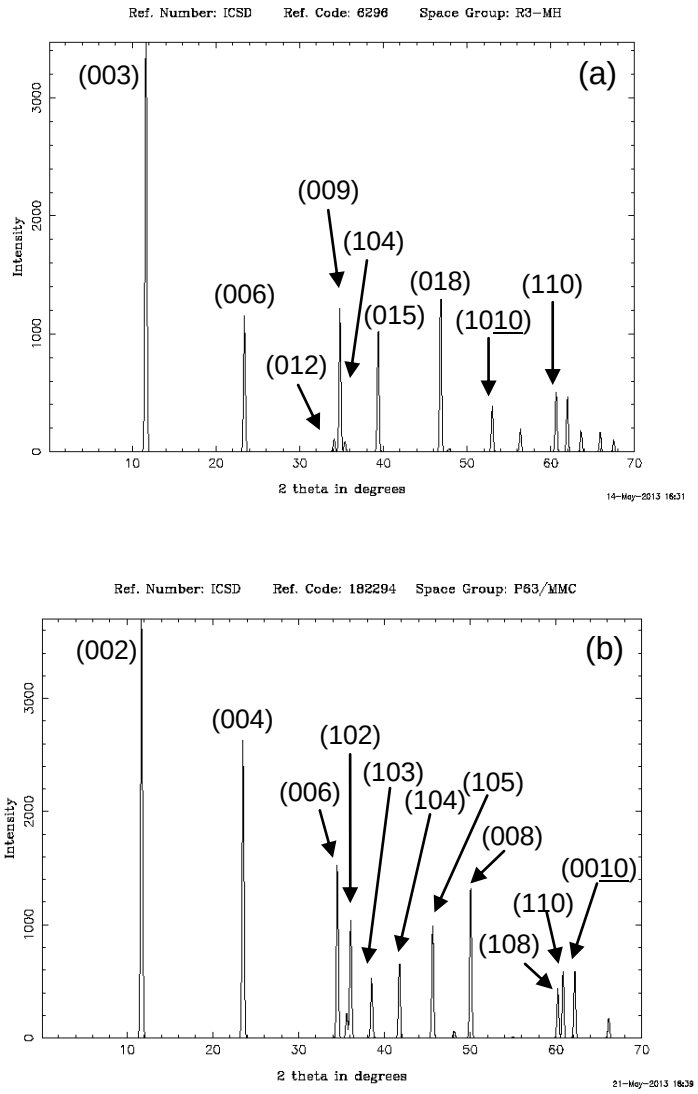

Figure 1.4. X-ray patterns of hydrotalcite ($Mg_4Al_2(OH)_{12}(CO_3)$•$3H_2O$) (a) with rhombohedral stacking squence[23] (b) with hexagonal stacking squence.[25]

Hydrocalumite is a colourless to light green mineral, $[Ca_2Al(OH)_6Cl_{1-x}(OH)_x \bullet 3H_2O]$, that is a calcium-based LDH.[3, 26] Hydrocalumite-like materials (Ca_2Al-LDHs) are generally found in hydration products of cement such as Friedel's salt $[Ca_2Al(OH)_6Cl \bullet H_2O$, Ca_2Al-Cl],[27, 28] and monosulfate $[Ca_4Al_2(OH)_{12}SO_4 \bullet H_2O$, Ca_4Al_2-$SO_4]$.[29, 30] The polytypes and polymorphs of some Ca_2Al-LDH materials have been studied.[3, 26-28, 31] The coordination numbers of Ca^{2+} and Al^{3+} ions in the Ca_2Al-LDH structures are 7 and 6, respectively. Each Ca^{2+} ion coordinates with the seventh oxygen atom from an intercalated water molecule, with the exception of nitrate intercalated Ca_2Al-LDH as the Ca^{2+} ion coordinates with oxygen atoms from both intercalated water and the nitrate ions.[31]

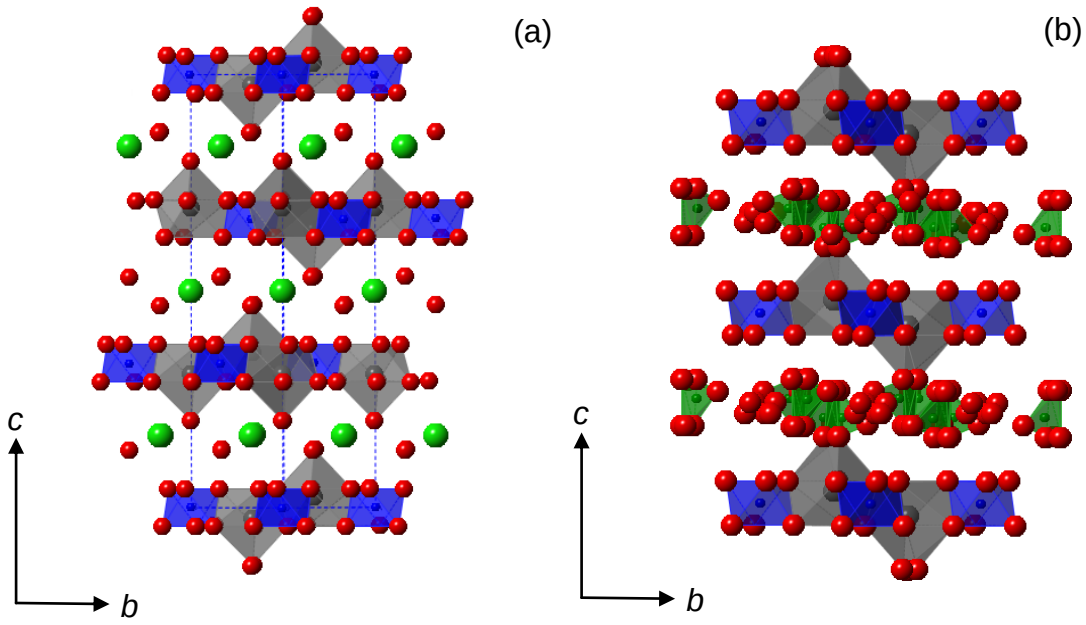

Figure 1.5. The structures of hydrocalumite showing the co-ordination of Ca with O from H_2O in (a) $Ca_2Al(OH)_6Cl \bullet H_2O$ and the co-ordination of Ca with O from nitrate in (b) $Ca_2Al(OH)_6NO_3 \bullet 2H_2O$. H atoms are omitted for clarity. Nitrate ions are disordered.

1.2 Preparation of LDHs

Over the years, there has been a growing interest in the development of new LDH syntheses. LDH materials can be synthesised with a variety of divalent and trivalent cations, and with a range of cation compositions depending on the compatibility of the ionic radii of the cations to form the LDH layers. The size and morphologies of the LDH particles can be controlled by the synthesis methods and conditions. A number of the synthetic techniques have been successfully employed in the preparation of LDHs.

Conventional techniques have been simplified and used to develop large scale production for industrial purposes, while advanced techniques are still needed to acquire better properties such as smaller LDH particle sizes with greater surface area.

1.2.1 Co-precipitation method

The co-precipitation method has been used since the 1920s. The formation of LDH crystals nucleate when the mixed metal solution precipitate under basic conditions, and further grow and increase in size and crystallinity, while anions are directly intercalated between the metal hydroxide layers.[32] This technique is suitable for the spontaneous intercalation of anions during the formation of the metal hydroxide layers. Furthermore, this method has been used to synthesise large and diverse shaped anion intercalated LDHs.[33, 34, 35, 36]

In the preparation of LDHs, the effect of pH,[37] temperature, reaction time[38] solvent[39, 40] and even physical technique[41] such as stirring speed of reactors, on size and morphologies have been investigated. A series of nanosized colloidal LDHs were successfully synthesised by co-precipitation from metal salts dissolved in methanol in the presence of NaOH.[39, 40] The pH and temperature utilised for the synthesis process are important factors in controlling the solubility of the precursors, increasing the yield, as well as the crystallinity of the LDH materials. The co-precipitation method is the synthetic technique widely used to support industries.[42-44]

Several synthetic modifications including urea or hexamethylenetetramine hydrolysis has been used during co-precipitation to achieve crystallinity and morphologies.[45] Highly crystalline LDHs with micron size platelets can be obtained using urea or hexamethylenetetramine hydrolysis during the homogeneous precipitation reaction.

1.2.2 Reverse microemulsion method

Reverse microemulsion is one of the techniques used to control and create LDHs as nano-sized particles by adding surfactants to form reverse micelles in the oil-phase. The size and morphologies of the LDHs are limited by the micelles in which they form when the amount of surfactant added is greater than the critical micelle concentration. This

technique has been applied to synthesise nano-materials such as Pt, Rh, Pd, and Ir.[46-55] O'Hare *et al.* reported the first synthesis of LDHs using this method.[56-59]

1.2.3 Ion-exchange reaction

Ion exchange intercalation is a useful technique when the co-precipitation method is inapplicable. An ion-exchange reaction may take place between an intercalated LDH phase and a concentrated solution of the desired anion. The extent of ion-exchange reaction depends on the affinity for the desired anion, solubility of the desired anion, pH of the reaction medium, and the stability of LDH layers.

1.2.4 Advanced synthesis techniques

In recent years, new techniques have been designed to produce various LDH morphologies ranging from common platelets, spheres, rods, fibrous structures, to LDH films on substrates.

Template-directed synthesis has been applied to synthesise spherical LDH structures. Coral-like MgAl-LDH microsphere has been synthesised using the ethylene glycol/methanol/dodecyl sulfate non-aqueous polar solvent/surfactant system.[60] Silica beads have been used as templates to prepare LDH as the building block on the surface of the template, giving the LDH shell walls.[61] A schematic diagram of the synthesis of an LDH shell on a silica substrate is shown in Figure 1.6.

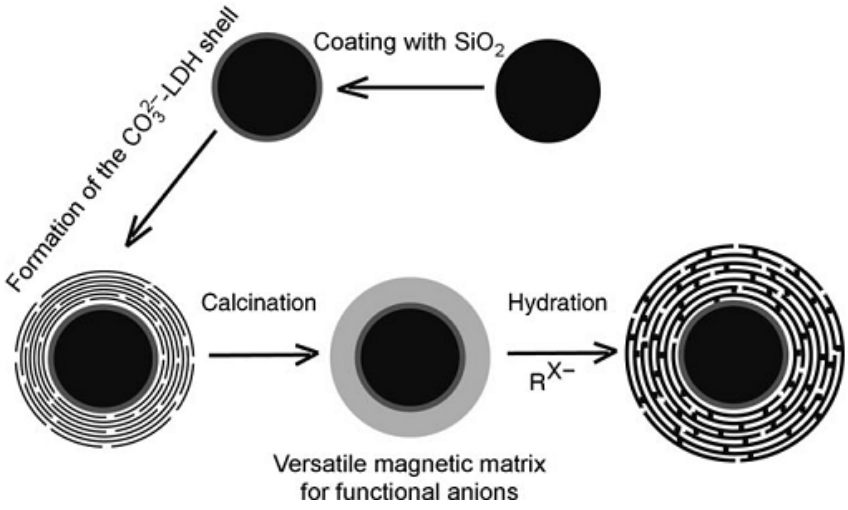

Figure 1.6. A schematic diagram of the synthesis of the LDH shell on Silica substrate.[61]

MgAl-LDH have been synthesised using the hydrothermal method to achieve wire- and rod-shaped morphologies. Furthermore, ZnCoFe-LDH nanowires can be synthesised in a water-in-oil microemulsion.[62]

Face-on oriented building blocks of platelet-like LDH platelets shown in Figure 1.7 can be prepared by solvent evaporation, spin-coating, electrochemical deposition, and colloid deposition. MgAl-LDH films have been prepared using solvent evaporation on polyethylene substrates.[63] The electrochemical deposition technique may be used to prepare LDH films due to the positive charge of the LDH colloid. ZnAl-LDH, CoAl-LDH, and NiAl-LDH films have been synthesised on different electrode surfaces.[64-66] The spin-coating technique enables MgAl-LDH films to be prepared on a magnesium-containing alloy substrate.[67]

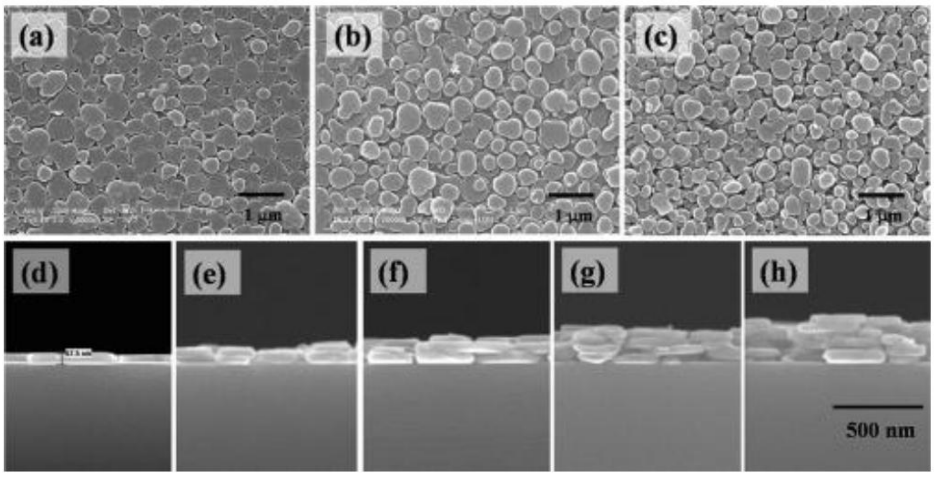

Figure 1.7. SEM images of (a) 1 layer, (b) 3 layers, (c) 5 layers of MgAl-LDH on Si substrate, cross-sectional views of; (d) 1 layer, (e) 2 layers, (f) 3 layers, (g) 4 layers, and (h) 5 layers of MgAl-LDH on Si substrate.[68]

Perpendicular-oriented LDH films (edge-on oriented LDH) have been prepared by *in situ* growth during hydrothermal synthesis.[69] The growth kinetics of these LDH microcrystals have been investigated to support the possibility of templating the formation of the edge-on orientated MgAl-LDH film.[70]

In order to synthesise nanomaterials, exfoliation technique has become an interesting technique. In the past few years, there are a number of publications related to the synthesis and application of LDH nanosheets, especially synthesised by the exfoliation method.[71] The first study of the exfoliation of LDHs was reported in 1999.[72] ZnAl-NO_3 LDH can be

exfoliated using sodium dodecyl sulfate and butanol. The delamination of LiAl-LDHs intercalated with different surfactants including sodium dodecyl sulfate, sodium octyl sulfate, sodium 4-octylbenzenesulfonate, sodium dodecylbenzenesulfonate.[73] In addition, dodecyl sulfate intercalated MgAl-, CoAl-, NiAl-, and ZnAl-LDHs were reported to be exfoliated in toluene.[74, 75]

The delamination of amino acid intercalated LDH in formamide was first reported in 2001.[76] The authors mentioned that the delamination occurs due to the strong hydrogen bonding between the intercalated anions and the polar solvent. Other amino acid intercalated LDHs (NiAl-, CoAl-, and ZnAl-LDHs) have been studied.[77] Recent investigations have reported that MgAl-NO_3 LDH can be successfully exfoliated in formamide.[78]

1.3 Applications of LDHs

LDHs have a high anion exchange capacity (typically number range mequiv•g^{-1}), and the interlayer anion can be easily exchanged by organic and inorganic anions. Because of the interesting structural features of LDHs, these materials have been examined for a number of applications such as catalysts[79-88], scavengers of pollutant anions,[89, 90] CO_2 adsorbents,[91-96] drug delivery,[39, 97-100] and additives for polymer application.[101-105] More recently, the use of LDHs in the synthesis of inorganic/organic nanocomposites has become a new emerging class of material. Synthetic LDHs offer elemental precision and chemical homogeneity for the inorganic phase and the LDH/polymer nanocomposites exhibit improved mechanical, thermal, gas barrier properties and reduced flammability. Hydrocalumite-like structures (Ca_2Al-LDHs) are the by-products of cement hydration and they play several important roles[29, 106-108] (i.e., to accelerate or retard the hydration reaction) to create the desired physical properties of ready mixed concrete.

To improve the physical properties of these composite materials, making the admixture LDH materials on the nano-scale may be effective. The ability of LDH nanoparticles to enhance the physical and chemical properties of pristine materials has been exploited in many applications. For example, due to their high reactivity and surface area, nanoparticles are currently used in electronics, pharmaceuticals, cosmetics, biomedicine, catalysis and materials sciences.[109]

1.4 Uses of LDHs in cement

1.4.1 History of cement

Cement is one of the first structural materials invented by humanity. *'Cement'* comes from the Latin phrase, *'opus caementum'*, or chip work, which refers to the aggregate often used in building applications. Simple cement, discovered by the ancient Romans was originally made of lime, volcanic ash, and crushed clay. However, the access to volcanic ash was limited and cement processes such as grinding and heating techniques were lost after the fall of the Roman Empire. The development of cement chemistry started when Smeaton was commissioned to rebuild the Eddystone lighthouse in Cornwall, England. He found that impure limestone with noticeable clay deposits produced extremely strong cement. The term '*Portland cement'* has been officially used since 1824 when Aspidin filed the first patent for cement production.

The American Society for Testing and Materials (ASTM) has defined Portland cement as a hydraulic cement produced by pulverizing Portland-cement clinker, which usually contains calcium sulfate and blended hydraulic cement. Portland cement can contribute to the strength-gaining properties of cement by making cement with or without other constituents. When sand and gravel are added to cement, the aggregate is called concrete.

1.4.2 Cement production process

Cement technology is very traditional and the original basic principles still remain currently efficient. However, the development of production techniques has been driven by the aim of reducing energy consumption, raising awareness and taking action to reduce the impact on the environment. The cement manufacturing process is summarised in Figure 1.8. The raw materials, including limestone, clay, laterite, and sand are ground separately by crushers. The amount of each raw material is calculated, using 'Bogue equations'[110] (Equation 1.1 – 1.4), according to the required cement phase composition of the clinker, the final product from cement kilns. The total weight percentage of the main oxides is equal to about 95 percent and the distribution is as follows: CaO 60 – 70%, SiO_2 18 – 22%, Al_2O_3 4 – 6%, Fe_2O_3 2 – 4%. The remaining 5% accounts for minor components such as MgO, K_2O, TiO_2, Mn_2O_3 and SO_3.[111]

Tricalcium silicate = $(4.071 \times \%CaO) - (7.70 \times \%SiO_2)$ **Equation 1.1**
$- (1.430 \times \%Fe_2O_3) - (6.718 \times \%Al_2O_3) - (2.852 \times \%SO_3)$

Dicalcium silicate = $(2.867 \times \%SiO_2) - (0.7544 \times \%C_3S)$ **Equation 1.2**

Tricalcium aluminate = $(2.6504 \times \%Al_2O_3) - (1.6920 \times \%Fe_2O_3)$ **Equation 1.3**

Tetracalcium aluminoferrite = $3.043 \times \%Fe_2O_3$ **Equation 1.4**

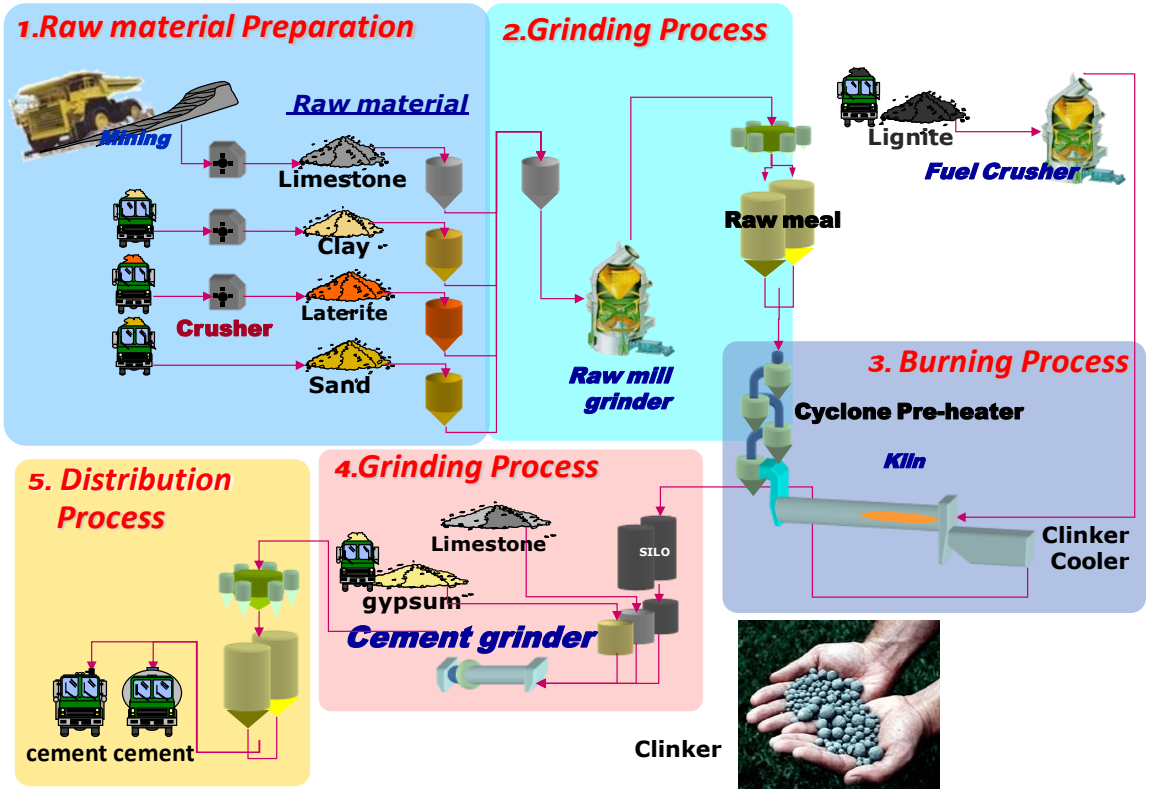

Figure 1.8. A summary of the cement manufacturing process of Portland cement.

Raw materials are mixed and ground in order to obtain greater homogeneity. The blended raw material is then transferred to a cyclone preheater. The gas temperature (*ca.* 350 ^{o}C) in the preheater is selected to reduce the moisture content of the raw material. The raw material is transferred due to the rotating kiln (called rotary kiln). The raw material is heated to higher temperature. At approximately 800 ^{o}C, the raw material is decomposed due to the decomposition of carbonate, a process called calcination. The gas temperature increases along the kiln from the cyclone preheater to a burner. After the calcination, silicate (also called belite) forms between 900 and 1200 ^{o}C. A liquid phase occurs and promotes the reaction between belite and lime that forms Alite at temperatures above 1300 ^{o}C.

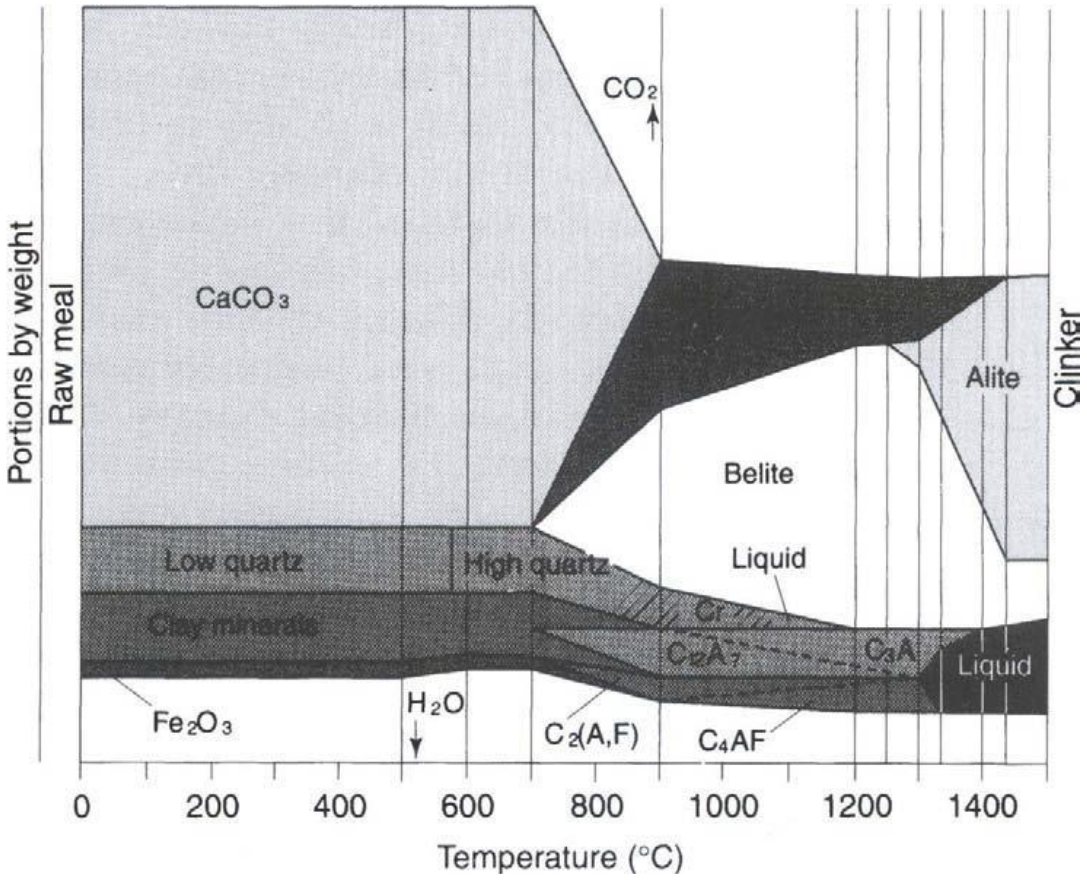

Figure 1.9. An approximate composition phase diagram of Portland cement. C_2(A,F) is meta-stable phase of tricalcium aluminate formation.[110]

The molten phase is rapidly quenched using clinker coolers in order to control the rate of cooling. The liquid phase in the kiln cools down and glassy silica and tricalcium aluminate (C_3A) crystallises out at 1450 ^oC. The product formed as a result of the quenching process is called a 'clinker'. The average size of a clinker grain is approximately a few centimetres. The composition of cement phases present in a clinker is summarised in Table 1.1. The main constituents of clinker are slightly impure due to the minor elements in the raw materials from mining. Two major components of the cement phase are commonly found in clinkers; calcium silicate is crucial to the development of the durability of hydrated cement, while calcium aluminate influences the setting time of cement. The clinker is ground and mixed with the appropriate amount of gypsum by ball mills in order to obtain the specific surface area (also called 'Blaine') of 300 – 350 m^2/kg for general purpose cement and a higher surface area of 450 – 650 m^2/kg for rapid setting cement. These final-products are called cement.

Table 1.1. Summary of the approximate composition of Portland cement.[110]

	Composition (% wt)
Tricalcium silicate (Ca_3SiO_5, C_3S)	42 – 65
Dicalcium silicate (Ca_2SiO_4, C_2S)	10 – 30
Tricalcium aluminate ($Ca_3Al_2O_6$, C_3A)	0 – 16
Tetracalcium aluminoferrite ($Ca_2(Al_xFe_{1-x})_2O_5$; $0 < x < 0.7$, C_4AF)	1 – 17
Magnesium oxide (MgO)	0.5 – 6
Alkali sulfates (Na_2SO_4, K_2SO_4)	0.5 – 3
Excess calcium oxide (CaO)	0.2 – 4

1.4.3 Cement hydration

Cement hydration occurs when cement is mixed with water. A partial hydration of cement can take place in humid air. However, cement requires a sufficient amount of water in order to hydrate completely which is defined by the water to cement weight ratio (w/c). The w/c value normally used is between 0.3 – 0.6 as it provides an optimal range in which the cement produced has a great durability with an acceptable flowability. The amount of water added can affect the rheology and the hydration progress of the cement suspension which is called 'fresh cement paste'. The fresh cement paste hardens as the hydration process progresses and ultimately becomes set in place. The hydration reactions in

Portland cement are very complex. The rate of hydration and the hydration products of each cement compound differ from one another as shown in Figure 1.10.

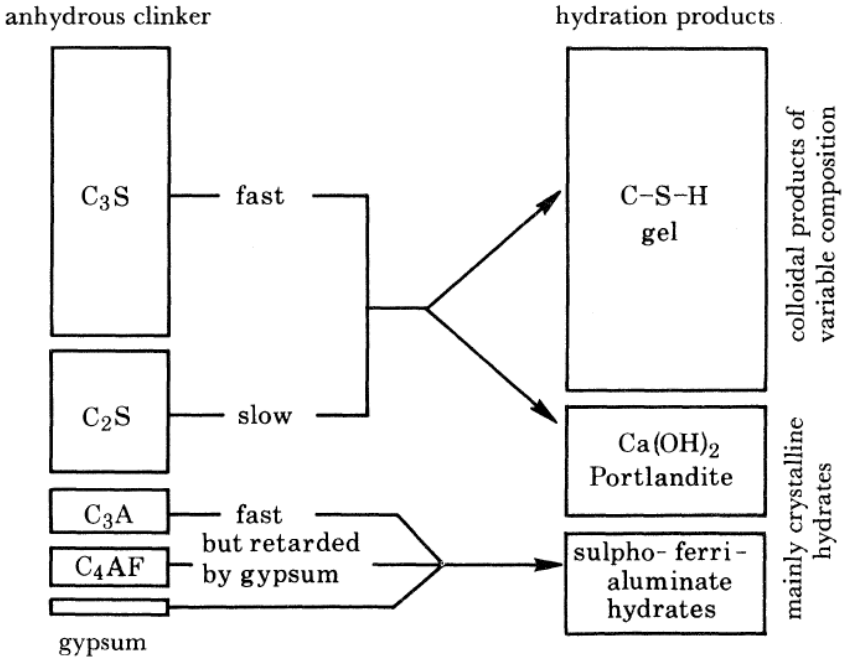

Figure 1.10. Schematic representation of the anhydrous constituents in Portland cement clinker and the hydration products formed during hydration. The areas of the 'boxes' give the approximate volume proportions of the phases. C-S-H = Calcium silicate hydrate.[112]

Overall, the progress of hydration correlates with a variety of chemical and physical effects which are as follows:

(1) The cement phase composition and the presence of foreign ions within the crystalline lattices of the individual clinker phase.

(2) The fineness of cement particles, in particular, the particle size distribution and specific surface area.

(3) The water/cement ratio used.

(4) The curing temperature.

(5) By the presence of chemical admixtures, *i.e.*, chemical substances added in small amounts to modify the hydration rate and properties of the cement paste.

1.4.3.1 Calcium silicate hydrate (C-S-H)

Calcium silicate hydrate, described by the generic term 'C-S-H', is generally formed by the hydration of tricalcium silicate (C_3S) or dicalcium silicate (C_2S).[113] These cement phases account for about 75 %wt of a Portland cement.[114] The morphology of C-S-H is a reticular structure consisting of irregular fibres growing from the surfaces of the cement grains and bridging the spaces between grains, causes which the strength development of cement paste.[115-118] The hydration product occupies about 60 %v of the total hydration products. Structurally, the C-S-H is very poorly crystalline with a Ca/Si ratio of 1.7 – 2.0. Bernal[113] reported that the C-S-H structure has a layer structure related to that of a crystalline mineral called Tobermorite [$Ca_5Si_6O_{16}(OH)_2 \bullet 4H_2O$]. Another crystal mineral called Jennite [$Ca_9Si_6O_{18}(OH)_6 \bullet 8H_2O$] has also been suggested. More recently, it has been concluded, that the C-S-H structure depends on the Ca/Si ratio.[118-120] C-S-H with a ratio between 0.83 - 1.25 is formed as Tobermorite, while the Ca/Si ratio for Jennite is between 1.5 and 2.25. Both of the proposed structures are significantly more crystalline than the material formed in cement pastes under normal conditions.

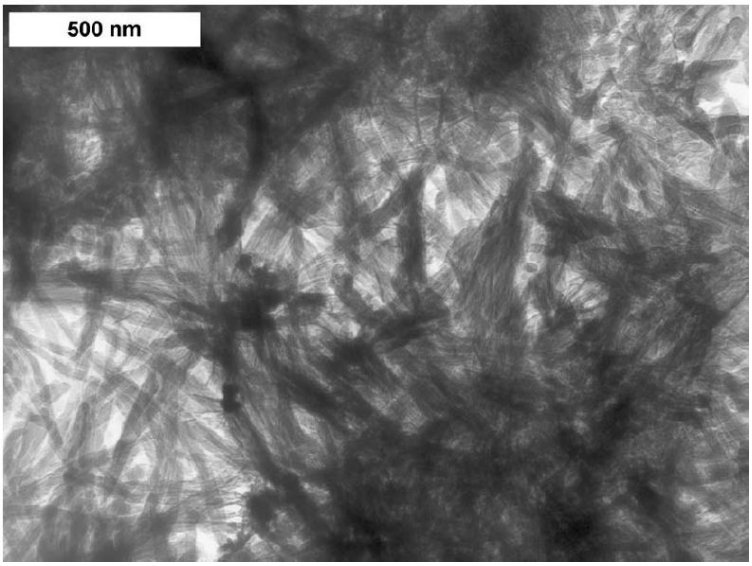

Figure 1.11. TEM image of C-S-H present in cement paste with a water to cement ratio of 0.4, hydrated at 20 ^{o}C for 3 months.[118]

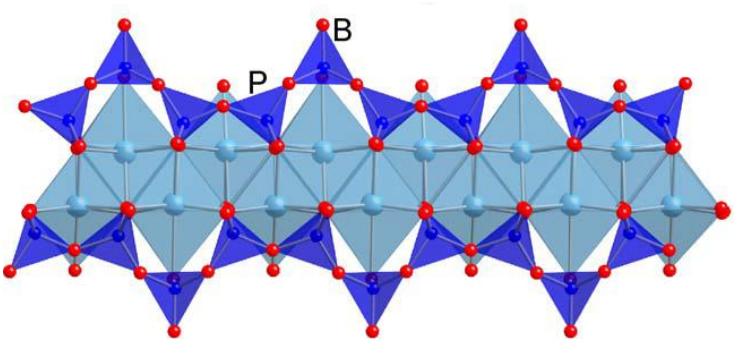

Figure 1.12. View of the C-S-H structure with a Ca/Si ratio between 0.83 – 1.25 (called Tobermorite) projected along (210).[118] Si atoms in a tetrahedral hydroxyl coordination are shown in blue, while the seven coordinated Ca atoms are shown in light blue. The C-S-H chain has a kinked pattern where some silicate tetrahedra share O–O edges with the central Ca–O layer (called 'paired' tetrahedral, P) and others that do not (called 'bridging' tetrahedral, B).

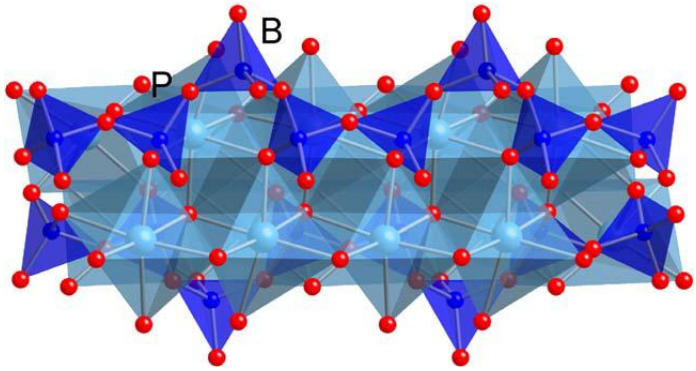

Figure 1.13. View of the C-S-H structure with a Ca/Si ratio between 1.5 – 2.25 (called Jennite) projected along (100).[118] Si atoms in a tetrahedral hydroxyl coordination are shown in blue, while the seven coordinated Ca atoms are shown in light blue. 'Paired' and 'Bridging' tetrahedra are labelled 'P' and 'B', respectively.

1.4.3.2 Calcium aluminate hydrate (C-A-H)

The calcium aluminate hydrate results from the hydration of tricalcium aluminate (C_3A) and tetracalcium aluminoferrite (C_4AF). These cement phases comprise less than 20 %wt of the bulk of cement. Their hydration reactions are very important in cement, as they can dramatically affect the overall setting of cement. In the absence of any additional additives, tricalcium aluminate undergoes hydration and forms two intermediate hexagonal phases, called C_2AH_8 ($Ca_2Al_2O_4•8H_2O$) and C_4AH_{19} ($Ca_4Al_2O_4•19H_2O$). C_2AH_8 and C_4AH_{19} are meta-stable phases which belong to a large group of monosulfate (AFm) phases, $[Ca_2(Al,Fe)(OH)_6]X•nH_2O]$ where *X* denotes an anion. C_2AH_8 and C_4AH_{19} contain $[Ca_2Al(OH)_6]^+$ sheets with OH^- or $[Al(OH)_4]^-$, together with water, in the interlayer region. These phases transform spontaneously to the fully hydrated and thermodynamically stable cubic phase which sometimes has silicate incorporated into the structure, and is called hydrogarnet $[Ca_3Al_2(SiO_4)_{3-x}(OH)_{4x};\ 0 \leq x \leq 3]$. These very rapid and exothermic hydrations of tricalcium aluminate cause the cement setting to 'flash set'. Therefore, gypsum is used to slow down the tricalcium aluminate hydration. In the presence of gypsum, tricalcium aluminate reacts with gypsum and produces ettringite, $[Ca_6Al_2(SO_4)_3(OH)_{12}•26H_2O$, AFt]. As gypsum becomes increasingly consumed, both C_2AH_8 and C_4AH_{19} become significant phases and ettringite will in turn react with these C_2AH_8 and C_4AH_{19} phases to give a calcium monosulfatoaluminate hydrate, called monosulfate $[Ca_4Al_2(OH)_{12}(SO_4)•6H_2O$, Ca_4Al_2-SO_4, also called AFm].[29, 110, 121] Tetracalcium aluminoferrite (C_4AF) hydrates relatively similarly to C_3A. The composition of calcium aluminoferrite may vary between an Al/Fe ratio of 0.43 and 2.33.The rate of hydration is significantly lower than that of C_3A depending on the Al/Fe ratio. It generally decreases with increasing Fe content.[122]

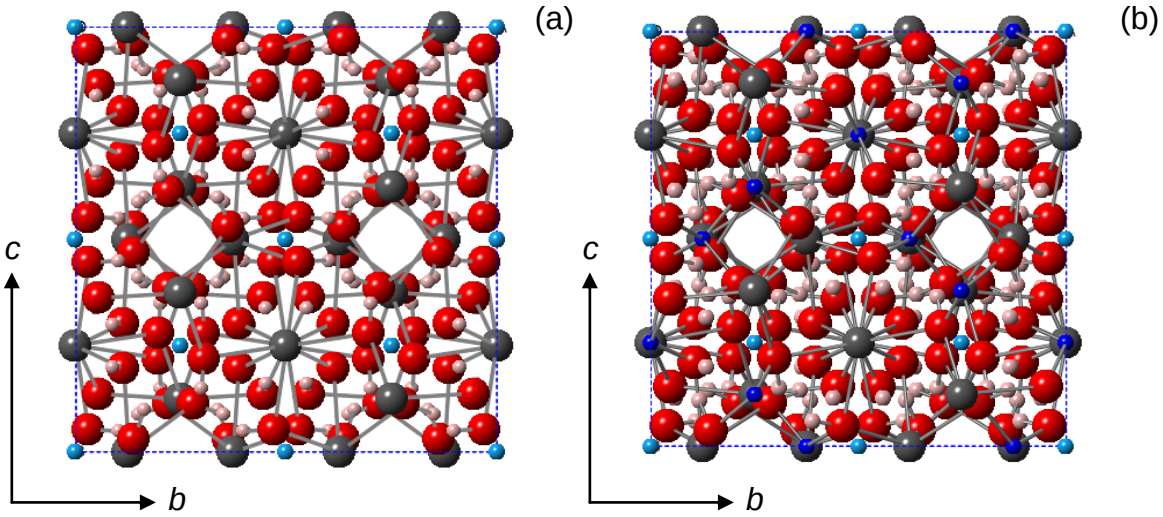

Figure 1.14. Crystal structures of hydrogarnet (a) $Ca_3Al_2(OH)_{12}$, and (b) $Ca_3Al_2(SiO_4)_{2.16}(OH)_{3.36}$ (ICSD 15380). Ca atoms are displayed in grey, O atoms in red, Al atoms in light blue, Si atoms in dark blue.[123]

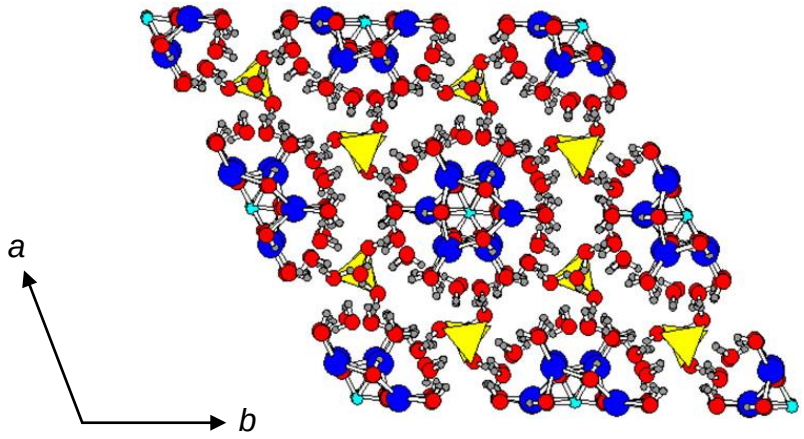

Figure 1.15. Crystal structure of ettringite projected on the (001) plane.[121] Ca atoms are displayed as blue circles, O atoms in red, Al atoms in light blue, SO_4^{2-} tetrahedral in yellow and H atoms in grey.

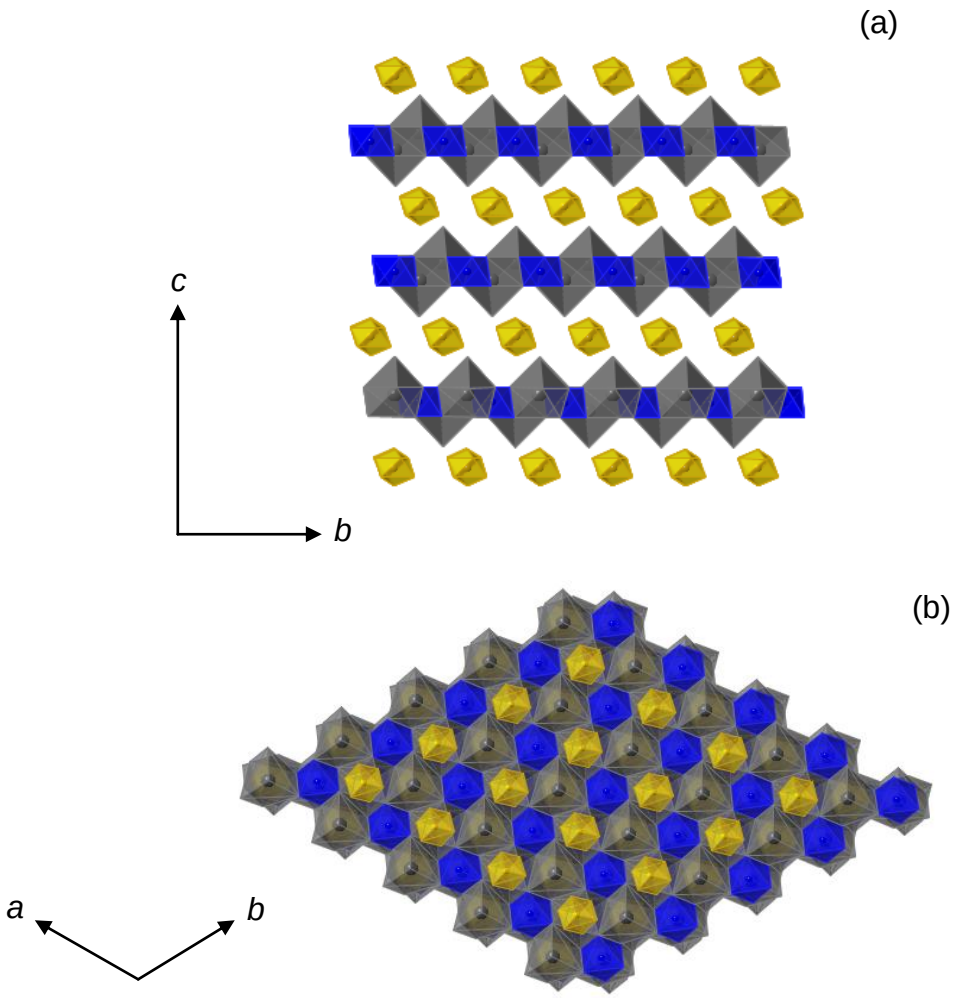

Figure 1.16. View of monosulfate (Ca_4Al_2-SO_4) along (a) the *a*-axis and (b) the *c*-axis showing the relative positions of sulfate ions (in yellow).[124] Al atoms in an octahedral hydroxyl coordination show in blue, while Ca atoms with the seven hydroxyl coordination show in grey.

The hydration and hydration products of C_3A, especially Ettringite are of particular interest because of their significant effects on cement setting. This hydrated phase is present as rod-like material in the early stages of cement hydration and can grow further to fill pores or cracks in hardened cement. It is believed that it can enhance the durability of hardened cement. The formation of Ettringite in the initial stage has a positive effect, while the Ettringite formation can cause damage in hardened concrete due to the expansion of the Ettringite phase. For many years, the studies of generic hydration of C_3A have been investigated. The thermal decomposition of Ettringite has been a subject of much discussion. It is observed that the temperature of thermal decomposition of Ettringite depends on pressure and humidity. In recent years, the formation of Ettringite,

and monosulfate in hydrothermal hydration of Portland cement have been studied by *in situ* synchrotron X-ray powder diffraction in comparison with the hydration of calcium aluminium oxide and gypsum mixtures. It is found that Ettringite can be converted to monosulfate when gypsum is consumed.[29] In addition, Meller *et al.* reported the thermal decomposition of calcium monosulfate to hydrogarnet [$Ca_3Al_2(OH)_{12}$] using *in situ* synchrotron X-ray diffraction.[125]

In order to improve the workability of cement paste, water reducing agents have been discovered and are now generally used. The interaction between water reducing agents and cement is still under investigation to prove whether water reducing agents adsorb on the surface of a hydrating cement grain. Yoshioka *et al.* reported the higher adsorption of water reducing agents on C_3A and C_4AF than on the C_3S and C_2S phases.[126]

Water reducing agents are adsorbed on the cement particles and act as dispersants by electrostatic and/or steric repulsion effects. The negative zeta potential of cement particles in pastes can be increased by adding superplasticizers, causing larger electrostatic repulsive forces between cement particles. The resulting steric repulsion between cement particles help to avoid the formation of agglomerates. As a result, the water requirement of a concrete or mortar mixture for a given workability can therefore be reduced, without losing its ability to maintain density and strength. The workability of concrete or mortar mixtures can hence be increased while water content remains fixed, providing unchanged workability and strength.

There are a number of publications reporting the study of water reducing agent adsorption on the formation of cement hydration products such as Ettringite, monosulfate, Syngenite ($K_2SO_4 \bullet CaSO_4 \bullet H_2O$), Portlandite, and Gypsum using the zeta potential technique. The results show that Syngenite, Portlandite, and Gypsum do not adsorb water reducing agents, while the additive can adsorb on cement grains mainly where the ettringite and monosulfate crystallise.[30] Ettringite can be produced in the presence of water reducing agents.

1.4.4 Use of Ca_2Al-LDHs in cement

Monosulfate has become an interesting material when it was found that water reducing agents such as β-naphthalene sulfonate formaldehyde (BNS) can intercalate into this layered calcium aluminate phase.[127] The intercalation of a polycarboxylate-type water reducing agent into a C_3A hydration product has been successfully studied. It was observed that C_3A can hydrate in aqueous polycarboxylate media and partially incorporate the anionic polymer within the galleries of the $[Ca_2Al(OH)_6]^+$layers.[128-130]

Monosulfate is a by-product of tricalcium aluminate hydration. The material has a hydrocalumite-like structure $[Ca_2Al(OH)_6{}^+X_{1/n}{}^{n-}\bullet yH_2O$, Ca_2Al-X LDHs] which is a layered material with interesting properties. The structure of Ca_2Al-X LDHs contains positively charged mixed metal hydroxide layers separated by charge-balancing hydrated anions between the layers. The interlayer anions may be replaced by anion exchange.

There are a number of publications investigating the synthesis of LDH-based additives for use in cement, such as $[Ca_2Al(OH)_6]Cl\bullet nH_2O$ for use as a hardening accelerator.[44] More recently, the intercalation of water reducing agents in Ca_2Al-X LDHs has been studied.[131] It may be possible to use LDHs to enhance the properties of cement. One way in which this may be achieved is by the synthesis of nano-sized Ca_2Al-LDHs. Furthermore, additive-intercalated LDHs may act as multifunctional additives because the LDHs can act as seed crystals for the hydration products of cement. LDH/polymer nanocomposites and these novel additives could allow us to overcome some of the disadvantages of cement such as low tensile and flexural strengths, its tendency to crack with changes in temperature and moisture, and relatively high moisture absorption and permeation.[108, 132-135]

1.5 Aims of this thesis

The aim of this thesis was to study LDH-based materials as models to obtain a better understanding of the interaction between organic admixtures and the cement phases.[107, 136, 137] It is hoped that new additive-intercalated LDHs could become much more effective multi-functional components in concrete. Thus the primary objective of this aspect was to develop novel LDH materials for use in cement.

The synthesis of novel doped variants of $[Ca_2Al(OH)_6]Cl•nH_2O$, by incorporating gallium in the LDH layers, $[Ca_2Ga_xAl_{(1-x)}(OH)_6]Cl•nH_2O$ ($Ca_2Ga_xAl_{(1-x)}$-Cl) LDH with *x* between 0 and 1, has been undertaken using the co-precipitation method.

In order to understand the effect of LDH-based additives on cement hydration, the intercalation of lignosulfonate, naphthalene sulfonate and polycarboxylate into $Ca_2Al(OH)_6NO_3•6H_2O$ (Ca_2Al-NO_3) has been investigated and their effects on cement hydration was studied using time-resolved X-ray diffraction and ultrasound shear-wave reflection studies.

To improve the efficiency of LDH-based additives, the synthesis of new nano-size additive-intercalated LDHs was investigated. Ca_2Al-NO_3 has been synthesised using non-ionic surfactant reverse micelles. The reverse micelle approach has also been applied to the synthesis of nitrite-intercalated layered double hydroxide $Ca_2Al(OH)_6NO_2•6H_2O$ (Ca_2Al-NO_2), in order to prepare a novel system for cement applications that exhibits multifunctional behaviour: acting both as a corrosion inhibitor, as well as a hydration accelerator.

In recent years, the use of LDHs in the synthesis of inorganic/organic nanocomposites has created a new emerging class of material. Synthetic LDHs offer elemental precision and chemical homogeneity for the inorganic phase. LDH/polymer nanocomposites exhibit improved mechanical, thermal, and gas barrier properties and reduced flammability. Hydrocalumite-like materials (Ca_2Al-LDHs) could be prepared in a suitable form in order to act as an attractive component with enhanced physical properties in polymer nanocomposites. In order to achieve a high dispersion of the Ca_2Al-LDHs in polymer nanocomposites,[138-141] a synthesis of highly dispersed Ca_2Al-LDH with hydrophobic surfaces is required. The synthesis of nanosized calcium aluminium LDHs in dodecylsulfate reverse micelles has been investigated.

1.6 References

1. M. Catti, G. Ferraris, S. Hull and A. Pavese, *Physics and Chemistry of Minerals*, 1995, **22**, 200-206.
2. R. Allmann, *Acta Crystallographica Section B*, 1968, **24**, 972-977.
3. H. Taylor, *Mineralogical Magazine*, 1973, **39**, 377-389.
4. F. Li, J. Liu, D. G. Evans and X. Duan, *Chemistry of Materials*, 2004, **16**, 1597-1602.
5. W. Jones, *Supramolecular Organization and Materials Design*, Cambridge University Press, 2008.
6. A. I. Khan and D. O'Hare, *Journal of Materials Chemistry*, 2002, **12**, 3191-3198.
7. F. Cavani, F. Trifirò and A. Vaccari, *Hydrotalcite-type anionic clays: preparation, properties and applications*, Elsevier, 1991.
8. J. L. Atwood, J.-M. Lehn, G. Alberti and T. Bein, *Comprehensive supramolecular chemistry. Vol. 7, Solid-state supramolecular chemistry: two-and three-dimensional inorganic networks*, 1996.
9. F. Kovanda, K. Jirátová, J. Rymeš and D. Koloušek, *Applied Clay Science*, 2001, **18**, 71-80.
10. J. Liu, F. Li, D. G. Evans and X. Duan, *Chemical Communications*, 2003, **4**, 542-543.
11. K. Parida, M. Satpathy and L. Mohapatra, *Journal of Materials Chemistry*, 2012, **22**, 7350-7357.
12. F. Bruna, R. Celis, I. Pavlovic, C. Barriga, J. Cornejo and M. Ulibarri, *Journal of Hazardous Materials*, 2009, **168**, 1476-1481.
13. S. Velu, V. Ramaswamy and S. Sivasanker, *Chemical Communications*, 1997, **21**, 2107-2108.
14. S. Velu, D. P. Sabde, N. Shah and S. Sivasanker, *Chemistry of Materials*, 1998, **10**, 3451-3458.
15. S. Velu, K. Suzuki, M. Okazaki, T. Osaki, S. Tomura and F. Ohashi, *Chemistry of Materials*, 1999, **11**, 2163-2172.
16. P. Koilraj and S. Kannan, *Journal of Colloid and Interface Science*, 2010, **341**, 289-297.
17. A. J. Marchi and C. R. Apesteguía, *Applied Clay Science*, 1998, **13**, 35-48.
18. X. Duan and D. G. Evans, *Layered Double Hydroxides*, Springer, 2006.
19. A. V. Besserguenev, A. M. Fogg, R. J. Francis, S. J. Price, D. O'Hare, V. P. Isupov and B. P. Tolochko, *Chemistry of Materials*, 1997, **9**, 241-247.
20. K. A. Tarasov, D. O'Hare and V. P. Isupov, *Inorganic Chemistry*, 2003, **42**, 1919-1927.
21. G. R. Williams, S. J. Moorhouse, T. J. Prior, A. M. Fogg, N. H. Rees and D. O'Hare, *Dalton Transactions*, 2011, **40**, 6012-6022.
22. A. M. Fogg, G. R. Williams, R. Chester and D. O'Hare, *Journal of Materials Chemistry*, 2004, **14**, 2369-2371.
23. R. Allmann and H. Jepsen, *Neues Jahrbuch für Mineralogie, Monatshefte*, 1969, 544-551.
24. A. Besserguenev, A. Fogg, R. Francis, S. Price, D. O'Hare, V. Isupov and B. Tolochko, *Chemistry of Materials*, 1997, **9**, 241-247.
25. S. Krivovichev, V. Yakovenchuk, E. Zhitova, A. Zolotarev, Y. A. Pakhomovsky and G. Y. Ivanyuk, *Mineralogical Magazine*, 2010, **74**, 821-832.
26. F. Buttler, L. Dent Glasser and H. Taylor, *Journal of the American Ceramic Society*, 1959, **42**, 121-126.

27. J. Rapin, G. Renaudin, E. Elkaim and M. Francois, *Cement and Concrete Research*, 2002, **32**, 513-520.
28. G. Renaudin, J.-P. Rapin, E. Elkaim and M. François, *Cement and Concrete Research*, 2004, **34**, 1845-1852.
29. A. N. Christensen, T. R. Jensen and J. C. Hanson, *Journal of Solid State Chemistry*, 2004, **177**, 1944-1951.
30. J. Plank and C. Hirsch, *Cement and Concrete Research*, 2007, **37**, 537-542.
31. G. Renaudin, J. P. Rapin, B. Humbert and M. François, *Cement and Concrete Research*, 2000, **30**, 307-314.
32. I. M. Kolthoff, *The Journal of Physical Chemistry*, 1931, **36**, 860-881.
33. W. T. Reichle, *Journal of Catalysis*, 1985, **94**, 547-557.
34. S. Bonnet, C. Forano, A. de Roy, J. P. Besse, P. Maillard and M. Momenteau, *Chemistry of Materials*, 1996, **8**, 1962-1968.
35. W. Kagunya, Z. Hassan and W. Jones, *Inorganic Chemistry*, 1996, **35**, 5970-5974.
36. A. I. Tsyganok, K. Suzuki, S. Hamakawa, K. Takehira and T. Hayakawa, *Chemistry Letters*, 2001, **30**, 24.
37. Q. Wang, H. H. Tay, Z. Guo, L. Chen, Y. Liu, J. Chang, Z. Zhong, J. Luo and A. Borgna, *Applied Clay Science*, 2012, **55**, 18-26.
38. Z. P. Xu, G. Stevenson, C.-Q. Lu and G. Q. Lu, *The Journal of Physical Chemistry B*, 2006, **110**, 16923-16929.
39. Z. P. Xu, G. S. Stevenson, C.-Q. Lu, G. Q. Lu, P. F. Bartlett and P. P. Gray, *Journal of the American Chemical Society*, 2006, **128**, 36-37.
40. J. A. Gursky, S. D. Blough, C. Luna, C. Gomez, A. N. Luevano and E. A. Gardner, *Journal of the American Chemical Society*, 2006, **128**, 8376-8377.
41. S. Zeng, X. Xu, S. Wang, Q. Gong, R. Liu and Y. Yu, *Materials Chemistry and Physics*, 2013.
42. Y. Zhao, F. Li, R. Zhang, D. G. Evans and X. Duan, *Chemistry of Materials*, 2002, **14**, 4286-4291.
43. Z. Gu, X. Xiang, G. Fan and F. Li, *The Journal of Physical Chemistry C*, 2008, **112**, 18459-18466.
44. S. Xu, Z. Chen, B. Zhang, J. Yu, F. Zhang and D. G. Evans, *Chemical Engineering Journal*, 2009, **155**, 881-885.
45. M. Adachi-Pagano, C. Forano and J.-P. Besse, *Journal of Materials Chemistry*, 2003, **13**, 1988-1993.
46. J. Eastoe, M. J. Hollamby and L. Hudson, *Advances in Colloid and Interface Science*, 2006, **128–130**, 5-15.
47. M. Li, H. Schnablegger and S. Mann, *Nature*, 1999, **402**, 393-395.
48. A. P. Herrera, O. Resto, J. G. Briano and C. Rinaldi, *Nanotechnology*, 2005, **16**, S618.
49. T. Hyeon, *Chemical Communications*, 2003, **8**, 927-934.
50. Y. Lee, J. Lee, C. J. Bae, J. G. Park, H. J. Noh, J. H. Park and T. Hyeon, *Advanced Functional Materials*, 2005, **15**, 503-509.
51. S. Sathyamurthy, K. J. Leonard, R. T. Dabestani and M. P. Paranthaman, *Nanotechnology*, 2005, **16**, 1960.
52. L. Qi, *Encyclopedia of Surface and Colloid Science. Second Edition. New York: Taylor & Francis*, 2006, 6183.
53. T. Tan, S. Liu, Y. Zhang, M. Han and S. Selvan, *Comprehensive Nanoscience and Technology*, 2011, **5**, 399-441.
54. K. Ratinac, H. Zhu, L. Stadtmueller and S. Ringer, in *Materials Forum*, 2002, pp. 44-73.

55. K. Holmberg, *Journal of Colloid and Interface Science*, 2004, **274**, 355-364.
56. G. Hu, N. Wang, D. O'Hare and J. Davis, *Journal of Materials Chemistry*, 2007, **17**, 2257-2266.
57. G. Hu and D. O'Hare, *Journal of the American Chemical Society*, 2005, **127**, 17808-17813.
58. C. J. Wang, Y. A. Wu, R. M. Jacobs, J. H. Warner, G. R. Williams and D. O'Hare, *Chemistry of Materials*, 2010, **23**, 171-180.
59. A. Wongariyakawee, F. Schäeffel, J. H. Warner and D. O'Hare, *Journal of Materials Chemistry*, 2012, **22**, 7751-7756.
60. P. Gunawan and R. Xu, *Journal of Materials Chemistry*, 2008, **18**, 2112-2120.
61. L. Li, Y. Feng, Y. Li, W. Zhao and J. Shi, *Angewandte Chemie International Edition*, 2009, **48**, 5888-5892.
62. H. Wu, Q. Jiao, Y. Zhao, S. Huang, X. Li, H. Liu and M. Zhou, *Materials Characterization*, 2010, **61**, 227-232.
63. N. Iyi, Y. Ebina and T. Sasaki, *Langmuir*, 2008, **24**, 5591-5598.
64. M. S. Yarger, E. M. Steinmiller and K.-S. Choi, *Inorganic Chemistry*, 2008, **47**, 5859-5865.
65. E. Scavetta, B. Ballarin, M. Gazzano and D. Tonelli, *Electrochimica Acta*, 2009, **54**, 1027-1033.
66. A. Khenifi, Z. Derriche, C. Forano, V. Prevot, C. Mousty, E. Scavetta, B. Ballarin, L. Guadagnini and D. Tonelli, *Analytica Chimica Acta*, 2009, **654**, 97-102.
67. F. Zhang, M. Sun, S. Xu, L. Zhao and B. Zhang, *Chemical Engineering Journal*, 2008, **141**, 362-367.
68. J. H. Lee, S. W. Rhee and D.-Y. Jung, *Journal of the American Chemical Society*, 2007, **129**, 3522-3523.
69. X. Lei, L. Yang, F. Zhang, D. G. Evans and X. Duan, *Chemistry Letters*, 2005, **34**, 1610-1611.
70. Z. Lü, F. Zhang, X. Lei, L. Yang, D. G. Evans and X. Duan, *Chemical Engineering Science*, 2007, **62**, 6069-6075.
71. Q. Wang and D. O'Hare, *Chemical Reviews*, 2012, **112**, 4124-4155.
72. M. Adachi-Pagano, C. Forano and J.-P. Besse, *Chemical Communications*, 2000, 91-92.
73. M. Singh, M. I. Ogden, G. M. Parkinson, C. Buckley and J. Connolly, *Journal of Materials Chemistry*, 2004, **14**, 871-874.
74. V. V. Naik, T. Ramesh and S. Vasudevan, *The Journal of Physical Chemistry Letters*, 2011, **2**, 1193-1198.
75. V. V. Naik and S. Vasudevan, *Langmuir*, 2011, **27**, 13276-13283.
76. T. Hibino and W. Jones, *J. Mater. Chem.*, 2001, **11**, 1321-1323.
77. T. Hibino, *Chemistry of Materials*, 2004, **16**, 5482-5488.
78. L. Li, R. Ma, Y. Ebina, N. Iyi and T. Sasaki, *Chemistry of Materials*, 2005, **17**, 4386-4391.
79. V. R. Constantino and T. J. Pinnavaia, *Catalysis Letters*, 1994, **23**, 361-367.
80. S. Bhattacharjee, T. J. Dines and J. A. Anderson, *Journal of Catalysis*, 2004, **225**, 398-407.
81. M. Chibwe and T. J. Pinnavaia, *Journal of the Chemical Society, Chemical Communications*, 1993, 278-280.
82. H. Zhang, R. Qi, D. G. Evans and X. Duan, *Journal of Solid State Chemistry*, 2004, **177**, 772-780.
83. M. Veronica, B. Graciela, A. Norma and L. Miguel, *Chemical Engineering Journal*, 2008, **138**, 602-607.

84. V. R. L. Constantino and T. J. Pinnavaia, *Inorganic Chemistry*, 1995, **34**, 883-892.
85. M. L. Kantam, B. V. Prakash, C. R. V. Reddy and B. Sreedhar, *Synlett*, 2005, **2005**, 2329-2332.
86. F. Li, Q. Tan, D. G. Evans and X. Duan, *Catalysis Letters*, 2005, **99**, 151-156.
87. X. Guo, F. Zhang, D. G. Evans and X. Duan, *Chemical Communications*, 2010, **46**, 5197-5210.
88. A. Alejandre, F. Medina, X. Rodriguez, P. Salagre, Y. Cesteros and J. Sueiras, *Applied Catalysis B: Environmental*, 2001, **30**, 195-207.
89. S. V. Prasanna, R. Rao and P. V. Kamath, *Journal of Colloid and Interface Science*, 2006, **304**, 292-299.
90. T. Kameda, M. Saito and Y. Umetsu, *Journal of Alloys and Compounds*, 2005, **402**, 46-52.
91. Q. Wang, J. Luo, Z. Zhong and A. Borgna, *Energy & Environmental Science*, 2011, **4**, 42-55.
92. Q. Wang, H. H. Tay, D. J. W. Ng, L. Chen, Y. Liu, J. Chang, Z. Zhong, J. Luo and A. Borgna, *ChemSusChem*, 2010, **3**, 965-973.
93. Q. Wang, Z. Wu, H. H. Tay, L. Chen, Y. Liu, J. Chang, Z. Zhong, J. Luo and A. Borgna, *Catalysis Today*, 2011, **164**, 198-203.
94. Q. Wang, H. H. Tay, Z. Guo, L. Chen, Y. Liu, J. Chang, Z. Zhong, J. Luo and A. Borgna, *Applied Clay Science*, 2012, **55**, 18-26.
95. M. Ram Reddy, Z. Xu, G. Lu and J. Diniz da Costa, *Industrial & Engineering Chemistry Research*, 2006, **45**, 7504-7509.
96. B. M. Choudary, S. Madhi, N. S. Chowdari, M. L. Kantam and B. Sreedhar, *Journal of the American Chemical Society*, 2002, **124**, 14127-14136.
97. J.-H. Choy, J.-S. Jung, J.-M. Oh, M. Park, J. Jeong, Y.-K. Kang and O.-J. Han, *Biomaterials*, 2004, **25**, 3059-3064.
98. A. I. Khan, L. Lei, A. J. Norquist and D. O'Hare, *Chem. Commun.*, 2001, 2342-2343.
99. B. Li, J. He, D. G Evans and X. Duan, *Applied Clay Science*, 2004, **27**, 199-207.
100. Z. P. Xu and G. Lu, *Pure and Applied Chemistry*, 2006, **78**, 1771-1779.
101. M.-F. Chiang and T.-M. Wu, *Composites Science and Technology*, 2010, **70**, 110-115.
102. D.-Y. Wang, A. Leuteritz, Y.-Z. Wang, U. Wagenknecht and G. Heinrich, *Polymer Degradation and Stability*, 2010, **95**, 2474-2480.
103. M. Zheludkevich, S. Poznyak, L. Rodrigues, D. Raps, T. Hack, L. Dick, T. Nunes and M. Ferreira, *Corrosion Science*, 2010, **52**, 602-611.
104. E. Káfuňková, K. Lang, P. Kubát, M. Klementová, J. Mosinger, M. Šlouf, A.-L. Troutier-Thuilliez, F. Leroux, V. Verney and C. Taviot-Guého, *Journal of Materials Chemistry*, 2010, **20**, 9423-9432.
105. D.-Y. Wang, A. Das, F. R. Costa, A. Leuteritz, Y.-Z. Wang, U. Wagenknecht and G. Heinrich, *Langmuir*, 2010, **26**, 14162-14169.
106. T. Matschei, B. Lothenbach and F. Glasser, *Cement and Concrete Research*, 2007, **37**, 118-130.
107. L. Raki, J. Beaudoin, R. Alizadeh, J. Makar and T. Sato, *Materials*, 2010, **3**, 918-942.
108. L. Raki, J. Beaudoin and L. Mitchell, *Cement and Concrete Research*, 2004, **34**, 1717-1724.
109. Y. Ju-Nam and J. R. Lead, *Science of the Total Environment*, 2008, **400**, 396-414.
110. P. Hewlett, *Lea's chemistry of Cement and Concrete*, Butterworth-Heinemann, 2003.

111. S. Ghosh, *Cement and concrete science & technology*, Thomas Telford, 1991.
112. D. Double, P. Hewlett, K. Sing and J. Raffle, *Philosophical Transactions of the Royal Society of London. Series A, Mathematical and Physical Sciences*, 1983, **310**, 53-66.
113. L. E. Copeland, D. Kantro and G. J. Verbeck, *Chemistry of hydration of Portland cement*, Portland Cement Association, Research and Development Laboratories, 1960.
114. J. J. Chen, J. J. Thomas, H. F. Taylor and H. M. Jennings, *Cement and Concrete Research*, 2004, **34**, 1499-1519.
115. H. M. Jennings and J. W. Bullard, *Cement and Concrete Research*, 2011, **41**, 727-735.
116. H. F. Taylor, *Journal of the American Ceramic Society*, 1986, **69**, 464-467.
117. I. G. Richardson, *Cement and Concrete Research*, 1999, **29**, 1131-1147.
118. I. G. Richardson, *Cement and Concrete Research*, 2004, **34**, 1733-1777.
119. P. D. Tennis and H. M. Jennings, *Cement and Concrete Research*, 2000, **30**, 855-863.
120. H. M. Jennings, *Cement and Concrete Research*, 2000, **30**, 101-116.
121. S. M. Clark, B. Colas, M. Kunz, S. Speziale and P. J. Monteiro, *Cement and Concrete Research*, 2008, **38**, 19-26.
122. I. van Odler, *Lea's Chemistry of Cement and Concrete*, 2003, 241.
123. C. Cohen-Addad, P. Ducros and E. Bertaut, *Acta Crystallographica*, 1967, **23**, 220-230.
124. P. Villars, K. Cenzual, J. Daams, R. Gladyshevskii, O. Shcherban, V. Dubenskyy, V. Kuprysyuk and I. Savysyuk, in *Structure Types. Part 8: Space Groups (156) P3m1–(148) R-3*, Springer, 2010, pp. 691-691.
125. N. Meller, K. Kyritsis and C. Hall, *Journal of Solid State Chemistry*, 2009, **182**, 2743-2747.
126. K. Yoshioka, E.-i. Tazawa, K. Kawai and T. Enohata, *Cement and Concrete Research*, 2002, **32**, 1507-1513.
127. V. Fernon, A. Vichot, N. Le Goanvic, P. Colombet, F. Corazza and U. Costa, *ACI Special Publication*, 1997, **173**.
128. J. Plank, Z. Dai and P. Andres, *Materials letters*, 2006, **60**, 3614-3617.
129. J. Plank, Z. Dai, N. Zouaoui and D. Vlad, *ACI Special Publication*, 2006, **239**.
130. J. Plank, H. Keller, P. R. Andres and Z. Dai, *Inorganica Chimica Acta*, 2006, **359**, 4901-4908.
131. L. Raki and J. J. Beaudoin, US Patent 8,404,041, 2013.
132. D. Van Gemert, L. Czarnecki, M. Maultzsch, H. Schorn, A. Beeldens, P. Łukowski and E. Knapen, *Cement and Concrete Composites*, 2005, **27**, 926-933.
133. A. Beeldens, D. Van Gemert, H. Schorn, Y. Ohama and L. Czarnecki, *Materials and structures*, 2005, **38**, 601-607.
134. S. Donatello, M. Tyrer and C. Cheeseman, *Construction and Building Materials*, 2009, **23**, 1761-1767.
135. L. Wang, S. Su, D. Chen and C. A. Wilkie, *Polymer Degradation and Stability*, 2009, **94**, 770-781.
136. R. Gollop and H. Taylor, *Cement and Concrete Research*, 1994, **24**, 1347-1358.
137. R. Gollop and H. Taylor, *Cement and Concrete Research*, 1996, **26**, 1029-1044.
138. F. Leroux and J.-P. Besse, *Chemistry of Materials*, 2001, **13**, 3507-3515.
139. O. Wilson Jr, T. Olorunyolemi, A. Jaworski, L. Borum, D. Young, A. Siriwat, E. Dickens, C. Oriakhi and M. Lerner, *Applied Clay Science*, 1999, **15**, 265-279.

140. F. R. Costa, M. Abdel-Goad, U. Wagenknecht and G. Heinrich, *Polymer*, 2005, **46**, 4447-4453.
141. L. Qiu, W. Chen and B. Qu, *Polymer Degradation and Stability*, 2005, **87**, 433-440.

Chapter 2: Synthesis and Characterisation of Gallium Doped $[Ca_2Al(OH)_6]Cl{\bullet}nH_2O$ LDHs

2.1 Introduction

Friedel's salt is the common name of chloride intercalated Ca_2Al-LDH ($Ca_2Al(OH)_6Cl{\bullet}nH_2O$, Ca_2Al-Cl) in cement chemistry. This compound was first mentioned by Friedel in 1897, when investigating the reaction between lime and aluminum chloride.[1-4] The product from the reaction called hydrated tetracalcium bichloroaluminate is a type of AFm (monosulfate) phase, which is a family of products from cement hydration. AFm phases are composed of positively charged layers of $[Ca_2Al(OH)_6]^+$, negatively charged interlayers containing coordinated water (X^- and nH_2O; where X^- is an anion generally found in the cement hydration system,[5-9] such as Cl^-, CO_3^{2-}, and SO_4^{2-}).

A number of publications have reported the effect of Friedel's salt on cement hydration, Friedel's salt can slow down chloride attack which is the main factor of structural damage in reinforced concrete located near marine environments.[3, 4, 10-13] The chloride ions cause the initiation of corrosion by external penetration into the concrete. Steel corrosion in concrete occurs at high concentration of chloride. Chloride binding can delay achieving the threshold chloride concentration required to trigger corrosion by removing chloride ions from the hydration system. Chloride is captured in cement hydration due to the adsorption of the bulk Cl^- ions present in the hydration system into $[Ca_2Al(OH)_6]^+$, from the hydration of calcium aluminate phases.

Over the years, LDHs have been synthesised and applied in industry. A number of synthetic LDHs were studied for removal of arsenate from aqueous systems.[14-18] The synthesis of ternary LDHs[19-22] for industry applications is also of interest.[22, 23] $Mg_{(2-x)}Ca_xAl$-Cl; $0 \leq x \leq 2.0$, were investigated as absorbents to remove triplepolyphosphate (triphosphate).[24] A series of $Mg_6Al_{(2-2x)}Ga_{2x}(OH)_{16}CO_3.nH_2O$; where $0 < x < 1$, was synthesised and studied as CO_2 adsorbents.[25] It was found that the CO_2

adsorptivity and stability increases with gallium substitution in comparison to unsubstituted hydrotalcites.

The large-scale production of Ca_2Al-Cl was investigated for use as a concrete hardening accelerator.[26, 27] The novel doped variants of $[Ca_2Al(OH)_6]Cl•nH_2O$ may be more reactive than pristine Ca_2Al-LDH due to the distortion of the LDH structure. The primary objective of this chapter is to investigate the possibility of preparing a mixed Ga/Al layered double hydroxides.

2.2 Study of pH effect on the synthesis of $[Ca_2Ga(OH)_6]Cl•nH_2O$

The effect of pH on the Ca_2Ga-Cl synthesis has been investigated in order to achieve optimum crystallinity of the LDH. 0.97 g of $CaCl_2•2H_2O$, and 0.84 g of $Ga(NO_3)_3•H_2O$ were mixed and added to 10 ml of water. After mixing, the solution was transferred into a glass Luer tip style syringe. Separately, 250 ml of a mixture of DI water and ethanol in a 2:3 ratio was prepared and adjusted to pH 4 using HCl solution. 2M NaOH was used to adjust pH of the reaction which was varied from pH 10.5, 11.0, and 11.5.

This precursor solution was then added into the water/ethanol mixture and the pH was controlled at 10.5 ± 0.1, 11.0 ± 0.1, and 11.5 ± 0.1 by adding 2M NaOH. All mixtures were stirred continuously at 65 ^oC for 2 days. All solid products were isolated by vacuum filtration and removed impurities by washing extensively with deionised water, followed by a small amount of acetone to facilitate drying, and left to dry under vacuum for approximately 4 hours.

2.2.1 X-ray powder diffraction data

The X-ray diffraction patterns of Ca_2Ga-Cl LDHs, formed in reactions with different pH, are shown in Figure 2.1. The XRD data for Ca_2Ga-Cl LDHs can be indexed using a rhombohydral unit cell with a = 5.83 Å, c = 24.0 Å, corresponding to the chloride intercalated LDH.[28] The LDH synthesis at pH 10.5 provided the highest crystallinity of LDH as shown in Table 2.1. Portlandite can be observed in Ca_2Ga-Cl sample synthesised at pH 11.5.

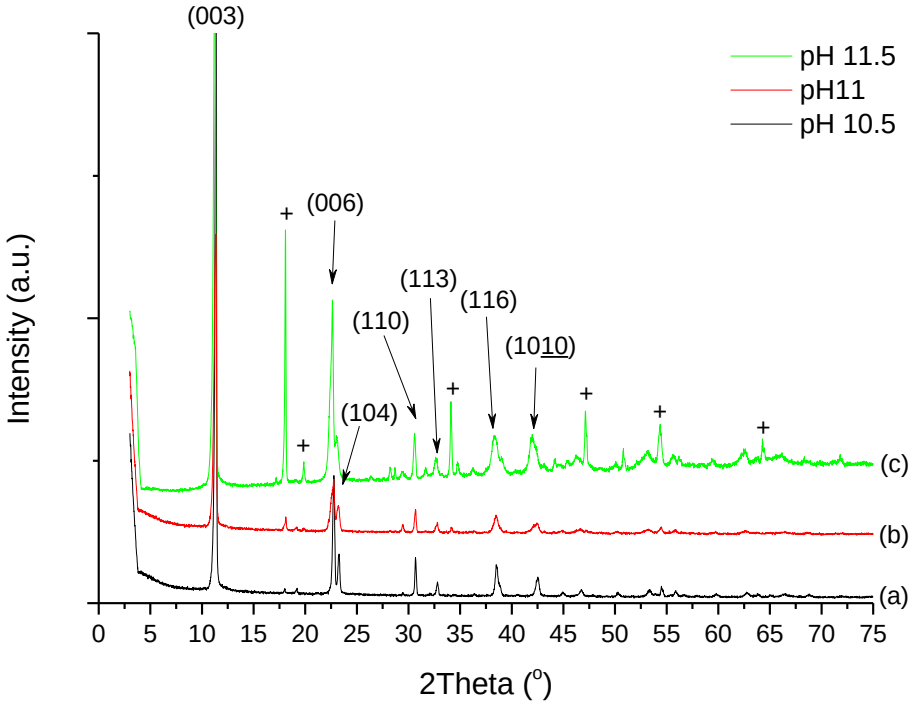

Figure 2.1. XRD data for Ca_2Ga-Cl at different pHs. + corresponds to portlandite [$Ca(OH)_2$]. The Bragg reflections are indexed to the rhombohedral cell, a = 5.83 Å and c = 24.0 Å.

Table 2.1. A summary of the X-ray diffraction data for Ca_2Ga-Cl LDHs.

Sample	(003) Bragg reflection			
	Position/2θ	d-spacing/Å	FWHM/°	CDS/nm
Ca_2Ga-Cl pH 10.5	11.35	7.80	0.13	60.7
Ca_2Ga-Cl pH 11	11.35	7.80	0.23	34.3
Ca_2Ga-Cl pH 11.5	11.27	7.85	0.20	39.5

FWHM = full width at half maximum, Scherrer equation ($CDS = K\lambda(\beta\cos\theta)^{-1}$); K = 0.89,[29]

CDS = Crystalline Domain Size.

2.3 Synthesis of Gallium doped variants of $[Ca_2Al(OH)_6]Cl•nH_2O$

The synthesis of novel doped variants of $[Ca_2Al(OH)_6]Cl•nH_2O$ by incorporating gallium in the LDH layers, $[Ca_2Ga_xAl_{(1-x)}(OH)_6]Cl•nH_2O$ ($Ca_2Ga_xAl_{(1-x)}$-Cl) LDH where x = 0, 0.05, 0.10, 0.15, 0.20, 0.30, 0.40, 0.50, 0.60, 0.70, 0.80, 0.90, and 1.00, were undertaken using the co-precipitation method.[30] A series of $Ca_2Ga_xAl_{(1-x)}$-Cl LDHs were prepared by varying the concentration of the gallium (III) cations used in the synthesis, x, from 0, 0.05, 0.10, 0.15, 0.20, 0.30, 0.40, 0.50, 0.60, 0.70, 0.80, 0.90 and 1.00.

250 ml of a mixture of DI water and ethanol in a 2:3 ratio was prepared and adjusted to pH 4 using HCl solution, followed by 2M NaOH until pH 10.5 was reached. Separately, $CaCl_2•2H_2O$, $Al(NO_3)_3•9H_2O$, and $Ga(NO_3)_3•H_2O$ was mixed and added then to 10 ml of water. The ratio of the salts was varied depending on the amount of gallium doped into the LDHs designed (section 7.3). After mixing, the solution was transferred into a glass Luer tip style syringe. This solution was then added into a water/ethanol mixture and pH is controlled to be at 10.5 ± 0.1 by adding 2M NaOH. The mixture was stirred continuously at 65 ^oC for 2 days. All solid products were isolated by vacuum filtration and washed extensively with deionised water to remove impurities, followed by a small amount of acetone to facilitate drying.

2.3.1 X-ray powder diffraction data

The X-ray diffraction patterns of a series of $Ca_2Ga_xAl_{(1-x)}$-Cl samples ($0 < x < 1$) are shown in Figure 2.2 and 2.3. The data illustrate that the c parameter (3x interlayer spacing) of the $Ca_2Ga_xAl_{(1-x)}$-Cl; $0 < x < 1$ samples are similar. The c parameter of these samples varies between 23.3 and 23.6 Å with an approximate 7.8 Å interlayer d-spacing due to Cl anion intercalation.[30] The slight variation of the observed interlayer spacing may be due to small variations in the orientation or quantity of the interlayer water.

The XRD pattern of Ca_2Al-Cl can be indexed using a rhombohedral unit cell with a = 5.74, c = 23.3. Small amounts of gibbsite and portlandite are observed in Ca_2Al-Cl. Ca_2Al-LDHs co-precipitate as highly crystalline solids when the pH of the reaction is 11.5. The LDHs are more crystalline when more gallium is doped into the system. Doping with Ga^{3+} has a clear influence on the formation of the LDHs. When x = 0.05 and 0.10, the amount of Ga^{3+} ions present is not sufficient to incorporate Ga^{3+} into the layers. The ratio

between Ca^{2+} and Al^{3+} in solution is not ideal and $Ca(OH)_2$ and $Al(OH)_3$ form as impurities. At higher Ga^{3+} doping, the d-spacing of the (110) Bragg reflection becomes slightly larger because the higher amount of Ga^{3+}, which has a larger ionic radius than Al^{3+}. All $Ca_2Ga_xAl_{(1-x)}$-Cl XRD patterns can be indexed using a rhombohydral unit cell with a value range of *a* between 5.74 Å[28] and 5.82 Å, while the pattern of Ca_2Ga-Cl can be indexed using a rhombohedral unit cell with a = 5.82 Å, c = 23.5 Å. A summary of the unit cell parameters are given in Table 2.2.

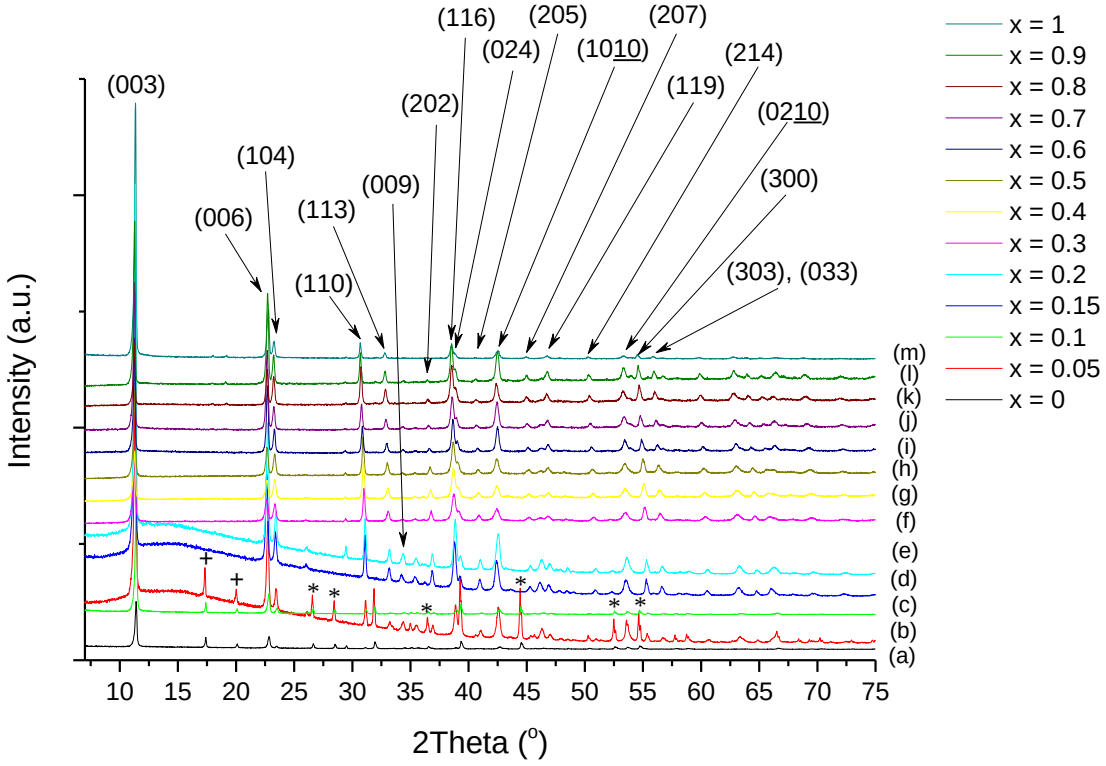

Figure 2.2. Summary of the XRD data for $Ca_2Ga_xAl_{(1-x)}$-Cl LDHs; (a) x = 0, (b) x = 0.05, (c) x = 0.1, (d) x = 0.15, (e) x = 0.2, (f) x = 0.3, (g) x = 0.4, (h) x = 0.5, (i) x = 0.6, (j) x = 0.7, (k) x = 0.8, (l) x = 0.9, (m) x = 1.0. + corresponds to gibbsite [$Al(OH)_3$] and * corresponds to portlandite [$Ca(OH)_2$].

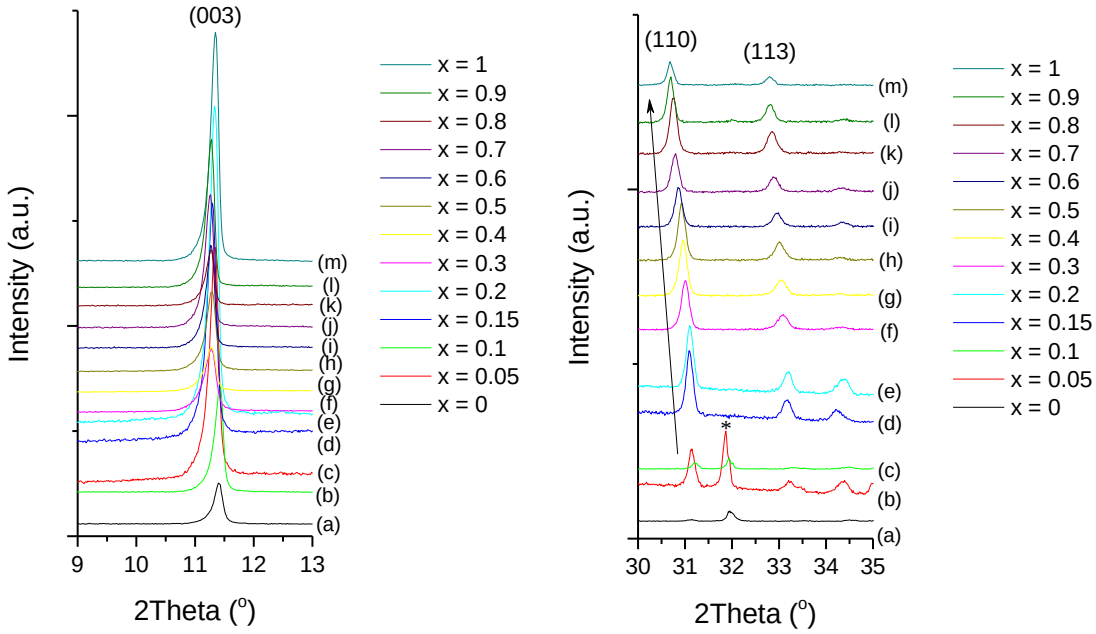

Figure 2.3. Summary of the powder XRD data showing the (003) and (110) Bragg reflections of (a) – (m) $Ca_2Ga_xAl_{(1-x)}$-Cl LDHs where x = (a) 0, (b) 0.05, (c) 0.1, (d) 0.15, (e) 0.2, (f) 0.3, (g) 0.4, (h) 0.5, (i) 0.6, (j) 0.7, (k) 0.8, (l) 0.9, and (m) 1.0. * corresponds to portlandite [$Ca(OH)_2$].

Table 2.2. Calculated unit cell parameters for $Ca_2Ga_xAl_{(1-x)}$-Cl; $0 < x < 1$.

$Ca_2Ga_xAl_{(1-x)}$-Cl	Unit cell parameters (Å)	
(x)	a	c
0	5.74	23.3
0.05	5.74	23.3
0.1	5.74	23.3
0.15	5.74	23.5
0.2	5.76	23.4
0.3	5.76	23.5
0.4	5.78	23.5
0.5	5.78	23.5
0.6	5.80	23.6
0.7	5.80	23.6
0.8	5.82	23.6
0.9	5.82	23.6
1.0	5.82	23.5

[#] x corresponds to the molar amount of $Ga(NO_3)_3 \bullet H_2O$ added to the reaction mixture.

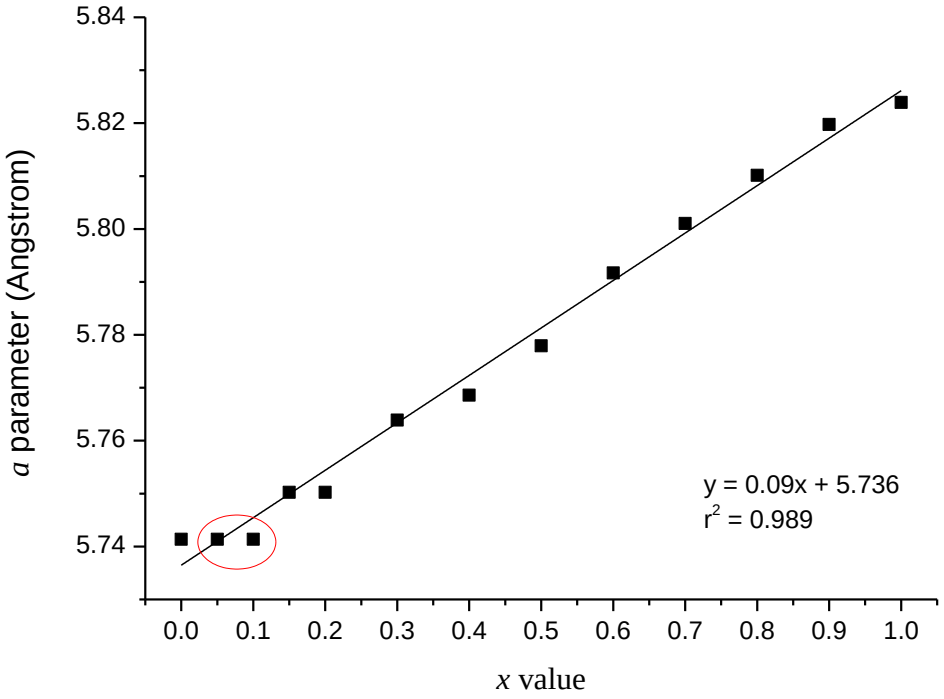

Figure 2.4. A plot of *a* parameter of $Ca_2Ga_xAl_{(1-x)}$-Cl LDHs VS the amount of gallium incorporated in Ca_2Al-Cl defined by *x* value from $Ca_2Ga_xAl_{(1-x)}$-Cl. The *x* value corresponds to the molar amount of $Ga(NO_3)_3 \bullet H_2O$ added to the reaction mixture. The *a* parameters of $Ca_2Ga_xAl_{(1-x)}$-Cl LDHs without Ga^{3+} incorporation present in red circle.

The full width at half maximum (FWHM) values of the (110) Bragg reflections (Table 2.3) observed in $Ca_2Ga_xAl_{(1-x)}$-Cl LDHs are constant for low amounts of Ga^{3+} doping.

Small change in the full width at half maximum (FWHM) values of the (110) Bragg reflections are observed in $Ca_2Ga_xAl_{(1-x)}$-Cl for *x* between 0.3 – 0.5 and 0.7 – 0.8 in comparison to those of the reflections in Ca_2Al-Cl and Ca_2Ga-Cl LDHs. Application of the Scherrer equation would suggest that the crystalline domain length along the *a*- and *b*-axes decreases which might be due to the Ga^{3+} doping affecting a distortion of the LDH layers. These appears to be no systematic trend in the crystallinity of $Ca_2Ga_xAl_{(1-x)}$-Cl; where $0 < x < 1$ along the *c*- axis.

Table 2.3. A summary of the selected Bragg reflection positions and line width from the X-ray diffraction data for $Ca_2Ga_xAl_{(1-x)}$-Cl; $0 < x < 1$.

$Ca_2Ga_xAl_{(1-x)}$-Cl	Bragg Reflection							
	(110)				(003)			
(x)	d-spacing (Å)	2θ (^{o})	FWHM (^{o})	CDS (nm)	d-spacing (Å)	2θ (^{o})	FWHM (^{o})	CDS (nm)
0	2.87	31.1	0.13	62.7	7.75	11.4	0.13	60.7
0.05	2.87	31.1	0.13	62.7	7.75	11.4	0.13	60.7
0.1	2.87	31.1	0.13	62.7	7.75	11.4	0.13	60.7
0.15	2.87	31.1	0.13	62.7	7.82	11.3	0.17	46.4
0.2	2.88	31.0	0.13	62.7	7.80	11.3	0.17	46.4
0.3	2.88	31.0	0.17	48.0	7.84	11.3	0.17	46.4
0.4	2.89	30.9	0.17	48.0	7.84	11.3	0.17	46.4
0.5	2.89	30.9	0.17	48.0	7.84	11.3	0.13	60.7
0.6	2.90	30.8	0.13	62.7	7.85	11.3	0.13	60.7
0.7	2.90	30.8	0.17	47.9	7.86	11.2	0.13	60.7
0.8	2.91	30.7	0.17	47.9	7.85	11.3	0.17	46.4
0.9	2.91	30.7	0.13	62.7	7.85	11.3	0.13	60.7
1.0	2.91	30.7	0.13	62.7	7.82	11.3	0.13	60.7

FWHM = full width at half maximum, Scherrer equation ($CDS = K\lambda(\beta\cos\theta)^{-1}$); $K = 0.89$,[29]

CDS = Crystalline Domain Size, determined by Scherrer equation.

2.3.2 Infrared spectroscopy data

FTIR spectra of the $Ca_2Ga_xAl_{(1-x)}$-Cl; $0 < x < 1$ series in Figure 2.5 show the absorptions due to the stretching vibration of the hydroxyl groups of the inorganic layers and of the interlayer water between 3700-3000 cm^{-1}. The O-H bending vibration of the interlayer water is observed at 1624 cm^{-1}. The stretching vibration of M-O, M-O-M, and O-M-O bonds, where M denotes metal atoms, occur between 900 and 600 cm^{-1}.[31]

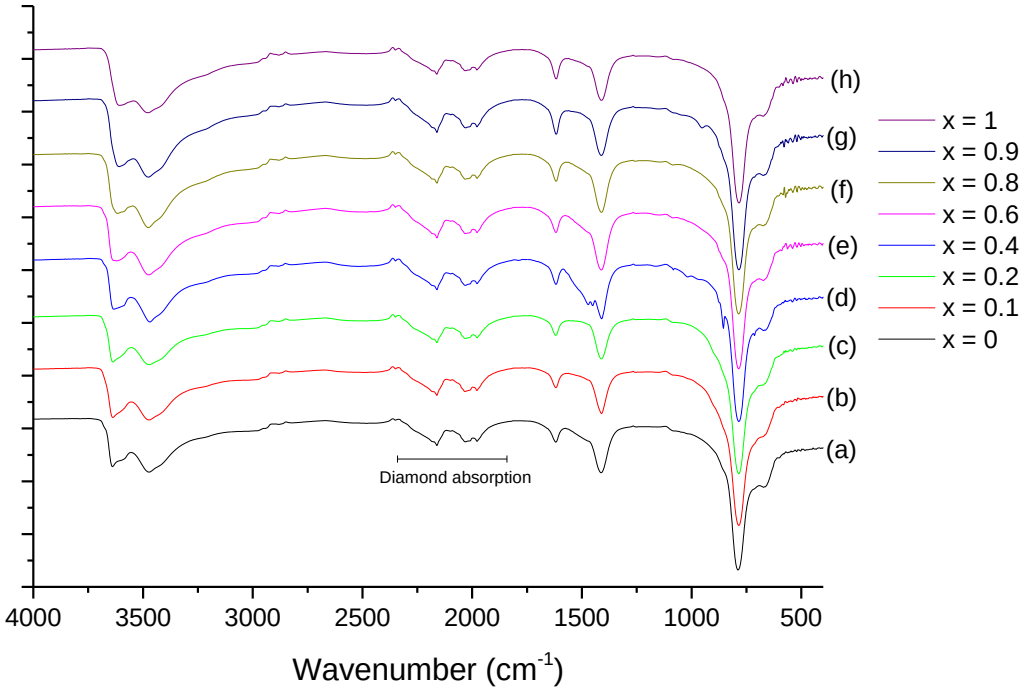

Figure 2.5. IR spectra of (a) – (h) $Ca_2Ga_xAl_{(1-x)}$-Cl LDHs where x = (a) 0, (b) 0.1, (c) 0.2, (d) 0.4, (e) 0.6, (f) 0.8, (g) 0.9, and (h) 1.0.

2.3.3 Electron microscopy study

The size and morphology of the $Ca_2Ga_xAl_{(1-x)}$-Cl samples were analysed by scanning electron microscopy (SEM). The SEM images (Figure 2.6) show that all samples are composed of platelet crystallites around 2µm in size. A number of individual platelets can be seen as well as some aggregates. The data suggest that the LDH particles synthesised by the co-precipitation method are similar to the morphology of monosulfate (Figure 2.6(g)), the hydration product of tricalcium aluminate cement paste reacted with gypsum. The corresponding EDX analysis indicates that Ga^{3+} cations incorporate into the $Ca_2Ga_xAl_{(1-x)}$-Cl materials when doping gallium with x = 0.15. However, the amount of gallium in the isolated LDHs is lower than that used in the reaction. When x is higher than 0.7, the amount of gallium in the LDH layer is higher than expected. It is possible that Al^{3+} can leach out from the layer to achieve the greater proportion of Ga^{3+}/Al^{3+} in order to form a more stable LDH layer, when Ga^{3+} is the major trivalent cation present. A summary of the EDX analysis of Ga^{3+} loading is detailed in Table 2.4.

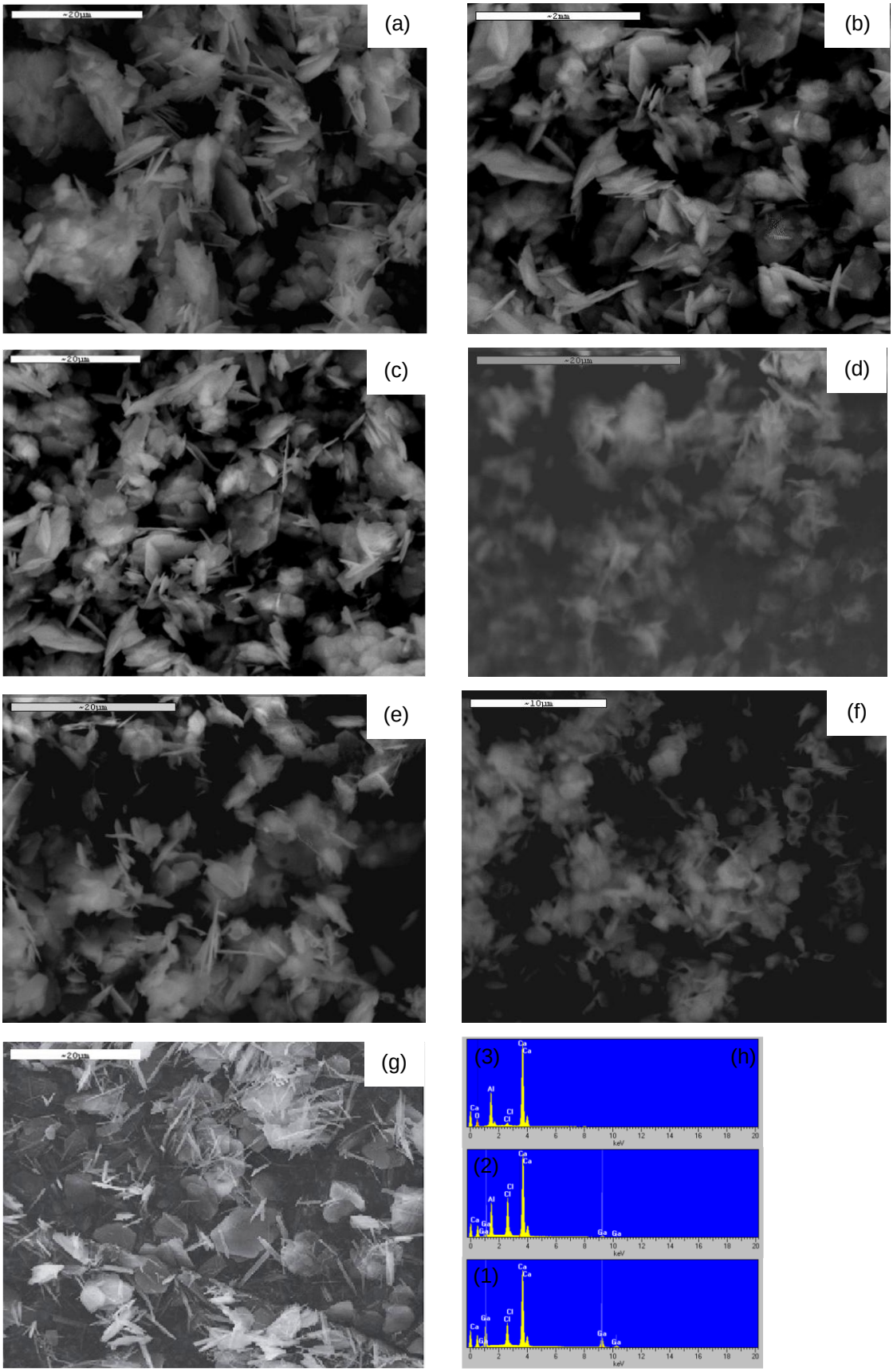

Figure 2.6. SEM images of $Ca_2Ga_xAl_{(1-x)}$-Cl; where x = (a) 0, (b) 0.2, (c) 0.4, (d) 0.6, (e) 0.8, (f) 1.0, and (g) monosulfate (hydration product of cement),[32] and (h) EDX spectra showing the chemical composition of the Ca_2Ga-Cl (1), $Ca_2Ga_{0.20}Al_{0.80}$-Cl (2), Ca_2Al-Cl (3).

Table 2.4. Loading of Ga^{3+} in the $Ca_2Ga_xAl_{(1-x)}$-Cl materials.

$Ca_2Ga_xAl_{(1-x)}$-Cl (x)	Expected Ga^{3+}/Al^{3+} atomic ratio	Observed (Ga^{3+}/Al^{3+} atomic ratio)	Observed x
0	0	0	0
0.05	0.053	0	0
0.1	0.11	0	0
0.15	0.18	0.045	0.043
0.2	0.25	0.11	0.10
0.3	0.43	0.24	0.19
0.4	0.67	0.50	0.33
0.5	1.00	0.84	0.46
0.6	1.50	1.35	0.57
0.7	2.33	2.42	0.71
0.8	4.00	4.28	0.81
0.9	9.00	10.8	0.91
1.0	∞	∞	1.0

The variation of the *a* parameter as a function of the observed gallium incorporation (*x* value) is in agreement with the Vegard's law,[33-35] demonstrating the existence of a continuous solid solution throughout the series $Ca_2Ga_xAl_{(1-x)}$-Cl. By linear regression the correlation between *a* parameter and *x* value can be derived: $a = (0.081 \pm 0.002)x + (5.744 \pm 0.001)$ (Figure 2.7). The equation can be compared to that expected for an ideal LDH layer structure built with $M(OH)_6$ octahedra. The *a* parameter of the rhombohedral unit cell for hydrotalcite was found equal to $\sqrt{2}d_{(M-OH)}$, where the metal-oxygen bond length $d_{(M\text{-}OH)}$ is related to main ionic radius within the hydroxide layer ($d_{(M\text{-}OH)} = r_m + r_{OH^-}$) and $\frac{da}{dr} = \sqrt{2}$. In case of the $Ca_2Ga_xAl_{(1-x)}$-Cl LDHs, the regular $M(OH)_6$ octahedra is not an idealised octahedral layer structure due to the coordination numbers of Ca^{2+} and Al^{3+} ions in the Ca_2Al-LDH structures are 7 and 6. Therefore, the *a* parameter of the rhombohedral unit cell for $Ca_2Ga_xAl_{(1-x)}$-Cl equal to $A \bullet d_{(M-OH)}$, where *A* = constant calculated from experimental value of *a* parameter and $d_{(M-OH)}$ of Ca_2Al-Cl and Ca_2Ga-Cl.

The mean ionic radius (r_m) can be calculated by the equation below:

$$r_m = 0.66 r_{Ca^{2+}} + 0.33x \bullet r_{Ga^{3+}} + 0.33(1-x) \bullet r_{Al^{3+}} \qquad \textbf{Equation 2.1}$$

$$\frac{dr_m}{dx} = 0.33(r_{Ga^{3+}} - r_{Al^{3+}}) \qquad \textbf{Equation 2.2}$$

A value can be calculated by the equation below:

$$a = A \times d_{(M-OH)} \qquad \textbf{Equation 2.3}$$

For Ca_2Al-Cl, using $a_{Ca_2Al-Cl} = 5.74$ Å, $r_{Ca^{3+}} = 0.99$ Å, $r_{Al^{3+}} = 0.535$ Å, $r_{OH^-} = 1.53$ Å;

$$a_{Ca_2Al-Cl} = A \times [(0.66 \bullet r_{Ca^{2+}} + 0.33 \bullet r_{Al^{3+}}) + r_{OH^-}] \qquad \textbf{Equation 2.4}$$

$$5.74 = A \times 2.360, \qquad A = 2.432 \qquad \textbf{Equation 2.5}$$

For Ca_2Ga-Cl, using $a_{Ca_2Ga-Cl} = 5.82$ Å, $r_{Ca^{3+}} = 0.99$ Å, $r_{Ga^{3+}} = 0.62$ Å, $r_{OH^-} = 1.53$ Å;

$$a_{Ca_2Ga-Cl} = A\times[(0.66\bullet r_{Ca^{2+}} + 0.33\bullet r_{Ga^{3+}}) + r_{OH^-}] \qquad \textbf{Equation 2.6}$$

$$5.74 = A\times 2.388, \qquad A = 2.437 \qquad \textbf{Equation 2.7}$$

$\frac{da}{dx}$ value can be calculated from $\frac{da}{dx} = \frac{da}{dr}\bullet\frac{dr}{dx}$, using $r_{Ga^{3+}} = 0.62$ Å, and $r_{Al^{3+}} = 0.535$ Å

$$\frac{da}{dx} = A\times 0.33(r_{Ga^{3+}} - r_{Al^{3+}}) \qquad \textbf{Equation 2.8}$$

$$\frac{da}{dx} = 2.44\times 0.33(r_{Ga^{3+}} - r_{Al^{3+}}) = 0.068 \qquad \textbf{Equation 2.9}$$

It can be explained a difference of $\frac{da}{dx}$ value that $M(OH)_6$ octahedra within the LDH layers are distorted.[33]

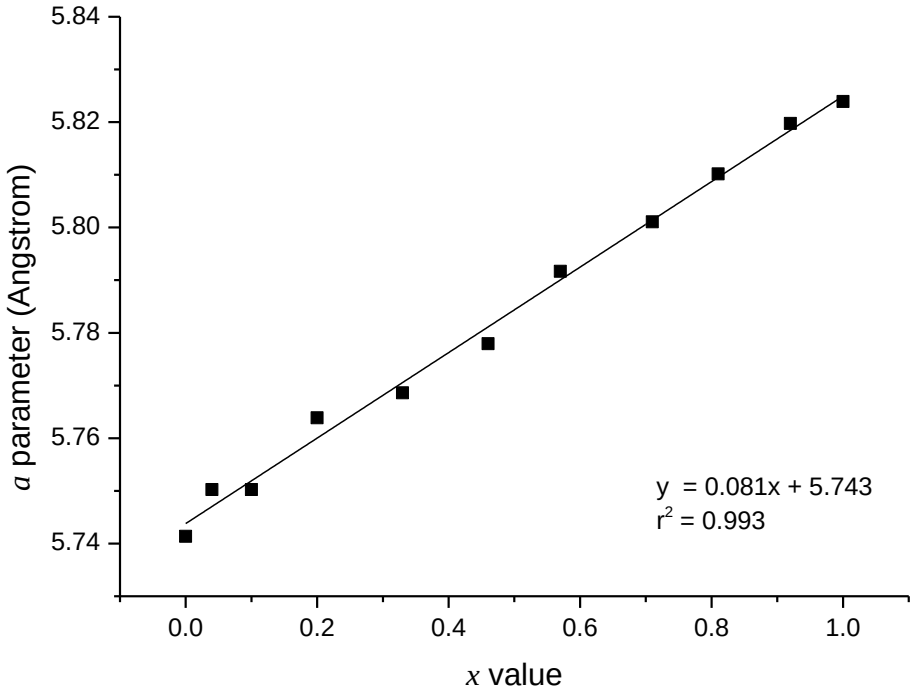

Figure 2.7. A plot of *a* parameter for $Ca_2Ga_xAl_{(1-x)}$-Cl LDHs VS the amount of gallium incorporated in $Ca_2Ga_xAl_{(1-x)}$-Cl.

2.3.4 Thermogravimetric and elemental analysis

Thermogravimetric analysis (TGA) was used to determine the thermal stability of the $Ca_2Ga_xAl_{(1-x)}$-Cl series. A typical TGA plot for a $Ca_2Ga_xAl_{(1-x)}$-Cl (x = 0.8) sample is shown in Figure 2.8. The elemental composition of the $Ca_2Ga_xAl_{(1-x)}$-Cl series can be determined from the TGA and EDX, which is summarised in Table 2.5.

From room temperature up to 150°C, cointercalated water is lost from LDH samples. Then loss of water from dehydroxylation of the LDH layers occurs. From 400 °C onwards, the loss of chlorine occurs. The final product remaining at 800 °C is a mixture of metal oxide, Mayenite ($Ca_{12}Al_{14}O_{33}$), and Lime (CaO) in case of Ca_2Al-Cl. For $Ca_2Ga_xAl_{(1-x)}$-Cl, the LDHs decompose to Calcium aluminogallate ($CaAlGaO_4$) and Lime (CaO), while Ca_2Ga-Cl decomposes to Monocalcium oxogallate ($CaGa_2O_4$) and Lime (CaO) at 800 °C.

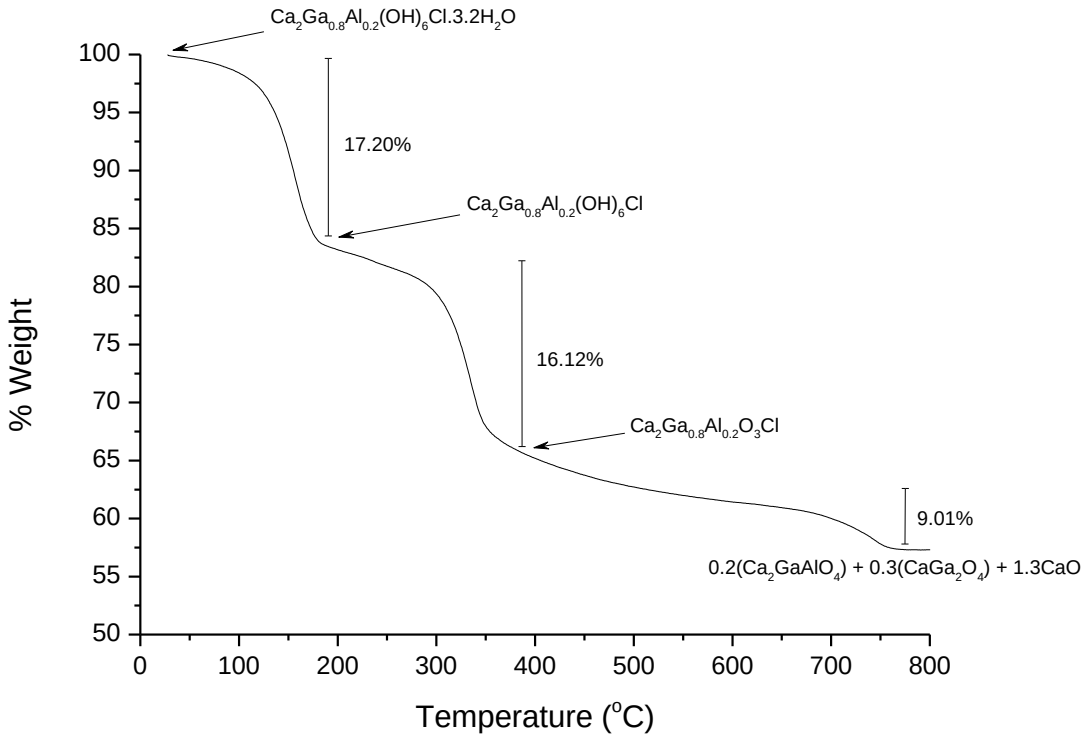

Figure 2.8. TGA plot for $Ca_2Ga_{0.8}Al_{0.2}(OH)_6Cl{\bullet}3.2H_2O$.

Table 2.5. Chemical composition and formula for $Ca_2Ga_xAl_{(1-x)}$-Cl series; $0 < x < 1$.

$Ca_2Ga_xAl_{(1-x)}$-Cl (x)	Ga/Ca atomic ratio*	Al/Ca atomic ratio*	Formula
0	0	0.50	$Ca_2Al(OH)_6Cl•1.1H_2O$
0.05	0	0.50	$Ca_2Al(OH)_6Cl•1.7H_2O$
0.1	0	0.50	$Ca_2Al(OH)_6Cl•1.5H_2O$
0.15	0.022	0.48	$Ca_2Ga_{0.04}Al_{0.96}(OH)_6Cl_{0.9}•3H_2O$
0.2	0.050	0.45	$Ca_2Ga_{0.1}Al_{0.9}(OH)_6Cl•2.6H_2O$
0.3	0.097	0.40	$Ca_2Ga_{0.2}Al_{0.8}(OH)_6Cl•2.7H_2O$
0.4	0.17	0.33	$Ca_2Ga_{0.33}Al_{0.67}(OH)_6Cl_{0.9}•2.6H_2O$
0.5	0.23	0.27	$Ca_2Ga_{0.46}Al_{0.54}(OH)_6Cl•3H_2O$
0.6	0.29	0.21	$Ca_2Ga_{0.57}Al_{0.43}(OH)_6Cl•2.6H_2O$
0.7	0.35	0.15	$Ca_2Ga_{0.71}Al_{0.29}(OH)_6Cl•3H_2O$
0.8	0.41	0.095	$Ca_2Ga_{0.81}Al_{0.19}(OH)_6Cl•3.2H_2O$
0.9	0.46	0.042	$Ca_2Ga_{0.92}Al_{0.08}(OH)_6Cl•3.3H_2O$
1.0	0.50	0	$Ca_2Ga(OH)_6Cl•2.7H_2O$

* Determined by Energy-dispersive X-ray spectroscopy technique.

2.4 Intercalation of organic anions in Ca_2Ga-Cl

Attempts were made to intercalate sodium styrene sulfonate, sodium butene dicarboxylate, sodium fumarate and ammonium poly(styrene sulfonate) into Ca_2Ga-Cl by ion exchange. The X-ray diffraction (XRD) results (Figure 2.9) show that only sodium styrene sulfonate intercalates successfully. This is evidenced by a large increase in the *c* parameter from 23.35 Å to 54.20 Å (Table 2.6 and Figure 2.10). The starting materials were destroyed by reaction with sodium fumarate and ammonium poly(styrene sulfonate). The XRD pattern for Ca_2Ga-fumarate is amorphous and the Ca_2Ga-Cl LDH dissolves when reacted with ammonium poly(styrene sulfonate). There is no reaction of the LDH with sodium butene dicarboxylate: the *c* parameter is not changed. As can be seen, the Ca_2Ga-butene dicarboxylate pattern also shows an impurity, which is identified as calcium carbonate. It is presumed that calcium ions leach from the LDH into the solution and form calcium carbonate by reacting with CO_2.

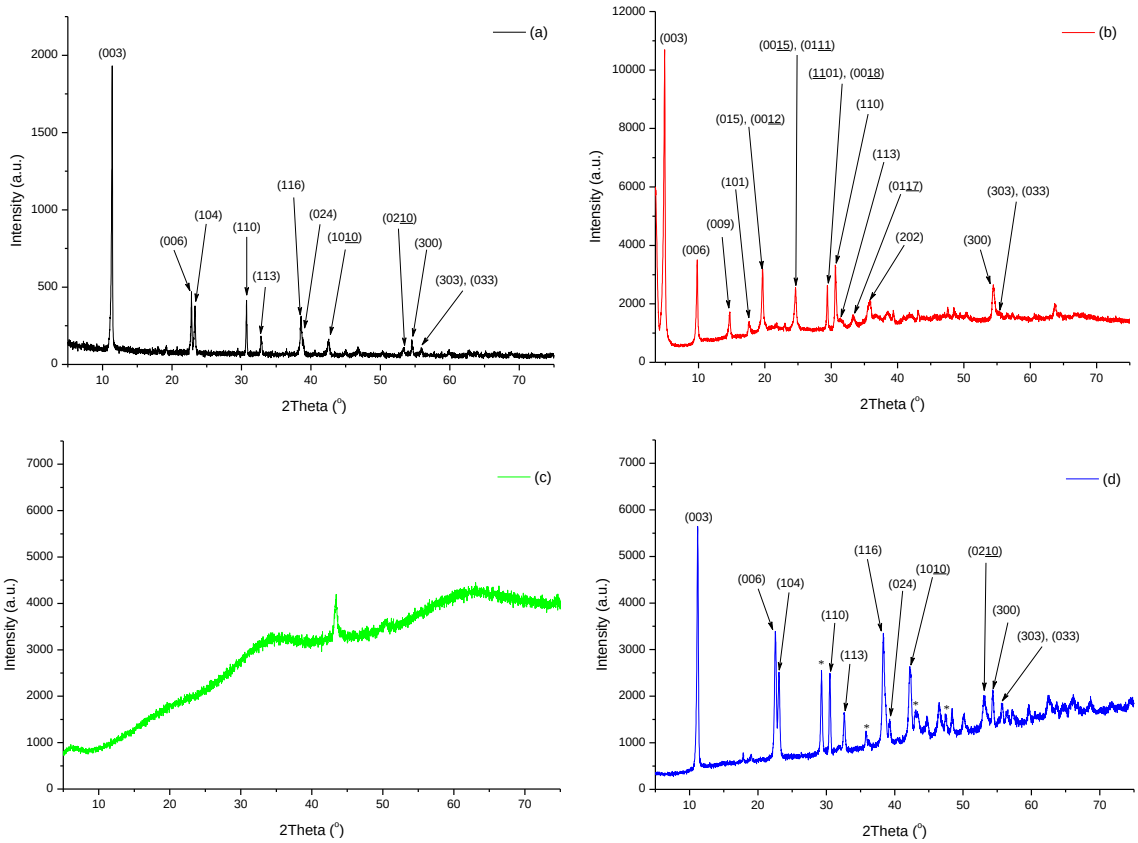

Figure 2.9. Powder XRD patterns of (a) Ca_2Ga-Cl, (b) Ca_2Ga-styrene sulfonate, (c) Ca_2Ga-fumarate, and (d) Ca_2Ga-butene dicarboxylate (* = $CaCO_3$ reflections).

Table 2.6. Calculated unit cell parameters of Ca_2Ga-styrene sulfonate LDH compared with the precursor compound.

Sample name	unit cell parameter (Å)		Interlayer distance (Å)
	a	*c*	
Ca_2Ga-Cl	5.81	23.35	7.78
Ca_2Ga-styrene sulfonate	5.82	54.20	18.07

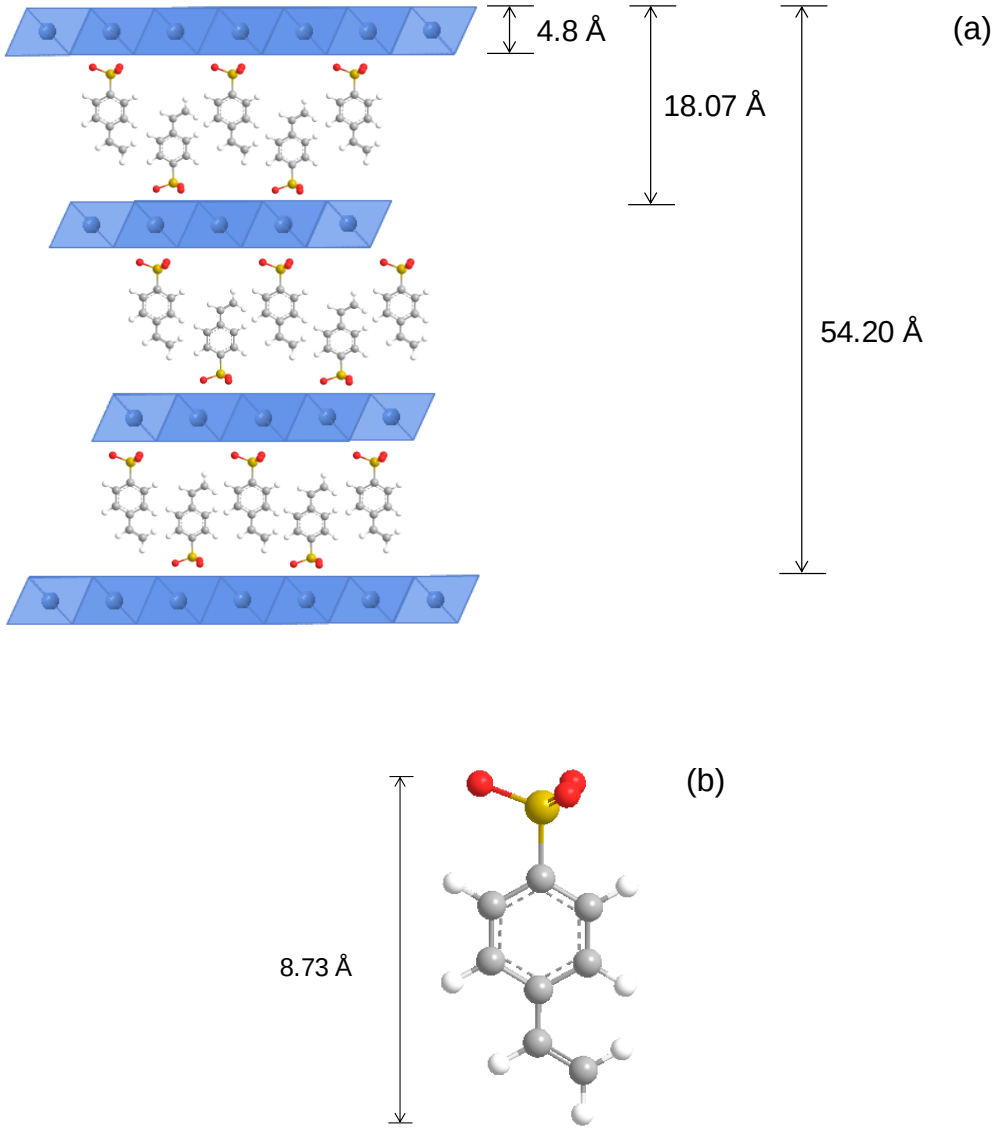

Figure 2.10. (a) Schematic illustration of Ca_2Ga-styrene sulfonate structure, and (b) the molecular structure of styrene sulfonate.

2.5 Conclusions

The effects of pH on the synthesis of Ca_2Ga-Cl have been studied. Highly crystalline Ca_2Ga-Cl can be prepared by the co-precipitation method at pH 10.5 ± 0.1. The XRD pattern of Ca_2Ga-Cl can be indexed using a rhombohedral unit cell with a = 5.82 Å, c = 24.0 Å.

The synthesis of the Ga-doped $Ca_2Al(OH)_6Cl•nH_2O$ LDHs ($Ca_2Ga_xAl_{(1-x)}$-Cl; where $0 < x < 1$) has been investigated. The XRD patterns for $Ca_2Ga_xAl_{(1-x)}$-Cl LDHs can be indexed using a rhombohedral unit cell with a value range of a parameter between 5.74 Å and 5.82 Å. The a parameter of $Ca_2Ga_xAl_{(1-x)}$-Cl increases with the amount of loading Ga^{3+} due to the larger ionic radii of Ga^{3+} cations. The a parameter varies linearly with Ga^{3+} composition (Vegard's law) indicates that a solid solution forms over the full composition range.

The intercalation of organic anions including; sodium styrene sulfonate, sodium butene dicarboxylate, sodium fumarate and ammonium poly(styrene sulfonate), in Ca_2Ga-Cl structure has been studied. Only Ca_2Ga-styrene sulfonate was successfully synthesised.

2.6 References

1. U. Birnin-Yauri and F. Glasser, *Cement and Concrete Research*, 1998, **28**, 1713-1723.
2. A. Terzis, S. Filippakis, H.-J. Kuzel and H. Burzlaff, *Zeitschrift für Kristallographie*, 1987, **181**, 29-34.
3. A. Suryavanshi, J. Scantlebury and S. Lyon, *Cement and Concrete Research*, 1996, **26**, 717-727.
4. H. Justnes, *Nordic Concrete Research Publications*, 1998, **21**, 48-63.
5. M. Francois, G. Renaudin and O. Evrard, *Acta Crystallographica Section C: Crystal Structure Communications*, 1998, **54**, 1214-1217.
6. G. Renaudin, F. Kubel, J.-P. Rivera and M. Francois, *Cement and Concrete Research*, 1999, **29**, 1937-1942.
7. G. Renaudin, M. Francois and O. Evrard, *Cement and Concrete Research*, 1999, **29**, 63-69.
8. F. Leroux, J. Ravaux and G. Renaudin, *Cement and Concrete Research*, 2011, **41**, 504-509.
9. J. Rapin, G. Renaudin, E. Elkaim and M. Francois, *Cement and Concrete Research*, 2002, **32**, 513-520.
10. M. Marinescu and J. Brouwers, in *Advances in Modeling Concrete Service Life*, Springer, 2012, pp. 125-131.
11. J. Ma, Z. Li, Y. Zhang and G. P. Demopoulos, *Hydrometallurgy*, 2009, **99**, 225-230.
12. A. K. Suryavanshi, J. D. Scantlebury and S. B. Lyon, *Cement and Concrete Research*, 1996, **26**, 717-727.
13. C. Arya and Y. Xu, *Cement and Concrete Research*, 1995, **25**, 893-902.
14. A. Violante, M. Pucci, V. Cozzolino, J. Zhu and M. Pigna, *Journal of Colloid and Interface Science*, 2009, **333**, 63-70.
15. F. Kovanda, E. Kovácsová and D. Koloušek, *Collection of Czechoslovak Chemical Communications*, 1999, **64**, 1517-1528.
16. N. Lazaridis, A. Hourzemanoglou and K. Matis, *Chemosphere*, 2002, **47**, 319-324.
17. B. Doušová, V. Machovič, D. Koloušek, F. Kovanda and V. Dorničák, *Water, Air, and Soil Pollution*, 2003, **149**, 251-267.
18. G. Gillman, *Science of the Total Environment*, 2006, **366**, 926-931.
19. K. Parida, M. Satpathy and L. Mohapatra, *Journal of Materials Chemistry*, 2012, **22**, 7350-7357.
20. F. Bruna, R. Celis, I. Pavlovic, C. Barriga, J. Cornejo and M. Ulibarri, *Journal of Hazardous Materials*, 2009, **168**, 1476-1481.
21. J. Liu, F. Li, D. G. Evans and X. Duan, *Chemical Communications*, 2003, **4**, 542-543.
22. J. Phillips and L. Vandeperre, *Journal of Nuclear Materials*, 2011, **416**, 225-229.
23. G. Carja, R. Nakamura and H. Niiyama, *Microporous and Mesoporous Materials*, 2005, **83**, 94-100.
24. J. Z. Zhou, Z. P. Xu, S. Qiao, J. Liu, Q. Liu, Y. Xu, J. Zhang and G. Qian, *Applied Clay Science*, 2011, **54**, 196-201.
25. C. T. Yavuz, B. D. Shinall, A. V. Iretskii, M. G. White, T. Golden, M. Atilhan, P. C. Ford and G. D. Stucky, *Chemistry of Materials*, 2009, **21**, 3473-3475.
26. S. Xu, B. Zhang, Z. Chen, J. Yu, D. G. Evans and F. Zhang, *Industrial & Engineering Chemistry Research*, 2011, **50**, 6567-6572.

27. S. Xu, Z. Chen, B. Zhang, J. Yu, F. Zhang and D. G. Evans, *Chemical Engineering Journal*, 2009, **155**, 881-885.
28. L. Vieille, I. Rousselot, F. Leroux, J.-P. Besse and C. Taviot-Guého, *Chemistry of Materials*, 2003, **15**, 4361-4368.
29. V. Drits, J. Srodon and D. Eberl, *Clays and Clay Minerals*, 1997, **45**, 461-475.
30. I. Rousselot, C. Taviot-Guého, F. Leroux, P. Léone, P. Palvadeau and J.-P. Besse, *Journal of Solid State Chemistry*, 2002, **167**, 137-144.
31. N. Thomas and M. Rajamathi, *Langmuir*, 2009, **25**, 2212-2216.
32. I. Baur, P. Keller, D. Mavrocordatos, B. Wehrli and C. A. Johnson, *Cement and Concrete Research*, 2004, **34**, 341-348.
33. K. Rozov, U. Berner, C. Taviot-Gueho, F. Leroux, G. Renaudin, D. Kulik and L. W. Diamond, *Cement and Concrete Research*, 2010, **40**, 1248-1254.
34. E. E. Sileo, M. Jobbágy, C. O. Paiva-Santos and A. E. Regazzoni, *The Journal of Physical Chemistry B*, 2005, **109**, 10137-10141.
35. K. Parida, L. Mohapatra and N. Baliarsingh, *The Journal of Physical Chemistry C*, 2012, **116**, 22417-22424.

Chapter 3: Intercalation of Lignosulfonate, Naphthalene Sulfonate and Polycarboxylate into $Ca_2Al\text{-}NO_3$ LDH and A Study of Their Effects on Cement Hydration

3.1 Introduction

Construction materials, especially concrete, are crucially important for mankind; concrete is the second largest used substance after water and at present the worldwide annual consumption of concrete is more than 11 billion m^3.[1] Cement is a hydraulic binder, *i.e.* a finely ground inorganic material which, when mixed with water, forms a paste which sets and hardens by means of hydration processes and which, after hardening, retains its strength and stability, even underwater.[1] According to International Energy Agency (IEA) data in 2007, approximately 9% of global manmade CO_2 emission are a result of cement production.[2] Demand for cement in industrial nations is increasing slowly, however in developing countries it rose by 55% in the 1990s. China accounted for 56 percent of world cement demand in 2010 while Thailand is the eighth largest global cement producer with 40 Mt/yr production in 2005. Nowadays, construction material manufacturers are fully aware of the environmental concerns, and so seek ways to consume less energy and natural resources, and emit less CO_2 gas.[3-10] CO_2 emission can be reduced by using less energy in cement production;[10] this could be achieved by producing different types of cement, such as Calcium Sulfoaluminate Cement.[10-12] This requires lower production temperatures than conventional cement (by 100 °C) and less $CaCO_3$ is used in its preparation. Another solution is to introduce novel additives as components in the cement composition.

The inorganic chemistry and crystalline phase evolution during cement hydration is very complex. The hydration reactions of cement are normally related to the heterogeneous reactions of cement powder, which includes several minerals. The formation of hydration products and the development of the micro-structural features are dependent on both subsequent interfacial reactions (topochemical phenomena) and solid-state reactions. The relative reactivity of the different cement phases with water is as follows: tricalcium aluminate ($Ca_3Al_2O_6$) > tricalcium silicate (Ca_3SiO_5) > dicalcium silicate (Ca_2SiO_4) ≈ tetracalcium aluminoferrite ($Ca_2(Al_xFe_{1-x})_2O_5$; $0 < x < 0.7$).[13] Normally, the aluminate

phases and their hydration products play an important role in the early hydration processes.[1, 14] At very early ages (0 – 1 hour), the behaviour of hydrating cement is governed by hydration reactions of the aluminate cement phases ($Ca_3Al_2O_6$).

If tricalcium aluminate ($Ca_3Al_2O_6$, C_3A) is allowed to hydrate rapidly, it gives rise to an undesirable quick set, called a 'flash set', forming hydrogarnet ($Ca_3Al_2(SiO_4)_{3-x}(OH)_{4x}$; $0 \leq x \leq 3$) and calcium hydroaluminate [$Ca_2Al(OH)_7 \cdot 6H_2O$, hydroxy AFm].[15-17] Gypsum ($CaSO_4$) is introduced by grinding with the cement clinker to act as a regulator for the hydration of cement in order to achieve acceptable setting characteristics. Under these conditions, the flowability and plasticity of the paste is preserved until the formation of cement hydrate phases and induces normal setting. Calcium sulfate reacts with tricalcium aluminate ($Ca_3Al_2O_6$) at room temperature to form the calcium trisulfoaluminate hydrate known as sulfate ettringite [$Ca_6Al_2(SO_4)_3(OH)_{12} \cdot 26H_2O$, AFt].[18] As gypsum becomes increasingly consumed (after 8 – 16 hours approximately), Friedel's salt ($Ca_2Al(OH)_6[Cl_{1-x}(OH)_x] \cdot 3H_2O$; $0 < x < 1$) will be formed in significant quantities. It reacts with ettringite to give a calcium monosulfatoaluminate hydrate, called monosulfate [$Ca_2Al(SO_4)_{0.5}(OH)_6 \cdot 3H_2O$, $Ca_2Al\text{-}SO_4$, also called AFm].[19] The formation of monosulfate at 25 ^oC takes around 8 – 11 days.[20] The AFm phase has a complex chemical and structural constitution in cement mixtures as this phase exhibits anion exchange reactions, so that its composition depends on the chemical environment.

3.1.1 Interesting anions in cement solution

During cement hydration, there are various cations and anions released into the system. At the beginning, the cement phases from the clinker-surface hydrate. Tricalcium aluminate (C_3A) is the most reactive phase releasing calcium and aluminium cations (Figure 3.1). These ions react in minutes with sulfate from gypsum ($CaSO_4$) to form an ettringite (AFt) precursor gel and Ettringite (AFt) needles, while tricalcium silicate release calcium cations and silicate anions to form calcium silicate hydrate (C-S-H) on the cement grains, and $Ca(OH)_2$ which causes the pH of the solution to become alkaline. The chemical formula for calcium silicate hydrate (C-S-H) depends on Ca/Si atomic ratio. The Ca/Si ratio of Tobermorite [$Ca_5Si_6O_{16}(OH)_2 \cdot 4H_2O$] is 0.83, while Jennite [$Ca_9Si_6O_{18}(OH)_6 \cdot 8H_2O$] contains the Ca/Si ratio of 1.5.[21-24] CO_2 in the air can easily dissolve in the solution at high pH introducing carbonate ions.[25]

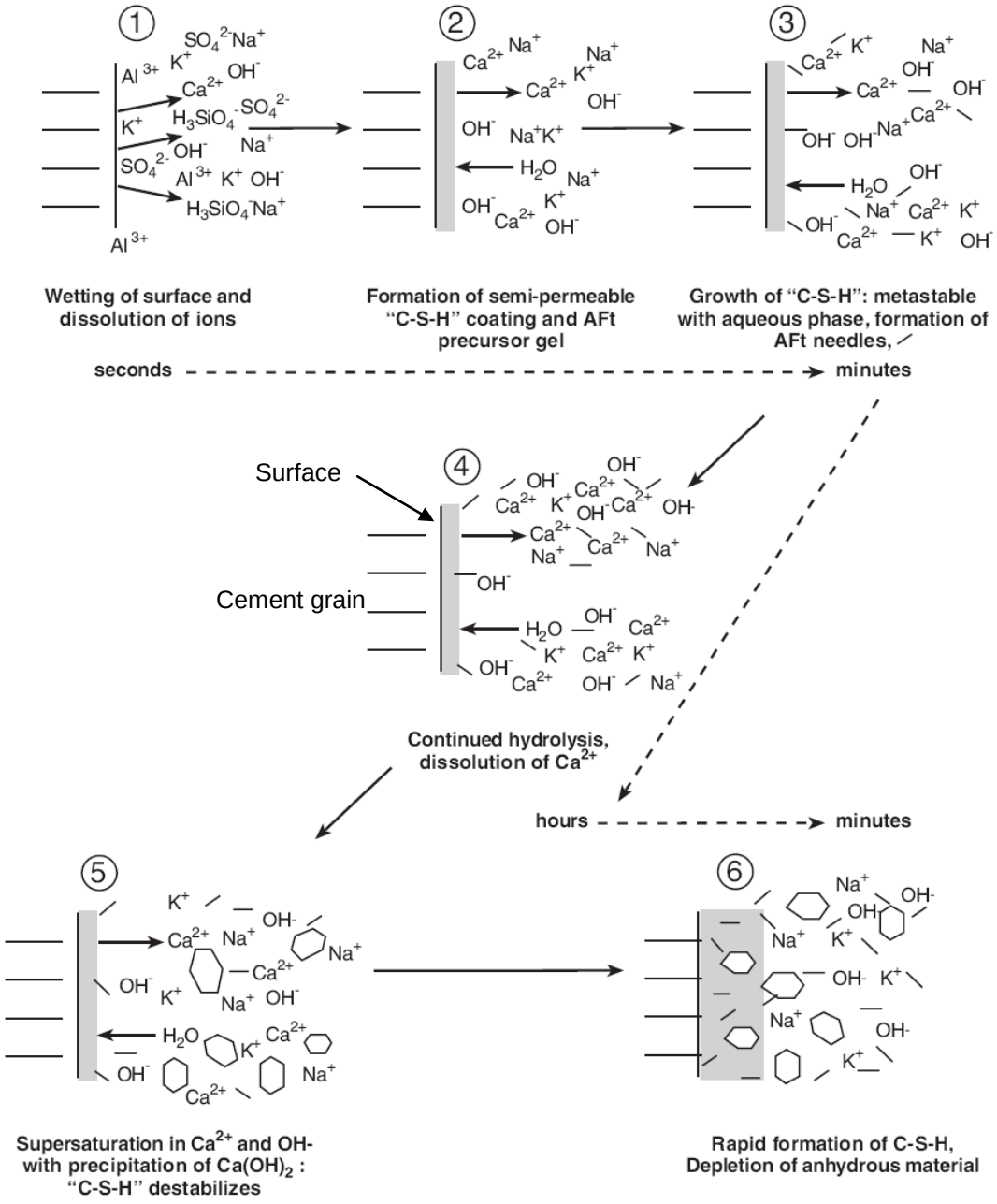

Figure 3.1. Summary of the ionic composition during the cement hydration process.[13]

After the initial period, cement hydration slows down and the induction period begins which lasts around 3 hours. Subsequently, the reactivity enters the acceleration period. During the period between 3 hours to a day after mixing, the C-S-H formation happens in two phases. The first stage induces the outer C-S-H production with growth out from the ettringite needles. The latter stage of C-S-H production occurs directly from the surface grains after a 10 hour period; this is due to the ions released from clinkers that are capable of penetrating through the hydrated phase into solution.

After 18 hours, tricalcium aluminate continues react with gypsum to form longer ettringite needles. The network of ettringite and C-S-H appears to form a hydrating shell and inner C-S-H forms inside this shell.[17] After 1–3 days of hydration, reactions slow down again and the deceleration period begins. Ettringite further reacts with excess sulfate in the system to produce monosulfate. The rate of hydration at this stage is likely dependent on the diffusion of water and ions into the anhydrous phase. After 2 weeks, the gaps between the hydrating shells and the cement grains are filled by inner C-S-H phases. The products from each hydration reaction occur according to their own reaction mechanism, reaction time and reaction rate. Most of the reactions in the cement hydration process are exothermic, the stages of the evolution of hydrating cement can be identified from the heat evolution curve shown in Figure 3.2.

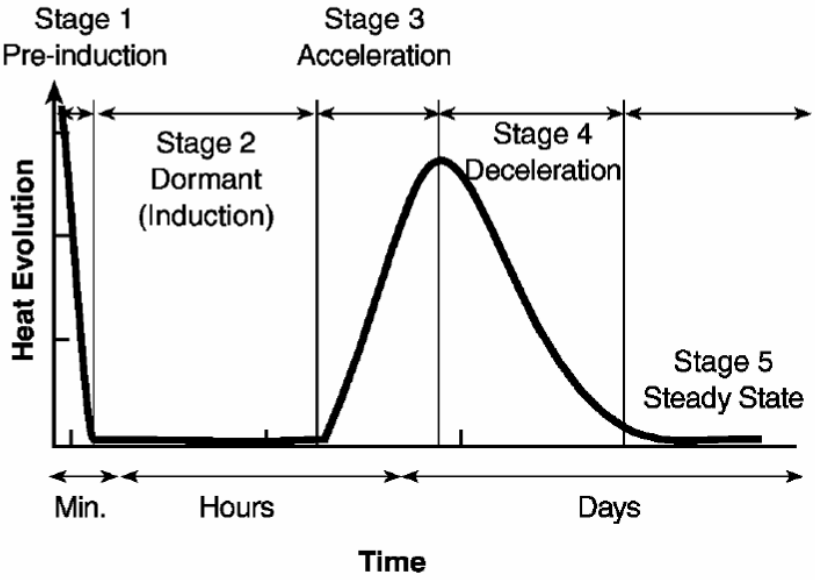

Figure 3.2. Schematic plot the of heat evolution during the hydration of Portland cement at 20 ^{o}C.[1, 17]

3.1.2 Chemical admixtures

To be suitable for a variety of building material applications; for example rebuilding, repair, construction, or making building components, cement manufacturers need to add a range of chemicals to all concrete formulations. Chemical admixtures are often used to alter the course of cement hydration reactions and the properties of fresh or hardened concrete. The goal of some chemical admixtures is to allow cement compositions to exhibit sufficient dispersibility when the amount of water is reduced. In addition, many features need to retain fluidity and processability as well as exhibiting improved durability and strength as a result of water reduction. Furthermore, the admixtures must ensure that the compositions of concrete or mortar mixture retain the correct end-product characteristics.[26]

The American Society for Testing and Materials (ASTM)[27] has classified hydraulic-cement concrete admixtures for specific purposes as follows:

Type A – Water-reducing admixtures
Type B – Retarding admixtures
Type C – Accelerating admixtures
Type D – Water-reducing and retarding admixtures
Type E – Water-reducing and accelerating admixtures
Type F – Water-reducing and high range admixtures
Type G – Water-reducing, high range and retarding admixtures
Type S – Specific performance admixtures

Water-reducing agents (called ‘Superplasticisers’) are commonly used in concrete technology to improve the workability of cementitious systems. They are adsorbed on the cement particles and act as dispersants by electrostatic and/or steric repulsion effects (Figure 3.3). The negative zeta potential of cement particles in pastes can be increased by adding superplasticisers, causing larger electrostatic repulsive forces between cement particles. The resulting steric repulsion of cement particles help to avoid the formation of agglomerates. As a result, the water requirement of a concrete or mortar mixture for a given workability can be reduced, without losing its ability to maintain density and

strength. The workability of concrete or mortar mixtures can hence be increased while water content remains fixed, providing unchanged workability and strength.[28-31]

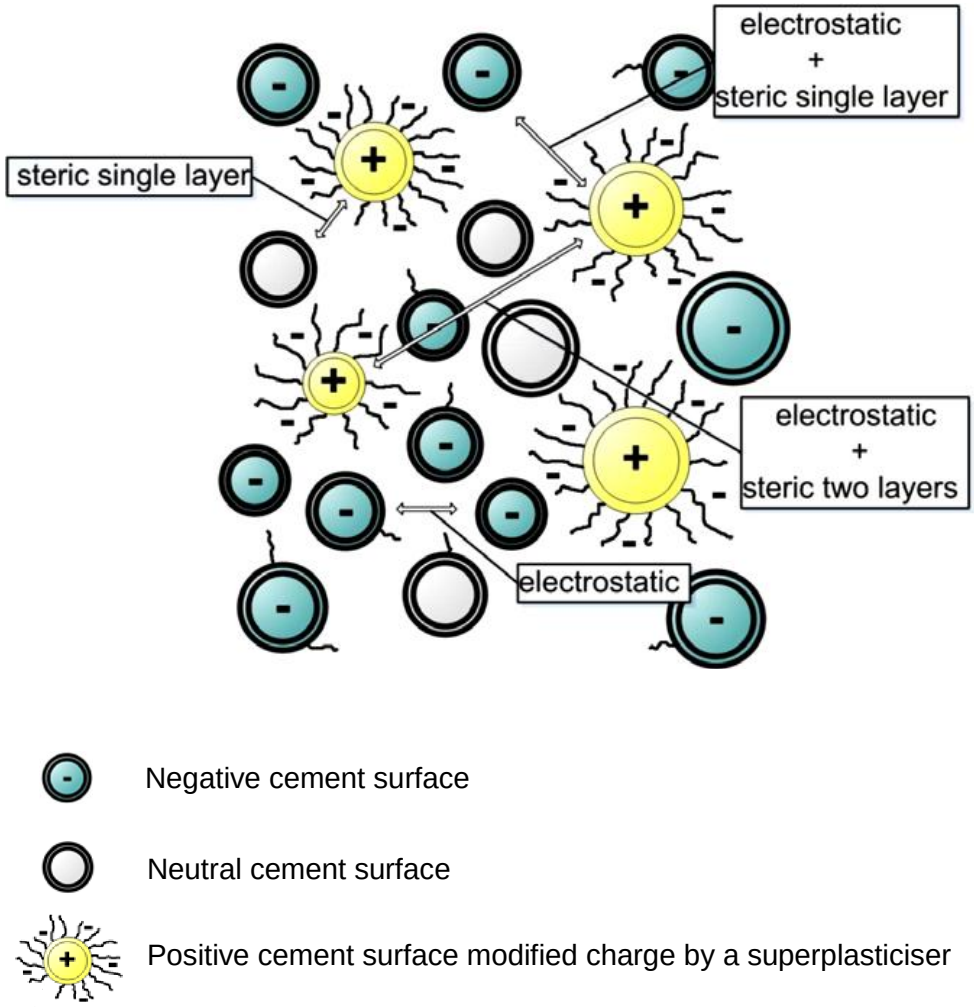

Figure 3.3. Schematic illustration showing the separation of cement particles due to electrostatic effect and the steric effects of the superplasticiser.[28, 30, 32]

However, the workability of cement-based materials containing superplasticisers also depends on various other parameters. The chemical composition and the molecular structure of the admixture has an influence on the rheology. The chemical composition of cement phases, especially the amount of tricalcium aluminate (C_3A) present and the availability of sulphate ions during early hydration, has a pronounced effect on the performance of the superplasticisers.[33]

Lignosulfonate is one of the water reducers categorised as type D (Water-reducing and retarding admixtures). This superplasticiser is an intrinsically complex biopolymer derived from chemical degradation of lignin, a by-product from the acid sulphite wood-pulping process. Lignin is an amorphous, cross-linked, and three-dimensional polyphenolic substance (Figure 3.4). There is no single defined structure of lignin and it varies from source to source.[34] Lignin is formed through nonselective condensation of three phenolic alcohol units (monolignols)[35]: *p*-coumaryl alcohol, coniferyl alcohol, and sinapyl alcohol, depicted in Figure 3.5 (5-Hydroxyconiferyl units have also been detected in lignocellulosic materials in low amounts.[36]) The ratio of the three major alcohols changes with cell and plant type. Whereas lignin from grasses is made up of all three alcohols, lignin in softwood is predominantly built from coniferyl alcohol, and hardwood lignin from coniferyl and sinapyl alcohol.

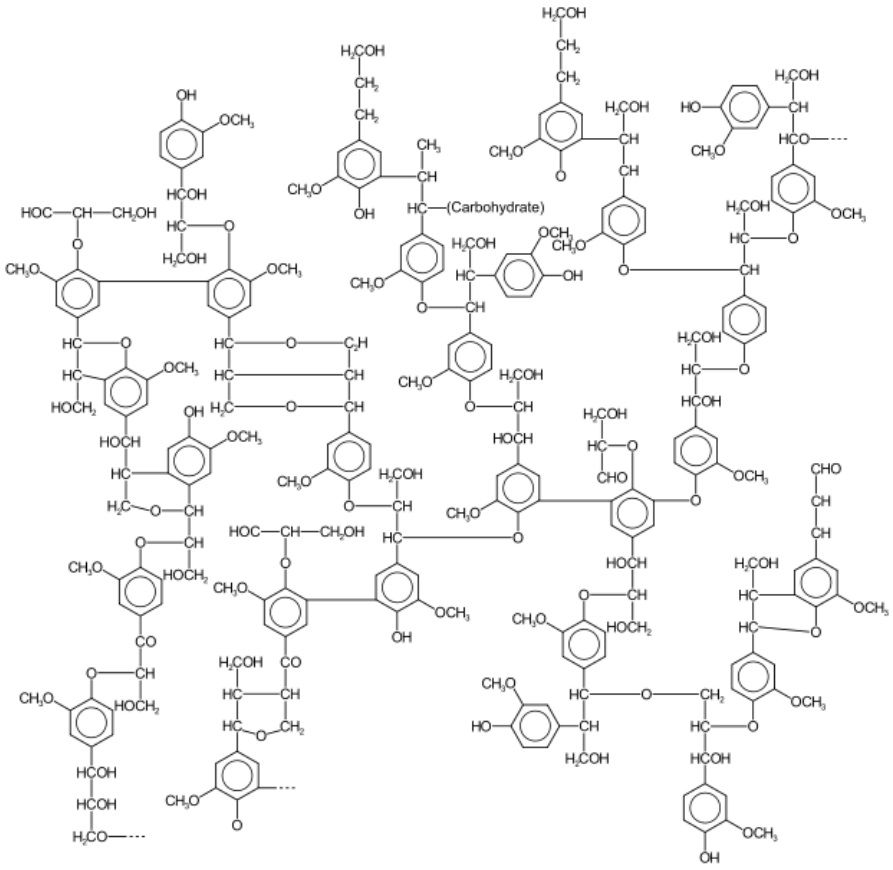

Figure 3.4. An example illustrating one of the proposed substructures for lignin.

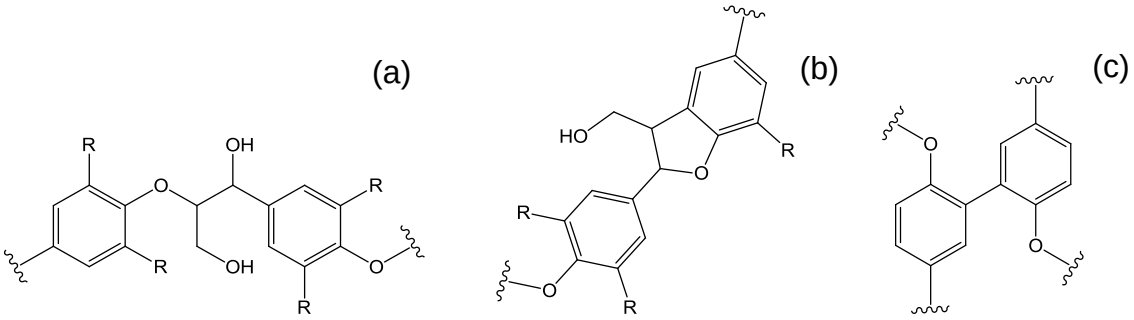

Figure 3.5. The structures of phenolic alcohol units (monolignols): (a) *p*-coumaryl alcohol, (b) coniferyl alcohol, and (c) sinapyl alcohol.

The crude-form of lignosulfonate contains many impurities such as pentose and hexose sugars which are powerful retarders. The impurities can be removed by fermentation followed by distillation. Calcium and sodium salts of lignosulfonate are most commonly used in admixture production. The purification and fractionation of crude lignosulfonate have enabled selection of products within a range of molecular weights. There is evidence that water-reducing capability increases with increasing molecular weight and decreasing carbohydrate content.

High-range water-reducing admixtures (type F) can be used at significantly higher dosages than ordinary water-reducing admixtures without unfavourable side effects such as the gross retardation for concrete setting.[37] These additives allow the volume of water to be greatly reduced while retaining the normal workability of concrete. All superplasticisers classified as type F consist of high molecular weight, water-soluble polymers, and are mostly synthetic admixtures, for example, sulfonated melamine-formaldehyde condensates and sulfonated naphthalene-formaldehyde condensates (Figure 3.6).[17]

Currently, the dosage requirement of these type F additives is excessive because of their rapid absorption onto the cement surface, the aggregation of the additives and the inefficient release kinetics. There are a number of publications on different approaches to improve the efficiency of additives.[38]

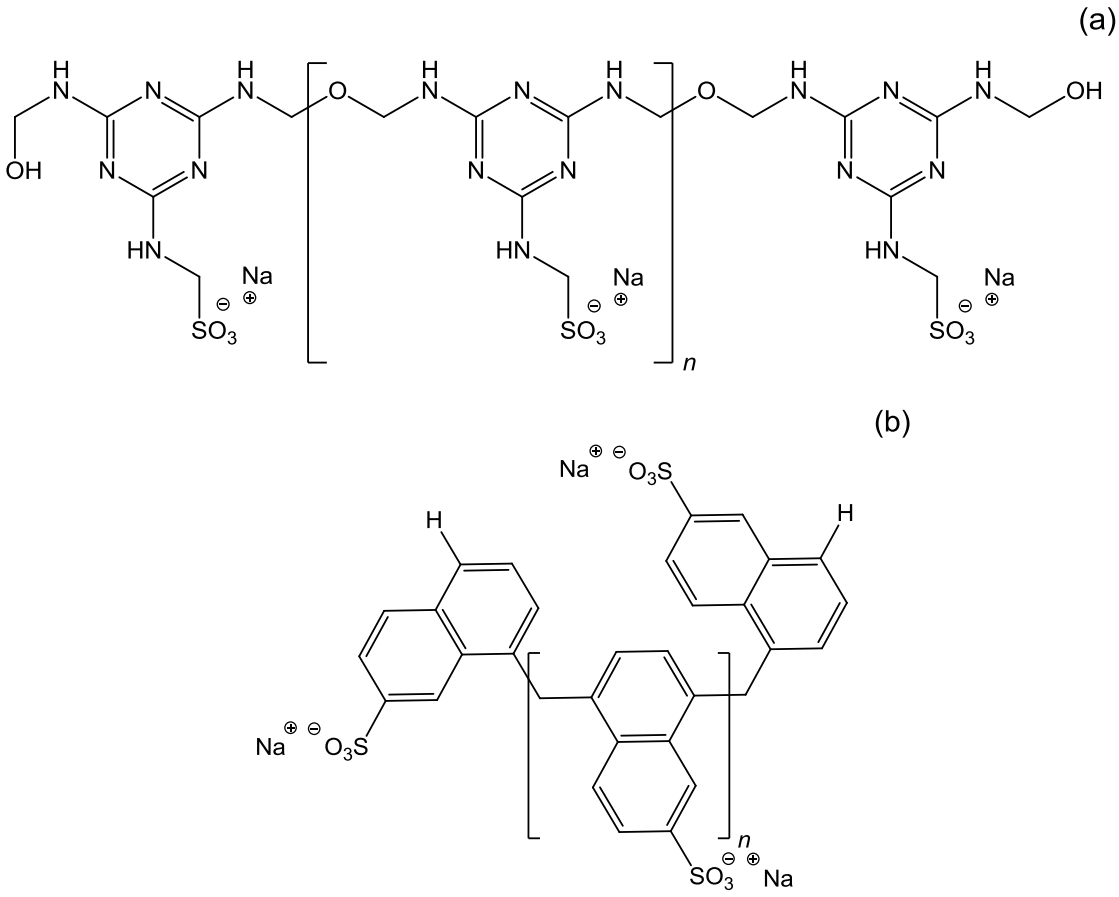

Figure 3.6. The structures of (a) sulfonated melamine-formaldehyde condensates, and (b) sulfonated naphthalene-formaldehyde condensates.

In recent years, a new class of superplasticisers has been studied, often referred to as polycarboxylate based comb polymers, which consist of one main linear chain with lateral carboxylate and ether groups (Figure 3.7).[30, 39] These compounds are designed by controlling side chain density, side chain length or the molecular weight of the polymer, which affect the efficiency of superplasticisers.[40] Dispersion is due to electrostatic repulsion (as in melamine and naphthalene admixtures) owing to the carboxylate groups, but also to the steric repulsion associated with the long lateral ether chains. The shorter main linear chain or longer and more numerous lateral chains of polycarboxylate can extend the fluidity duration of concrete or mortar mixtures. This new superplasticiser class has emerged as having the unique ability to improve the quality and economics of concrete products resulting from the increase of the electrostatic and steric repulsive force which is related to increasing dispersion of cement and cement hydrated particles.[28, 41]

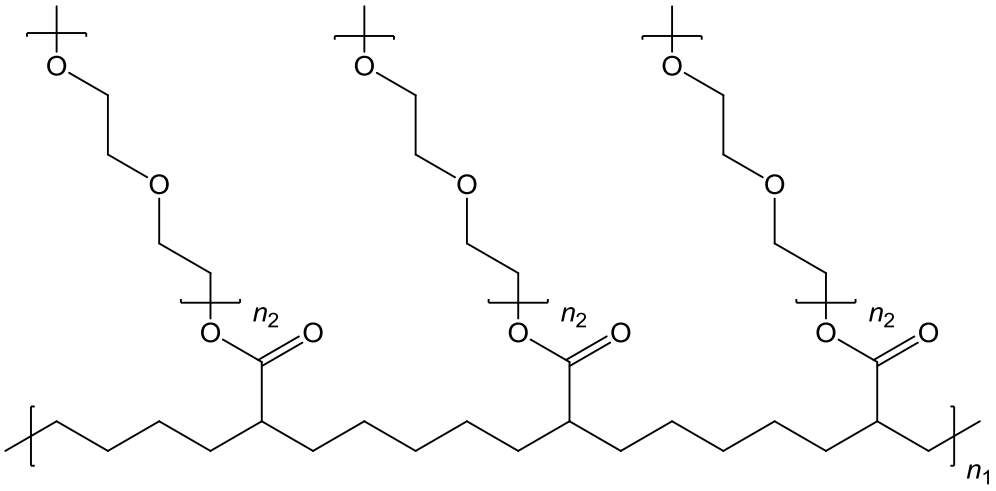

Figure 3.7. The structure model of comb based polycarboxylate n_1 units modified by polyethylene oxide n_2 units.[28, 41, 42] n_1 and n_2 are typicalliy in the range of 20 – 100.

Hydrocalumite-like structures [$Ca_2Al(OH)_6^+X_{1/n}^{n-}\bullet yH_2O$, Ca_2Al-X LDHs] are significant byproducts, for example monosulfate [$Ca_2Al(OH)_6(SO_4)_{0.5}\bullet 3H_2O$, AFm] phases which occur from the cement hydration of calcium aluminate (C_3A). The structure of Ca_2Al-X LDHs contains positively charged mixed metal hydroxide layers separated by charge-balancing hydrated anions between layers. The interlayer anions may be replaced through an anion exchange process. LDH-like materials can be used as models to obtain a better understanding of the interaction between organic admixtures and the cement phases.[38] Furthermore, it may be possible to use LDHs to enhance the properties of cement. One way in which this may be achieved is by the intercalation of the superplasticisers used as additives in cement applications into LDHs. These additive-intercalated LDHs could become very effective multi-functional releasing additives in concrete. If successful, this would constitute a novel additive system for use in cement.

3.1.3 Objectives of this work

In this chapter, the primary objective is the synthesis of new intercalated calcium aluminum LDHs (Ca_2Al-LDHs) for use in cement applications. Lignosulfonate, naphthalene sulfonate and polyacrylate are chosen as target guests for intercalation to compare their performance with the commercial cement additives; lignosulfonate-based superplasticiser (type D), sulfonated naphthalene-formaldehyde condensates (type F), and polycarboxylate (PC6). This chapter also studies kinetics of anion release from the new

Ca_2Al-LDHs in cement solution. This chapter also investigates the mechanical properties of the LDH-doped cement paste using an ultrasound-shear wave reflection technique.

3.2 Intercalation of superplasticisers in Ca_2Al-NO_3 LDH

Lignosulfonate, naphthalene sulfonate and polyacrylate were intercalated into calcium aluminum nitrate LDH [$Ca_2Al(OH)_6(NO_3)$•$6H_2O$, Ca_2Al-NO_3] by the ion-exchange method. The structures of the target guest anions used are shown in Figure 3.8.

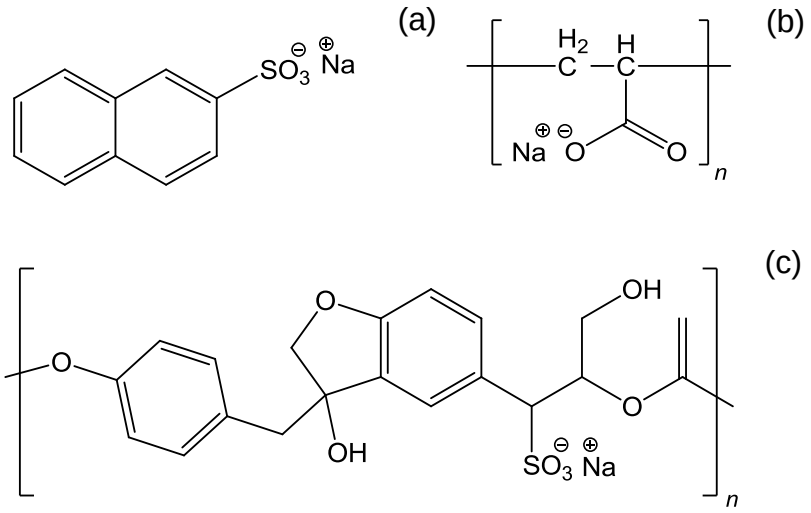

Figure 3.8. Molecular structures of selected superplasticisers: (a) sodium 2-naphthalene sulfonate, (b) sodium polyacrylate; n = 1,000, and (c) sodium lignosulfonate.

2.4 g of selected superplasticisers were added separately into deionised water. The pH in these solutions was adjusted to 11.5. The solution containing superplasticiser in each reaction was heated at 40 ^oC before adding 1 g of nitrate-intercalated Ca_2Al-LDH [$Ca_2Al(OH)_6(NO_3)$•$6H_2O$, Ca_2Al-NO_3]. All reactions were left at 40 ^oC under N_2 gas for 16 hours. The solid products were isolated by vacuum filtration and then washed with deionised water.

3.2.1 X-ray powder diffraction

X-ray powder diffraction was initially used to indicate the replacement of the nitrate anions in Ca_2Al-NO_3 by the superplasticisers. The XRD patterns of the Ca_2Al-NO_3 host material and superplasticiser-intercalated Ca_2Al-LDHs are shown in Figure 3.9. All the XRD patterns have been successfully indexed to a hexagonal cell where $a = b$ = 5.74 Å

and *c*-parameter varying from 22 – 35 Å (Table 3.1); Full XRD data is included in Appendix I.

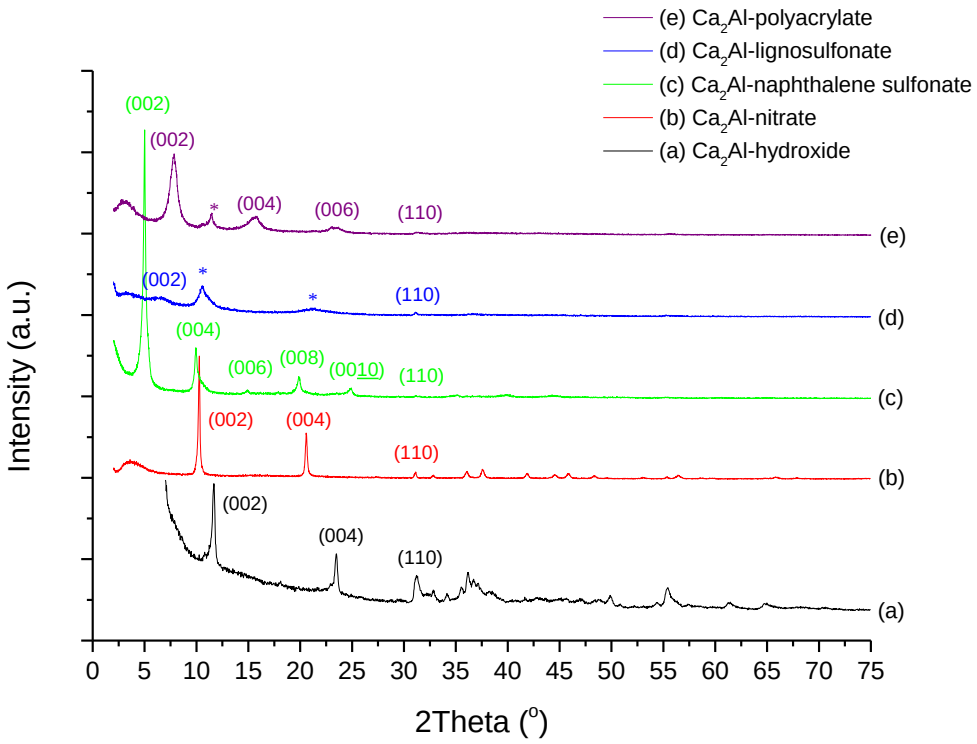

Figure 3.9. X-ray diffraction patterns of (a) Ca_2Al-OH, (b) Ca_2Al-NO_3, (c) Ca_2Al-naphthalene sulfonate, (d) Ca_2Al-lignosulfonate, and (e) Ca_2Al-polyacrylate. * marked the observation of Bragg reflections of Ca_2Al-NO_3.

The XRD data indicates an expansion of Ca_2Al-layers, as observed from the position of the (002) Bragg reflections, due to superplasticiser intercalation. For the naphthalene sulfonate-intercalated Ca_2Al-LDH (Ca_2Al-naphthalene sulfonate) (Figure 3.9(c)), the diffraction pattern shows that the material is highly crystalline. The observed interlayer spacing is consistent with a bi-layer orientation of the naphthalene sulfonate. The schematic illustration of Ca_2Al-naphthalene sulfonate and the molecular structure of naphthalene sulfonate are shown in Figure 3.10.

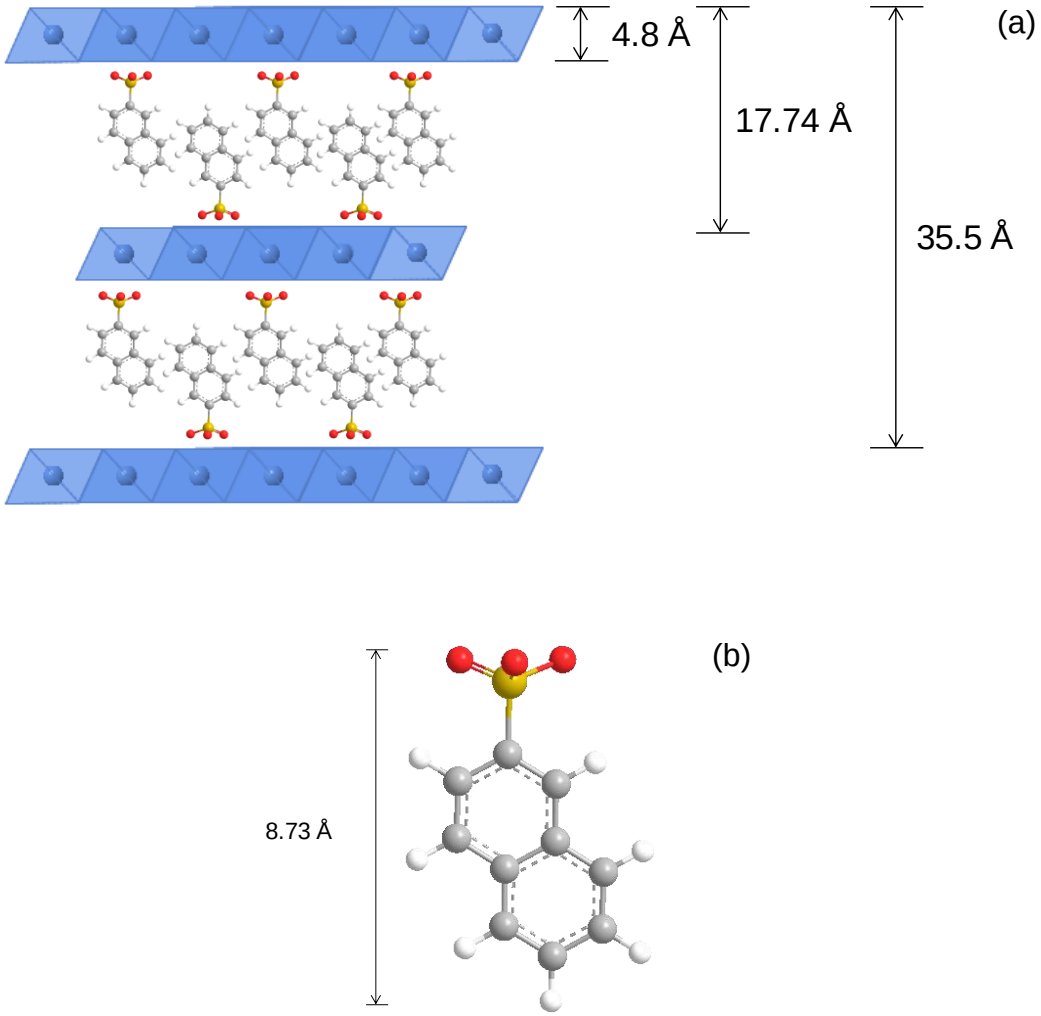

Figure 3.10. (a) Schematic illustration of possible Ca_2Ga-naphthalene sulfonate structure, and (b) the molecular structure of naphthalene sulfonate.

The XRD data for the lignosulfonate-intercalated Ca_2Al-LDH (Ca_2Al-lignosulfonate) (Figure 3.9(d)) is very broad which indicates a material with very low crystallinity presumably due to the structural variation of the lignosulfonate anions; as a result the structural orientation of the lignosulfonate within the layers is currently unknown. It is possible that the low molecular weight chains of the lignosulfonate solution may selectively intercalate into the Ca_2Al-LDH structure. Polyacrylate can also replace the nitrate anions in the LDH host as observed from the XRD pattern shown in Figure 3.9(e). The XRD pattern indicates that the structure is less crystalline than Ca_2Al-naphthalene sulfonate. The long chains of the acrylate polymers may be responsible for the poorer crystallinity of the LDH structure. The (002) and (004) Bragg reflections of Ca_2Al-NO_3,[43, 44] marked as * in Figure 3.9, can be found as impurities in Ca_2Al-lignosulfonate and

Ca_2Al-polyacrylate, corresponding to the presence of the nitrate absorption from IR data of Ca_2Al-lignosulfonate Section 3.2.2. The d-spacing data of the Ca_2Al-LDH superplasticiser intercalates is summarised in Table 3.1.

Table 3.1. d-spacing (Å) of superplasticiser intercalates and comparison with hydroxide- and nitrate-intercalated Ca_2Al-LDH.

	Guest intercalates in Ca_2Al-LDH				
	Hydroxide	Nitrate	Naphthalene sulfonate	Lignosulfonate	Polyacrylate
c parameter (Å)	15.16	17.21	35.47	27.80	22.53

[#] $a = b = 5.74$ Å indexed as a hexagonal unit cell.

3.2.2 Infrared spectroscopy data

The FTIR spectra of the Ca_2Al-superplasticiser materials all exhibit broad absorption bands over the range 3700-3000 cm^{-1}, with absorption maxima around 3670 cm^{-1} and 3450 cm^{-1} due to the stretching vibrations of the hydroxyl groups of the inorganic layers and of interlayer water (Figure 3.11 - Figure 3.13).

The IR spectrum for Ca_2Al-naphthalene sulfonate is shown in Figure 3.11. The absorbance for the C-H stretching vibration, C=C and C-H bending vibration are observed at 3030, 1500 and 860 cm^{-1}, respectively. Weak absorption bands at 1637 and 965 cm^{-1} are assigned to bending vibrations of the interlayer co-intercalated water molecules. The asymmetric and symmetric ν(S=O) stretching[45, 46] modes are observed at 1213 and 1060 cm^{-1} and the ν(O=S=O) bending is observed at 720 cm^{-1}. The IR spectrum of a bulk sample of CaAl-NO_3 exhibits features at 1415 and 1348 cm^{-1} due to the presence of intercalated NO_3^- anions (Figure 3.11(a)), which are not observed in the IR absorption spectrum of the Ca_2Al-naphthalene sulfonate phases.

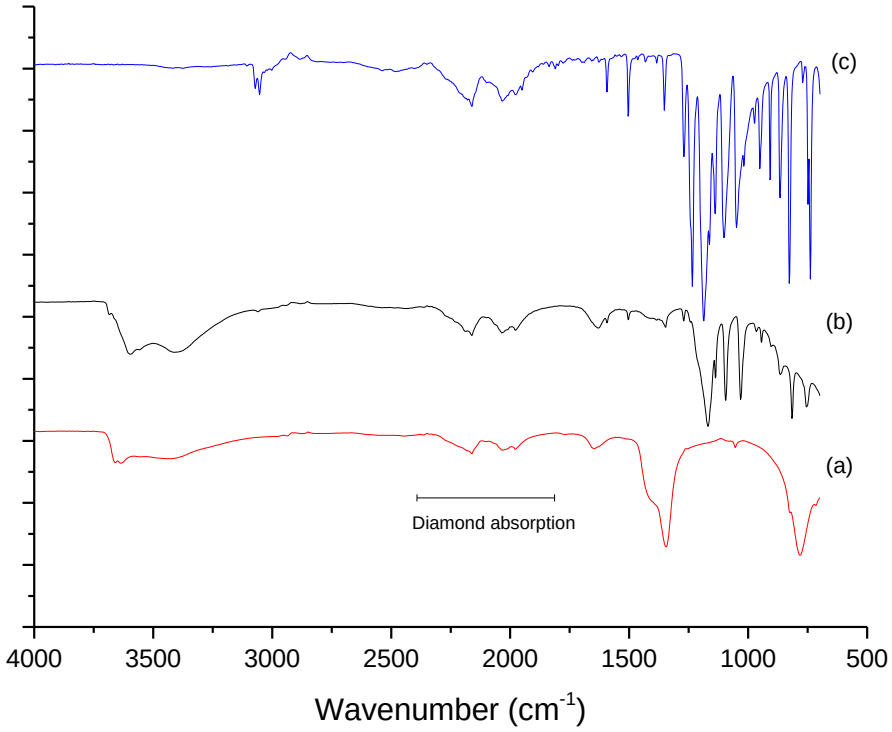

Figure 3.11. IR spectra of (a) Ca_2Al-NO_3, (b) Ca_2Al-naphthalene sulfonate, and (c) sodium naphthalene sulfonate.

The IR data of Ca_2Al-lignosulfonate is shown in Figure 3.12; there are various functional groups on the structure of lignosulfonate because of the huge and complex molecular structure, thus several weak absorbances are observed in the IR spectrum.[47] Absorbances due to the aromatic functional group can be found at 3030, 1500 and 860 cm^{-1}; these represent the C-H stretching, C=C bending, and C-H bending. The O-H stretching vibration of an alcohol functional group is present at 3200 cm^{-1}. The absorption bands of alkenyl C-H, alkenyl C=C, and alkyl C-H stretching vibrations occur at 3010, 1680, and 2950 cm^{-1}, respectively. The stretching vibration of the ketone C=O functional group can be observed at 1700 cm^{-1}. The sulfonate functional group gives asymmetric and symmetric ν(S=O) stretching absorbances at 1213 and 1060 cm^{-1} and the ν(O=S=O) bending mode at 720 cm^{-1}.[47] The weak IR spectrum of nitrate can be found in Ca_2Al-lignosulfonate at 1415 and 1348 cm^{-1}.

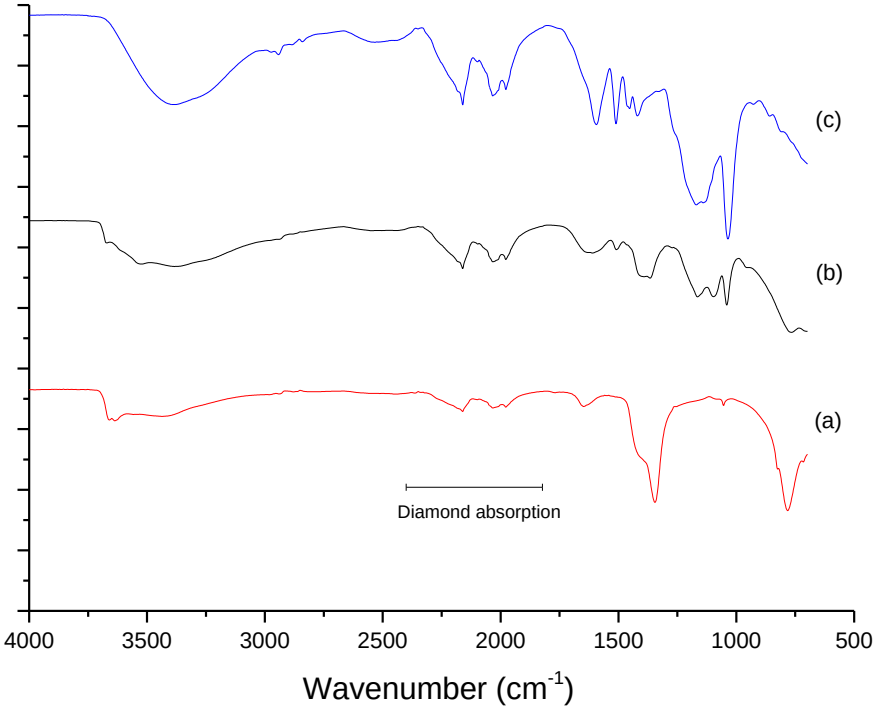

Figure 3.12. IR spectra of (a) $Ca_2Al\text{-}NO_3$, (b) Ca_2Al-lignosulfonate, and (c) sodium lignosulfonate.

The IR spectrum of Ca_2Al-polyacrylate (Figure 3.13), show absorbance due to the asymmetric stretching vibration of CH_3, and the asymmetric and symmetric stretching vibrations of the CH_2 moiety of the polymer chain appear at 2957, 2919 and 2850 cm^{-1}, respectively. The C=O stretching vibration of the carboxylate ion occurs at 1600 cm^{-1}.[48, 49]

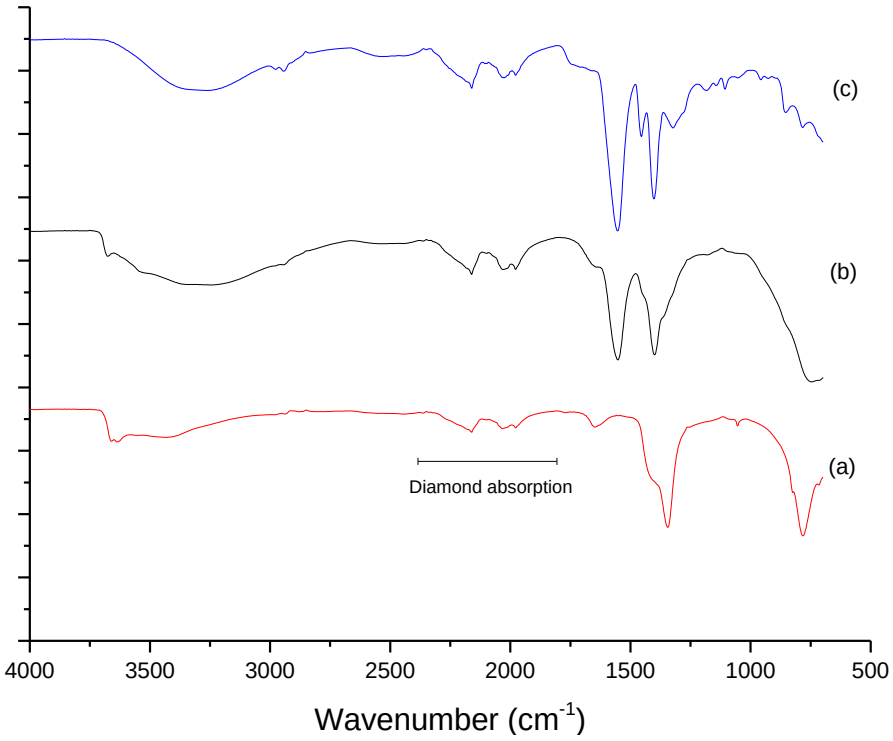

Figure 3.13. IR spectra of (a) $Ca_2Al\text{-}NO_3$, (b) Ca_2Al-polyacrylate, and (c) sodium polyacrylate.

3.2.3 Electron microscopy study

Scanning electron microscopy (SEM) was used to observe the morphology and particle size of the superplasticiser-intercalated Ca_2Al-LDHs. $Ca_2Al\text{-}NO_3$ obtained using co-precipitation gives platelet-shaped particles that are 10 micron in platelet diameter. After intercalation, the morphology and particle size of all the post-intercalated samples appear relatively consistent. It is postulated that the structure of the LDH materials were not destroyed during intercalation due to the topotactic process. The SEM images of the intercalated materials show little change in the thickness of the particles.

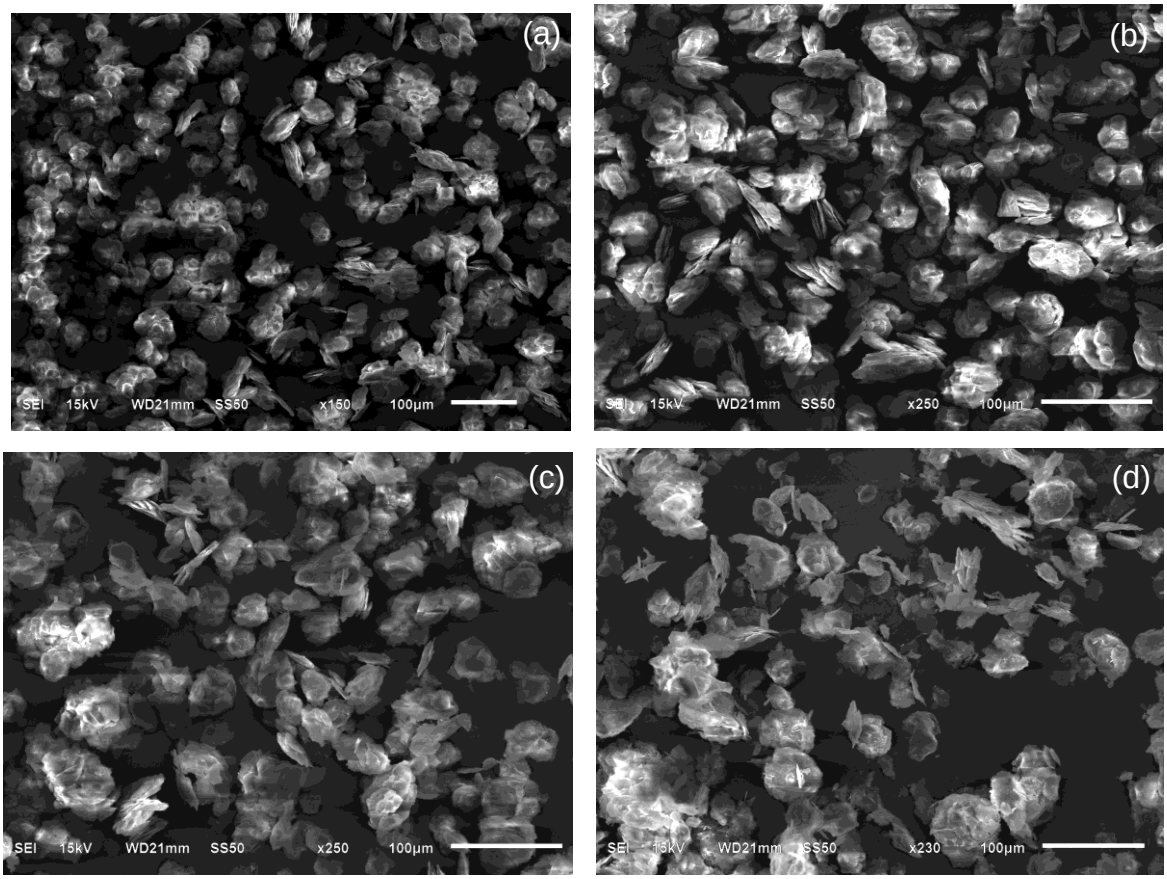

Figure 3.14. SEM images of (a) $Ca_2Al\text{-}NO_3$, (b) Ca_2Al-naphthalene sulfonate, (c) Ca_2Al-lignosulfonate, and (d) Ca_2Al-polyacrylate.

Energy-dispersive X-ray spectroscopy (EDX) was used to estimate the elemental composition. The small amount of sulfur detected corresponds to the sulfonate functional groups in naphthalene sulfonate and lignosulfonate intercalated Ca_2Al-LDHs. The Ca/Al atomic ratios of all samples after the ion-exchange reaction are in the range between 1.8 and 2.3 which are relatively close to that of the starting material.

Table 3.2. Atomic percentage of elements analysed by Energy-Dispersive X-ray spectroscopy technique (EDX).

	Atomic%			
Intercalated Ca_2Al-LDHs	Ca	Al	S	Ca/Al atomic ratio
Nitrate	7.8	4.1	-	1.9
Naphthalene sulfonate	7.8	3.3	3.8	2.4
Lignosulfonate	7.0	4.1	1.6	1.8
Polyacrylate	6.4	3.5	-	1.8

3.2.4 Thermogravimetric and elemental analysis

The Ca_2Al-superplasticiser LDHs were characterised by using thermogravimetric analysis (TGA) and elemental analysis to determine the amount of water and superplasiciser intercalated in the LDHs.

The TGA plot for Ca_2Al-naphthalene sulfonate shown in Figure. 3.15, the cointercalated water is lost at temperatures up to 150 °C, followed then by the loss of water from the hydroxide layers. From 400 °C onwards, the decomposition of guest anions occurs, resulting in a final product which is a mixture of Mayenite ($Ca_{12}Al_{14}O_{33}$, JCPDS 01-070-2144), and Lime (CaO, JCPDS 00-048-1467). The other organic intercalates all behave very similarly.

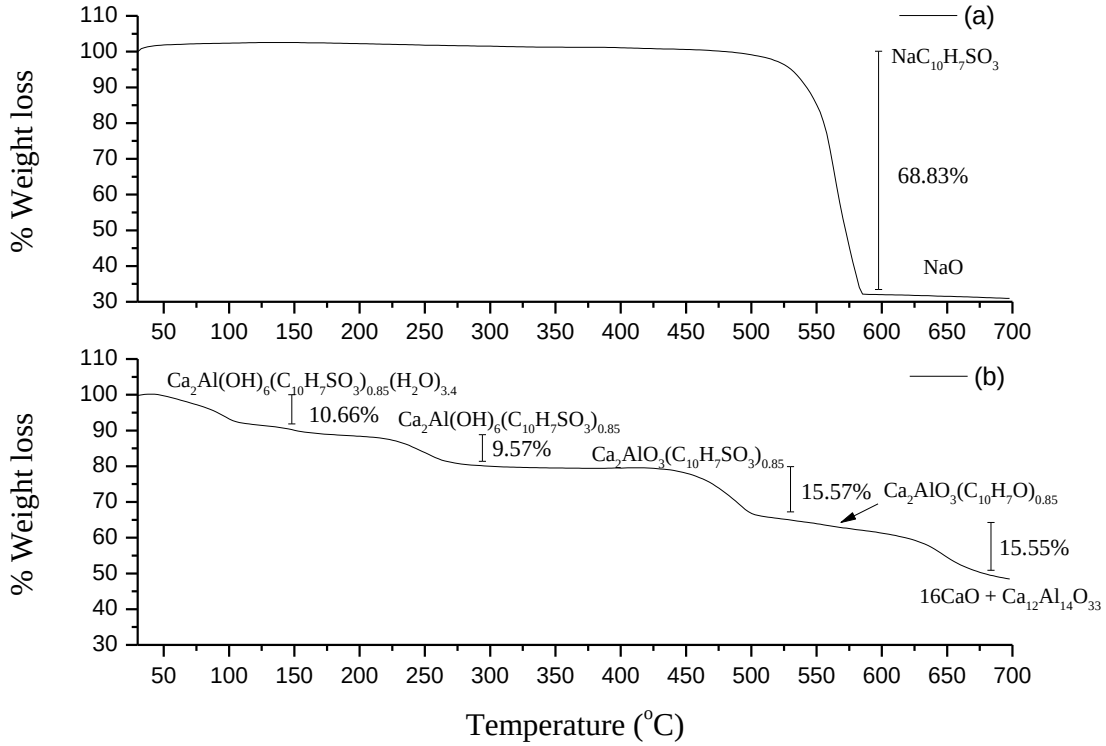

Figure 3.15. TGA plots for (a) Sodium naphthalene sulfonate, and (b) Ca_2Al-naphthalene sulfonate from 30 to 700°C.

The compositions of the organic-inorganic hybrid materials were calculated from thermogravimetric analysis and elemental analysis data, which are summarised in Table 3.3.

Table 3.3. Elemental analysis data for Ca_2Al-superplasticiser materials.

	Chemical composition, obs. (calc.)/(wt%)			
Intercalated Ca_2Al-LDHs	C	H	N	Formula
Naphthalene sulfonate	22.9	4.2	0.0	$[Ca_2Al(OH)_6](C_{10}H_7SO_3)_{0.85}•3.4H_2O$
	(22.9)	(4.2)	(0.0)	
Lignosulfonate	10.3	4.5	0.0	$[Ca_2Al(OH)_6](C_9H_8SO_5)_{0.33}•3.5H_2O$
	(10.3)	(4.5)	(0.0)	
Polyacrylate	9.2	4.9	0.0	$[Ca_2Al(OH)_6](C_3H_3O_2)•4.2H_2O$
	(9.3)	(4.9)	(0.0)	
Nitrate	0.0	4.8	3.6	$[Ca_2Al(OH)_6](NO_3)•6H_2O$
	(0.0)	(4.8)	(3.7)	

#The formula of lignosulfonate was approximately $C_9H_8SO_5^{3-}$

3.3 Release of superplasticisers from intercalated Ca_2Al-LDHs

The ionic composition of the liquid phase in cement plays a significant role in the hydration process, as do the additional chemicals added to the system. Understanding the effects of ionic composition on additives release can reveal how these additives have an influence on cement hydration. It is possible that anions released from cement grains could intercalate into the LDHs, thus replacing and promoting entry of additives into the liquid phase. To investigate this hypothesis, solutions containing the anions of interest including; hydroxide, silicate, sulfate and carbonate, were used to study the effects on the release of superplasticisers from LDHs.

To measure the release from the superplasticiser intercalated Ca_2Al-LDHs, each was introduced into various solutions containing anions expected to appear in a generic cement solution and also into a real cement pore solution isolated from cement paste (water to cement ratio = 0.8) without stirring to simulate cement hydration. The amount of LDH added per sample was chosen to be the same concentration as the superplasticiser used in commercial concrete applications (0.4%). The mixed solutions were then separated by centrifugation. Images of the isolated solutions following lignosulfonate release are shown in Figure 3.16. All separated solution were analysed by UV-VIS spectroscopy. The UV absorbance of naphthalene sulfonate, and lignosulfonate occur at 228 and 280 nm respectively.[34] The intensities of the absorption maxima were calibrated using a series of standard solutions. The percentage release of naphthalene sulfonate and lignosulfonate were calculated in comparison with the absorbance of superplasticiser-intercalated Ca_2Al-LDHs in HCl solution. Release profiles for Ca_2Al-naphthalene sulfonate and Ca_2Al-lignosulfonate are shown in Figure 3.17 and 3.18, respectively.

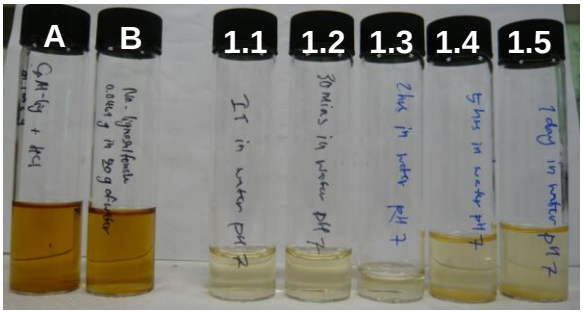

Ca_2Al-lignosulfonate in water at pH 7
1.1 At initial time
1.2 At 30 minutes
1.3 At 2 hours
1.4 At 5 hours
1.5 At 1 day

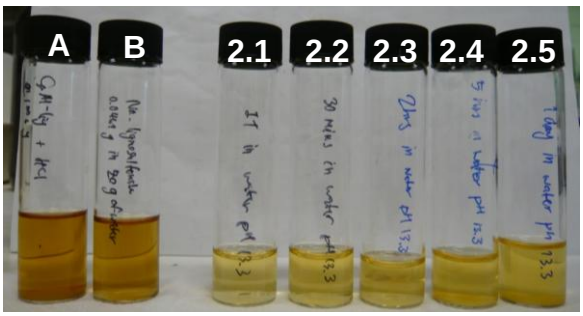

Ca_2Al-lignosulfonate in water at pH 13.3
2.1 At initial time
2.2 At 30 minutes
2.3 At 2 hours
2.4 At 5 hours
2.5 At 1 day

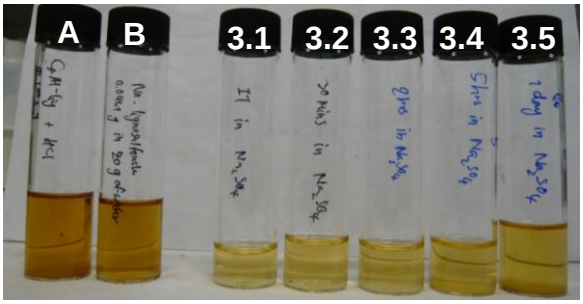

Ca_2Al-lignosulfonate in sulfonate solution
3.1 At initial time
3.2 At 30 minutes
3.3 At 2 hours
3.4 At 5 hours
3.5 At 1 day

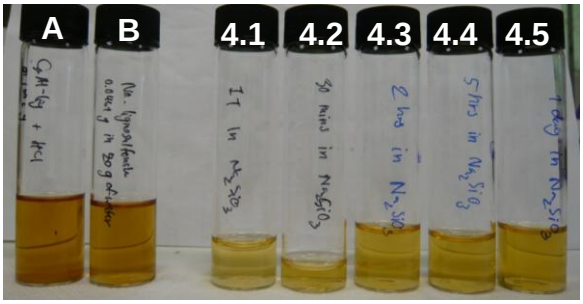

Ca_2Al-lignosulfonate in silicate solution
4.1 At initial time
4.2 At 30 minutes
4.3 At 2 hours
4.4 At 5 hours
4.5 At 1 day

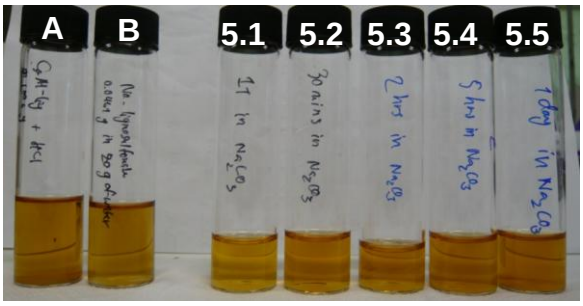

Ca_2Al-lignosulfonate in carbonate solution
5.1 At initial time
5.2 At 30 minutes
5.3 At 2 hours
5.4 At 5 hours
5.5 At 1 day

Figure 3.16. Images of the separated solutions following lignosulfonate release studies compared with Ca_2Al-lignosulfonate digested in HCl solution (A), and sodium lignosulfonate solution (B) containing lignosulfonate the same concentration as in (A).

The release of naphthalene sulfonate and lignosulfonate from the LDHs varies significantly depending on the pH and the nature of the anions in the solution. The release of the guests in water at pH 7 (Figure 3.17(a) and 3.18(a)) were evidently constant after 30 minutes while at a higher pH of 13.3 (Figure 3.17(b) and 3.18(b)), which is the observed pH in cement paste, resulted in a slight increase. The release profiles of naphthalene sulfonate and lignosulfonate in silicate solution (Figure 3.17(c) and 3.18(c)) are quite similar to the profiles of the guests in water at pH 13.3. In sulfate solution, Ca_2Al-naphthalene sulfonate exhibits a much greater quantity of anion release compared to Ca_2Al-lignosulfonate. The rate of release of the guests (Figure 3.17(e) and 3.18(e)) in carbonate solution increases much more rapidly than in other solutions due to the formation of calcium carbonate, as can be seen using XRD of the solid residues after the release, discussed later in Section 3.5. In almost every set of conditions, the overall release from Ca_2Al-naphthalene sulfonate is greater than Ca_2Al-lignosulfonate, possibly because of the smaller size of the naphthalene sulfonate. Naphthalene sulfonate anions can be replaced by various anions in solution; however, it is unable to reach complete release after 2 days.

Summary of the long time scale anion release efficiencies:

For Ca_2Al-naphthalene sulfonate;

$$CO_3^{2-} > SO_4^{2-} > Si_3O_7^{2-} \approx \text{water pH 13.3} \approx \text{water pH 7}$$

For Ca_2Al-lignosulfonate;

$$CO_3^{2-} > Si_3O_7^{2-} \geq \text{water pH 13.3} > SO_4^{2-} > \text{water pH 7}$$

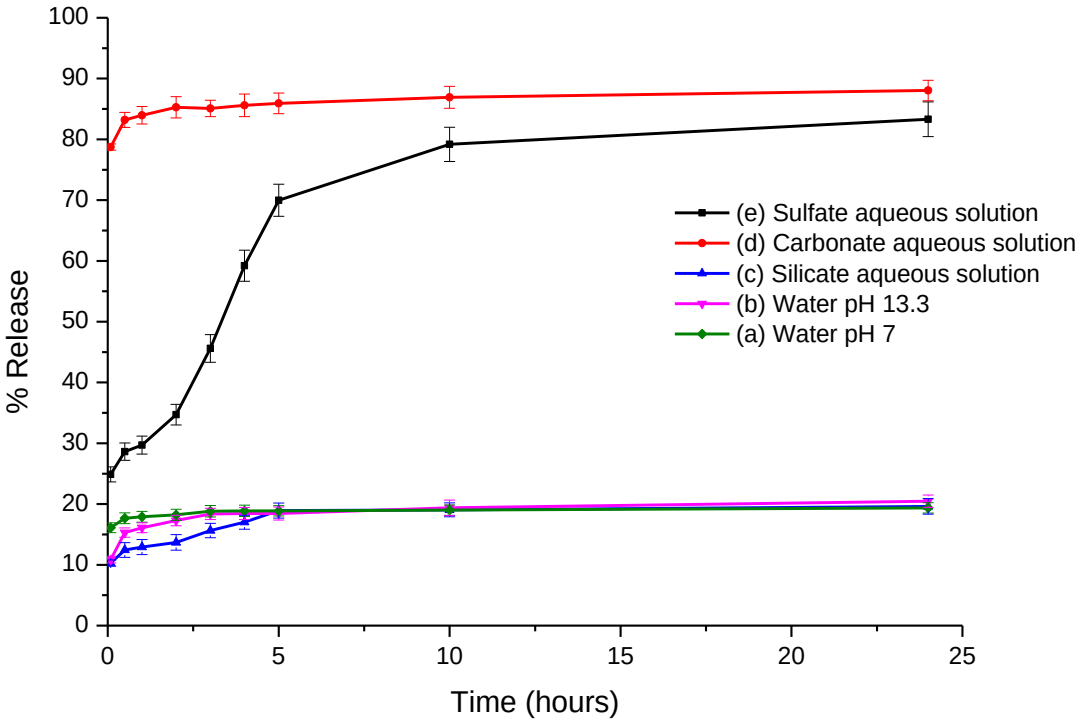

Figure 3.17. Release profiles of Ca_2Al-naphthalene sulfonate determined from the concentration of released naphthalene sulfonate in (a) water pH 7, (b) water pH 13.5, (c) $Na_2Si_3O_7$ solution, (d) Na_2CO_3 solution, and (e) Na_2SO_4 solution. Solid lines are just guides to the eye.

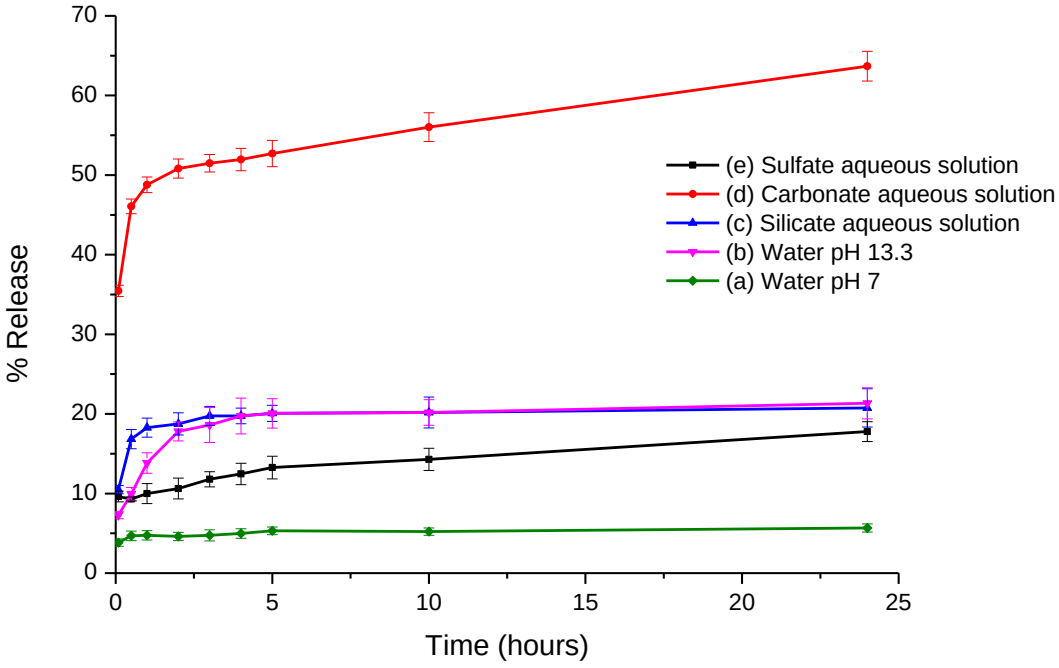

Figure 3.18. Release profiles of Ca_2Al-lignosulfonate determined from the concentration of released lignosulfonate in (a) water pH 7, (b) water pH 13.5, (c) $Na_2Si_3O_7$ solution, (d) Na_2CO_3 solution, and (e) Na_2SO_4 solution. Solid lines are just guides to the eye.

In a simulated cement solution, Ca_2Al-naphthalene sulfonate releases its anion at a faster rate than Ca_2Al-lignosulfonate, with 11.3 % more of the intercalated anion released after the first 5 minutes. The release of both superplasticisers then gradually increases with an 18 % difference after a 5-hour period. The release of the anions was lower than originally anticipated. It is possible that the simulated cement solution from the extraction process was isolated without exposure to CO_2 from the air as would be the case in general cement preparation. The amount of CO_3^{2-} in cement solution – to replace the anions between LDH layers and form $CaCO_3$ to release additives into the solution – is therefore less. Hence, the cause of a lower release of the anions into the solution compared to the other studies.

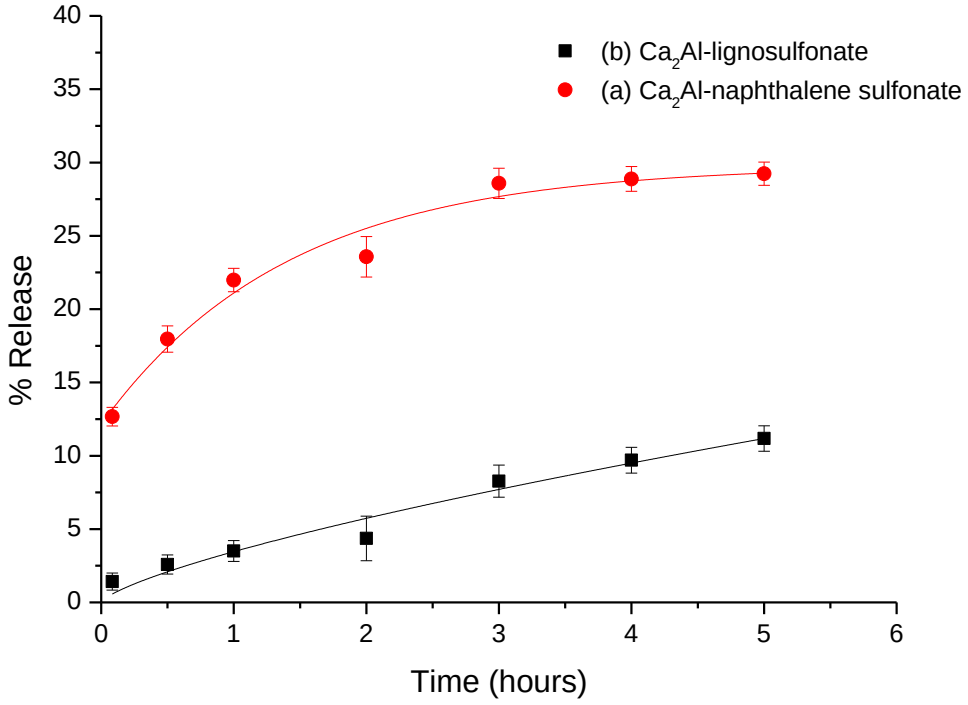

Figure 3.19. Release profiles of (a) Ca_2Al-naphthalene sulfonate, and (b) Ca_2Al-lignosulfonate in cement solution over the reaction time (water/cement ratio = 0.8). Solid lines are just guides to the eye.

3.4 Kinetic modelling of anion release from superplasticiser-intercalated Ca_2Al-LDHs

The anion release data from the superplasticiser-intercalated Ca_2Al-LDHs, were fitted to a range of release models. Release kinetics models have commonly been used to determine mechanistic data and calculate kinetics paremeters of reactions. Over the years, there are many kinetics models determined depending on the definition of the models. For example, Michaelis-Menten model is used to determine the kinetics of enzyme.[50] The Avrami-Erofe'ev model, the first-order model, the modified Freundlich model, and the parabolic diffusion model have been chosen for data fitting. The selected kinetics models are normally used for the study of ion-exchange kinetics in layered materials. The definition of the kinetics models and the detailed fitting of the superplasticiser release profiles are given in Appendix II and Appendix III. The kinetic data was fitted between t = 0 and t = 24 hours. The correlation coefficients of the fit to each of the kinetic models[51] are summarised in Tables 3.4, and 3.5.

For Ca_2Al-naphthalene sulfonate, the parabolic diffusion model and the Freundlich model reveal best fits with r^2 values ranging between 0.85 and 0.99 in each of the different anion solutions shown in Table 3.5.

Table 3.4. Correlation coefficient (r^2) for the least squares fits to the selected kinetic models for the naphthalene sulfonate release of Ca_2Al-LDH in different anion solutions.

Equation[#]	Correlation coefficient (r^2)					
	Water pH 7	Water pH 13.5	$Na_2Si_3O_7$	Na_2SO_4	Na_2CO_3	Cement Solution (w/c =0.8)
Avrami-Erofe'ev model $\alpha = 1 - \exp(-kt^n)$	0.00	0.94	0.94	0.84	0.10	0.98
The first-order model $dC_A/dt = -k'C_A$	0.26	0.36	0.29	0.73	0.05	0.85
Freundlich model $\alpha = K_F C_e^{1/n}$	0.90	0.86	0.85	0.90	0.82	0.96
Parabolic diffusion model $(\alpha/t = (4/\pi^{1/2})(D/r^2)^{1/2}(1/t^{1/2}) - (D/r^2))$	0.95	0.97	0.96	0.95	0.95	0.99

[#]Full details of kinetic models can be found in Appendix III.

The best fits for the lignosulfonate release data (Table 3.5) are also observed for both the parabolic diffusion model and the Freundlich model.

Table 3.5. Correlation coefficient (r^2) for the least squares fits to the selected kinetic models for the lignosulfonate release from Ca_2Al-lignosulfonate in different anion containing solutions.

Equation	Correlation coefficient (r^2)					
	Water pH 7	Water pH 13.5	$Na_2Si_3O_7$	Na_2SO_4	Na_2CO_3	Cement Solution (w/c =0.8)
Avrami-Erofe'ev model $\alpha = 1 - \exp(-kt^n)$	0.89	0.89	0.67	0.78	0.96	0.92
The first-order model $dC_A/dt = -k'C_A$	0.58	0.35	0.17	0.91	0.75	0.80
Freundlich model $\alpha = K_F C_e^{1/n}$	0.89	0.95	0.90	0.95	0.96	0.98
Parabolic diffusion model $(\alpha/t = (4/\pi^{1/2})(D/r^2)^{1/2}(1/t^{1/2}) - (D/r^2))$	0.97	0.93	0.99	0.95	0.97	0.99

[#]Full details of kinetic models can be found in Appendix III.

For the parabolic diffusion model, the least squares fitting (Appendix III) have been used to obtain a modified diffusion coefficient (D/r^2) which is divided by the square of a radius of diffusion. The radius of diffusion is a constant value, dependant on the type of diffusing particles. A summary of the modified diffusion coefficients obtained for Ca_2Al-LDHs in different anionic solutions as shown in Table 3.6.

Table 3.6. Kinetic parameters for Ca_2Al-naphthalene sulfonate, and Ca_2Al-lignosulfonate release based on parabolic diffusion model.

Equation	Kinetic parameters[b] (D/r^2, min^{-1}) from the parabolic diffusion model[a]					
	Water pH 7	Water pH 13.5	$Na_2Si_3O_7$	Na_2SO_4	Na_2CO_3	Cement Solution (w/c =0.8)
Ca_2Al-naphthalene sulfonate	0.0042	0.0025	0.0024	0.0057	0.0211	0.0036
Ca_2Al-lignosulfonate	0.0011	0.001	0.0026	0.003	0.010	0.0039

[a]Parabolic diffusion equation $(\alpha/t = (4/\pi^{1/2})(D/r^2)^{1/2}(1/t^{1/2}) - (D/r^2))$; [b]$D$ = Diffusion coefficient, and r = radius of cylindrical diffusion.

A higher diffusion coefficient value means a higher diffusivity of the material. In general, we observe that naphthalene sulfonate diffuses into solution significantly faster than lignosulfonate. The trends in the release reactivity of the displacing anions for naphthalene sulfonate and lignosulfonate Ca_2Al-LDHs are shown below.

The relative order of the diffusion coefficient for anion of release naphthalene sulfonate;

$$CO_3^{2-} >>> SO_4^{2-} > \text{Water pH 7} > \text{cement solution} > Si_3O_7^{2-} \approx \text{Water pH 13.5}$$

The relative order of the diffusion coefficient for anion of release lignosulfonate;

CO_3^{2-} >>> cement solution > SO_4^{2-} > $Si_3O_7^{2-}$ >Water pH 13.5 ≈ Water pH 7

The release of napthalene sulfonate and lignosulfonate from their respective intercalates has also been fitted to the modified Freundlich model. The least squares fit to the experimental data are shown in Figure 3.20 and 3.21. A summary of the kinetic parameters are given to Table 3.7 and 3.8.

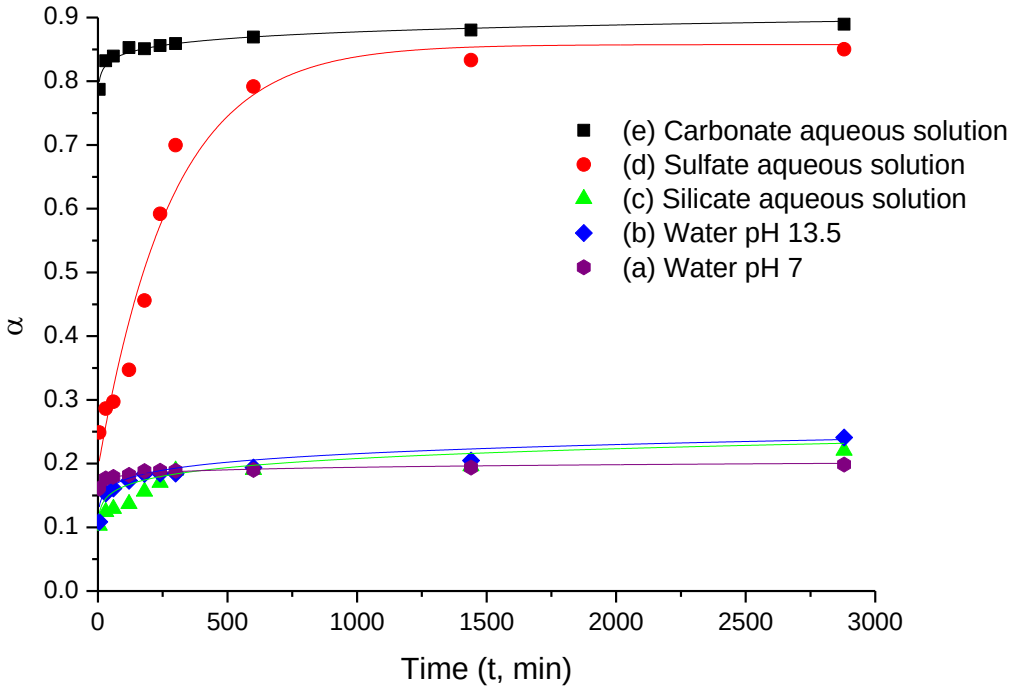

Figure 3.20. Naphthalene sulfonate release profiles from Ca_2Al-naphthalene sulfonate LDH suspended in (a) water pH 7, (b) water pH 13.5, (c) $Si_3O_7^{2-}$ solution, (d) SO_4^{2-} solution, and (e) CO_3^{2-} solution. The solid lines are least square fits to the Modified Freundlich model, exception for the release profile of Ca_2Al-naphthalene sulfonate LDH suspended in SO_4^{2-} solution fitted to the Avrami's model.

Table 3.7. Kinetic parameters obtained from least square fitting of the release of naphthalene sulfonate from Ca_2Al-naphthalene sulfonate in different anion solutions.

Ca_2Al-naphthalene sulfonate in solutions	Modified Freundlich model ($\alpha = K_F t^n$)	
	K_F (min^{-n})	*n*
Water pH 7	0.16±0.002	0.030±0.003
Water pH 13.5	0.11±0.017	0.093±0.025
Silicate solution	0.10±0.015	0.103±0.025
Carbonate solution	0.78±0.006	0.018±0.002

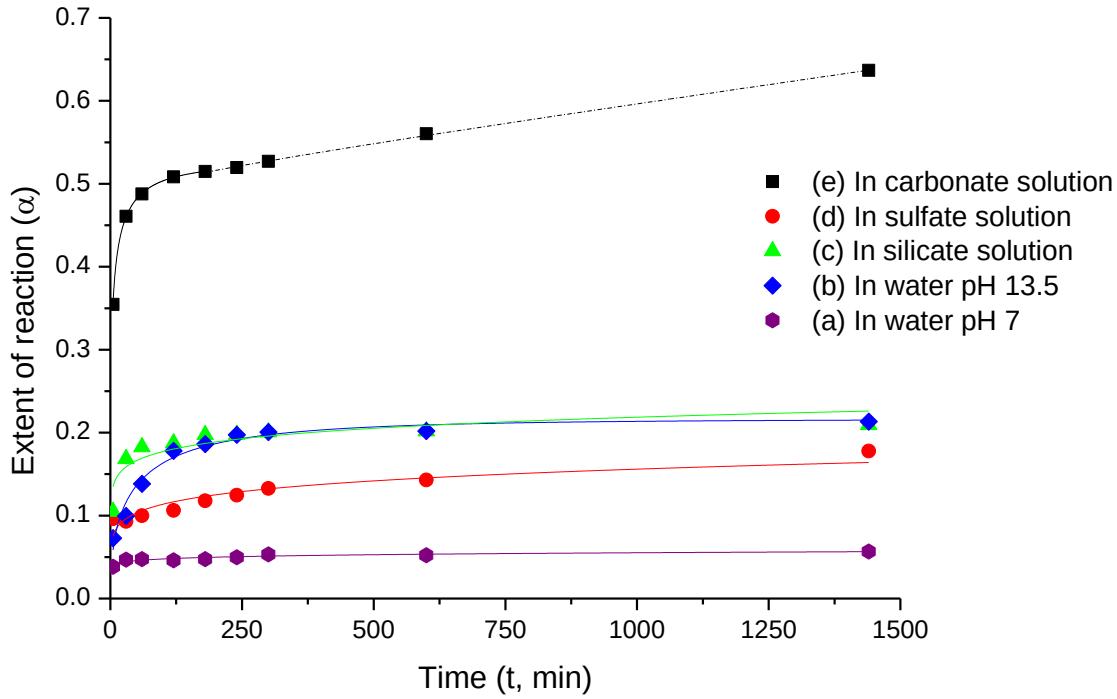

Figure 3.21. Lignosulfonate release profiles from Ca_2Al-lignosulfonate LDH suspended in: (a) water pH 7, (b) water pH 13.5, (c) $Na_2Si_3O_7$ solution, (d) Na_2SO_4 solution, and (e) Na_2CO_3 solution. The solid lines are least square fit to the Modified Freundlich's model, exception for the release profile of Ca_2Al-naphthalene sulfonate LDH suspended in water pH 13.5 and CO_3^{2-} solution fitted to the Avrami's model.

Table 3.8. Kinetic parameters by curve fitting from the selected kinetic models, for the release of lignosulfonate from Ca_2Al-lignosulfonate in different anion solutions.

Ca_2Al-lignosulfonate in solutions	Modified Freundlich model ($\alpha = K_F t^n$)	
	K_F (min^{-n})	*n*
Water pH 7	0.06±0.007	0.14±0.02
Silicate solution	0.12±0.01	0.09±0.02
Sulfate solution	0.07±0.01	0.17±0.03
Carbonate solution	$8.7x10^{-5}$±5.4 $x10^{-6}$	0.013±0.006

In cement solution, naphthalene sulfonate is released significantly faster than lignosulfonate (Figure 3.22). All these data can be fitted to the Modified Freundlich model (Table 3.9).

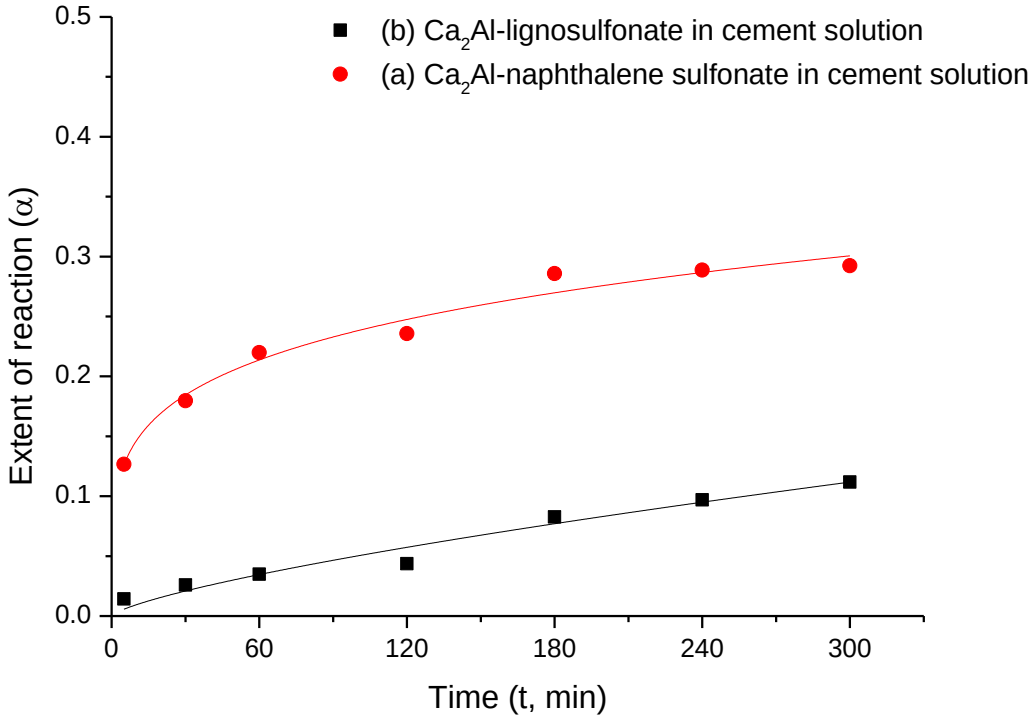

Figure 3.22. Anion release profiles from: (a) Ca_2Al-naphthalene sulfonate LDH, and (b) Ca_2Al-lignosulfonate LDH using cement solution over the reaction time (water/cement ratio = 0.8). Solid lines are least squares fit to the modified Freundlich model.

Table 3.9. Kinetic parameters obtained by least square fitting to the Modified Freundlich model, for the release of naphthalene sulfonate and lignosulfonate anions in cement solution.

	r^2	Modified Freundlich model ($\alpha = K_F t^n$)	
		K_F	*n*
Naphthalene sulfonate	0.97	0.090±0.008	0.21±0.02
Lignosulfonate	0.96	$0.002 \pm 9.0 \times 10^{-4}$	0.73±0.09

The observation that the rate of naphthalene sulfonate release by the cement solution is faster than lignosulfonate may be due to the steric effects of lignosulfonate molecules or low charge density of this anion. However, the release for both LDHs is lower than expected, when compared with the release behaviour of superplasticiser-intercalated Ca_2Al-LDHs in basic anion solutions. We presume this is due to the significantly low concentration of anions in the cement solution.

3.5 Mechanistic considerations

There are a number of publications discussing the kinetic studies on layered double hydroxides, clays and zeolites. Duan *et al.* investigated the release behaviour of antioxidant drugs from LDHs.[52-54] These drugs were capable of being release from LDHs *via* a two-stage process: a rapid release (stage I) followed by a slow release (stage II), in which stage I and stage II were successfully simulated with the modified Freundlich model and parabolic diffusion model, respectively (Figure 3.23). The data fitting indicates that stages I and II can be described by external surface diffusion *via* ion exchange and intraparticle diffusion.

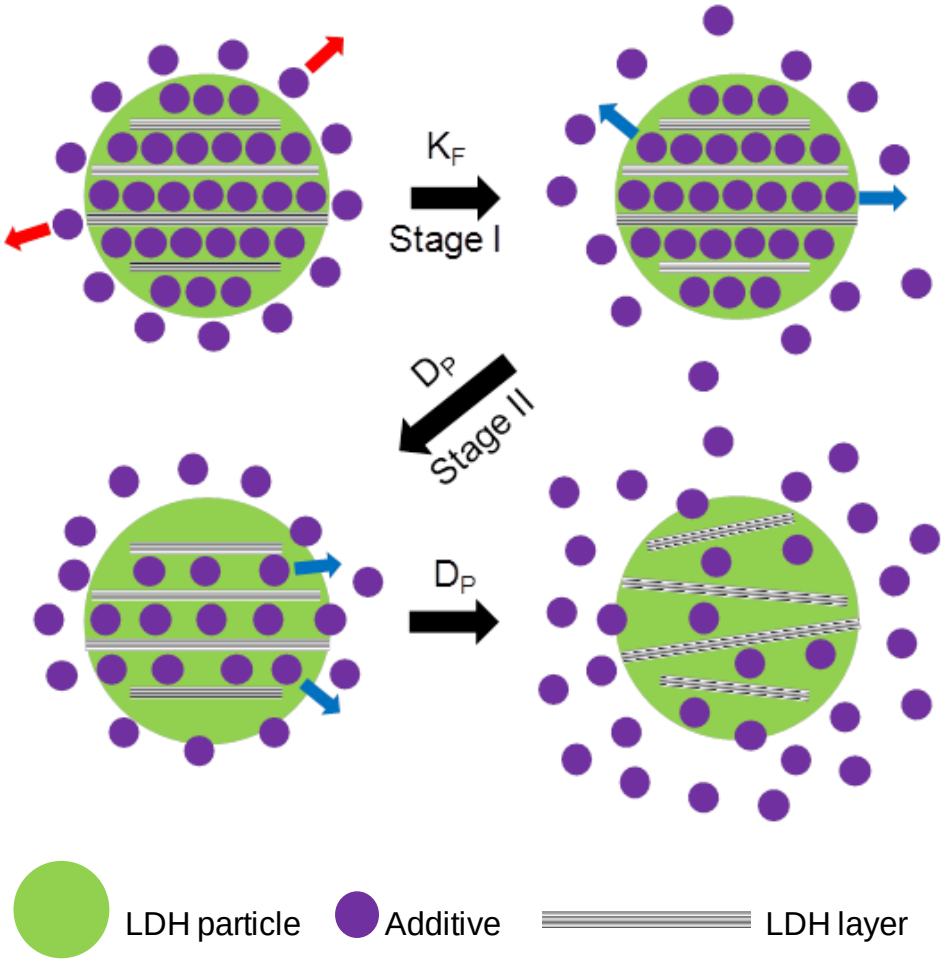

Figure 3.23. Schematic mechanisms of additive release based on the Freundlich model [Stage I, Heterogeneous surface desorption control (red arrows)] with rate constant, K_F, and the parabolic diffusion model [Stage II, the intraparticle diffusion control (blue arrows)] with diffusion coefficient, D_P.

We prepose that a similar two-stage process occur for the release of naphthalene sulfonate and lignosulfonate from those respective LDHs. The kinetics models previously mentioned to explain the mechanism of additive release have been used to study the release behaviour over time. The curve fitting of Ca_2Al-naphthalene sulfonate and Ca_2Al-lignosulfonate in different anion solutions, as well as in cement solution are shown in Figure 3.20, 3.21, and 3.22, respectively. Kinetic parameters for the release of naphthalene sulfonate and lignosulfonate are summarised in Table 3.7, 3.8, and 3.9.

For Ca_2Al-naphthalene sulfonate, the naphthalene sulfonate on particle surfaces can release into water at pH 7, and the interparticle release seems to be completed after approximately 5 hours mixing. In water at pH 13.5 and silicate solution, naphthalene sulfonate can release from surfaces during the process which all release data are fitted with the modified Freundlich model. In the case of sulfate solution, the data set is significantly compatible with Avrami's equation, in which the release is dominated by phase boundary control or diffusion control. In carbonate solution, the mechanism derived from curve fitting is the release from particle surfaces with the reaction being completed after approximately 2 hours after mixing. From the high value of the extent of reaction (α) found at the beginning of the reaction, it can be postulated that naphthalene sulfonate can release quickly from between the LDH layers, without the diffusion from naphthalene sulfonate between LDH layers. Carbonate destroys the LDH structure and naphthalene sulfonate is therefore, immediately released.

3.6 The study of anion exchange using on X-ray diffraction

XRD was also used to investigate the change to the LDHs following suspension in solutions containing CO_3^{2-}, SO_4^{2-} and $Si_3O_7^{2-}$.

In alkaline solution, the XRD data for Ca_2Al-naphthalene sulfonate changes as a function of time. The d-spacing of the (002) Bragg reflection changes from 17.72 Å (Figure 3.25(a)) to 19.97 Å (Figure 3.24(b)). The LDH initially swells in the presence of OH^- ions. Once, the hydroxide ions penetrate the layers they trigger naphthalene sulfonate release to form Ca_2Al-OH, $Ca_4Al_2O_7.xH_2O$. Portlandite [$Ca(OH)_2$] and sodium calcium aluminate [$Na_4Ca_3(AlO_2)_{10}$] which appear after 30 minutes (Figure 3.24(c)). The Ca_2Al-naphthalene sulfonate and Ca_2Al-OH can exfoliate and as result, these impurities dissolve into the solution after 2 days of mixing. Schematic mechanism for naphthalene sulfonate release in alkaline solution is shown in Figure 3.25.

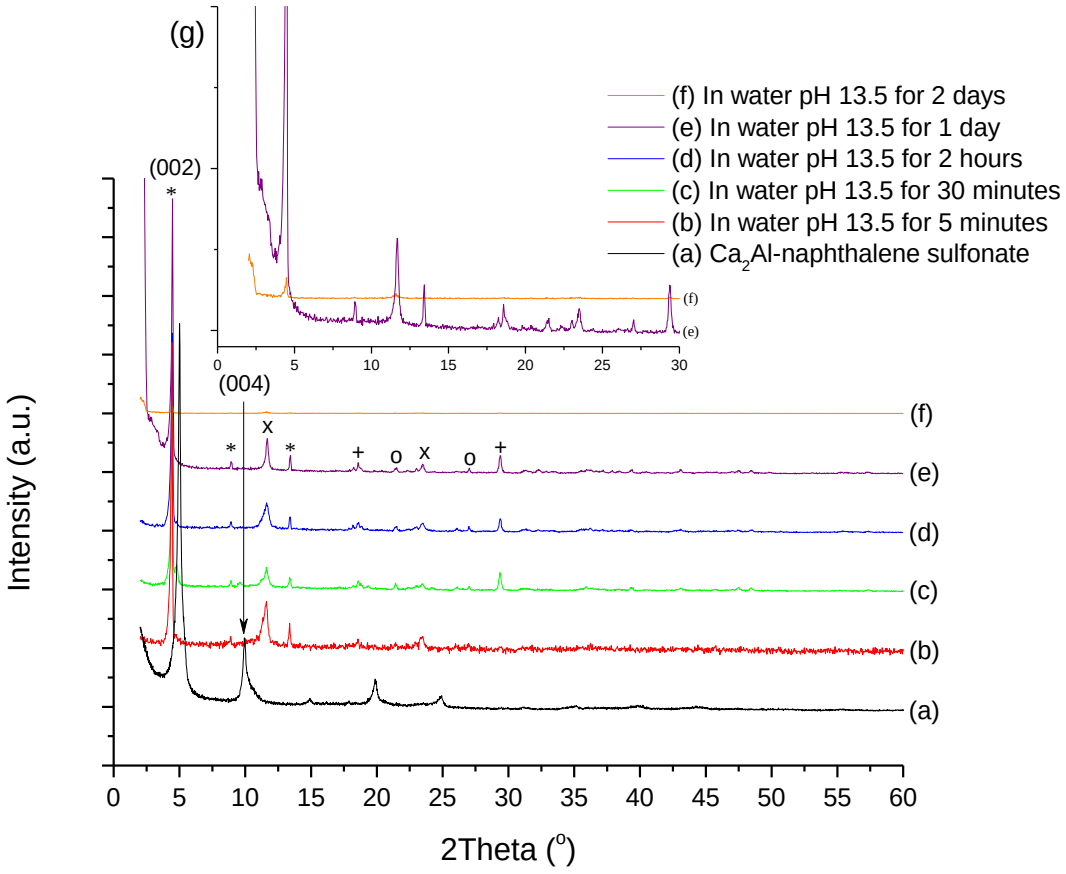

Figure 3.24. XRD patterns of naphthalene sulfonate intercalated Ca_2Al-LDH after mixing in water pH 13.5 over time, where * correspond to swelled naphthalene sulfonate intercalated LDH; x Ca_2Al-OH, + corresponds to Portlandite [$Ca(OH)_2$], and o corresponds to sodium calcium aluminate [$Na_4Ca_3(AlO_2)_{10}$]. (g) XRD patterns of Ca_2Al-naphthalene sulfonate at high magnification.

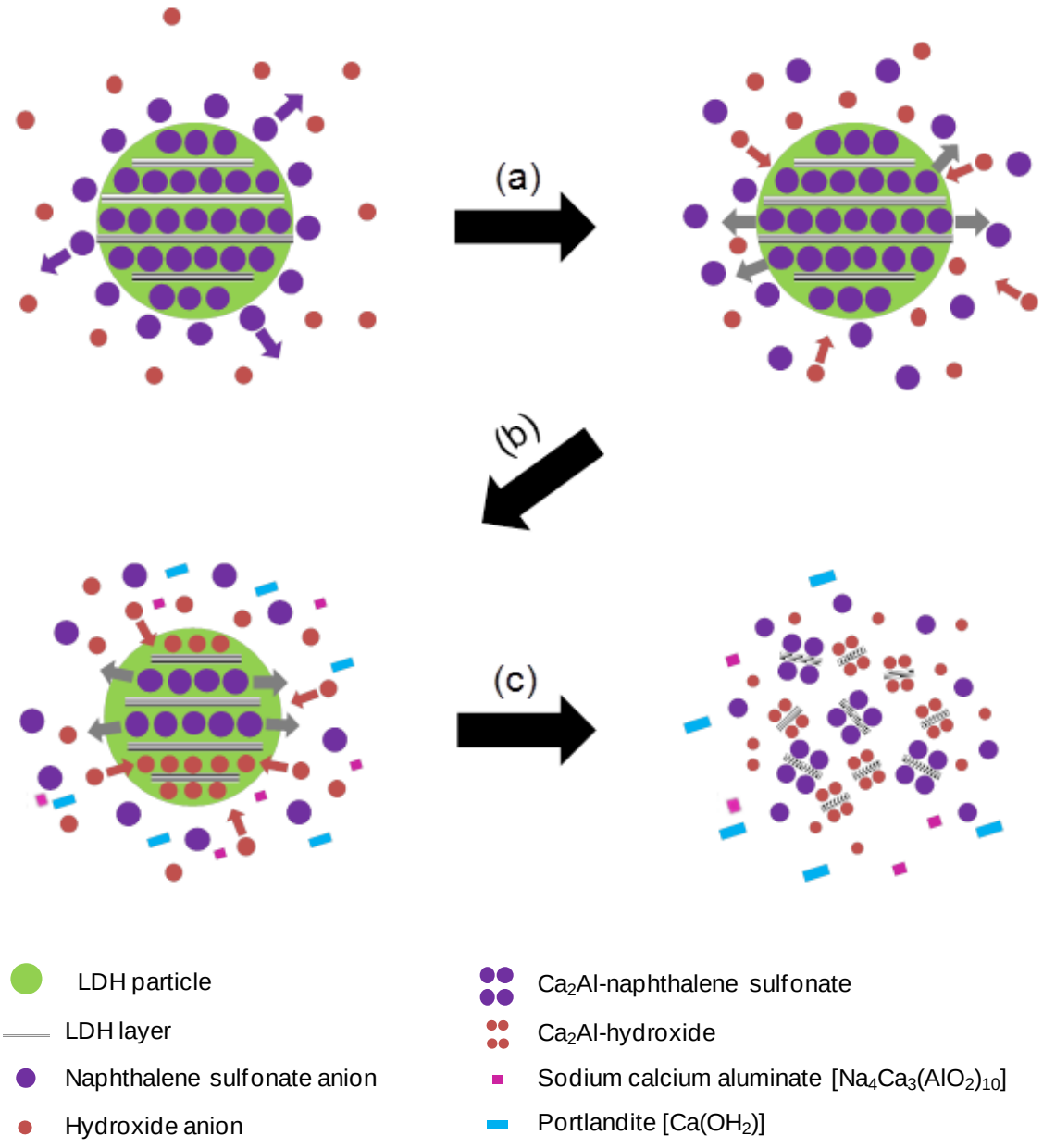

Figure 3.25. Schematic mechanism for naphthalene sulfonate release in water pH 13.5: (a) heterogeneous surface desorption control (purple arrows); (b) intraparticle diffusion control (grey arrows), hydroxide intercalation (red arrows), portlandite ($Ca(OH)_2$) formation, and sodium calcium aluminate ($Na_4Ca_3(AlO_2)_{10}$] formation, and (c) exfoliation of LDHs.

No significant change in the diffraction pattern was observed when Ca_2Al-naphthalene LDH is suspended in silicate solutions with the exception of small amounts of Albite ($Na_{1.0-x}Ca_xAl_{1.0+x}Si_{3.0-x}O_8$; $0.0 < x < 0.1$) and portlandite [$Ca(OH)_2$] appearing after 30 minutes (Figure 3.26(c)), and 2 hours of mixing (Figure 3.26(d)), respectively.

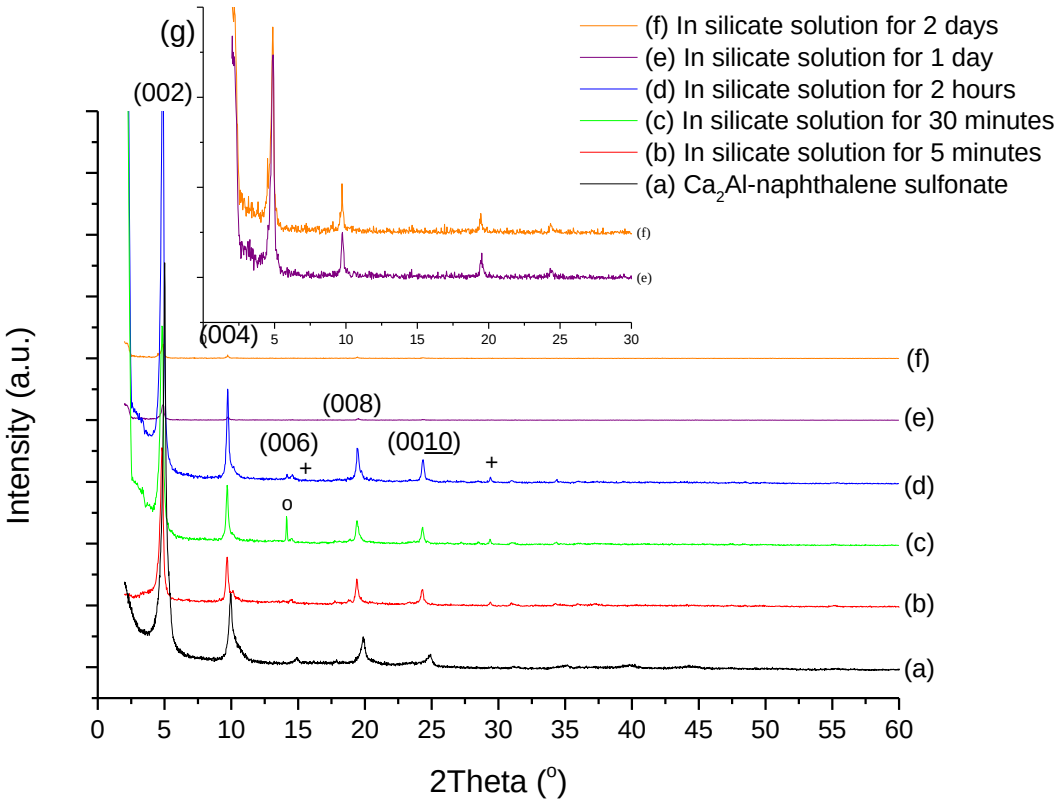

Figure 3.26. XRD pattern series of naphthalene sulfonate intercalated Ca_2Al-LDH after mixing in silicate solution. o corresponds to albite ($Na_{1.0-x}Ca_xAl_{1.0+x}Si_{3.0-x}O_8$; $0.0 < x < 0.1$), and + correspond to portlandite [$Ca(OH)_2$]. (g) XRD patterns of Ca_2Al-naphthalene sulfonate at high magnification.

In sulfate solution, naphthalene sulfonate is released into solution due to the formation of ettringite [$Ca_6Al_2(SO_4)_3(OH)_{12}•26H_2O$] and gypsum ($CaSO_4•2H_2O$) after 2 hours of mixing (Figure 3.28(d)). Portlandite $Ca(OH)_2$ can be observed after one day (Figure 3.27(e)). At two days mixing, the decrease in the intensity of the (002) Bragg reflection becomes evident, hence indicating that naphthalene sulfonate LDH is capable of exfoliating (Figure 3.27(f)).

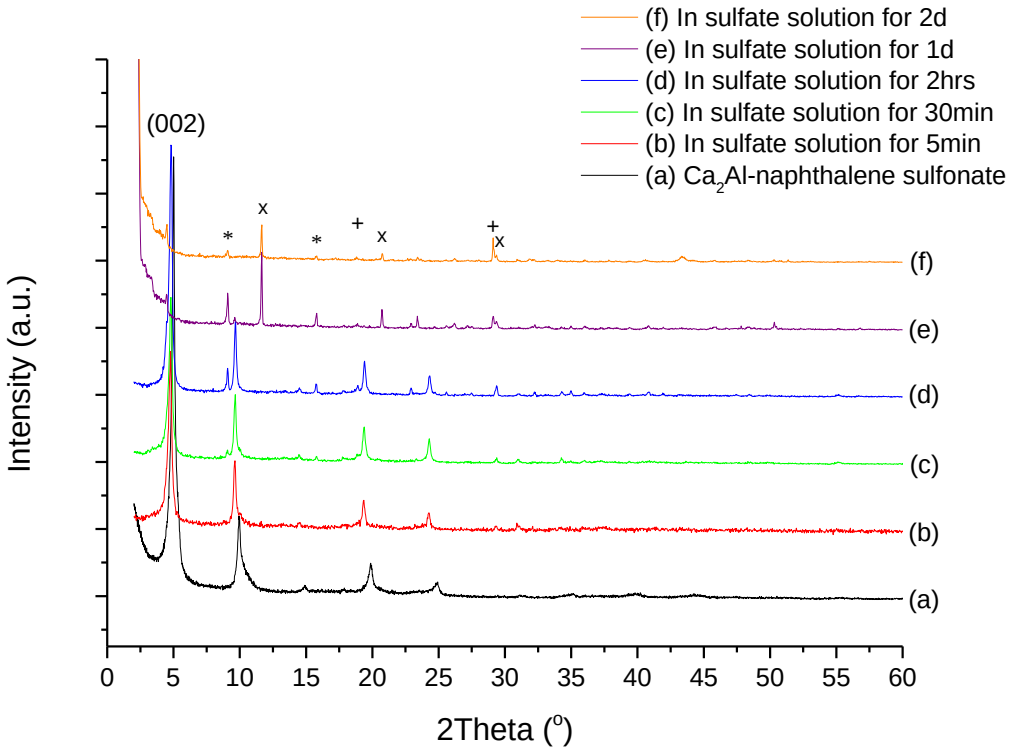

Figure 3.27. XRD data for naphthalene sulfonate intercalated Ca_2Al-LDH after suspending in a sulfate solution. * corresponds to ettringite [$Ca_6Al_2(SO_4)_3(OH)_{12}•26H_2O$], x corresponds to gypsum ($CaSO_4•2H_2O$), + corresponds to portlandite [$Ca(OH)_2$].

Suspension of Ca_2Al-naphthalene sulfonate in the solution containing carbonate anions leads to the formation of calcite after 5 minutes (Figure 3.28). The XRD data shows no reflections due to the presence of naphthalene sulfonate LDH after 30 minutes, only calcite ($CaCO_3$) is observed.

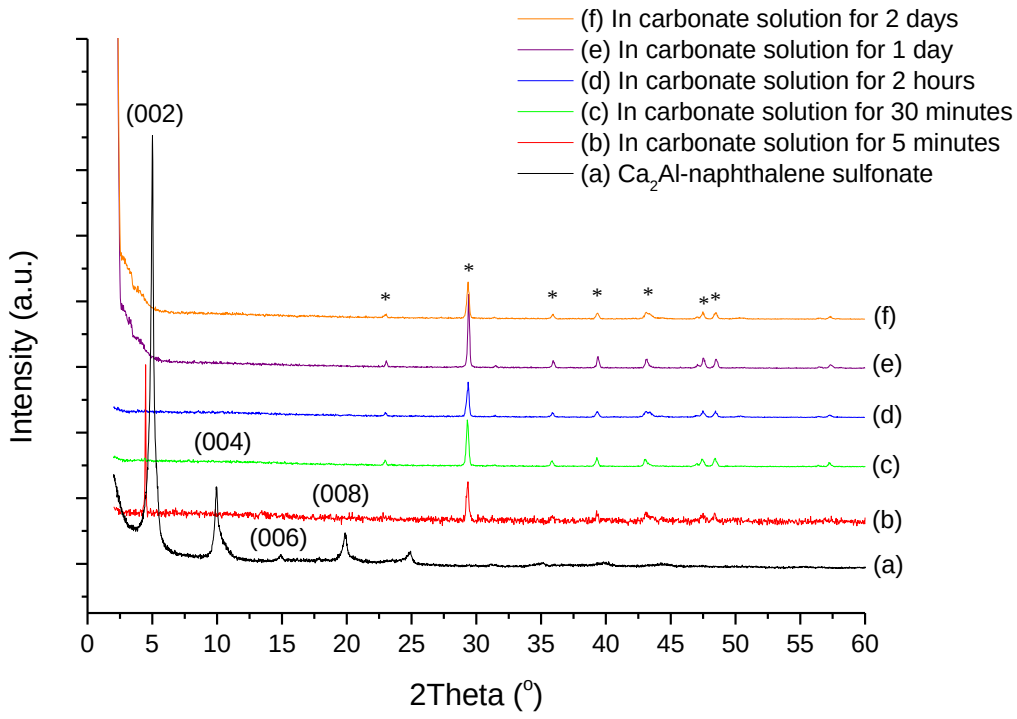

Figure 3.28. XRD pattern series of naphthalene sulfonate intercalated Ca_2Al-LDH after suspending in carbonate solution. * corresponds to calcite ($CaCO_3$).

In summary, naphthalene sulfonate intercalated Ca_2Al-LDH rapidly reacts with CO_3^{2-} to release naphthalene sulfonate and form calcite, $CaCO_3$. Suspension of Ca_2Al-naphthalene sulfonate in a sulfate solution, results in the formation of ettringite and gypsum after 30 minute mixing. The LDH structure is destroyed completely after 1 day. In contrast, the LDH structure is quite stable in water at pH 7, water at pH 13.5 and in a silicate solution.

3.7. Time-resolved *in situ* X-ray diffraction study of superplasticiser release from Ca_2Al-LDHs

In situ X-ray diffraction has been used to study the release of superplasticisers from Ca_2Al-LDHs following suspension in solutions containing sulfate or silicate anions.

Time-resolved *in situ* XRD data were collected at beamline I12 at the Diamond Light Source (DLS). Monochromatic X-rays (55.35 keV) were passed through a suspension of 0.1 g of Ca_2Al-naphthalene sulfonate in 5 ml of 0.08 M silicate solution. Further details about sample stage (carousel) and the experimental set up (Figure 3.29) are described in Section 7.2.1. The time-dependence of the XRD data are shown in Figure 3.30 and 3.31.

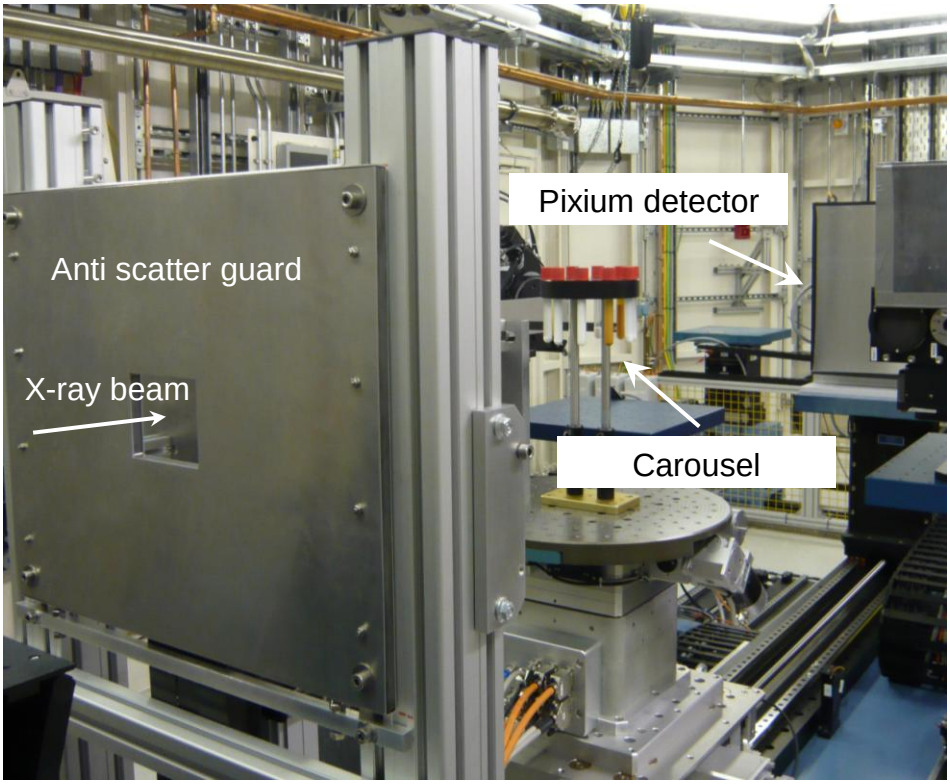

Figure 3.29. The setup on beamline I12 at Diamond Light Source.

The XRD data shows that the Ca_2Al-naphthalene sulfonate is stable in the silicate solution, there is no evidence of any silicate intercalation or any decomposition of the LDH into other crystalline phases.

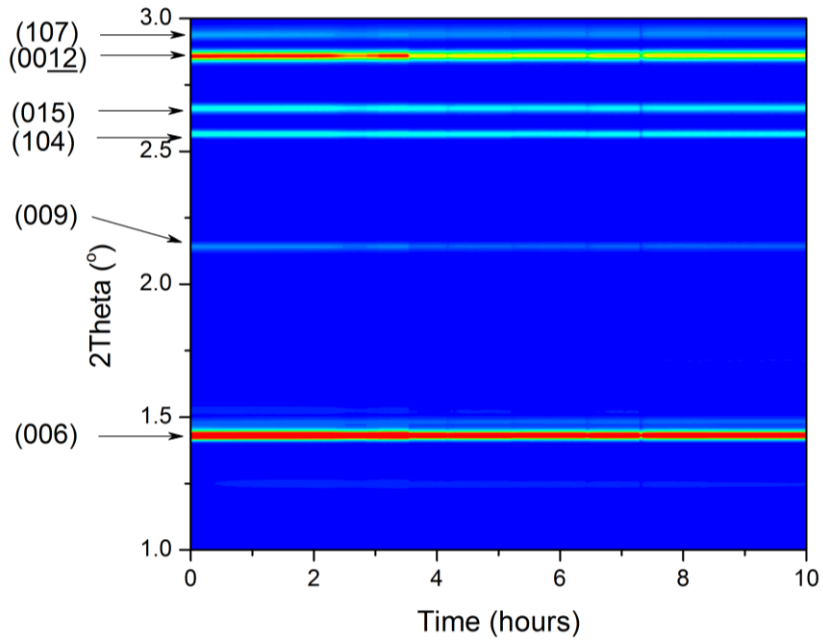

Figure 3.30. Contour plot showing the stability of Ca_2Al-naphthalene sulfonate in silicate solution.

Figure 3.32 shows the XRD data for a suspension of 0.1 g Ca_2Al-naphthalene sulfonate in 5 ml of 0.08 M sulfate solution. It is observed that the Bragg reflections for Ca_2Al-naphthalene sulfonate decrease rapidly with the simultaneous formation of ettringite and gypsum. However, the reflections for the reaction do not go to completion as LDH are still present after 10 hours.

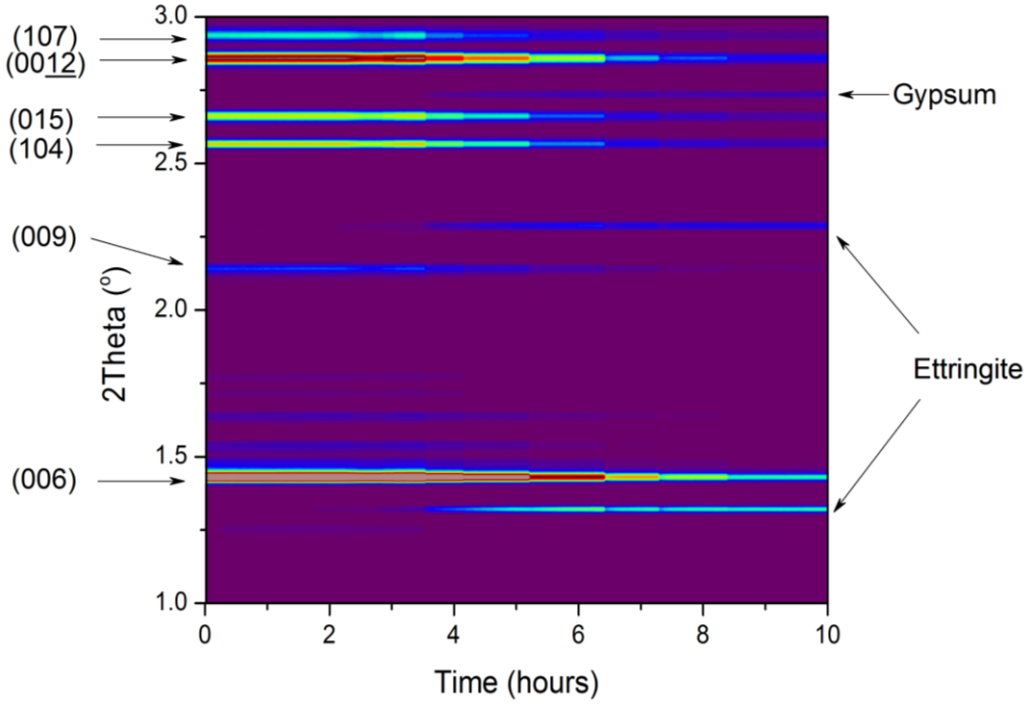

Figure 3.31. Contour plot showing the mechanism of Ca_2Al-naphthalene sulfonate in sulfate solution.

The *in situ* XRD data for Ca_2Al-lignosulfonate and Ca_2Al-polyacrylate suspended in silicate and sulfate solutions show no significant change after 10 hours.

3.8 Time-resolved *in situ* X-ray diffraction studies on cement hydration

Time-resolved in situ XRD data were recorded during the hydration of SKK^{TM} cement with a water/cement ratio of 0.4 (Figure 3.32). Initially the XRD data contain Bragg reflections that can be mainly indexed to tricalcium silicate (Ca_3SiO_5). However, the formation of ettringite and calcium hydroxide can be observed during the hydration process. The integrated intensities of the Bragg reflections for the major crystalline phases are shown in Figure 3.33.

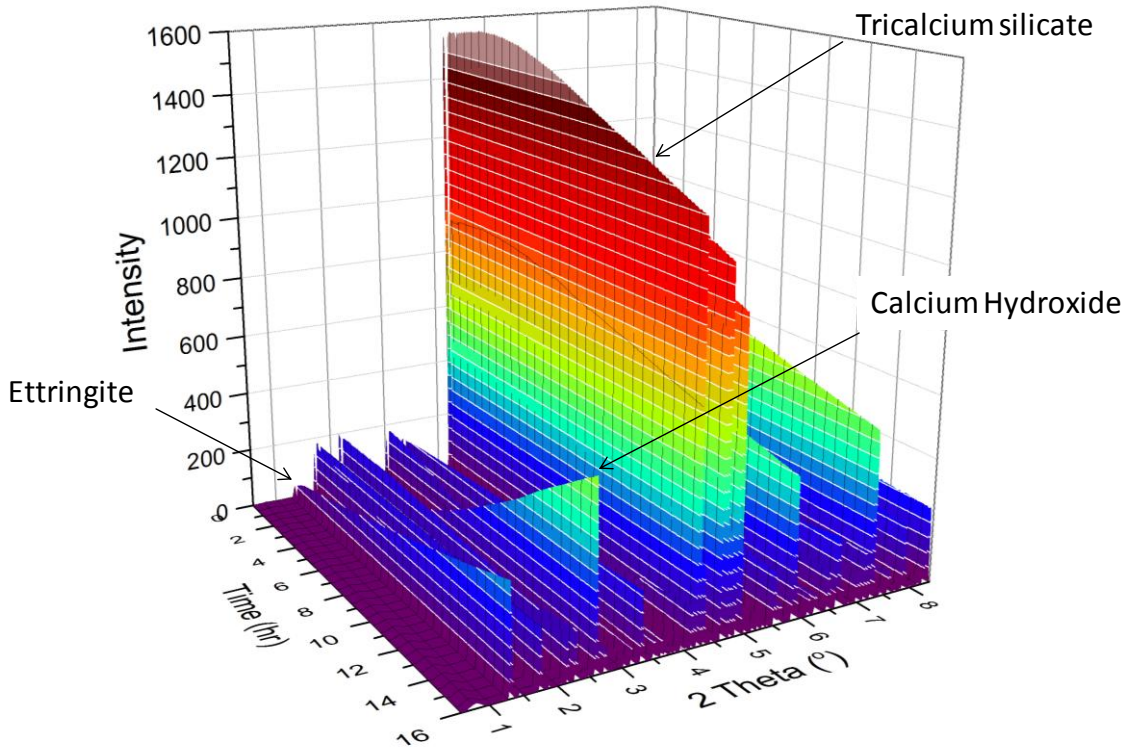

Figure 3.32. 3D plot of the time dependence of the XRD of cement during hydration at a water/cement ratio of 0.4.

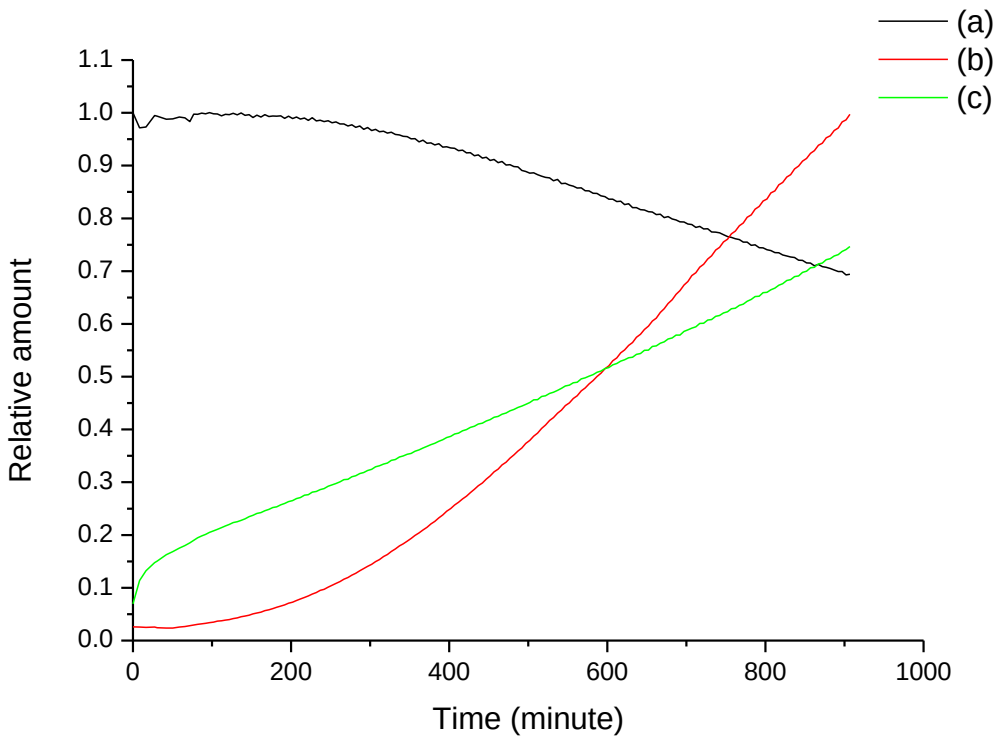

Figure 3.33. The integrated intensities of the Bragg reflections for the major crystalline phases in SKK cement during hydration; (a) tricalcium silicate, (b) $Ca(OH)_2$, and (c) Ettringite. Water to cement ratio of 0.4.

3.9 Time-resolved *in situ* X-ray diffraction studies of superplasticiser intercalated Ca_2Al-LDHs on cement hydration

Time-resolved *in situ* XRD data were recorded for the hydration of SKK cement containing a range of functional additives in order to determine their effects on cement hydration.

Superplasticiser intercalated Ca_2Al-LDHs including Ca_2Al-lignosulfonate, Ca_2Al-naphthalene sulfonate, and Ca_2Al-polyacrylate were studied in comparison to the hydration of plain cement. In addition, commercial superplasticisers named Type D (lignosulfonate type superplasticiser) and PC6 (polycarboxylate type superplasticiser) were used to compare the efficiency with Ca_2Al-lignosulfonate and Ca_2Al-polyacrylate on cement hydration.

Figure 3.34 shows the time-dependence of the XRD during SKK cement hydration containing 2 %wt of Ca_2Al-OH. Integrated intensites of the Bragg reflections of the key phases are plotted as a function of time in Figure 3.35.

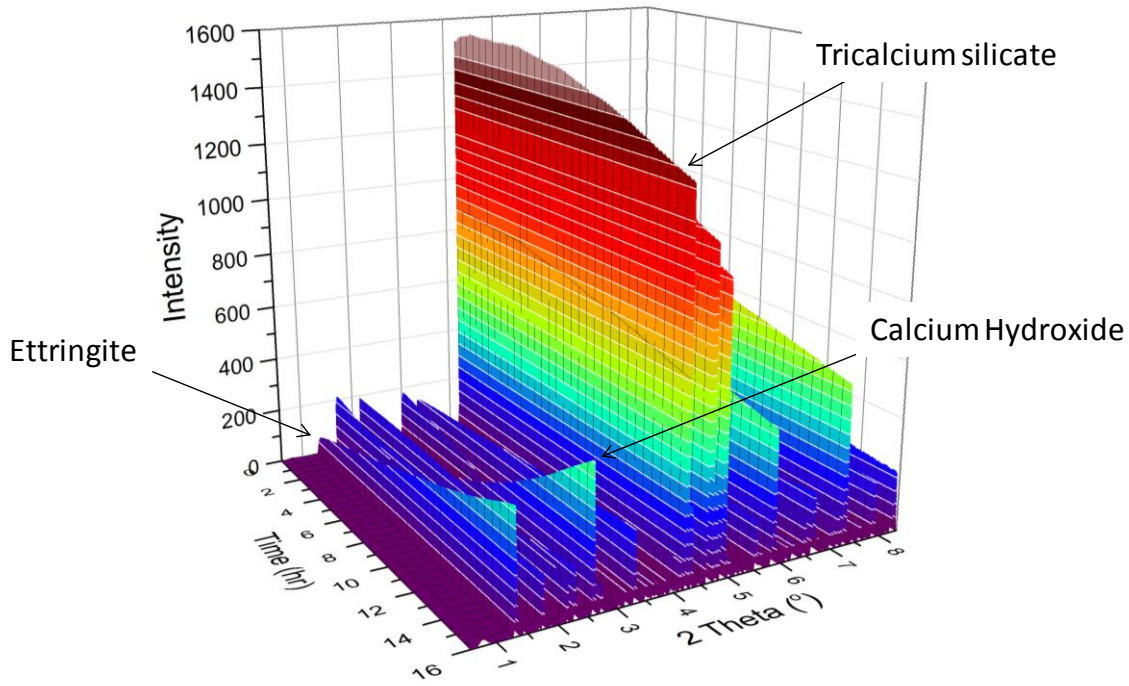

Figure 3.34. 3D plot of the time dependence of the XRD of cement during hydration with 2 %wt added Ca_2Al-OH at water to cement ratio of 0.4.

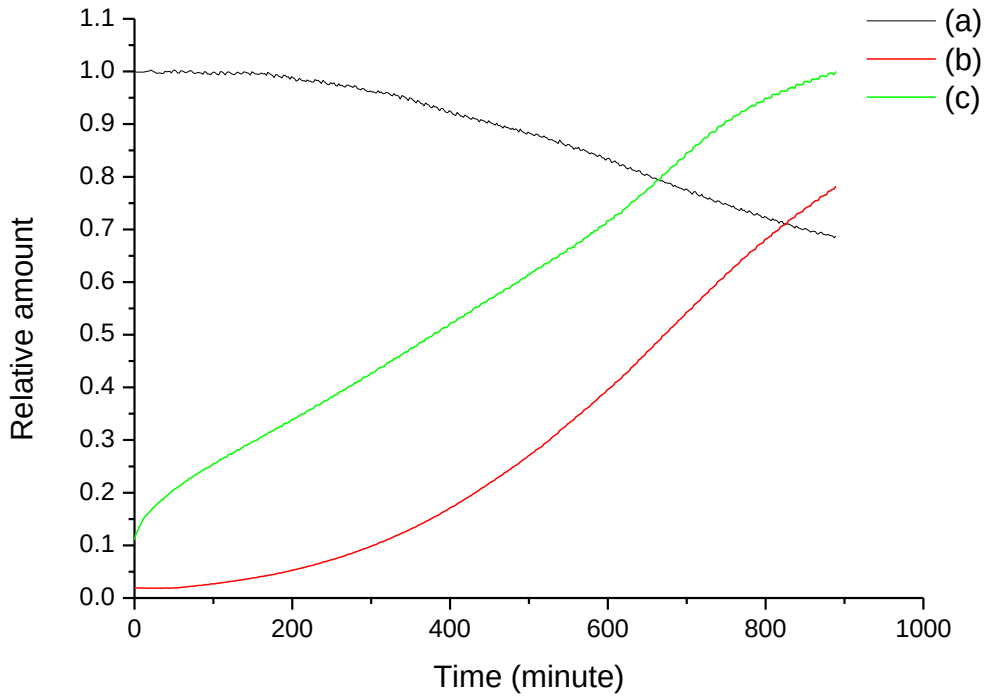

Figure 3.35. The integrated intensities of the Bragg reflections for the major crystalline phases of SKK cement; (a) tricalcium silicate, (b) $Ca(OH)_2$, and (c) Ettringite. (During cement hydration with 2 %wt added Ca_2Al-OH at water to cement ratio of 0.4).

In a generic cement system, tricalcium aluminate, which is the most reactive phase, releases calcium and aluminium cations. These ions can immediately react with sulfate from gypsum to form ettringite. Gypsum is added to avoid the formation of hydrogarnet [$Ca_3Al_2(SiO_4)_{3-x}(OH)_{4x}$, $0 \leq x \leq 3$] which causes rapid setting of concrete (also called 'flash set'). Therefore, the increase in the amount of ettringite could be used to predict the retardation of tricalcium aluminate hydration. Tricalcium silicate further releases calcium cations and silicate anions to form calcium silicate hydrate (C-S-H) and calcium hydroxide. The decrease in the amount of the cement phase can reflect the progress of tricalcium silicate hydration.

3.9.1 Tricalcium silicate and calcium hydroxide

The intensities of tricalcium silicate Bragg reflection at 6.0 Å and calcium hydroxide Bragg reflection at 4.9 Å have been used to calculate the relative amounts of each phase. Hydroxide-intercalated Ca_2Al-LDH has been used to investigate the effects of the LDH on the hydration of cement (Figure 3.36 and 3.37). It is found that the Ca_2Al-OH can slightly accelerate the hydration of tricalcium silicate. In addition, 1% of Ca_2Al-OH is a suitable amount of the LDH to add in order to yield a higher hydration rate of tricalcium silicate. The growth of calcium hydroxide in cement samples corresponds to the hydration of tricalcium silicate.

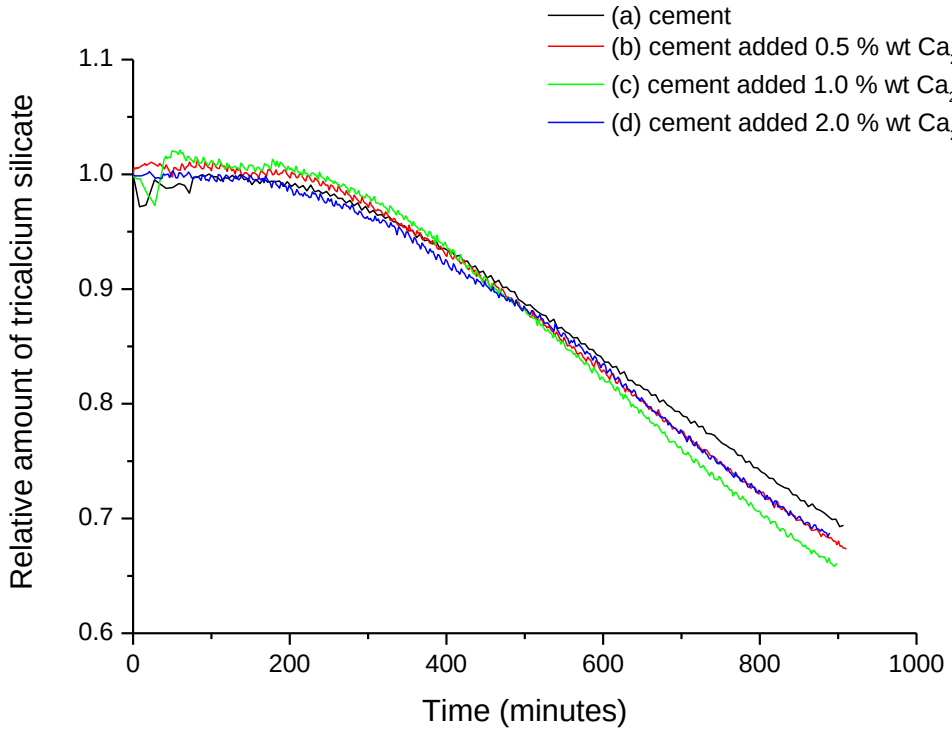

Figure 3.36. Relative amounts of tricalcium silicate in SKK cement during hydration.

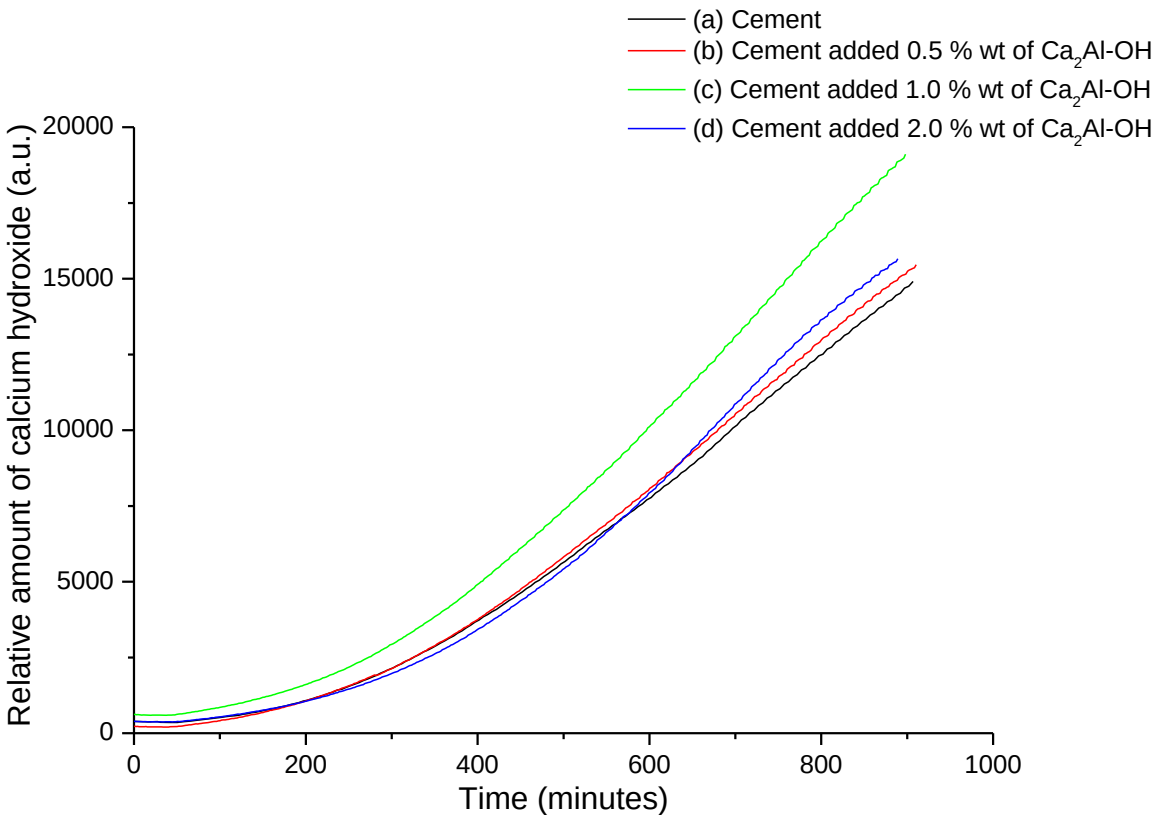

Figure 3.37. Relative amounts of calcium hydroxide in SKK cement during hydration.

During the progress of cement hydration, cement with added Ca_2Al-lignosulfonate results in less consumption of tricalcium silicate in comparison to that of plain cement. In addition, the increase amount of calcium hydroxide produced as a result of cement hydration corresponds to the decrease amount of tricalcium silicate. (Figure 3.38) The retarding/accelerating effect of additives on cement hydration are summaried as shown below.

Ca_2Al-lignosulfonate > Ca_2Al-naphthalene sulfonate ≈ Plain cement > Ca_2Al-polyacrylate

← Retard Accelerate →

The decrease in tricalcium silicate (cement hydration) by the additives is shown in Figure 3.38. Commercial superplasticisers, type D (lignosulfonate-based superplasticiser) and PC6 (polycarboxylate-based superplasticiser), have been used to study the mechanism of cement hydration in comparison with Ca_2Al-lignosulfonate and Ca_2Al-acrylate, respectively. For type D (Figure 3.38(e)), the additive can significantly affect the process of cement hydration as can be observed by the constant relative amount of tricalcium silicate present even after 16 hours. This additive can retard the reaction much more effectively than Ca_2Al-lignosulfonate. PC6 can retard the process of cement hydration while Ca_2Al-acrylate, in contrast, slightly accelerates.

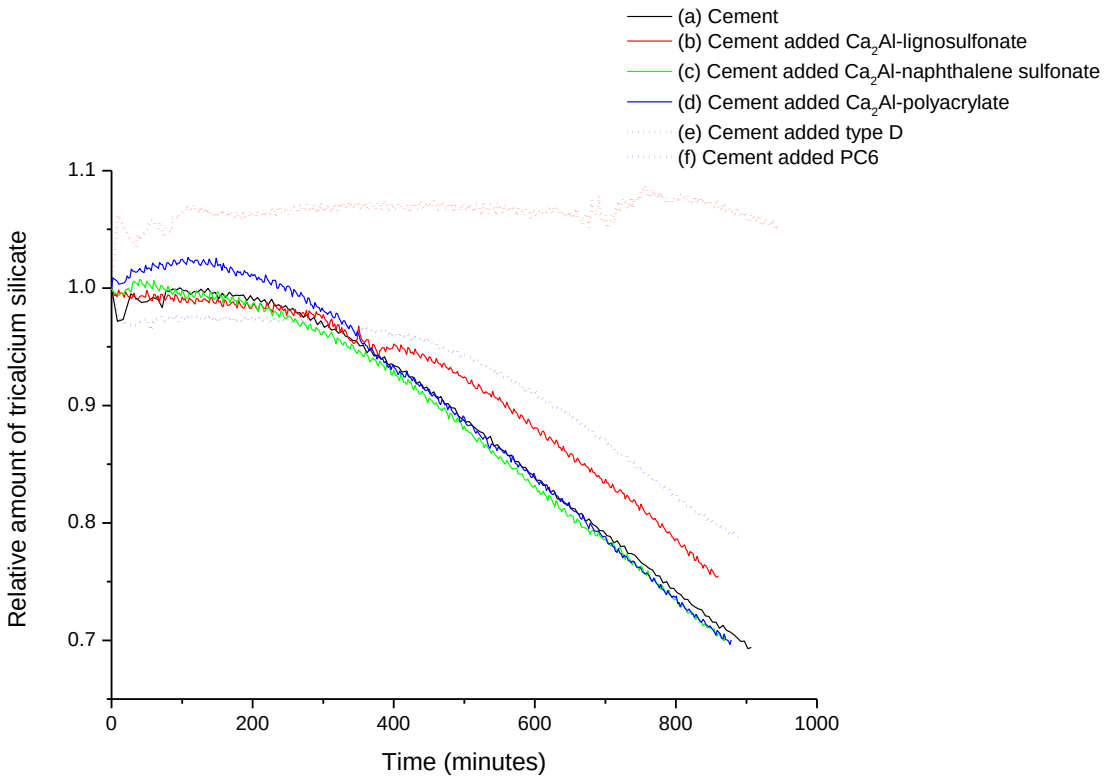

Figure 3.38. Relative amounts of tricalcium silicate in SKK cement during hydration.

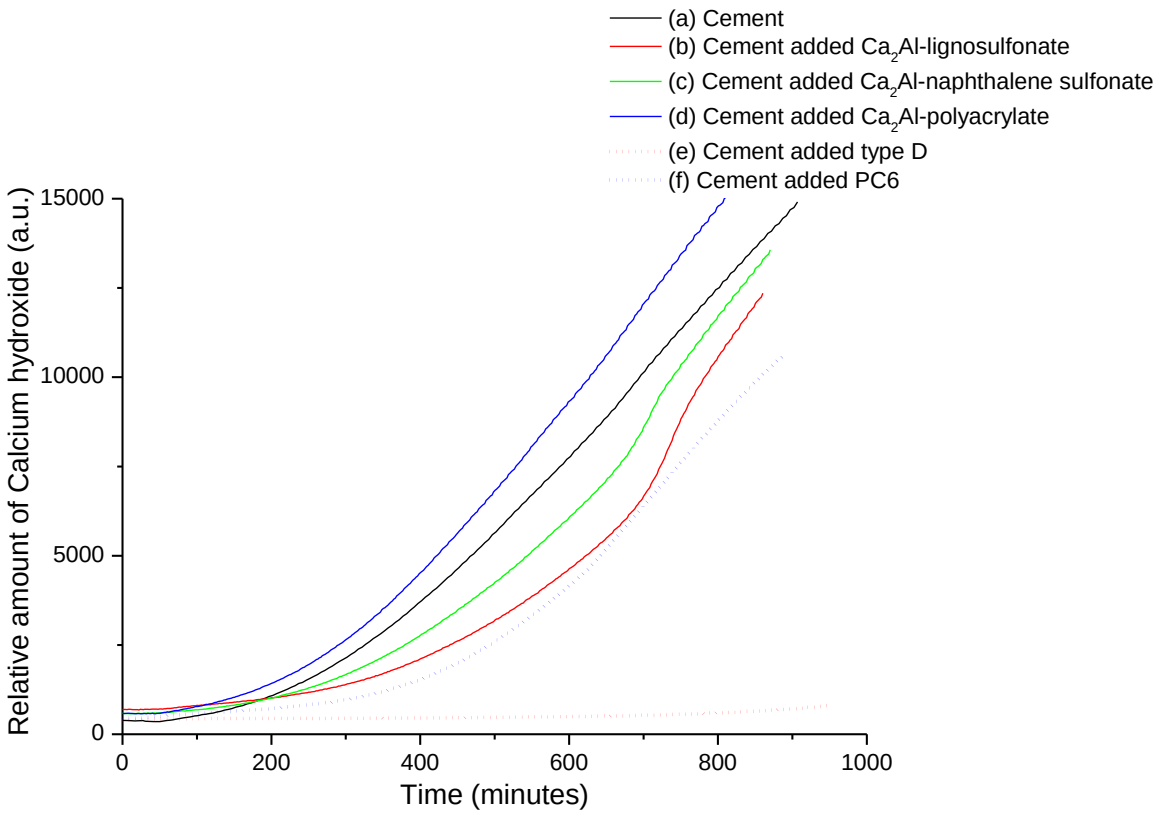

Figure 3.39. Relative amounts of calcium hydroxide in SKK cement during hydration.

3.9.2 Ettringite

The intensity of ettringite reflection at 9.7 Å were used to calculate the relative amounts of ettringite. For Ca_2Al-OH, the higher growth of ettringite formation can be found in a series of cement added Ca_2Al-OH. Cement containing additional 2 %wt Ca_2Al-OH demonstrated to have the highest rate of ettringite formation (Figure 3.40).

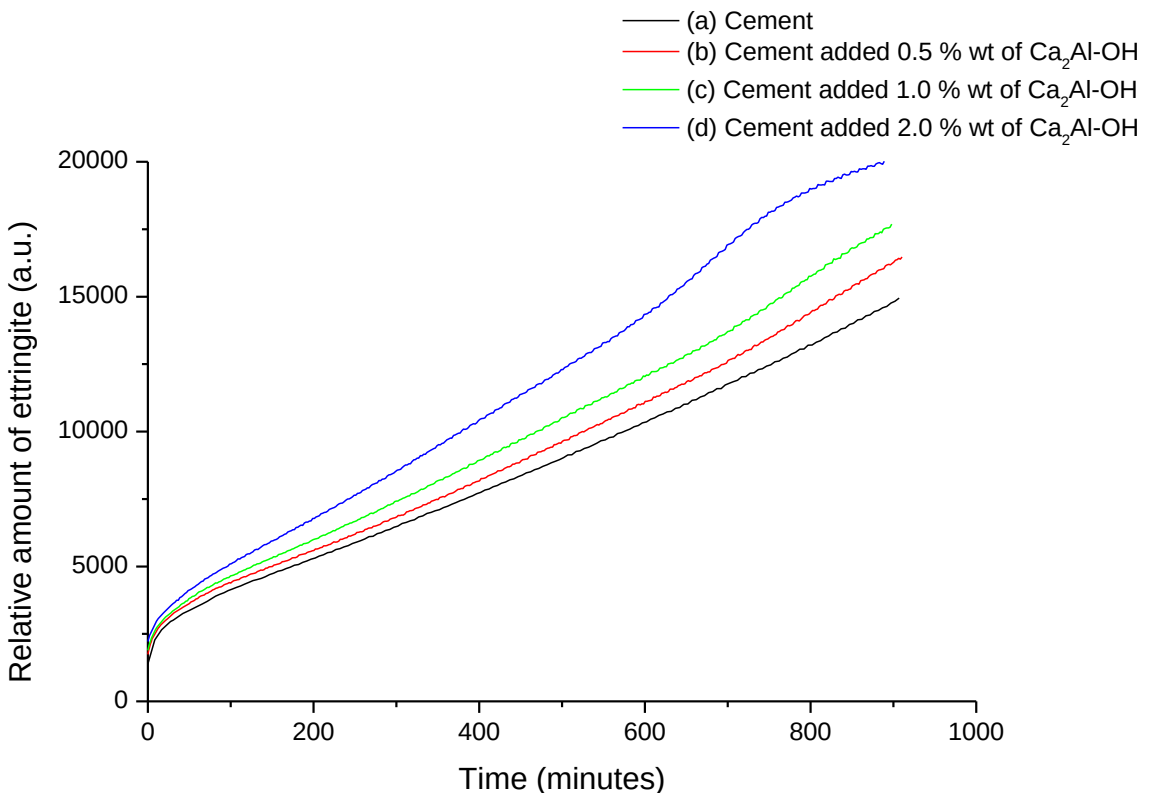

Figure 3.40. Relative amounts of ettringite in SKK cement during hydration.

The growth progression of ettringite in cement with added superplasticisers and superplasticiser-intercalated Ca_2Al-LDHs is slower than that in plain cement (except for PC6) (Figure 3.41).

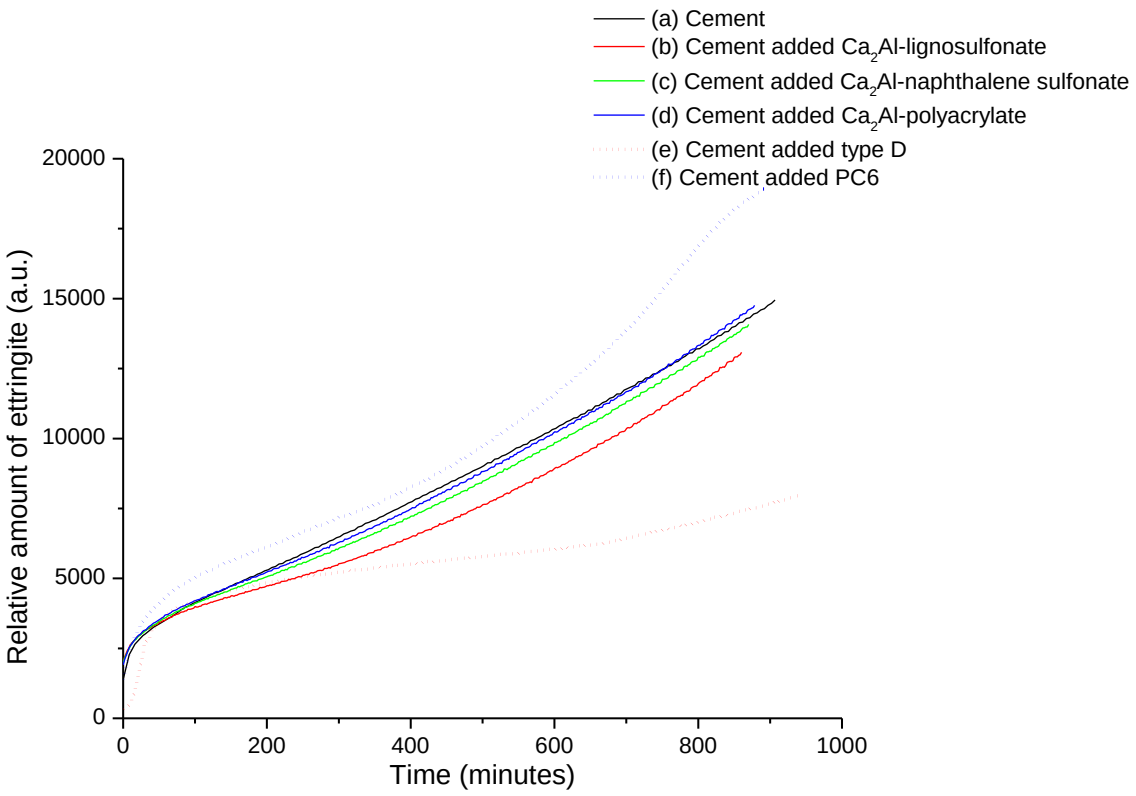

Figure 3.41. Relative amounts of ettringite in SKK cement during hydration.

The *in situ* X-ray data have been analysed to study the behaviour of additives on cement hydration. The retardation of cement hydration can be found. The effects of the additives on the phases present during cement hydration are shown below;

Ca_2Al-lignosulfonate > Ca_2Al-naphthalene sulfonate ≈ Plain cement > Ca_2Al-polyacrylate

Retard Accelerate

Addition of 1 %wt Ca_2Al-OH to SKK cement increases the amount of $Ca(OH)_2$ produced.

In term of the growth of ettringite formation, the superplasticiser-intercalated LDHs is lower than for plain cement, while higher than plain cement when Ca_2Al-OH is added.

The results can support that superplasticiser-intercalated LDHs have a significant retarding effect on tricalcium silicate hydration while the hydration of cement with added Ca_2Al-OH is negligible compared with the hydration of plain cement. The slower growth progression of ettringite in cement samples can be found in cement added superplasticiser-intercalated Ca_2Al-LDHs while Ca_2Al-OH can accelerate the ettringite formation.

3.10 Effects of superplasticiser-intercalated Ca_2Al-LDHs on the physical properties during cement hydration

The effects of the various additives on the evolution of the physical properties of cement during hydration were investigated using ultrasound shear wave loss equipment.[55-58] Ultrasound shear wave reflection is a method to measure the storage elastic modulus (*G'*) of a material. A bespoke cell for measuring the ultrasound shear wave reflection during cement hydration has been developed by Dr. Andrew Jupe.

Cement and water are rapidly mixed at a water/cement ratio of 0.4 in a high speed mixer. The cement paste was subsequently transferred into a cylindrical tube (Figure 3.42(b)) connected to a quartz sample stage (Figure 3.42(a)) which is a digitiser that generates ultrasound pulses. The amplitude and phase of the reflected wave change during cement hydration was recorded. Cement paste becomes more physically rigid over time as observed in Figure 3.42(c). Loss of amplitude and the phase shift of the shear wave were used as parameters to calculate the elastic modulus (*G'*) (Section 7.2.2).

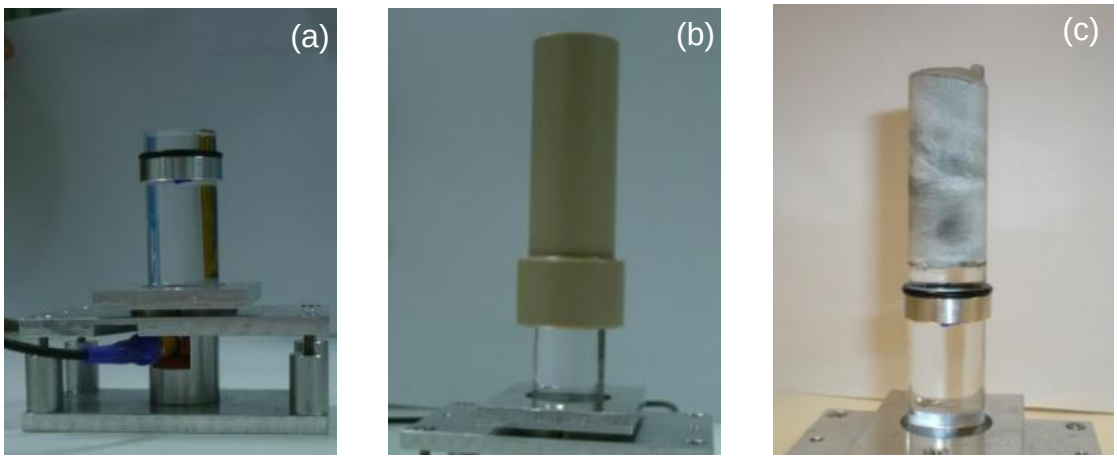

Figure 3.42. Pictures of (a) a quartz sample stage including digitiser, (b) a cylindrical tube on top of the sample stage, and (c) cement sample after ultrasound reflection measurement.

A commercially used SKK cement was studied in comparison with SKK cement with a range of additives. The amount of additive used each time was fixed at 0.4 %wt. The time-dependence of the elastic modulus (*G'*) of SKK cement during the hydration is shown in Figure 3.43. This behaviour was then compared to the time-dependence of *G'* following the addition of a range of additives including Ca_2Al-superplasticiser.

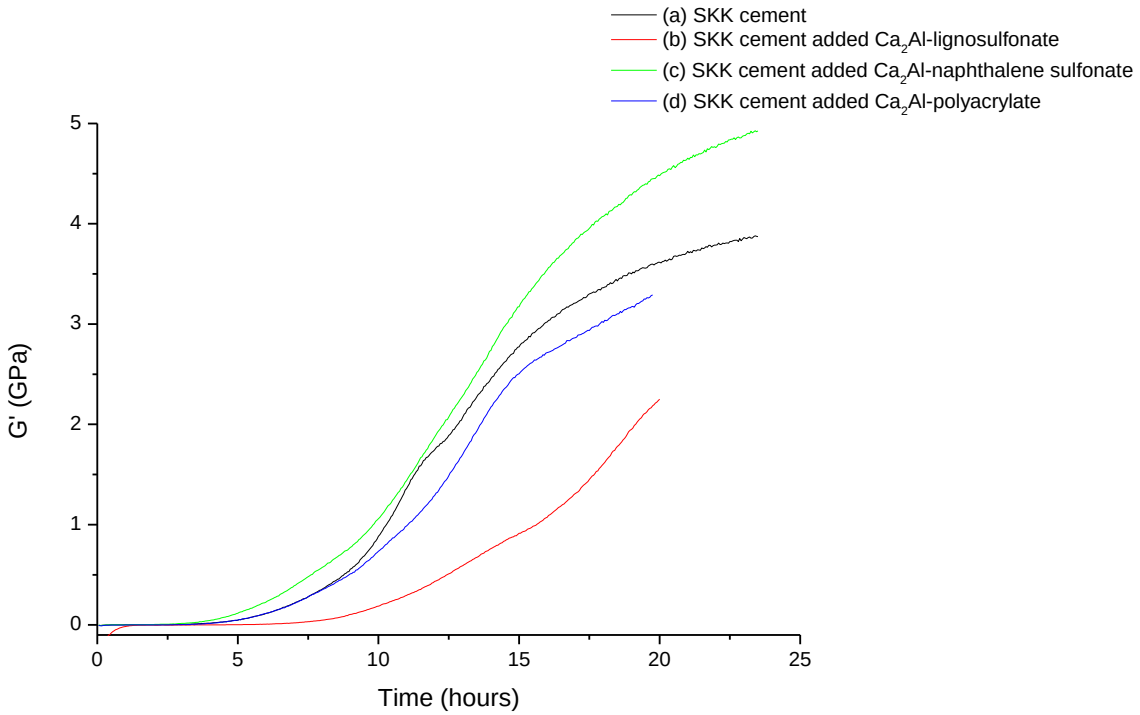

Figure 3.43. Time-dependence of the storage elastic modulus (*G'*) of cement during hydration: (a) SKK cement, and SKK cement with added; (b) Ca_2Al-lignosulfonate, (c) Ca_2Al-naphthalene sulfonate, and (d) Ca_2Al-polyacrylate.

From the inspection of the time-dependence of *G'*, the setting point of the cement mixture can be determined when *G'* starts to increase from zero. The setting point data are summarised in Table 3.10. The storage elastic modulus plots of all cement samples can be found in Appendix IV. The data indicates that cement with added Ca_2Al-lignosulfonate sets significantly slower than that of plain SKK cement. The addition of Ca_2Al-naphthalene sulfonate accelerates the hydration reaction. In contrast, the change in the elastic behaviour of cement after the addition of Ca_2Al-polyacrylate is negligible compared to the behaviour of plain cement.

Table 3.10. The setting point of cement samples determined from the storage elastic modulus data.

Cement samples*	Setting point (hours)
SKK cement	3.3
SKK cement with added Ca_2Al-OH	4.9
SKK cement with added Ca_2Al-lignosulfonate	5.1
SKK cement with added sodium lignosulfonate	3.8
SKK cement with added Type D	10.3
SKK cement with added Ca_2Al-naphthalene sulfonate	2.1
SKK cement with added sodium naphthalene sulfonate	3.6
SKK cement with added Type F	1.1
SKK cement with added Ca_2Al- polyacrylate	3.3
SKK cement with added sodium polyacrylate	4.5
SKK cement with added PC6	7.8

Type D = commercial lignosulfonate-based superplasticiser, Type F = commercial sulfonated naphthalene-formaldehyde condensates, PC6 = commercial polycarboxylate-based superplasticiser. * Concentration of additives of 0.4 %wt.

Compared to the commercial additives (Type D, F, and PC6), cements containing equivalent amounts of superplasticiser-intercalated Ca_2Al-LDHs can significantly accelerate cement hydration with the exception of Ca_2Al-lignosulfonate. There are two possible factors by which superplasticiser-intercalated Ca_2Al-LDHs can affect cement hydration: (I) the effect of the additive after release into cement system, and (II) the increase in hydration rate due to the seeding effect of Ca_2Al-LDH framework. In the cases of Ca_2Al-naphthalene sulfonate and Ca_2Al-polyacrylate, the additives have a lower retarding effect on the cement hydration reaction compared with Ca_2Al-lignosulfonate, this observation is supported by both the ultrasound and *in situ* X-ray diffraction data. The seeding effect can be a dominating factor. The LDH particles could act as a seed crystals that enhance the nucleation rate of the cement hydration products, similar behaviour to calcite nanosized particles, silica fume, or colloidal silica (well-known in the cement industry).

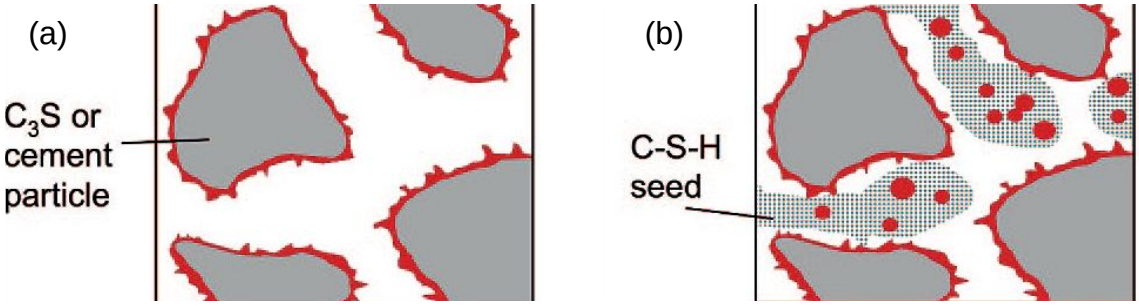

Figure 3.44. A schematic mechanism of the early stages of cement hydration (a) without seed crystals, and (b) with seed crystals.[59] (Hydration reaction takes place in the red region (C-S-H = Calcium silicate hydrate, a cement hydration phase)

Hydroxide-intercalated Ca_2Al-LDH has been used to study the effect of the LDHs on the hydration of cement. Unexpectedly, the rate of cement hydration was found to be lower in cement with added Ca_2Al-OH in comparison to the hydration of generic SKK cement. Ca_2Al-OH (also called hydroxy-AFm) is a kind of monosulfate (AFm) which is produced as a by-product of calcium aluminate cement. During the early stages of hydration, Ca_2Al-OH and hydrogarnet $[Ca_3Al_2(SiO_4)_{3-x}(OH)_{4x},\ 0 \leq x \leq 3]$ can form and in turn, induce a stiffening of the hydration paste, resulting in a 'flash set' in concrete that lacks a retarder such as gypsum. In generic cement systems, gypsum is used to generate ettringite and to avoid the formation of hydrogarnet and Ca_2Al-OH. Recently, Ca_2Al-OH has been observed to be present prior to the formation of ettringite.[16, 60] The quantity of Ca_2Al-OH decreases when ettringite is produced. It can be postulated that slower hydration reaction rates are possibly due to the presence of Ca_2Al-OH at the beginning of the process which helps the formation of ettringite to retard cement setting. The hypothesis can also be supported by the dramatic growth of ettringite observed using *in situ* X-ray diffraction. Given that there is a high tendency for Ca_2Al-OH and gypsum to react to form ettringite, the seeding effect is unable to dominate the setting of cement without the aid of ion encounter effect which is the case seen here with superplasticiser-intercalated LDHs.

Various commercial superplasticisers have been used to study the physical properties of cement during hydration compared to superplasticiser-intercalated Ca_2Al-LDHs. Cement with added type D hydrated slower compared to the hydration of plain cement. This corresponds to the common use of type D (lignosulfonate-based superplasticiser), which normally acts as a water-reducer and also a retardant in cement setting. Although Ca_2Al-lignosulfonate can retard cement setting more effectively than sodium

lignosulfonate, it is however, still less efficient than type D. As for type F (sulfonated naphthalene-formaldehyde condensates), it is predominately used to create a water-reducing effect which does not significantly affect the hydration rate. Cement with added Ca_2Al-naphthalene sulfonate started to set at a slightly slower rate in comparison to cement with added type F. For PC6 (polycarboxylate-based superplasticiser), the setting point of cement with the additive was evidently much slower than cement with added Ca_2Al-polyacrylate. However, the elastic modulus obtained after the setting point dramatically increases which is indicative that the cement paste hardened very rapidly. Ca_2Al-polyacrylate can accelerate cement setting slightly faster than sodium polyacrylate.

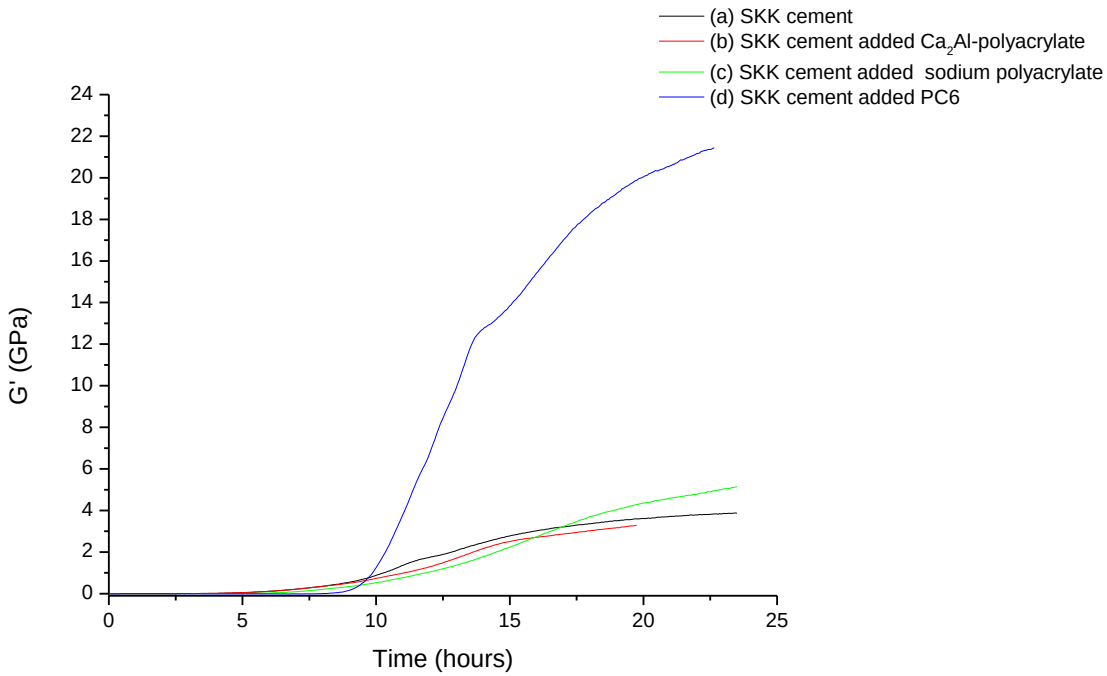

Figure 3.45. Time-dependence of the storage elastic modulus of cement during hydration: (a) SKK cement, SKK cement added; (b) Ca_2Al-polyacrylate, (c) sodium polyacrylate, and (d) PC6.

Although, ultrasound shear-wave reflection technique provides information relating to the reactivity in terms of the extent of the hydration reactions, viscosity studies would directly validate the physical effect of the added superplastisers in cement pastes. As a follow up, rheometer and zeta-potential would be suitable techniques to employ as a means to further investigate these properties.

3.11 Conclusions

Ca_2Al-LDHs intercalated with naphthalene sulfonate, lignosulfonate, and polyacrylate have been successfully synthesised. The materials are crystalline phases with the exception of Ca_2Al-lignosulfonate which seems to be highly disordered. The release of the intercalated anions have been studied in solutions containing anions that are expected to be present in typical cement mixtures. The anion release behaviour for these LDHs are different depending on the chemical composition of the solution. The order of the anion release efficiency is shown below:

For Ca_2Al-naphthalene sulfonate;

$$CO_3^{2-} > SO_4^{2-} > Si_3O_7^{2-} \approx \text{water pH } 13.5 \approx \text{water pH } 7$$

For Ca_2Al-lignosulfonate;

$$CO_3^{2-} > Si_3O_7^{2-} \geq \text{water pH } 13.5 > SO_4^{2-} > \text{water pH } 7$$

The anion release data have been fitted to several kinetic models; both the parabolic diffusion model and the modified Freundlich model were determined to be the best fit. The kinetic analysis indicates that the anion release behaviour from these materials is dominated by the anion diffusion between LDH layers. The diffusion coefficient for naphthalene sulfonate is higher than that for lignosulfonate. The kinetic data is consistent with naphthalene sulfonate and lignosulfonate release from LDHs occurring by heterogeneous surface desorption, followed by diffusion of superplasticisers from LDH layers (also called intraparticle diffusion control). Ca_2Al-naphthalene sulfonate ions can react with sulfate to form ettringite. $[Ca_6Al_2(SO_4)_3(OH)_{12}\bullet 26H_2O]$. It is postulated that Ca_2Al-OH and ettringite are formed when Ca_2Al-naphthalene sulfonate is added into a cement system.

The effect of superplasticiser-intercalated Ca_2Al-LDHs on cement hydration have been studied using ultrasound shear-wave reflection measurement. The time-dependence of *G'* and the setting time have been studied. Ca_2Al-naphthalene sulfonate can accelerate the hydration reaction while Ca_2Al-lignosulfonate generates a retarding effect. The hydration behaviour of cement with added Ca_2Al-polyacrylate is similar to plain SKK cement. In comparison to commercial additives, superplasticiser-intercalated Ca_2Al-LDHs induce

faster cement hydration. Ca_2Al-OH has been synthesised and used to investigate the influence of this LDH on the hydration reaction. It was discovered that this material can retard cement setting as it facilitates the formation of ettringite. The seeding effect is unable to dominate the setting of cement because of the high reactivity of Ca_2Al-OH to form ettringite without the aid of the ion encounter effect as seen in superplasticiser-intercalated LDHs.

3.12 References

1. P. Hewlett, *Lea's chemistry of Cement and Concrete*, Butterworth-Heinemann, 2003.
2. L. Perez-Lombard, J. Ortiz and C. Pout, *Energy and Buildings*, 2008, **40**, 394-398.
3. M. Schneider, M. Romer, M. Tschudin and H. Bolio, *Cement and Concrete Research*, 2011, **41**, 642-650.
4. H. M. Jennings and J. W. Bullard, *Cement and Concrete Research*, 2011, **41**, 727-735.
5. E. M. Gartner and D. E. Macphee, *Cement and Concrete Research*, 2011, **41**, 736-749.
6. J. W. Phair, *Green Chemistry*, 2006, **8**, 763-780.
7. K. L. Scrivener and A. Nonat, *Cement and Concrete Research*, 2011, **41**, 651-665.
8. E. Gartner, *Cement and Concrete Research*, 2004, **34**, 1489-1498.
9. D. V. Gemert, *Cement and Concrete Composites*, 2005, **27**, 926.
10. J. Damtoft, J. Lukasik, D. Herfort, D. Sorrentino and E. Gartner, *Cement and Concrete Research*, 2008, **38**, 115-127.
11. P. Metha, *World Cement Technology*, 1980, **1**, 166-177.
12. F. Glasser and L. Zhang, *Cement and Concrete Research*, 2001, **31**, 1881-1886.
13. D. Double, P. Hewlett, K. Sing and J. Raffle, *Philosophical Transactions of the Royal Society of London. Series A, Mathematical and Physical Sciences*, 1983, **310**, 53-66.
14. L. E. Copeland, D. Kantro and G. J. Verbeck, *Chemistry of Hydration of Portland Cement*, Portland Cement Association, Research and Development Laboratories, 1960.
15. G. Lager, T. Armbruster and J. Faber, *American Mineralogist*, 1987, **72**, 756-765.
16. N. Meller, K. Kyritsis and C. Hall, *Journal of Solid State Chemistry*, 2009, **182**, 2743-2747.
17. C. Jolicoeur and M.-A. Simard, *Cement and Concrete Composites*, 1998, **20**, 87-101.
18. A. N. Christensen, T. R. Jensen and J. C. Hanson, *Journal of Solid State Chemistry*, 2004, **177**, 1944-1951.
19. H. Berman and E. Newman, *Jour. Res. National Bureau of Standards*, 1963, **1**, 67.
20. A. N. Christensen, T. R. Jensen and J. C. Hanson, *Journal of Solid State Chemistry*, 2004, **177**, 1944-1951.
21. H. M. Jennings, *Cement and Concrete Research*, 2000, **30**, 101-116.
22. I. G. Richardson, *Cement and Concrete Research*, 2004, **34**, 1733-1777.
23. I. G. Richardson, *Cement and Concrete Research*, 1999, **29**, 1131-1147.
24. P. D. Tennis and H. M. Jennings, *Cement and Concrete Research*, 2000, **30**, 855-863.
25. K. Andersson, B. Allard, M. Bengtsson and B. Magnusson, *Cement and Concrete Research*, 1989, **19**, 327-332.
26. T. Yuasa, H. Kawakami and T. Hirata, EP Patent 1016638, 2002.
27. A. C494, ASTM International West Conshohocken, PA, 2004.
28. H. Uchikawa, S. Hanehara and D. Sawaki, *Cement and Concrete Research*, 1997, **27**, 37-50.
29. J. Plank and B. Sachsenhauser, *Cement and Concrete Research*, 2009, **39**, 1-5.
30. J. Plank and C. Hirsch, *Cement and Concrete Research*, 2007, **37**, 537-542.
31. J. Plank and B. Yu, *Applied Clay Science*, 2010, **47**, 378-383.

32. L. Ferrari, J. Kaufmann, F. Winnefeld and J. Plank, *Journal of Colloid and Interface Science*, 2010, **347**, 15-24.
33. B. Lothenbach, F. Winnefeld and R. Figi, *Proceedings of the 12th ICCC, Montreal, Canada*, 2007, 9-12.
34. E. G. Swenson and T. Thorvaldson, *Detection of Lignosulfonate Retarder in Cement Suspensions and Pastes*, Division of Building Research, National Research Council, 1960.
35. F. S. Chakar and A. J. Ragauskas, *Industrial Crops and Products*, 2004, **20**, 131-141.
36. S. P. Chundawat, G. T. Beckham, M. E. Himmel and B. E. Dale, *Annual Review of Chemical and Biomolecular Engineering*, 2011, **2**, 121-145.
37. B.-G. Kim, S. Jiang, C. Jolicoeur and P.-C. Aïtcin, *Cement and Concrete Research*, 2000, **30**, 887-893.
38. L. Raki, J. Beaudoin and L. Mitchell, *Cement and Concrete Research*, 2004, **34**, 1717-1724.
39. A. Zingg, F. Winnefeld, L. Holzer, J. Pakusch, S. Becker, R. Figi and L. Gauckler, *Cement and Concrete Composites*, 2009, **31**, 153-162.
40. F. Winnefeld, A. Zingg, L. Holzer, R. Figi, J. Pakusch and S. Becker, in *Proc 12th International Congress on the Chemistry of Cement, Montréal, CD-ROM*, 2007.
41. S. Rai and N. Gajbhiye, *Indian Journal of Chemical Technology*, 2008, **15**, 349.
42. J. Plank, C. Schroefl, M. Gruber, M. Lesti and R. Sieber, *Journal of Advanced Concrete Technology*, 2009, **7**, 5-12.
43. G. Renaudin, J. P. Rapin, B. Humbert and M. François, *Cement and Concrete Research*, 2000, **30**, 307-314.
44. G. Renaudin and M. Francois, *Acta Crystallographica Section C: Crystal Structure Communications*, 1999, **55**, 835-838.
45. Q. Tao, J. Yuan, R. L. Frost, H. He, P. Yuan and J. Zhu, *Applied clay science*, 2009, **45**, 262-269.
46. P. Zhang, G. Qian, H. Cheng, J. Yang, H. Shi and R. L. Frost, *Spectrochimica Acta Part A: Molecular and Biomolecular Spectroscopy*, 2011, **79**, 548-553.
47. M. Y. A. Mollah, W. Yu, R. Schennach and D. L. Cocke, *Cement and Concrete Research*, 2000, **30**, 267-273.
48. A. Radosavljević, D. Božanić, N. Bibić, M. Mitrić, Z. Kačarević‐Popović and J. Nedeljković, *Journal of Applied Polymer Science*, 2012, **125**, 1244-1251.
49. D. Lee, R. Condrate Sr and J. Reed, *Journal of Materials Science*, 1996, **31**, 471-478.
50. R. Sorensen and N. Novak, *Biochemical Education*, 1996, **24**, 3.
51. M. Kithome, J. Paul, L. Lavkulich and A. Bomke, *Soil Science Society of America Journal*, 1998, **62**, 622-629.
52. C. R. Young, C. Dietzsch, M. Cerea, T. Farrell, K. A. Fegely, A. Rajabi-Siahboomi and J. W. McGinity, *International Journal of Pharmaceutics*, 2005, **301**, 9.
53. X. Kong, L. Jin, M. Wei and X. Duan, *Applied Clay Science*, 2010, **49**, 324-329.
54. T. Kodama, Y. Harada, M. Ueda, K.-i. Shimizu, K. Shuto and S. Komarneni, *Langmuir*, 2001, **17**, 6.
55. A. C. Jupe, A. P. Wilkinson and G. P. Funkhouser, *Cement and Concrete Research*, 2012.
56. Y. Akkaya, T. Voigt, K. V. Subramaniam and S. P. Shah, *Materials and Structures*, 2003, **36**, 507-514.

57. T. Voigt, Z. Sun and S. P. Shah, *Cement and Concrete Composites*, 2006, **28**, 307-316.
58. T. Voigt, G. Ye, Z. Sun, S. P. Shah and K. van Breugel, *Cement and Concrete Research*, 2005, **35**, 858-866.
59. J. J. Thomas, H. M. Jennings and J. J. Chen, *The Journal of Physical Chemistry C*, 2009, **113**, 4327-4334.
60. S. Pourchet, L. Regnaud, J.-P. Perez and A. Nonat, *Cement and Concrete Research*, 2009, **39**, 989-996.

Chapter 4: Synthesis of Ca_2Al-LDHs Nanoplates Using Non-ionic Surfactant Reverse Micelles

4.1 Introduction

Cement manufacturers are currently seeking novel ways to control the hydration reactions in cement. Chemical admixtures are often used to alter the course of cement hydration reactions and the properties of fresh or hardened concrete. The goal of some chemical admixtures is to allow cement compositions to exhibit sufficient dispersibility when the amount of water is reduced. In addition, many features need to retain fluidity and processability as well as exhibiting improved durability and strength as a result of water reduction.[1-5] The admixtures must ensure that the compositions of concrete or mortar mixtures maintain the correct end-product characteristics.[6, 7] To improve the efficiency of the admixtures, several procedures have been studied,[4, 8, 9] *i.e.*, the modification of the molecular structure of additives for the purpose of superplasticisers[10-13] and the control of particle sizes to enhance the seeding effect as a means to accelerate the cement hydration. In addition, there have been a number of research articles describing procedures for the intercalation of anions and polymer admixtures by using LDH-like materials.[14-17]

Sodium nitrate and calcium nitrate are conventionally used as accelerators to increase the hydration reactions of cement.[18-20] To improve the reactivity of these accelerators, creating additive-intercalated LDHs with nano-size particles may prove to be effective, due to the greater surface area. One of the potential materials likely to be compatible for use as a nano-cement additive is nitrate intercalated Ca_2Al-LDH ($Ca_2Al(OH)_6NO_3{\bullet}6H_2O$, Ca_2Al-NO_3).[21, 22] This type of material has been synthesised by several techniques, such as co-precipitation and hydrothermal. Therefore, it is of interest to study whether nano-sized hydrocalumite-like materials (Ca_2Al-LDHs) can be produced containing nitrate anions, and whether these materials are more efficient additives for cement applications.

The reverse micelle microemulsion technique has been shown to control the size, shape, composition and morphology of nano-size inorganic particles.[23-32] O'Hare *et al.* reported the first synthesis of a layered double hydroxide (LDH) using this approach.[33-36] The use of non-ionic surfactants to form reverse micelles is a recent synthetic technique

development, that reduces and/or avoids the intercalation of surfactants into the LDH layers.[32, 37] In this chapter, we report the synthesis of a range of nanosized $Ca_2Al\text{-}NO_3$ LDHs using reverse micelle emulsions formed by a range of non-ionic surfactants.

4.2 Reverse microemulsion theory and Hydrophile-Lipophile Balance (HLB) concept

Reverse microemulsion (technically called water-in-oil (W/O) microemulsion) is a technique using stabilizing agents (surfactants) as modifiers, to allocate and limit the aqueous regions that contain precursors within an oil phase, to tailor the shape, size and morphology of the products formed in the aqueous region.[24] This technique is not only capable of controlling size and morphology of particles and size distribution, but can also inhibit the agglomeration of the product particles.[37] The stabilising agents can rearrange themselves in such a way that hydrophilic heads face in towards the aqueous phase and hydrophobic tails point out towards the oil phase. Within the Critical Micelle Concentration (CMC) range, the emulsifiers can form reverse micelles in an organic solvent.[23, 25, 27, 38, 39] Crystal growth is controlled by the reverse micelles which trap the aqueous solution inside the micelles. The Hydrophile-Lipophile Balance is a useful index as it indicates the solubility of surfactants, especially non-ionic surfactants, as it enables emulsifying agents to be selected.[40]

In general, micelles can be formed in many different solution conditions depending on the Hydrophile-Lipophile Balance (HLB) of the emulsifiers as defined in Equation 4.1. The calculated value can be determined hydrophilic and hydrophobic for different regions of surfactant molecules, as described by Griffin and Davies.[41-45]

$$HLB = 20 \times M_p / M \qquad \textbf{Equation 4.1}$$

Where;

M_p = Molecular mass of the hydrophilic portion of the surfactant molecule

M = Molecular mass of the whole surfactant molecule

The Hydrophile-Lipophile Balance (HLB) classifies the hydrophilicity of the stabilising agents and provides a prediction for the surfactants' behaviour.[43, 44, 46, 47] The HLB values fall in the range between 1 and 20. Hydrophilic surfactants with high water solubility, are represented by higher HLB values, while on the other hand, surfactants with low water solubility have lower HLB values. In order to prepare water-in-oil emulsions, more lipophilic surfactants should be used, with HLB values in the ranges of 4 to 6.

Table 4.1. Effect of Hydrophile-Lipophile Balance on the state of a surfactant in aqueous media.[48]

State of the surfactant in water	HLB value range	Corresponding application
Non-dispersible	1.5 – 3	Anti-foaming agent
	1 – 4	Emulsifier for W/O emulsions
Poorly dispersible	2 – 6	
Turbid unstable dispersion	6 – 8	Wetting agent
Turbid stable dispersion	8 – 10	
Semi-transparent dispersion	10 – 13	Emulsifier for O/W emulsions
Transparent solution	13 – 15	Detergent
	15 – 18	Solubiliser

Reverse micelles can have a range of different morphologies depending on the packing factor (also called shape factor) of the surfactants in the micellar assembly (Figure 4.1).[49] The packing factor can be used to predict aggregate shapes of the surfactants depending on the structural properties of the surfactants, such as the hydrophilic area, and the chain length of the hydrophobic region. The emulsifier hydrocarbon volume (v) is dependent on the interfacial attraction and the chain repulsion of the hydrophobic tail in each surfactant molecule.

$$\text{Packing factor (P)} = v/a_0 \cdot l \qquad \textbf{Equation 4.2}$$

Where; v = the emulsifier hydrocarbon volume,

a_0 = the polar head area,

l = fully extended chain length of the emulsifier

Surfactants which are suitable for use in an oil-in-water microemulsion system should have a packing parameter value below 1. In case of a water-in-oil microemulsion, then surfactants with a packing parameter greater than 1 tend to have higher stability.

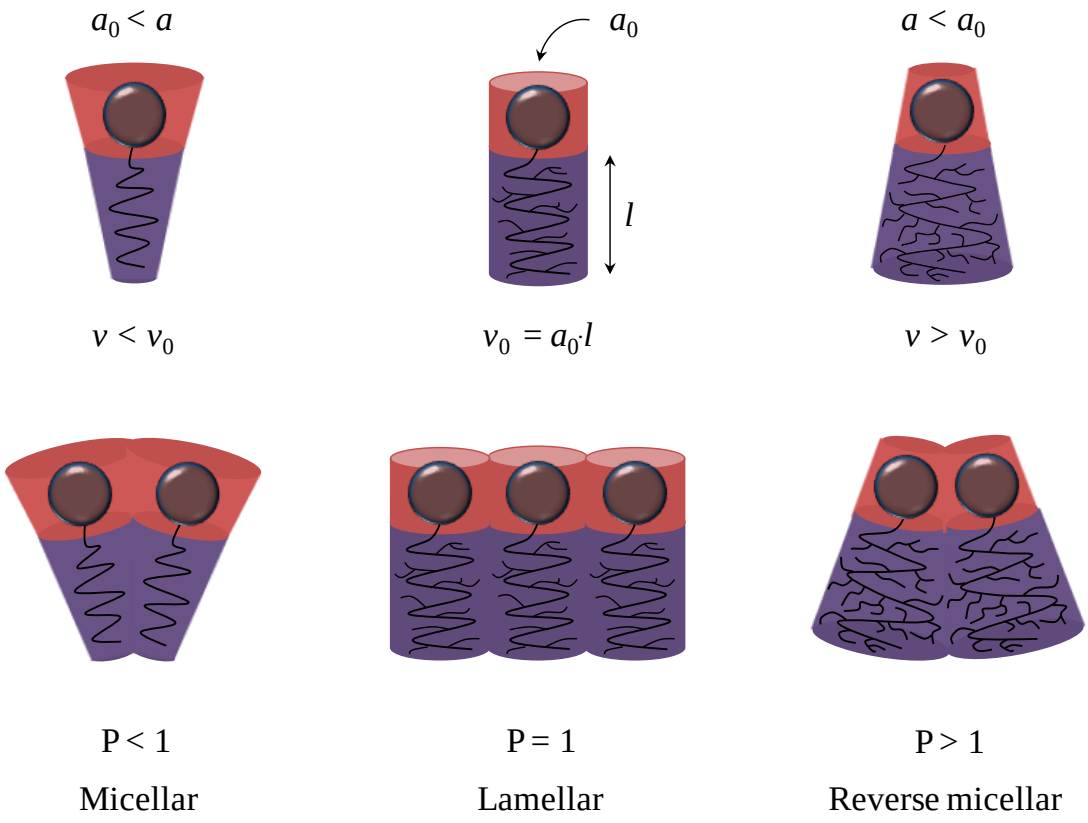

Figure 4.1. Schematic illustration of the molecular structures and aggregate shapes of surfactants at different packing factors (or called shape factors, P).

The relationship between the Hydrophile-Lipophile Balance (HLB) and the packing factor of surfactants have been studied.[49] Using both parameters, we can indirectly predict morphologies of materials based on the aggregate shapes of the surfactants as shown in Table 4.2. The data indicates that emulsifiers with HLB values within the ranges of 1 – 10 could result in inverse micelles formation in a water-in-oil microemulsion system. In this chapter, the polyethylene glycol dodecyl ether surfactant (Brij30) with a HLB = 9.7 and a critical micelle concentration (CMC) of 5 x 10^{-3} M, and the polyethylene oxide surfactant (Triton X100) with a HLB = 13.5 and a CMC of 2.4 x 10^{-5} M,[40, 50] were selected to investigate the relationship between HLB value and its effects on the particle size and morphology of LDHs prepared using a water-in-oil microemulsion system.

Table 4.2. Summary of the micelle structures of surfactant assemblies depending on packing factor and HLB value.[51]

Packing factor ($v/a_0 \cdot l$)	Schematic of micelle structures formed		HLB
	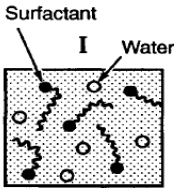	Isotropic	10 – 40
1/3	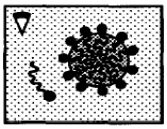	Micellar	
1/2	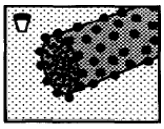	Hexagonal	
	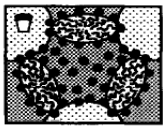	Cubic	
≈ 1	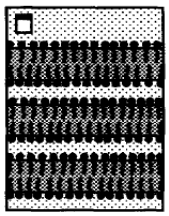	Lamellar	≈ 10
	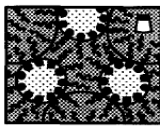	Inverse cubic	
> 1		Inverse hexagonal	
	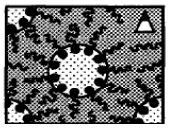	Inverse micellar	1 – 10

4.3 Synthesis of Ca_2Al-LDHs using non-ionic surfactant reverse micelles

The aqueous phase confined in an inverse micelle acts as a "nanoreactor" that facilitates the synthesis of the LDH. The nucleation and growth of the LDH platelets only occurs within the encapsulated water droplet (Figure 4.3). The size of water pools can be controlled by the amount of surfactant added, as defined by the water-to-surfactant molar ratio, w_B = [H_2O]/[Brij30]. Different inverse micelle systems were employed with water-to-surfactant molar ratios ranging between 1 and 20 in order to prepare the LDHs denoted as Ca_2Al-NO_3 BRM*w* (*w* = w_B) using polyethylene glycol dodecyl ether as the surfactant. Polyethylene glycol dodecyl ether (Brij 30) and butan-1-ol were added to isooctane. Spherical reverse micelles were formed when an aqueous solution of $Ca(NO_3)_2 \cdot 4H_2O$ and $Al(NO_3)_3 \cdot 9H_2O$ was introduced to this organic mixture followed by a solution of $NaNO_3$ and NaOH. Butan-1-ol was used as a co-surfactant to facilitate the formation of reverse micelles.

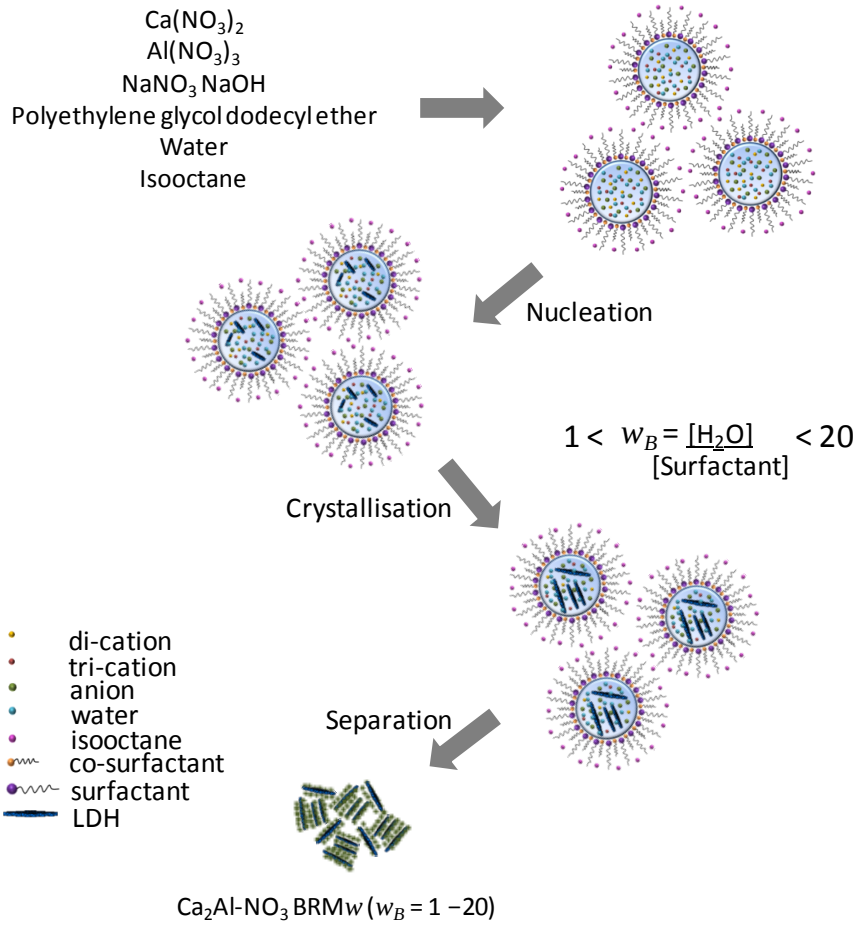

Figure 4.3. Schematic illustration of the nucleation and growth of Ca_2Al-NO_3 BRM*w* platelets (*w = 1 – 20*) in a polyethylene glycol dodecylether reverse micelle system.

4.3.1 X-ray powder diffraction data

The X-ray diffraction patterns of the LDHs Ca_2Al-NO_3 BRM*w*, formed in reactions with various water-to-surfactant ratios (*w*), are shown in Figure 4.4. The XRD data for the Ca_2Al-NO_3 BRM*w* series can be indexed using the unit cell dimensions of $[Ca_2Al(OH)_6NO_3{\cdot}6H_2O]$ (Figure 4.5).[52, 53] Refinement of the unit cell parameters is given in Figure 4.6. It was observed that the (002) Bragg reflection for the Ca_2Al-NO_3 BRM*w* phases become broader when the water-to-surfactant ratio (*w*) decreases (Figure 4.7). A slight shift in the position of the 00*l* Bragg reflection was also observed corresponding to a variation of the interlayer spacing between 8.43 and 8.55 Å (Table 4.3) which may be due to the different amounts of interlayer water, or the packing arrangement of the anions.

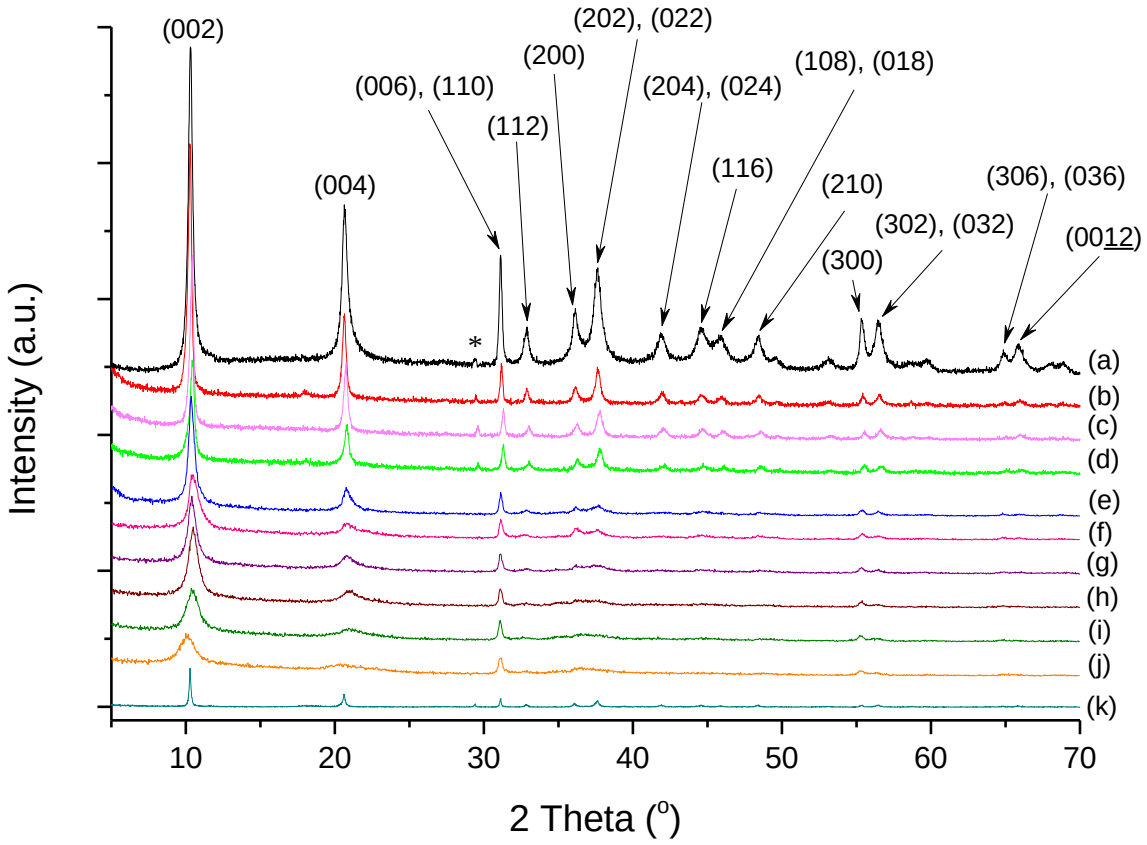

Figure 4.4. Summary of the powder XRD data for (a) Ca_2Al-NO_3 formed by co-precipitation, (b) – (j) Ca_2Al-NO_3 BRM*w* formed using reverse micelle microemulsions where *w* = (b) *19.6*, (c) *13.7*, (d) *10.6*, (e) *4.6*, (f) *3.4*, (g) *2.7*, (h) *2.3*, (i) *1.7*, (j) *1.4*, and (k) Ca_2Al-NO_3 formed without polyethylene glycol dodecyl ether in reaction (Ca_2Al-NO_3 WO). Reflections marked with * correspond to $CaCO_3$.

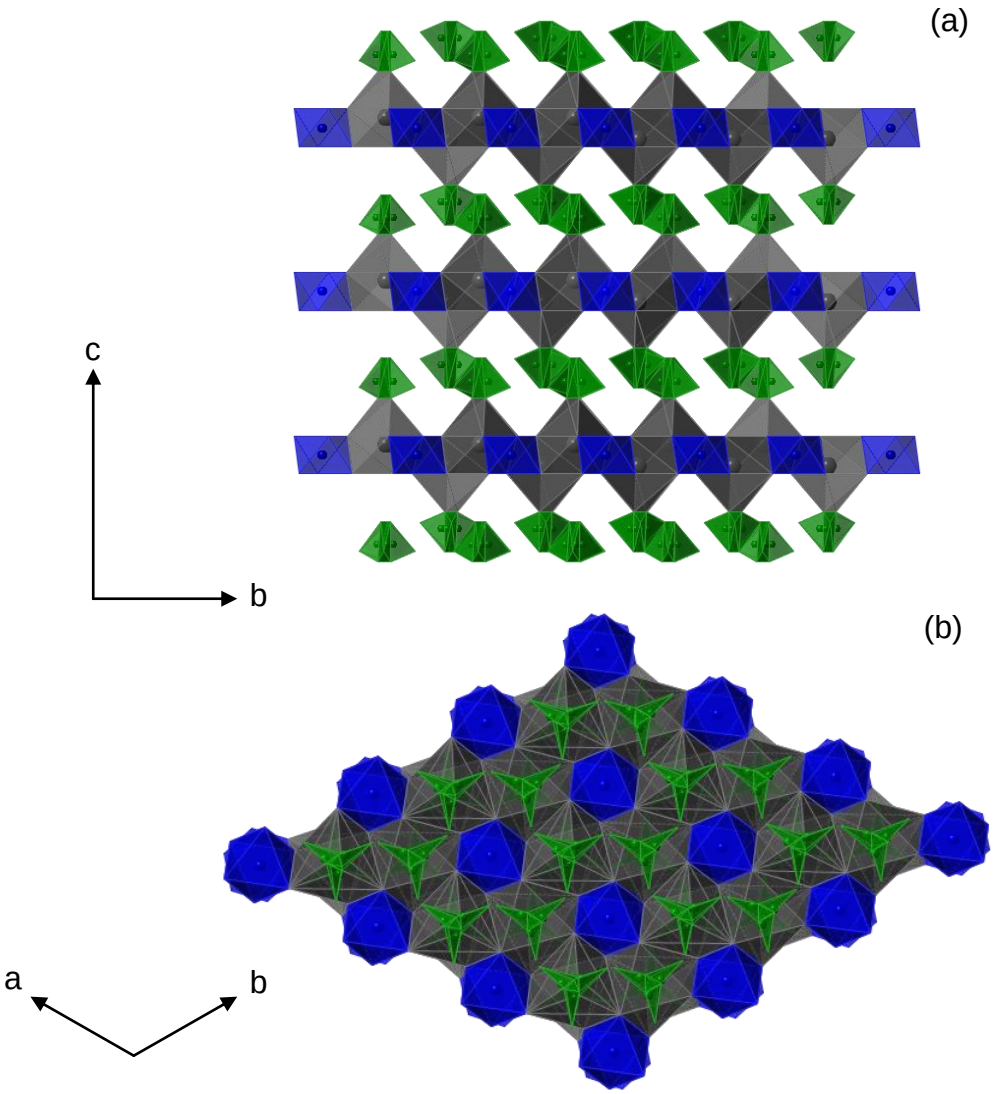

Figure 4.5. Views of $Ca_2Al\text{-}NO_3$ along (a) the *a*-axis and (b) the *c*-axis showing the relative positions of nitrates (in green) and their closest oxygen and metal ions.[52, 53] Al atoms in an octahedral hydroxyl coordination show in blue, while Ca atoms with the seven hydroxyl coordination shown in grey.

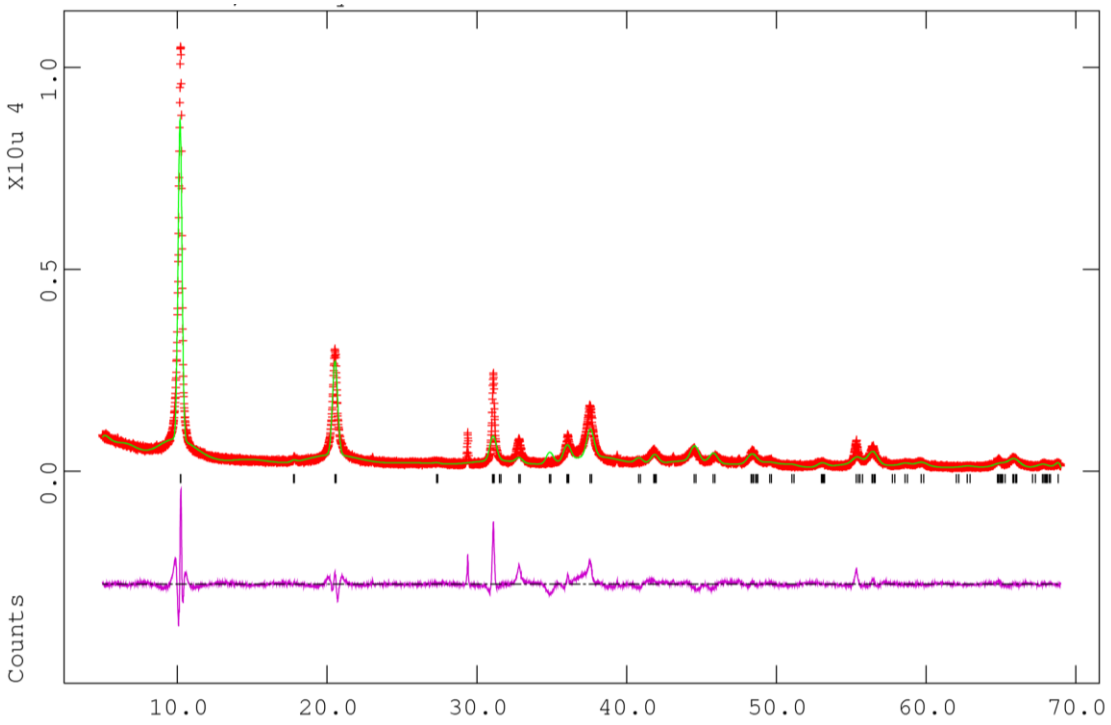

Figure 4.6. Profile analysis of the XRD data for $Ca_2Al\text{-}NO_3$ BRM*19.6* in the space group *P* – 3 *c*1: experimental X-ray diffraction (cross in red), calculated X-ray diffraction (line in green), Bragg reflections (ticks marked); the refined cell parameters are *a* = 5.7445(4) Å *c* = 17.1082(5) Å.

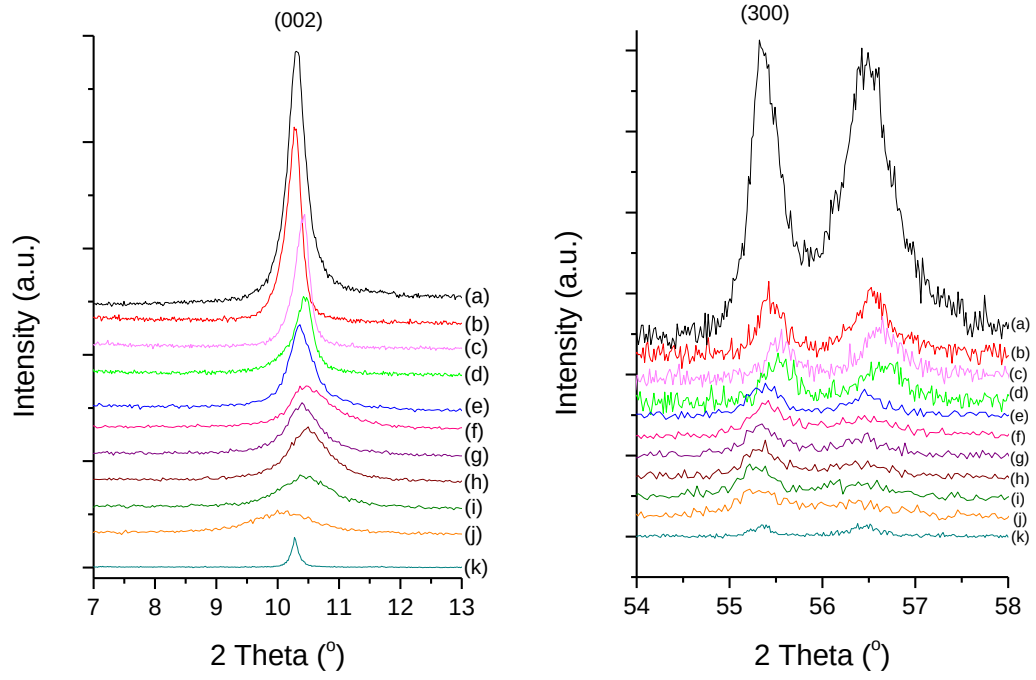

Figure 4.7. Summary of the powder XRD data showing the (002) and (300) Bragg reflections of (a) $Ca_2Al\text{-}NO_3$ formed by co-precipitation, (b) – (j) $Ca_2Al\text{-}NO_3$ BRM*w* formed using reverse micelle microemulsions where *w* = (b) *19.6*, (c) *13.7*, (d) *10.6*, (e) *4.6*, (f) *3.4*, (g) *2.7*, (h) *2.3*, (i) *1.7*, (j) *1.4*, and (k) $Ca_2Al\text{-}NO_3$ formed without polyethylene glycol dodecyl ether in reaction ($Ca_2Al\text{-}NO_3$ WO).

Similarly, a significant increase in the full width at half maximum (FWHM) value of the (002), and (004) Bragg reflections has been observed as the *w* value increases (Table 4.3, and Figure 4.8). Application of the Scherrer equation would suggest that the crystalline domain length along the *c*-axis decreases from 29.50 nm for $Ca_2Al\text{-}NO_3$ BRM*19.6* to 6.75 nm for $Ca_2Al\text{-}NO_3$ BRM*1.4*. The crystalline domain lengths derived from the line widths of the *00l* Bragg reflections are related to the thickness or stacking order in these platelet samples.

The full width at half maximum (FWHM) for the (300) Bragg reflection can also be determined (Table 4.3, and Figure 4.8). A small change in the width of this reflection can be observed which suggests that the in-plane crystallinity of the platelets is not greatly affected by the micelle pool volume. Overall, the increase in the amount of surfactant differently influences the crystallinity of the $Ca_2Al\text{-}NO_3$ along the *a*-, and *c*-axes.

$Ca_2Al\text{-}NO_3$ can also form in an organic solvent without the addition of polyethylene glycol dodecyl ether ($Ca_2Al\text{-}NO_3$ WO, Figure 4.4 (k)). Based on the FWHM of the (002) Bragg reflection, the crystalline domain size can be calculated as 32.2 nm, which is slightly higher than the crystalline domain size of $Ca_2Al\text{-}NO_3$ in solutions containing high water-to-surfactant ratios. The crystalline domain size of the LDHs prepared using a reverse micelle system with $10.6 < w < 19.6$ are close to value of the LDH formed by co-precipitation. The amount of surfactant present in these high water-to-surfactant ratio samples does not significantly affect the crystallinity of $Ca_2Al\text{-}NO_3$ in comparison to $Ca_2Al\text{-}NO_3$ formed without surfactants in the reverse micelle reaction, or formed by co-precipitation.

Table 4.3. A summary of the selected Bragg reflection line width from the X-ray diffraction data for $Ca_2Al\text{-}NO_3$ BRM*w* (*w = 1 – 20*).

$Ca_2Al\text{-}NO_3$	Bragg Reflection					
	(002)		(004)		(300)	
	FWHM/^{o}	CDS/nm	FWHM/^{o}	CDS/nm	FWHM/^{o}	CDS/nm
BRM*19.6*	0.27	29.5	0.27	29.8	0.27	33.2
BRM*13.7*	0.27	29.5	0.27	29.8	0.27	33.2
BRM*10.6*	0.40	19.7	0.33	23.9	0.33	26.5
BRM*4.6*	0.52	15.2	0.52	15.4	0.52	17.1
BRM*3.4*	0.65	12.2	0.52	15.4	0.52	17.1
BRM*2.7*	0.78	10.1	0.78	10.3	0.52	17.1
BRM*2.3*	0.78	10.1	0.65	12.3	0.78	11.4
BRM*1.7*	0.91	8.7	0.91	8.8	0.78	11.4
BRM*1.4*	1.17	6.8	1.82	4.4	0.78	11.4
WO	0.24	32.2	0.24	32.6	0.37	24.2
CP	0.27	29.5	0.54	14.9	0.33	26.5

FWHM = full width at half maximum, Scherrer equation ($CDS = K\lambda(\beta\cos\theta)^{-1}$); K = 0.89,[54]

CDS = Crystalline Domain Size, determined by Scherrer equation.

WO = $Ca_2Al\text{-}NO_3$ synthesised in an organic solvent without surfactant.

CP = $Ca_2Al\text{-}NO_3$ prepared by co-precipitation.

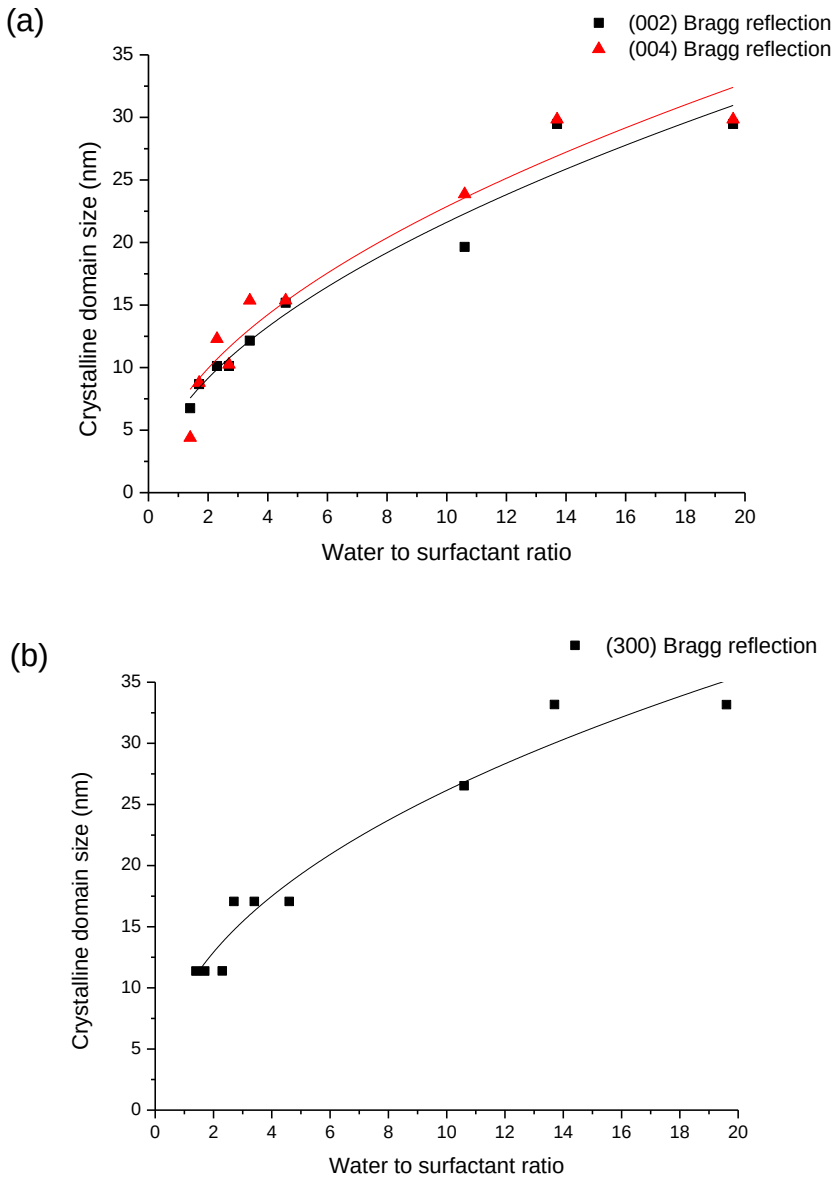

Figure 4.8. Plots of crystalline domain size of $Ca_2Al\text{-}NO_3$ against water-to-surfactant ratio using the full width at half maximum of: (a) (002), and (004); and (b) (300) Bragg reflections. The solid lines are a guide to the eye.

It was found that careful control of the post-synthesis processing was not required in order to obtain high quality samples due to the Hydrophile-Lipophile Balance properties (HLB) of polyethylene glycol dodecyl ether. Higher HLB values correspond to more strongly hydrophilic surfactants. The HLB value for the polyethylene glycol dodecyl ether is 9.7, which is sufficiently low enough for it to dissolve in organic solvents.[41, 49] Thus, the polyethylene glycol dodecyl ether used in these LDH syntheses could easily be removed from the reactions.

4.3.2 Infrared spectroscopy data

The FTIR spectra of the $Ca_2Al\text{-}NO_3$ BRM*w* series in Figure 4.9 show IR absorptions that represent the stretching vibrations of the hydroxyl groups in the inorganic layers and of the interlayer water between 3700-3000 cm^{-1}. The $Ca_2Al\text{-}NO_3$ samples also exhibited absorptions at 1415 and 1340 cm^{-1} which confirm the presence of intercalated NO_3^- anions, as seen by comparison to the corresponding IR spectrum of sodium nitrate.

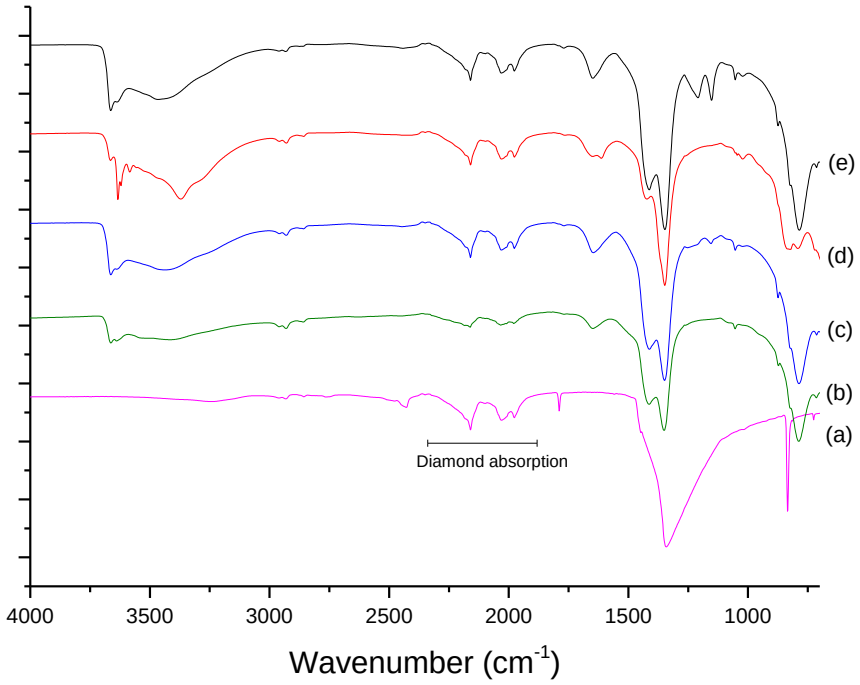

Figure 4.9. IR spectra of (a) $NaNO_3$, (b) $Ca_2Al\text{-}NO_3$ formed *via* co-precipitation, (c) $Ca_2Al\text{-}NO_3$ BRM*10.6*, (d) $Ca_2Al\text{-}NO_3$ BRM*13.7*, and (e) $Ca_2Al\text{-}NO_3$ BRM*19.6*.

4.3.3 Transmission Electron Microscopy (TEM) study

Transmission Electron Microscopy (TEM) has been used to determine the morphology, size and size distribution of the $Ca_2Al\text{-}NO_3$ LDH particles. The TEM images of the $Ca_2Al\text{-}NO_3$ BRM*w* in Figure 4.10 – 4.13 show that better control and modifications in the shape and morphologies of $Ca_2Al\text{-}NO_3$ LDHs can be achieved by adding surfactants. The TEM image of $Ca_2Al\text{-}NO_3$ without the presence of any surfactants (Figure 4.10(a)) reveals two different morphologies of the particles: (1) platelet-like and (2) flower-like structures (circled in red). The particles have a very broad size distribution, ranging from 50 nanometers to a few microns. The average diameter of particles decreases when the water-to-surfactant molar ratio decreases, which is in agreement with the crystalline domain sizes deduced from the diffraction data (Section 4.3.1). Hexagonal platelets were found for $Ca_2Al\text{-}NO_3$ BRM*19.6*, and $Ca_2Al\text{-}NO_3$ BRM*13.7* with mean particle diameters of 432.5 nm and 370.7 nm with standard deviations of 113.8 and 92.2 nm, respectively. The thickness can be determined from edge-on views of particle structures in both samples which were *ca.* 60 nm for $Ca_2Al\text{-}NO_3$ BRM*19.6* and *ca.* 42 nm for $Ca_2Al\text{-}NO_3$ BRM*13.7*. There were well-dispersed and more uniform platelets with a mean particle diameter of 137.3 nm with standard deviation of 23.8 nm in the case of the $Ca_2Al\text{-}NO_3$ BRM*10.6* (Figure 4.10(d)). No edge-on particle structure could be found for these samples. In the range $2.7 < w < 10.6$ depicted in Figure 4.11(a), 4.11(b), and 4.12(a), it was found that there is no difference in the particle size of materials made as more surfactant is added. However, additional surfactant affects the size distribution of the materials as can be seen by the narrowing of the distribution curves (Table 4.4). For $Ca_2Al\text{-}NO_3$ BRM*2.3* shown in Figure 4.12(c), a lot of particle aggregation can be observed. Particles roughly 50 nm in size were found in a different area at high magnification. For $Ca_2Al\text{-}NO_3$ BRM*1.7* (Figure 4.13(a)), platelet shaped particles similar in size to $Ca_2Al\text{-}NO_3$ BRM*2.3* were found, however, the morphology of most particles changed into layered feather-like structures in which the particle size of materials became larger (Figure 4.13(b)). A summary of the mean particle size of $Ca_2Al\text{-}NO_3$ synthesised using different reverse micelles conditions is shown in Figure 4.14.

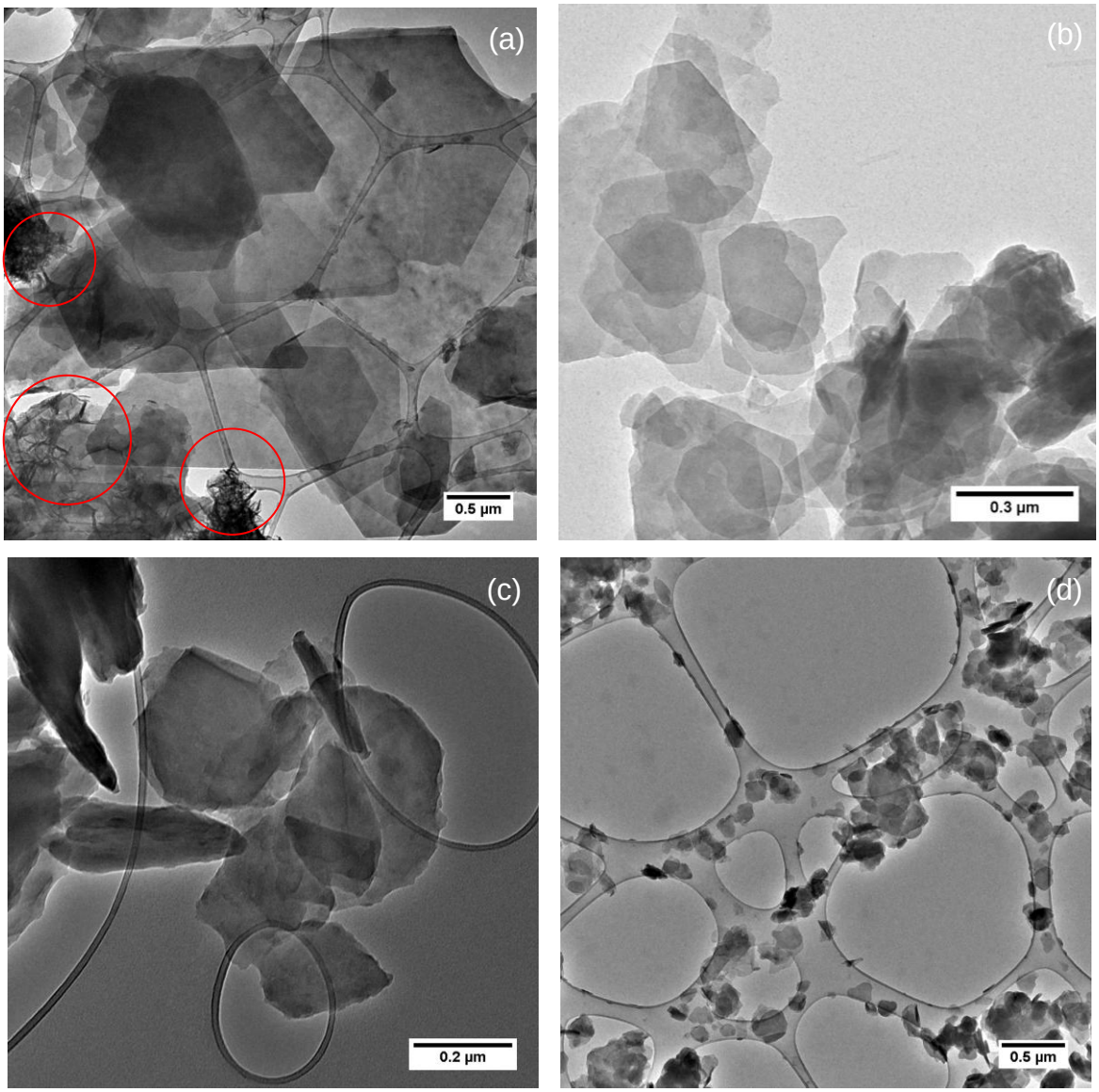

Figure 4.10. TEM images of (a) $Ca_2Al\text{-}NO_3$ made in organic solvent without surfactant (flower-like structure marked with circles in red), (b) $Ca_2Al\text{-}NO_3$ BRM*19.6*, (c) $Ca_2Al\text{-}NO_3$ BRM*13.7*, and (d) $Ca_2Al\text{-}NO_3$ BRM*10.6*.

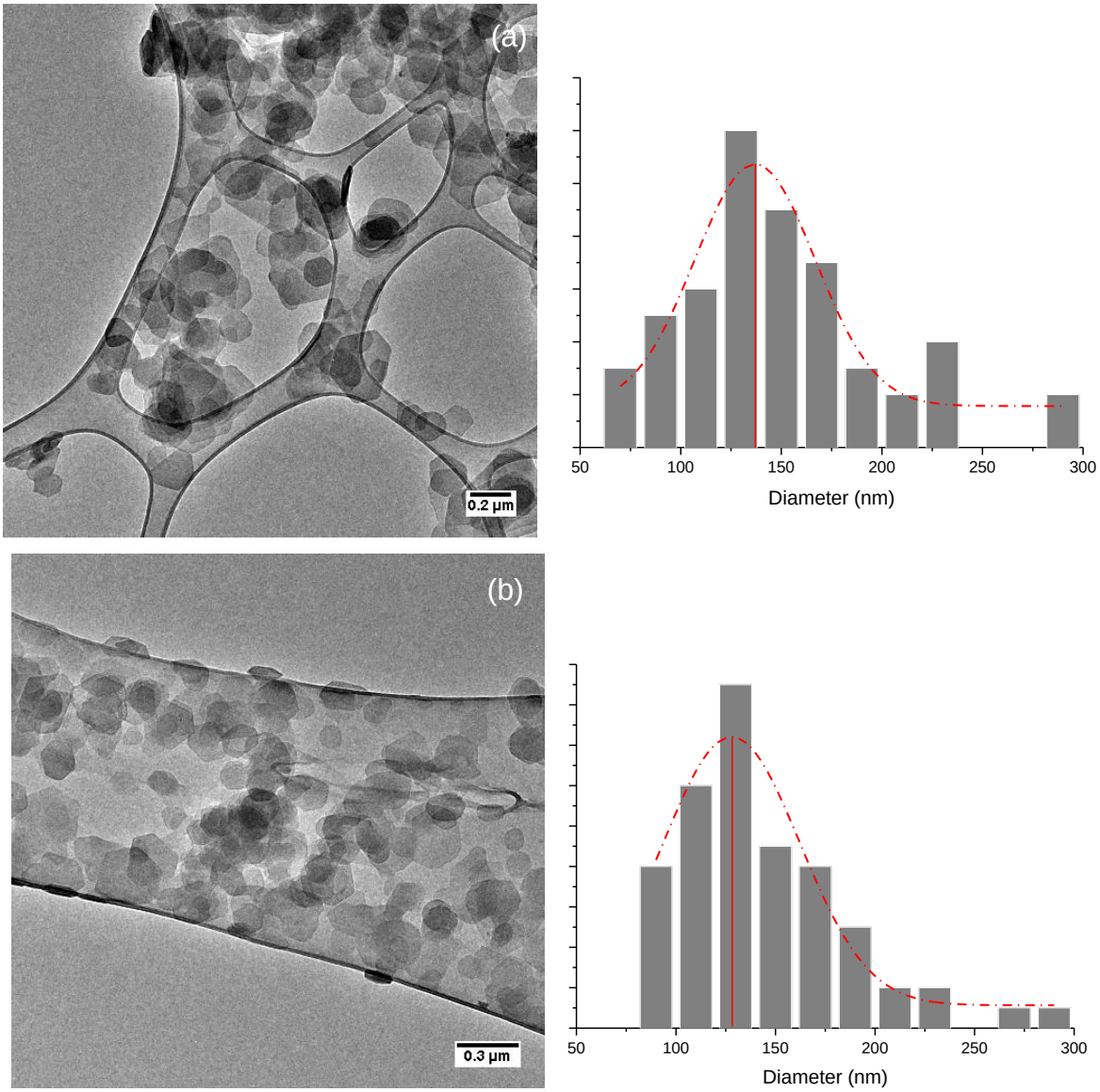

Figure 4.11. TEM images with size distribution of (a) $Ca_2Al\text{-}NO_3$ BRM*4.6*, and (b) $Ca_2Al\text{-}NO_3$ BRM*3.4*. The dash dotted lines in the size distribution data are best fit to the Gaussian equation.

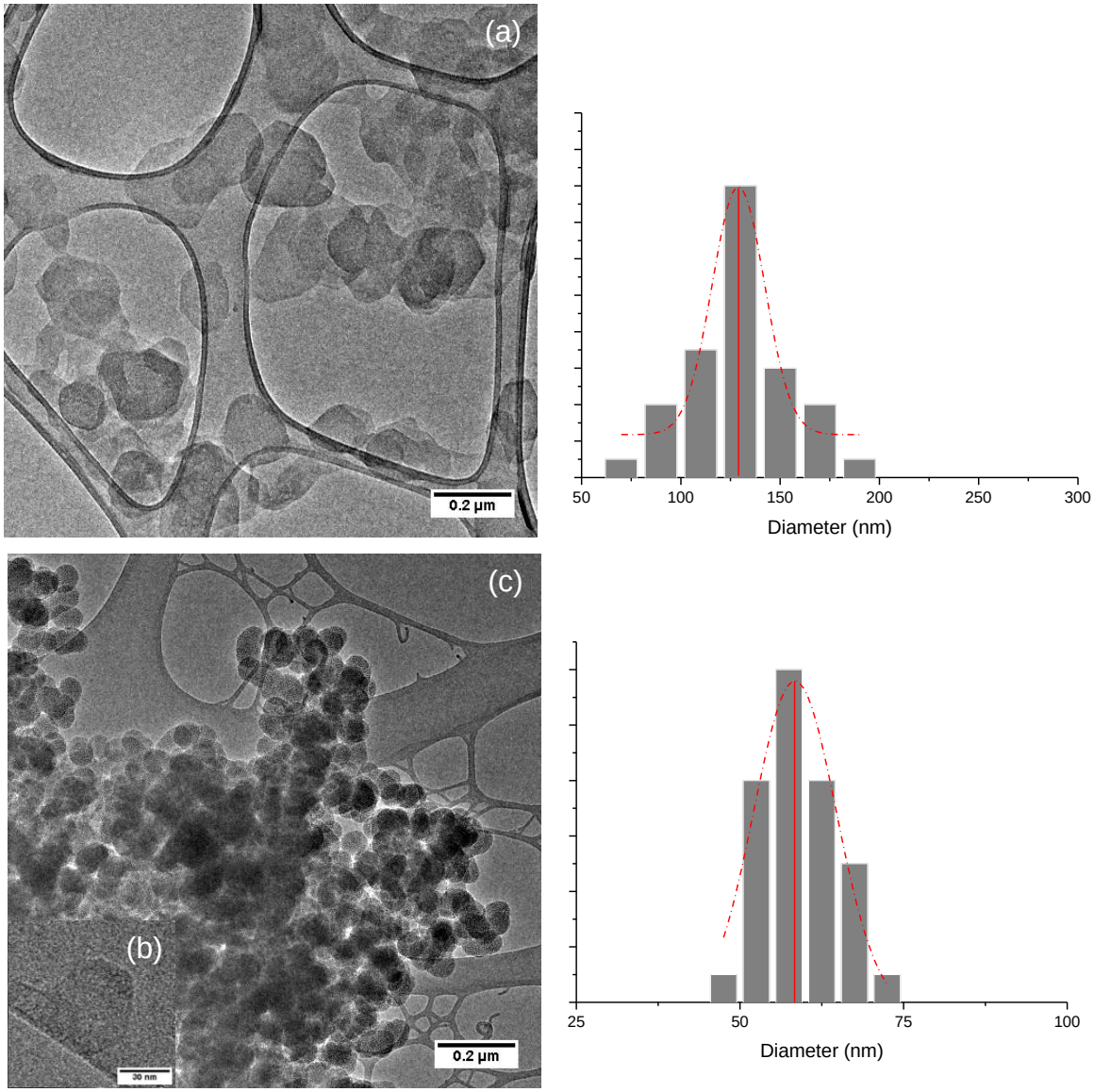

Figure 4.12. TEM images with size distribution of (a) $Ca_2Al\text{-}NO_3$ BRM*2.7*, (b) and (c) $Ca_2Al\text{-}NO_3$ BRM*2.3*. The dash dotted lines in the size distribution data are best fit to the Gaussian equation.

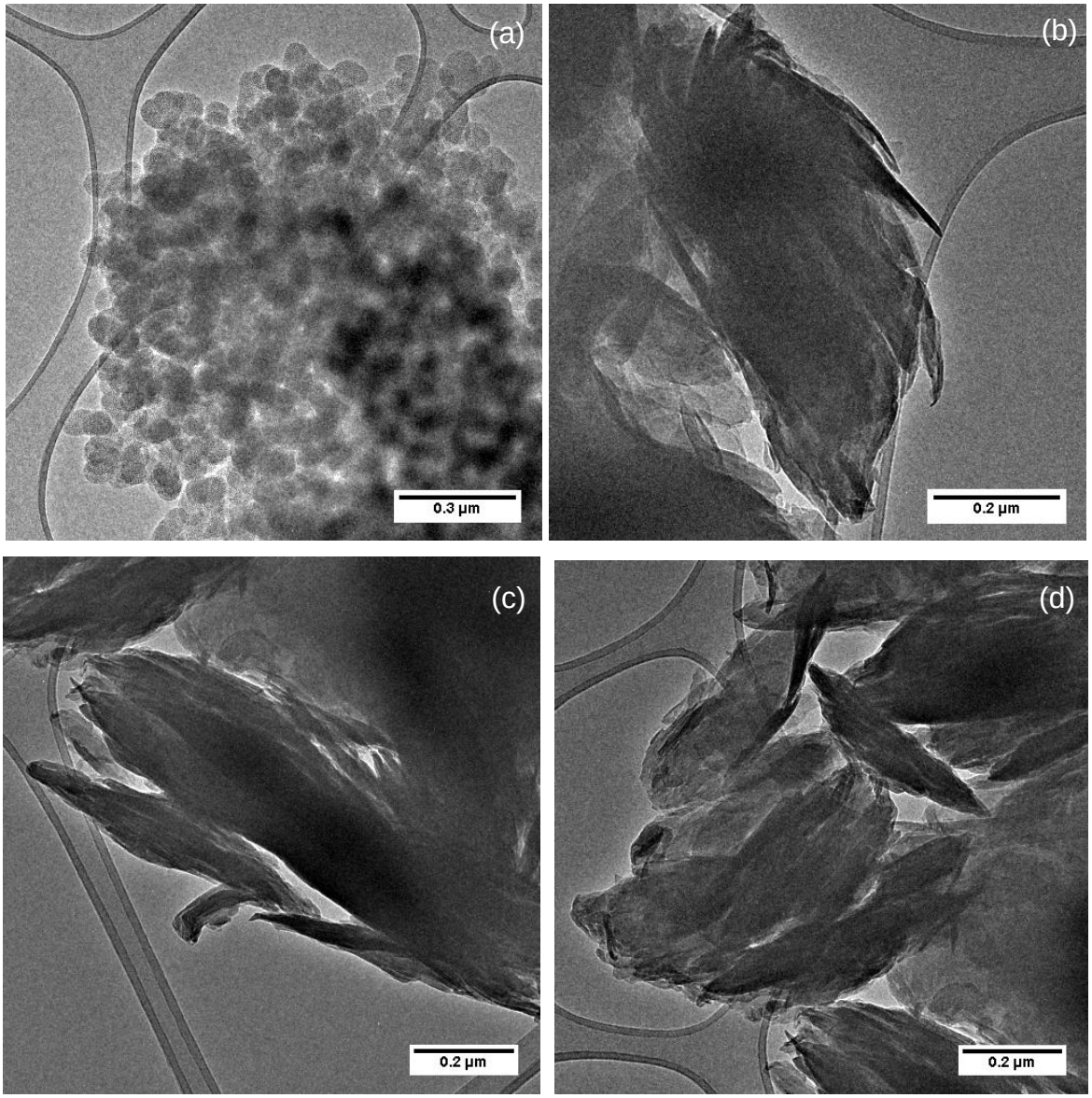

Figure 4.13. TEM images of (a), and (b) $Ca_2Al\text{-}NO_3$ BRM*1.7*; (c), and (d) $Ca_2Al\text{-}NO_3$ BRM*1.4*.

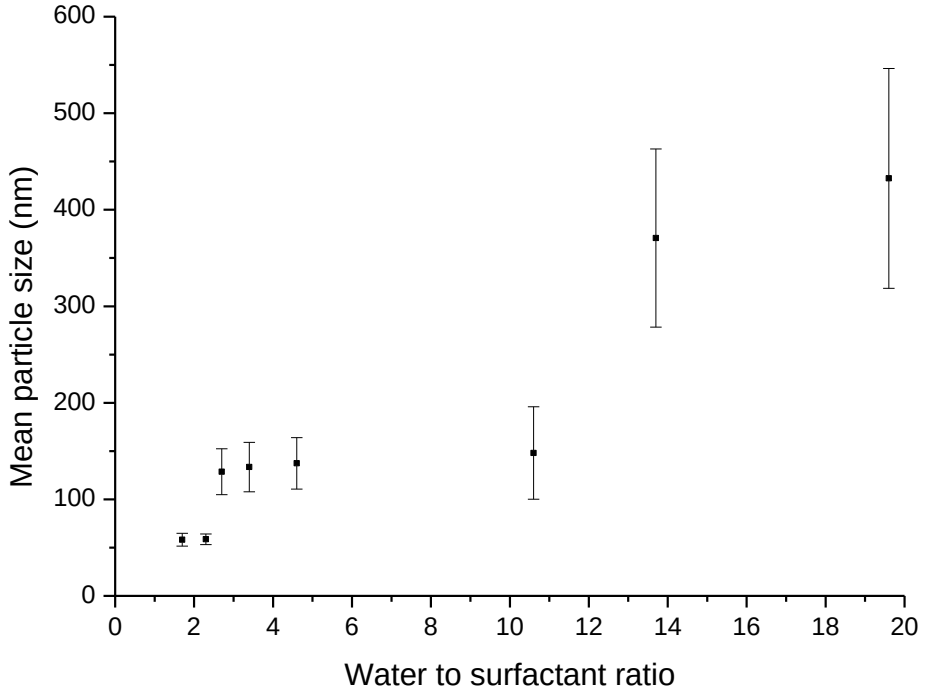

Figure 4.14. A summary of average particle size of $Ca_2Al\text{-}NO_3$ BRM*w* at different water-to-surfactant ratios (*w = 1 – 20*). Error bars show the first standard deviation from the means.

Table 4.4. Data of statistical analysis of $Ca_2Al\text{-}NO_3$ BRM*w* particle diameter.

Sample	Mean particle diameter (μ/nm)	Standard deviation (σ/nm)	Variance (σ^2/nm)
$Ca_2Al\text{-}NO_3$ BRM*19.6*	432.5	113.8	12950.4
$Ca_2Al\text{-}NO_3$ BRM*13.7*	370.7	92.2	8500.8
$Ca_2Al\text{-}NO_3$ BRM*10.6*	148.0	47.9	2294.4
$Ca_2Al\text{-}NO_3$ BRM*4.6*	137.3	26.6	707.6
$Ca_2Al\text{-}NO_3$ BRM*3.4*	133.5	25.6	655.4
$Ca_2Al\text{-}NO_3$ BRM*2.7*	128.7	23.8	566.4
$Ca_2Al\text{-}NO_3$ BRM*2.3*	58.7	5.5	30.3
$Ca_2Al\text{-}NO_3$ BRM*1.7*	58.3	6.6	43.6

Standard deviation $(\sigma) = \sqrt{\frac{1}{N-1}\sum_{i=1}^{N}(x_i-\mu)^2}$

Overall, the TEM data indicate that the water-to-surfactant ratio in the polyethylene glycol dodecyl ether reverse micelle microemulsion has an influence on the morphology, particle size, and size distribution of the LDHs. Once the particles attain their final size during preparation, surfactant molecules attach to the surface of the LDH particles, thus stabilising and protecting them against further growth. Therefore, size and shape of the nano-droplets created by the surfactants can be inferred from the size and morphology of the isolated materials. In the organic system without the addition of polyethylene glycol dodecyl ether, various morphologies and a wide size distribution of LDH particles were found; presumably the aqueous phase was unstable, and formed unclassified shaped regions. Spherical micelles can form when the surfactant is introduced into the system within the range of critical micelle concentration. As more surfactant is added into the system, the spherical micelles become smaller and more uniform. A schematic illustration of micelles formed in response to the addition of surfactant is shown in Figure 4.15.

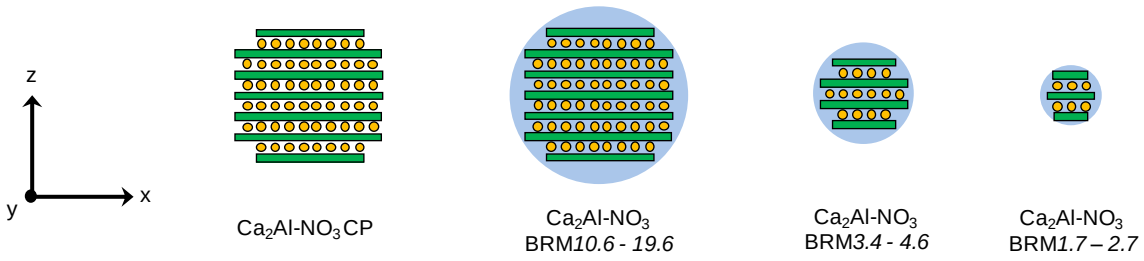

Figure 4.15. Schematic illustration of the LDH platelet size in the water pools controlled by polyethylene glycol dodecylether reverse micelles (BRM*w*) at different water-to-surfactant ratios (*w*).

At very high surfactant concentrations, an excess amount of surfactant prevents the formation of spherical shaped water pools. The hydrophilic heads of the surfactant could connect to form bigger water pools, while the hydrophobic tails could point out into the organic phase; thus causing micelles to transform from spherical to cylindrical morphologies. In the case of added polyethylene glycol dodecyl ether, cylindrical micelles occur when the water-to-surfactant ratio is below *1.7*. However, the crystal growth of the LDH platelets does not occur in this idealised cylindrical shape. Instead, a layered feather-like morphology was found in $Ca_2Al\text{-}NO_3$ BRM*1.7* and $Ca_2Al\text{-}NO_3$ BRM*1.4*. $Ca_2Al\text{-}NO_3$ LDH prefers to build up layers perpendicular to the length of cylindrical micelle and expands the LDH framework in *a*- and *b*-axes along the length of the cylindrical micelle. An illustration of the explanation is shown in Figure 4.16. The water pool formation in reverse micelles as a function of surfactant concentration is summarised in Figure 4.17.

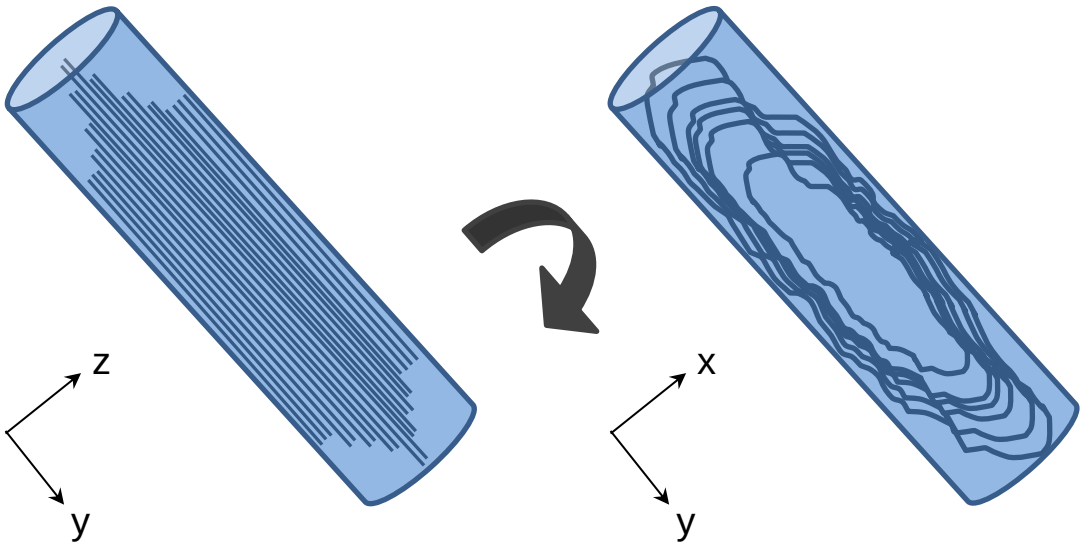

Figure 4.16. Cylindrical micelles showing the LDH growth planes when water-to-surfactant ratio in reactions is less than *1.7*. Surfactant molecules are omitted for clarity.

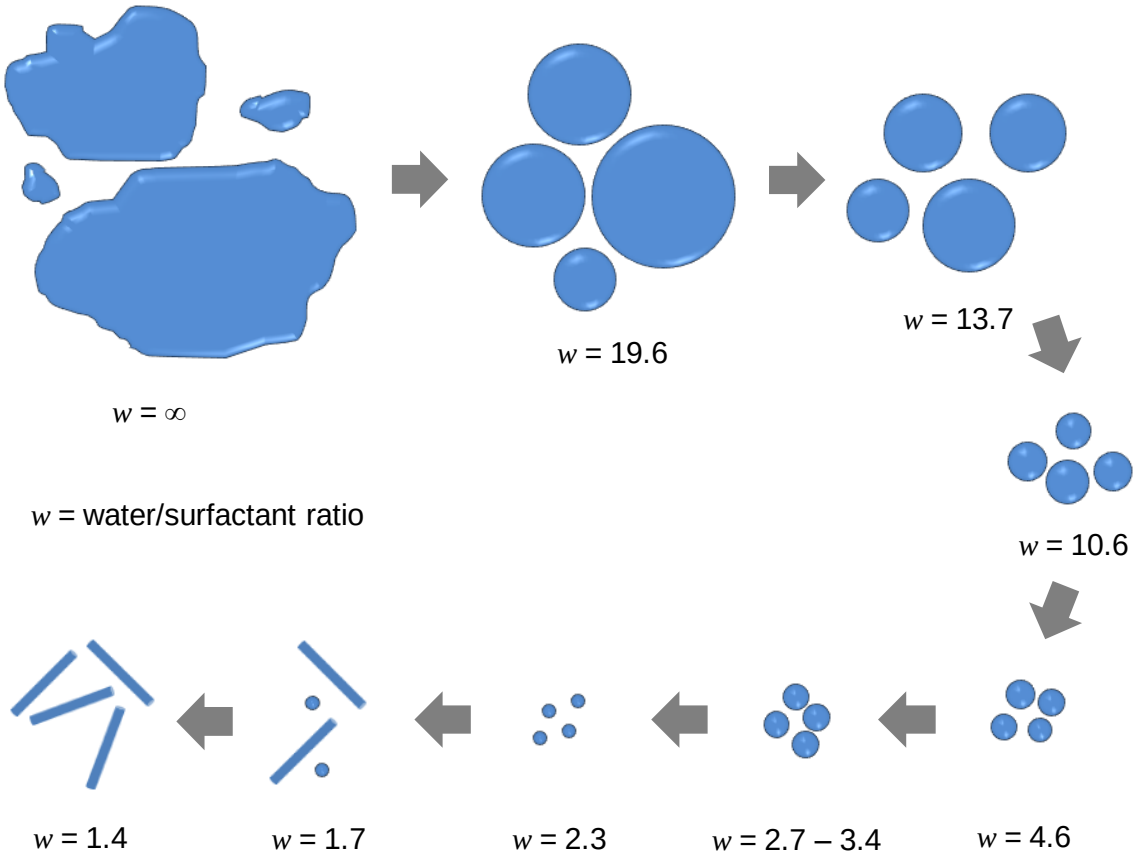

Figure 4.17. Schematic illustration of water pool formation in reverse micelles as a function of surfactant concentration. Surfactant molecules are omitted for clarity.

However, there are a number of publications investigated the study of micelle solutions by using Small angle neutron scattering (SANS) and found that the size of a typical micelle is around 50 Å and is made of about 100 surfactant molecules.[51, 55, 56] Small angle neutron scattering (SANS) is a technique used to observe micelle structures i.e. sizes and shapes and the micelle interactions by the scattering of a monochromatic beam of neutrons from the micelles dispersed in a homogeneous medium. The mean particle diameter of the synthetic LDHs observed by TEM is overall significantly larger than the typical size of micelle. It is possible to explain that the micelles can be grown up during aging stage of the synthesis due to the rigidity and the inter-micellar interaction of micelles.[37]

4.3.4 Atomic Force Microscopy (AFM) study

Atomic force microscopy has been used to study the morphologies and size distribution of $Ca_2Al\text{-}NO_3$ BRM*w* samples (Figure 4.18 and 4.19). All samples were highly dispersed in absolute ethanol with sonication, and then coated on Si wafer substrates and Highly Ordered Pyrolytic Graphite (HOPG). It was observed that $Ca_2Al\text{-}NO_3$ BRM*w* samples can be coated on Si wafers more firmly than on HOPG due to the higher surface charge of the Si wafers. Based on the AFM images it can be seen that, size and morphology of the LDHs change depending on the water-to-surfactant ratio employed; the size and morphologies become smaller and more uniform when the water-to-surfactant ratio decreases until $w = 2.3$. The morphologies of the LDH material become less structured and more cylindrical in shape when the water-to-surfactant ratio is below *2.3*. This again supports the hypothesis that the water pools made by the surfactants and the co-surfactants can be tailored in order to acquire different sized and shaped water pools.

In cases where the water-to-surfactant ratio is high, the surfactants and the co-surfactants can facilitate large spherical water pools, whereas systems containing more surfactants or co-surfactants can have smaller sized spherical water pools. In the cases of polyethylene glycol dodecyl ether (Brij 30), spherical shaped reverse micelles could be formed in organic solution by adding Brij 30 in the range of the critical micelle concentration. From this study, we can predict that the shape of the water pools can be spherical for water-to-surfactant ratios between the values of *2.3* and *10.6*. At lower water-to-surfactant ratios, the shape of the water pools would become more cylindrical and appear larger in size (Figure 4.18(a) and 4.19(b)).

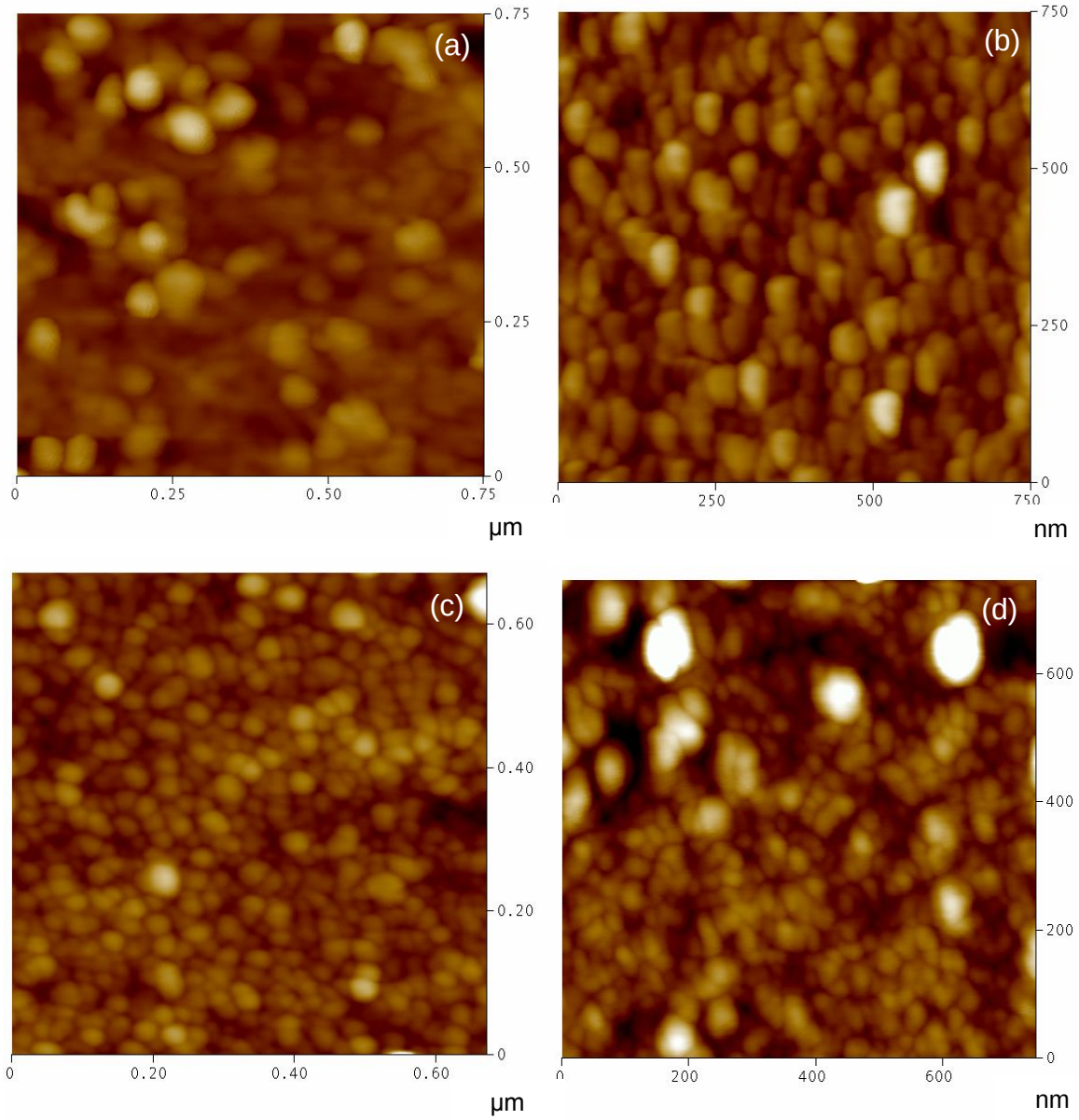

Figure 4.18. AFM images at high magnification (750 X 750 nm^2) on Si wafers of (a) $Ca_2Al\text{-}NO_3$ BRM*10.6*, (b) $Ca_2Al\text{-}NO_3$ BRM*4.6*, (c) $Ca_2Al\text{-}NO_3$ BRM*2.7*, and (d) $Ca_2Al\text{-}NO_3$ BRM*2.3*.

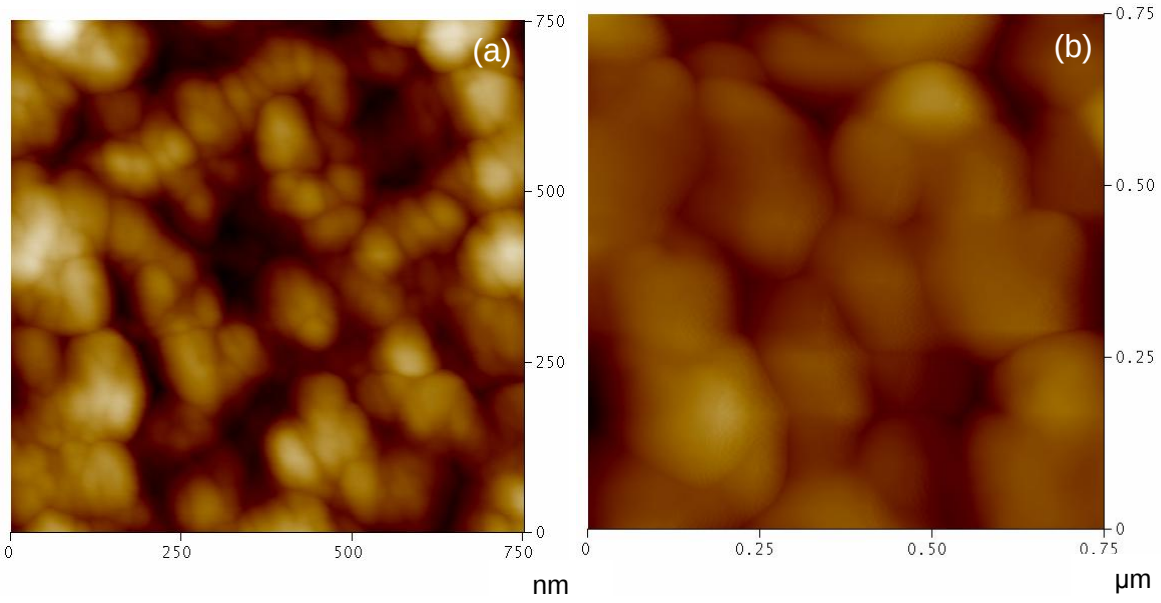

Figure 4.19. AFM images at high magnification (750 X 750 nm^2) on Si wafers of (a) $Ca_2Al\text{-}NO_3$ BRM*1.7*, and (b) $Ca_2Al\text{-}NO_3$ BRM*1.4*.

4.3.5 Scanning electron microscopy and energy-dispersive X-ray spectroscopy study

Scanning electron microscopy is another technique used to study both the morphology and the size of the particles. The SEM images of $Ca_2Al\text{-}NO_3$ BRM*19.6* and $Ca_2Al\text{-}NO_3$ BRM*13.7* are shown in Figure 4.20. The average particle sizes of the LDH samples are in close agreement with the TEM data previously discussed (Section 4.3.3). The SEM instrument was equipped with an energy-dispersive X-ray spectroscopy (EDX). Therefore, EDX spectroscopy was used to provide an estimation of the Ca/Al atomic ratios in these samples. The results are summarised in Table 4.4 given the surface sensitivity of the EDX technique. The samples show a Ca/Al atomic ratio of *ca.* 2.0.

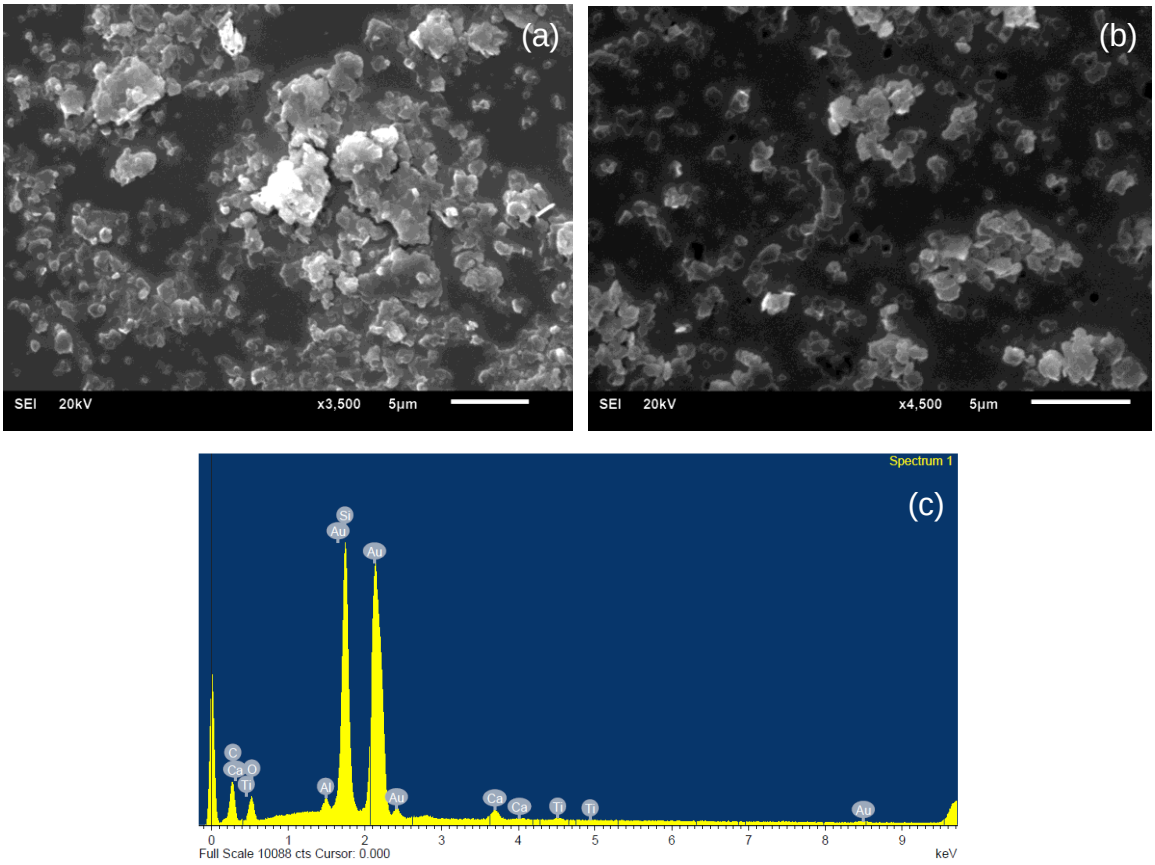

Figure 4.19. SEM images of (a) $Ca_2Al\text{-}NO_3$ BRM*19.6*, (b) $Ca_2Al\text{-}NO_3$ BRM*13.7*, and (c) EDX spectrum of $Ca_2Al\text{-}NO_3$ BRM*19.6* on Au/Ti/Si wafer substrate.

4.3.6 Thermogravimetric and elemental analysis

Thermogravimetric analysis (TGA) was used to determine the thermal stability of the $Ca_2Al\text{-}NO_3$ BRM*w* series. A typical TGA plot for a $Ca_2Al\text{-}NO_3$ BRM*w* sample is shown in Figure 4.21.

In general, results show that the cointercalated water is lost at temperatures up to 150 °C, followed by the loss of water by dehydroxylation of the LDH layers. From 400 °C onwards, the decomposition of nitrate occurs. The final product remaining at 700 °C is a mixture of Mayenite ($Ca_{12}Al_{14}O_{33}$, JCPDS 01-070-2144), and Lime (CaO, JCPDS 00-048-1467).

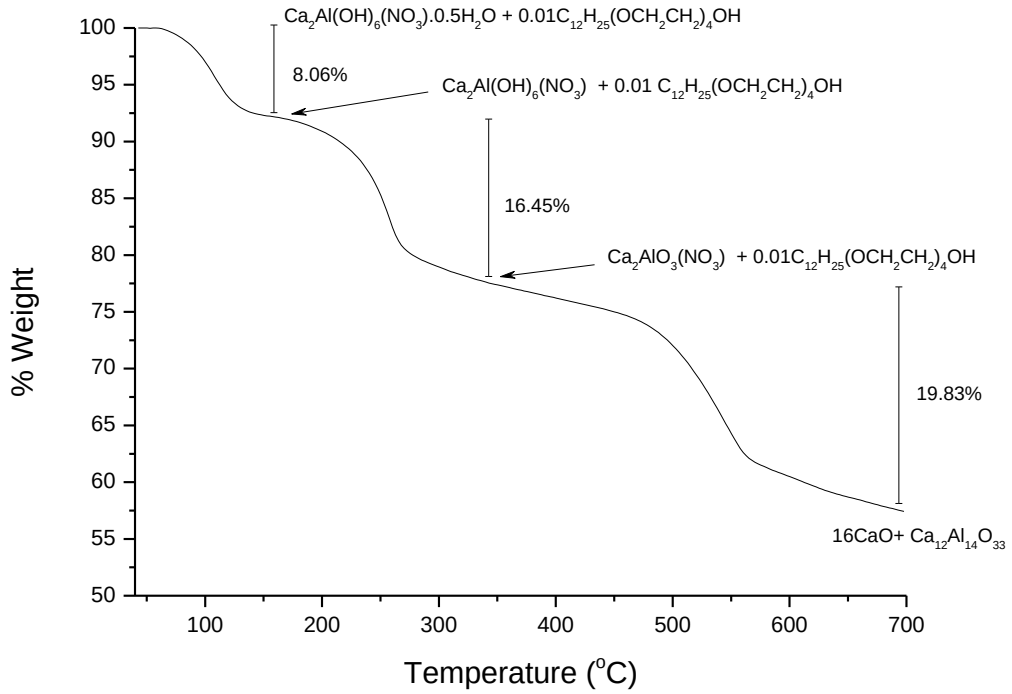

Figure 4.21. TGA plot for $Ca_2Al\text{-}NO_3$ BRM*13.7* from 30 to 700°C.

The elemental composition of the $Ca_2Al\text{-}NO_3$ BRM*w* series can be determined from the EDX, TGA and elemental analysis data, which is summarised in Table 4.5. Results show the $Ca_2Al\text{-}NO_3$ BRM*w* samples all contained minor amounts of organic impurities which are potentially due to the presence of adsorbed polyethylene glycol dodecyl ether surfactant which is possibly located on surface of the LDH particles.

Table 4.5. Chemical composition and formula of $Ca_2Al\text{-}NO_3$ BRM*w* series.

$Ca_2Al\text{-}NO_3$ BRM*w*	Chemical composition, obs. (calc.); (wt%)				
	Ca/Al mol ratio*	C	H	N	Formula
$Ca_2Al\text{-}NO_3$ CP	1.96	0.0 (0.0)	4.8 (4.8)	3.6 (3.7)	$Ca_2Al(OH)_6(NO_3)\bullet 6H_2O$
$Ca_2Al\text{-}NO_3$ BRM*19.6*	1.88	3.2 (3.2)	3.1 (3.2)	3.8 (4.0)	$Ca_2Al(OH)_6(NO_3)_{0.8}\bullet 0.5H_2O$ 3.8 % BRIJ30
$Ca_2Al\text{-}NO_3$ BRM*13.7*	2.10	0.9 (0.8)	2.6 (2.6)	5.0 (4.9)	$Ca_2Al(OH)_6(NO_3)\bullet 0.5H_2O$ 1.0 % BRIJ30
$Ca_2Al\text{-}NO_3$ BRM*10.6*	1.87	1.4 (1.5)	3.1 (3.2)	3.4 (3.5)	$Ca_2Al(OH)_6(NO_3)_{0.7}\bullet H_2O$ 1.7 % BRIJ30
$Ca_2Al\text{-}NO_3$ BRM*4.6*	1.90	1.3 (1.3)	3.3 (3.3)	3.8 (3.8)	$Ca_2Al(OH)_6(NO_3)_{0.8}\bullet 1.5H_2O$ 1.6 % BRIJ30
$Ca_2Al\text{-}NO_3$ BRM*3.4*	1.92	1.2 (1.3)	3.3 (3.3)	3.6 (3.8)	$Ca_2Al(OH)_6(NO_3)_{0.8}\bullet 1.5H_2O$ 1.6 % BRIJ30
$Ca_2Al\text{-}NO_3$ BRM*2.7*	1.84	1.7 (1.7)	3.4 (3.5)	3.3 (3.4)	$Ca_2Al(OH)_6(NO_3)_{0.7}\bullet 1.5H_2O$ 2.0 % BRIJ30
$Ca_2Al\text{-}NO_3$ BRM*2.3*	1.87	2.3 (2.4)	3.4 (3.5)	2.8 (3.0)	$Ca_2Al(OH)_6(NO_3)_{0.6}\bullet 1.3H_2O$ 2.8 % BRIJ30
$Ca_2Al\text{-}NO_3$ BRM*1.7*	1.89	3.2 (3.3)	3.5 (3.7)	2.6 (2.5)	$Ca_2Al(OH)_6(NO_3)_{0.5}\bullet 1.3H_2O$ 3.8 % BRIJ30
$Ca_2Al\text{-}NO_3$ BRM*1.4*	1.82	4.2 (4.3)	3.6 (3.8)	2.4 (2.5)	$Ca_2Al(OH)_6(NO_3)_{0.5}\bullet 1.2H_2O$ 5.0 % BRIJ30
$Ca_2Al\text{-}NO_3$ WO	1.88	0.0 (0.0)	2.9 (2.9)	2.5 (2.8)	$Ca_2Al(OH)_6(NO_3)_{0.5}\bullet 0.6H_2O$

* Determined by Energy-dispersive X-ray spectroscopy technique.

$C_{12}H_{25}(OCH_2CH_2)_4OH$ = polyethylene glycol dodecyl ether (BRIJ30) used as a surfactant to control micelles in reverse emulsion.

4.4 The effect of HLB number on morphologies and size of Ca_2Al-LDH materials.

Octyl phenol ethoxylate (TritonX100) with a HLB = 13.5 has been used to compare the effect of the HLB values of a surfactant on the morphologies of the isolated LDH materials. The series of Ca_2Al-NO_3 TRM*w* has been synthesised over the range of critical micelle concentration, with *w* = *49*, *65*, and *98*. The materials have been studied by powder X-ray diffraction, infrared spectroscopy, thermogravimetric analysis, elemental analysis, and transmission electron microscopy in order to compare the purity, crystallinity, size, and morphology of these materials within the series of Ca_2Al-NO_3 TRM*w* samples.

4.4.1 Powder X-ray diffraction data

The powder X-ray diffraction patterns of Ca_2Al-NO_3 TRM*w* (*w* = water-to-surfactant ratio at *49*, *65*, and *98*) are shown in Figure 4.22. The XRD data can be indexed using the unit cell dimension of $Ca_2Al(OH)_6NO_3{\bullet}6H_2O$.[53] The (004) Bragg reflection becomes significantly broader as the water-to-surfactant ratio (*w*) decreases from *98* to *49*.

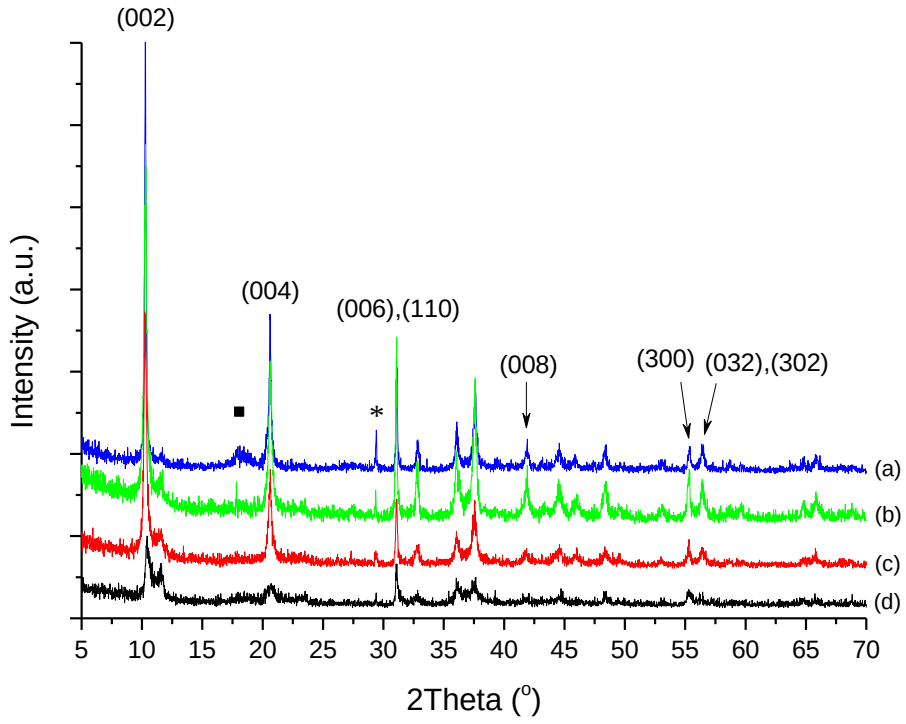

Figure 4.22. A summary of the powder XRD data for (a) Ca_2Al-NO_3 without octyl phenol ethoxylate in reaction (Ca_2Al-NO_3 WO), (b) Ca_2Al-NO_3 TRM*98*, (c) Ca_2Al-NO_3 TRM*65*, and (d) Ca_2Al-NO_3 TRM*49*. Reflections marked with ▪ corresponding to $Al(OH)_3$ and those marked with * correspond to $CaCO_3$.

The full width at half maximum (FWHM) analysis of the (004) Bragg reflections for $Ca_2Al\text{-}NO_3$ TRM*w* are shown in Table 4.6. The XRD data for $Ca_2Al\text{-}NO_3$ TRM*98* and TRM*65* give materials that are very similar to the equivalent material formed in the absence of surfactants.

Using a water-to-surfactant ratio of *49* results in the formation of a mixed phase material; the LDH compound is very poorly crystalline as determined by the FWHM of the (004) Bragg reflections. This is further supported by the TEM studies.

Table 4.6. A summary of the X-ray diffraction data for $Ca_2Al\text{-}NO_3$ TRM*w* (*w* = *49*, *65* and *98*).

Sample	(004) Bragg Reflection		(300) Bragg Reflection	
	FWHM/^{o}	CDS/nm	FWHM/^{o}	CDS/nm
$Ca_2Al\text{-}NO_3$ TRM*98*	0.29	27.5	0.32	27.3
$Ca_2Al\text{-}NO_3$ TRM*65*	0.20	39.9	0.33	27.2
$Ca_2Al\text{-}NO_3$ TRM*49*	0.82	9.7	0.52	17.1
$Ca_2Al\text{-}NO_3$ WO	0.24	32.6	0.37	24.2
$Ca_2Al\text{-}NO_3$ CP	0.54	14.9	0.33	26.5

FWHM = full width at half maximum, Scherrer equation ($CDS = K\lambda(\beta\cos\theta)^{-1}$), K = 0.89,[54]

CDS = Crystalline domain size, determined by scherrer equation.

WO = $Ca_2Al\text{-}NO_3$ synthesised in an organic solvent without surfactant.

CP = $Ca_2Al\text{-}NO_3$ prepared by co-precipitation.

4.4.2 Transmission electron microscopy study

Transmission electron microscopy technique shows that the morphologies and size distribution of the $Ca_2Al\text{-}NO_3$ TRM*w* series vary between samples. The morphologies of the LDH particles are relatively similar to the $Ca_2Al\text{-}NO_3$ synthesised in the organic system without adding octyl phenol ethoxylate. Flower-like structures can be found in $Ca_2Al\text{-}NO_3$ TRM*98*, as seen in the LDH made without the addition of a surfactant shown in Figure 4.23(b). The particle sizes in $Ca_2Al\text{-}NO_3$ TRM*65* were on average, slightly bigger than those observed in $Ca_2Al\text{-}NO_3$ TRM*98*. There is a broad particle size distribution found in $Ca_2Al\text{-}NO_3$ TRM*49* with a mean particle size of 240.63 nm and standard deviation of 132.14 nm.

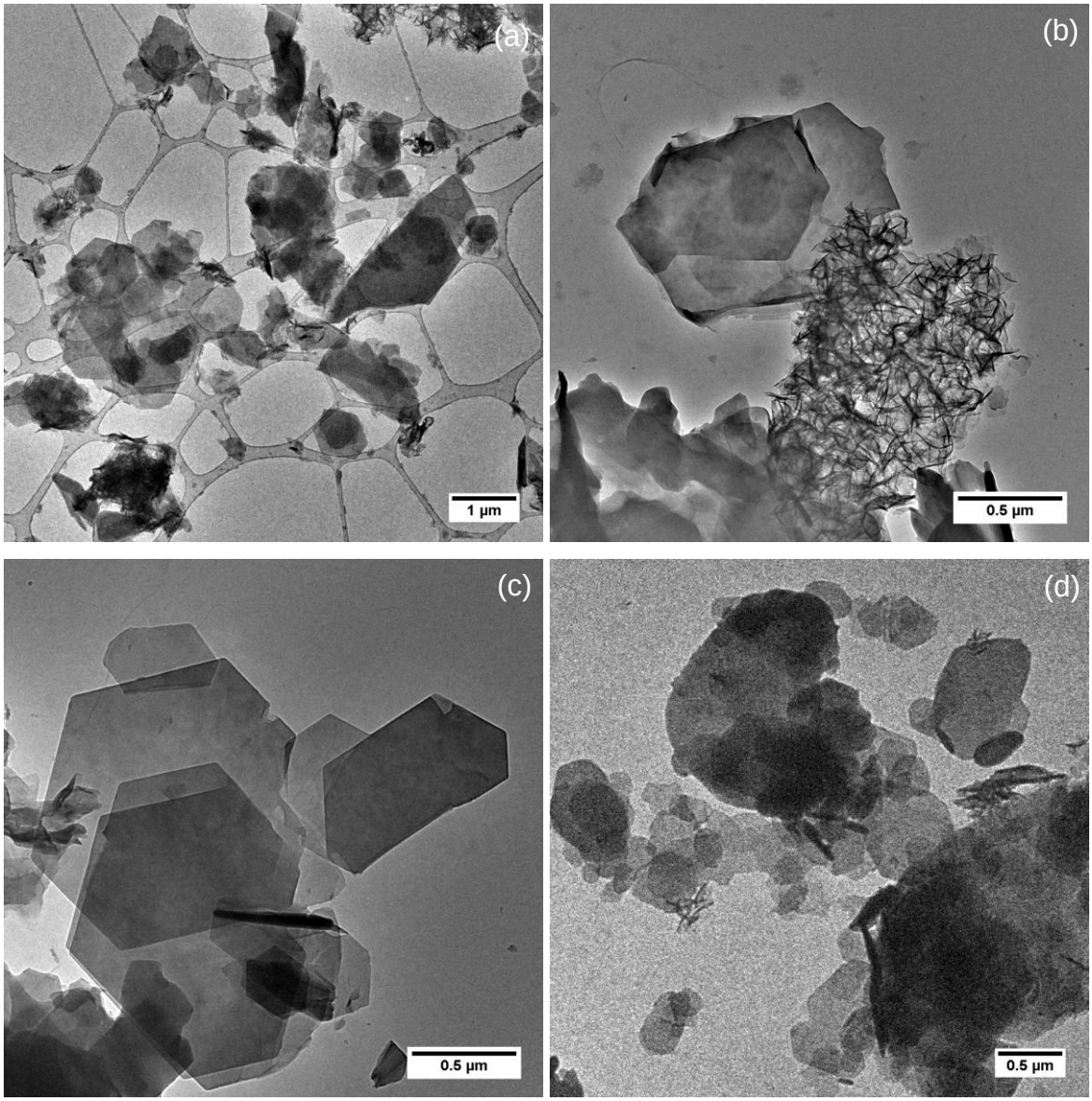

Figure 4.23. TEM images of (a) $Ca_2Al\text{-}NO_3$ made in organic solvent without surfactant, (b) $Ca_2Al\text{-}NO_3$ TRM*98*, (c) $Ca_2Al\text{-}NO_3$ TRM*65*, and (d) $Ca_2Al\text{-}NO_3$ TRM*49*.

4.4.3 Discussion

The series of $Ca_2Al\text{-}NO_3$ TRM*w* have been crystallised. Their particle crystallinity, size and morphology were compared with the series of $Ca_2Al\text{-}NO_3$ BRM*w* as previously described in Section 4.3. The data for the $Ca_2Al\text{-}NO_3$ TRM*w* series indicates that these materials contain impurities, do not adopt uniform shapes and have a wide size distribution. Hence, it can be concluded that octyl phenol ethoxylate (TritonX100) is not an effective surfactant in controlling the nucleation and growth of the LDH. Rigidity of micelles is one of the factors in controlling shape, size and stability of micelles. The colloidal stability of the microemulsion droplets plays a decisive role in the particle size

and distribution during the formation of LDH particles. In this chapter, there were two different types of surfactants, classified by their Hydrophile-Lipophile Balance (HLB) value, which were used to modify the shape and sizes of micelles. It was found that morphologies and size distribution of the series of $Ca_2Al\text{-}NO_3$ TRM*w* were more variable when the surfactant with a higher HLB value was used in comparison to the $Ca_2Al\text{-}NO_3$ BRM*w* series. Hydrophile-Lipophile Balance (HLB) is a significantly useful measure defining a balance that exists between the hydrophilicity and hydrophobicity of surfactant molecules. Octyl phenol ethoxylate (Triton X100), the surfactant with higher HLB value has a greater hydrophilicity, thus causing it to become unstable in organic matrices even when used within the ranges of critical micelle concentration. The micelle formation of the surfactant could become easier to give variation of size and shape of micelles, which can be observed in LDH particles after synthesis. Therefore, based on the study, surfactants with lower HLB values should be better stabilisers for water-in-oil emulsion systems.[49]

4.5 Conclusions

The synthesis of $Ca_2Al\text{-}NO_3$ LDHs *via* a non-ionic surfactant reverse microemulsion has been investigated. The use of different non-ionic surfactants have successfully been studied in terms of the amount and type of surfactant used, as classified by the Hydrophile-Lipophile Balance (HLB) values. Two different surfactants with varying HLB values were used to study their effects on the morphology and size distribution of the $Ca_2Al\text{-}NO_3$ LDHs. The $Ca_2Al\text{-}NO_3$ BRM*w* series made using polyethylene glycol dodecyl ether (Brij 30) gave uniform shape and sized platelet particles. The size and morphology of the particles could be controlled by varying the amount of polyethylene glycol dodecyl ether used. $Ca_2Al\text{-}NO_3$ platelets were formed with water-to-surfactant ratios in the critical micelle concentration. Feather-like $Ca_2Al\text{-}NO_3$ LDHs were formed at lower water-to-surfactant ratios, which we infer is due to the formation of cylindrical shaped micelles.

In the case of $Ca_2Al\text{-}NO_3$ TRM*w* synthesised by adding octyl phenol ethoxylate, which has higher Hydrophile-Lipophile Balance (HLB), the data shows the surfactant has a negligible effect on the morphology and the size of $Ca_2Al\text{-}NO_3$ LDHs. The morphology of $Ca_2Al\text{-}NO_3$ TRM*w* after synthesis is relatively similar to $Ca_2Al\text{-}NO_3$ made in organic solvent without octyl phenol ethoxylate.

This work demonstrates that the reverse microemulsion technique can be a suitable technique to make nanoplatelet LDHs with control over the morphology and size. However, one factor that needs to be considered is the solubility of the surfactant, as defined by its Hydrophile-Lipophile Balance (HLB) value. The solubility of the surfactants can affect the stability of micelles in the solution, giving various morphologies of LDH particles after synthesis. The nature, the surface activity of surfactants, and the colloidal stability of microemulsion droplets play critical roles on the particle size and distribution during the preparation of LDH particles. Hydrophilic surfactants with high water solubility are good stabilisers for oil-in-water emulsions and have high HLB values, while surfactants with low water solubility are good stabilizers for water-in-oil emulsions.

4.6 References

1. S. Hanehara and K. Yamada, *Cement and Concrete Research*, 1999, **29**, 1159-1165.
2. M. Collepardi, *Cement and Concrete Composites*, 1998, **20**, 103-112.
3. E.-i. Tazawa and S. Miyazawa, *Cement and Concrete Research*, 1995, **25**, 281-287.
4. K. Yamada, T. Takahashi, S. Hanehara and M. Matsuhisa, *Cement and Concrete Research*, 2000, **30**, 197-207.
5. M. Şahmaran, H. A. Christianto and İ. Ö. Yaman, *Cement and Concrete Composites*, 2006, **28**, 432-440.
6. E. Freeman, Y.-M. Gao, R. Hurt and E. Suuberg, *Fuel*, 1997, **76**, 761-765.
7. K. Yoshioka, E.-i. Tazawa, K. Kawai and T. Enohata, *Cement and Concrete Research*, 2002, **32**, 1507-1513.
8. M. R. Rixom and N. P. Mailvaganam, *Chemical Admixtures for Concrete*, Taylor & Francis, 1999.
9. F. Winnefeld, S. Becker, J. Pakusch and T. Götz, *Cement and Concrete Composites*, 2007, **29**, 251-262.
10. M. Pei, D. Wang, X. Hu and D. Xu, *Cement and Concrete Research*, 2000, **30**, 1841-1845.
11. J. Plank, K. Pöllmann, N. Zouaoui, P. Andres and C. Schaefer, *Cement and Concrete Research*, 2008, **38**, 1210-1216.
12. J. Plank and B. Sachsenhauser, *Cement and Concrete Research*, 2009, **39**, 1-5.
13. C. Schröfl, M. Gruber and J. Plank, in *Ultra High Performance Concrete (UHPC)–2nd International Symposium on Ultra High Performance Concrete, Kassel*, 2008, pp. 383-390.
14. J. Plank, Z. Dai and P. Andres, *Materials letters*, 2006, **60**, 3614-3617.
15. J. Plank, Z. Dai and N. Zouaoui, *Journal of Physics and Chemistry of Solids*, 2008, **69**, 1048-1051.
16. S. Xu, B. Zhang, Z. Chen, J. Yu, D. G. Evans and F. Zhang, *Industrial & Engineering Chemistry Research*, 2011, **50**, 6567-6572.
17. L. Raki, J. J. Beaudoin and L. Mitchell, *Cement and Concrete Research*, 2004, **34**, 1717-1724.
18. H. Justnes and E. C. Nygaard, *Cement and Concrete Research*, 1995, **25**, 1766-1774.
19. S. Aggoun, M. Cheikh-Zouaoui, N. Chikh and R. Duval, *Construction and Building Materials*, 2008, **22**, 106-110.
20. R. L. Angstadt, US patent US3836589, 1969.
21. F. Millange, R. I. Walton, L. Lei and D. O'Hare, *Chemistry of Materials*, 2000, **12**, 1990-1994.
22. M. Meyn, K. Beneke and G. Lagaly, *Inorganic Chemistry*, 1990, **29**, 5201-5207.
23. J. Eastoe, M. J. Hollamby and L. Hudson, *Advances in Colloid and Interface Science*, 2006, **128–130**, 5-15.
24. M. Li, H. Schnablegger and S. Mann, *Nature*, 1999, **402**, 393-395.
25. A. P. Herrera, O. Resto, J. G. Briano and C. Rinaldi, *Nanotechnology*, 2005, **16**, S618.
26. T. Hyeon, *Chemical Communications*, 2003, **8**, 927-934.
27. Y. Lee, J. Lee, C. J. Bae, J. G. Park, H. J. Noh, J. H. Park and T. Hyeon, *Advanced Functional Materials*, 2005, **15**, 503-509.

28. S. Sathyamurthy, K. J. Leonard, R. T. Dabestani and M. P. Paranthaman, *Nanotechnology*, 2005, **16**, 1960.
29. L. Qi, *Encyclopedia of Surface and Colloid Science. Second Edition. New York: Taylor & Francis*, 2006, 6183.
30. T. Tan, S. Liu, Y. Zhang, M. Han and S. Selvan, *Comprehensive Nanoscience and Technology*, 2011, **5**, 399-441.
31. K. Ratinac, H. Zhu, L. Stadtmueller and S. Ringer, in *Materials Forum*, 2002, pp. 44-73.
32. K. Holmberg, *Journal of Colloid and Interface Science*, 2004, **274**, 355-364.
33. G. Hu, N. Wang, D. O'Hare and J. Davis, *Journal of Materials Chemistry*, 2007, **17**, 2257-2266.
34. G. Hu and D. O'Hare, *Journal of the American Chemical Society*, 2005, **127**, 17808-17813.
35. C. J. Wang, Y. A. Wu, R. M. Jacobs, J. H. Warner, G. R. Williams and D. O'Hare, *Chemistry of Materials*, 2010, **23**, 171-180.
36. A. Wongariyakawee, F. Schäeffel, J. H. Warner and D. O'Hare, *Journal of Materials Chemistry*, 2012, **22**, 7751-7756.
37. M. A. Lopez-Quintela, *Current Opinion in Colloid & Interface Science*, 2003, **8**, 137-144.
38. S. Qiu, J. Dong and G. Chen, *Journal of Colloid and Interface Science*, 1999, **216**, 230-234.
39. Y. Ju-Nam and J. R. Lead, *Science of the Total Environment*, 2008, **400**, 396-414.
40. X. Jin, D. A. Streett, C. A. Dunlap and M. E. Lyn, *Biological Control*, 2008, **46**, 226-233.
41. H. Schott, *Journal of Pharmaceutical Sciences*, 1969, **58**, 1131-1133.
42. H. Schott, *Journal of Colloid and Interface Science*, 1989, **133**, 527-529.
43. H. Kunieda and K. Shinoda, *Journal of Colloid and Interface Science*, 1985, **107**, 107-121.
44. H. Kunieda and N. Ishikawa, *Journal of Colloid and Interface Science*, 1985, **107**, 122-128.
45. R. C. Pasquali, M. P. Taurozzi and C. Bregni, *International Journal of Pharmaceutics*, 2008, **356**, 44-51.
46. I. Capek, *Advances in Colloid and Interface Science*, 2004, **110**, 49-74.
47. H. Kunieda and M. Yamagata, *Langmuir*, 1993, **9**, 3345-3351.
48. P. M. Kruglyakov, *Studies in Interface Science*, 2000, **9**, v-viii.
49. J. Israelachvili, *Colloids and Surfaces A: Physicochemical and Engineering Aspects*, 1994, **91**, 1-8.
50. S. K. Hait and S. P. Moulik, *Journal of Surfactants and Detergents*, 2001, **4**, 303-309.
51. P. Goyal and V. Aswal, *Current Science*, 2001, **80**, 972-979.
52. G. Renaudin, J. P. Rapin, B. Humbert and M. François, *Cement and Concrete Research*, 2000, **30**, 307-314.
53. G. Renaudin and M. Francois, *Acta Crystallographica Section C: Crystal Structure Communications*, 1999, **55**, 835-838.
54. V. Drits, J. Srodon and D. Eberl, *Clays and Clay Minerals*, 1997, **45**, 461-475.
55. S. V. G. Menon, P. S. Goyal, B. A. Dasannacharya and P. Thiyagarajan, *Physical Review E*, 1996, **53**, 6569-6572.
56. P. Hassan, G. Fritz and E. W. Kaler, *Journal of Colloid and Interface Science*, 2003, **257**, 154-162.

Chapter 5: Synthesis and Characterisation of Nitrite Intercalated Calcium Aluminum Layered Double Hydroxides

5.1 Introduction

The synthesis of nitrate intercalated layered double hydroxides in non-ionic surfactant reverse micelles has been successfully investigated in Chapter 4. Some of the parameters which can influence the size and shape of the as-prepared LDH particles using a reverse microemulsion have been discussed. In this chapter, the reverse micelle approach has been investigated for the synthesis of nitrite-intercalated layered double hydroxides. The aim of this work is to prepare novel LDHs that may be used as multifunctional additives in cements.

Steel corrosion in concrete is one of the major causes of premature deterioration of reinforced concrete structures (Figure 5.1).[1-3] In general, reinforcing steel tends to passivate with a thin adhering film of Fe_2O_3 under the alkaline conditions of cement hydration. This film is normally stable at pHs higher than 12.5 (Equations 5.1 – 5.4). Chloride ions can migrate into concrete from the environment, especially on contact with sea water. If the mobile chloride ions reach the embedded steel and exceed a certain critical concentration, the pH is lowered which affects the hydration reactions. At pH below 11.5 the normally passivated surface of the steel can be destroyed and iron chloro-complexes can be synthesised, initiating an active corrosion area (Equation 5.5).[4-8]

$$Fe\ (metal) \rightarrow Fe^{2+} + 2e^{-} \qquad \textbf{Equation 5.1}$$

$$Fe^{2+} + 2OH^{-} \rightarrow Fe(OH)_2 \qquad \textbf{Equation 5.2}$$

$$4Fe(OH)_2 + 2H_2O + O_2 \rightarrow 4Fe(OH)_3 \qquad \textbf{Equation 5.3}$$

$$4Fe(OH)_3 \rightarrow 2Fe_2O_3 \bullet 6H_2O\ ;\ \text{stable at pH} > 12.5 \qquad \textbf{Equation 5.4}$$

In the case, where chloride ion penetration occurs, the pH decreases;

$$Fe(OH)_2 + Cl^{-} \rightarrow \text{Iron Chloro-complexes} \qquad \textbf{Equation 5.5}$$

Figure 5.1. Images of steel corrosion in reinforce concrete.

There are many additives commonly considered to be corrosion inhibitors for reinforced concrete. For example, nitrite based corrosion inhibitors have been widely used. In particular, calcium nitrite is preferred over other corrosion inhibitors (sodium nitrite, sodium benzoate), because of the compatibility of the inhibitor with the complex chemistry of concrete.[4-8] Nitrite helps to protect against formation of iron chloro-complexes (corrosion products) by competing against the reaction of chloride and $Fe(OH)_2$ (Figure 5.5), and in doing so favouring formation of the desirable Fe_2O_3 film:

$$Fe(OH)_2 + 2NO_2^- \rightarrow Fe_2O_3 + NO + H_2O \qquad \textbf{Equation 5.6}$$

It is proposed that the efficiency of nitrite-based corrosion inhibitors could be increased by controlled nitrite release from layered double hydroxides. In addition to releasing nitrite ions into the concrete, chloride ions might be trapped into LDH layers to replace nitrite. Furthermore, in Chapter 3 it was shown that the LDH materials can accelerate cement hydration.[9] Therefore nitrite-intercalated LDH may offer the opportunity of a multi-functional additive in cement. Furthermore, to improve the efficiency these additives, we propose to prepare nano-size LDH materials. This chapter describes the use of reverse microemulsion techniques to prepare nano-sized study $Ca_2Al(OH)_6NO_2.nH_2O$.

5.2 Synthesis of nano-sized nitrite intercalated Ca_2Al-LDHs via non-ionic surfactant reverse micelles

Following the procedure outlined in Section 4.3, 4 ml each of butan-1-ol and polyethylene glycol dodecyl ether (Brij 30) were added to 200 ml of isooctane. Polyethylene glycol dodecyl ether with a water to surfactant ratio of 10.6 was added to organic solution. Aqueous solutions were prepared separately: 0.13 g of $Al(OH)_3$ and 1.37 g of $NaNO_2$ were mixed in 4.5 ml of 4M NaOH. The aqueous mixture was then introduced to the organic solution dropwise followed by the addition of 2.9 g of 30 %wt of $Ca(NO_2)_2$ solution. The mixture was stirred vigorously at room temperature for 3 days. The product is denoted as Ca_2Al-NO_2 BRM*w* (*w* = 10.6) (Figure 5.2). Ca_2Al-NO_2 BRM*10.6* has been characterised and compared with Ca_2Al-NO_2 CP formed *via* precipitation. The solid products are separated by centrifugation and then washed with a mixture of ethanol and water. For Ca_2Al-NO_2 CP, 0.6 g of NaOH and 0.13 g of $Al(OH)_3$ were mixed in 250 ml of deionised water. 1.37 g of $NaNO_2$ was added to the solution after the $Al(OH)_3$ had completely dissolved. 2.90 g of 30 %wt $Ca(NO_2)_2$ solution was then added dropwise. This solution was stirred vigorously at room temperature for 3 days.

5.2.1 X-ray powder diffraction data

For the XRD data for Ca_2Al-NO_2 BRM*10.6* and Ca_2Al-NO_2 CP are shown in Figure 5.2. The XRD data for Ca_2Al-NO_2 BRM*10.6* and Ca_2Al-NO_2 CP can be indexed to the unit cell as shown in Table 5.1. The interlayer separation along *c*-axis for Ca_2Al-NO_2 BRM*10.6* and Ca_2Al-NO_2 CP are 7.58 Å and 7.57 Å, respectively. There is no appearance for the XRD pattern representing the intercalation of polyethylene glycol dodecyl ether between layers, or the precipitation of calcium surfactants. Ca_2Al-NO_2 BRM*10.6* shows significant peak broadening of the (002) Bragg reflection. We observe large differences in the values derived from the Scherrer equation calculation between Ca_2Al-NO_2 BRM*10.6* and Ca_2Al-NO_2 CP as shown in Table 5.1. Comparing the crystalline domain sizes obtained from the (002) Bragg reflections of the analogous nitrate Ca_2Al-NO_3 with the nitrite Ca_2Al-NO_2, it can be seen that the crystalline domain size depends on the individual material synthesised even at the same water to surfactant ratio.

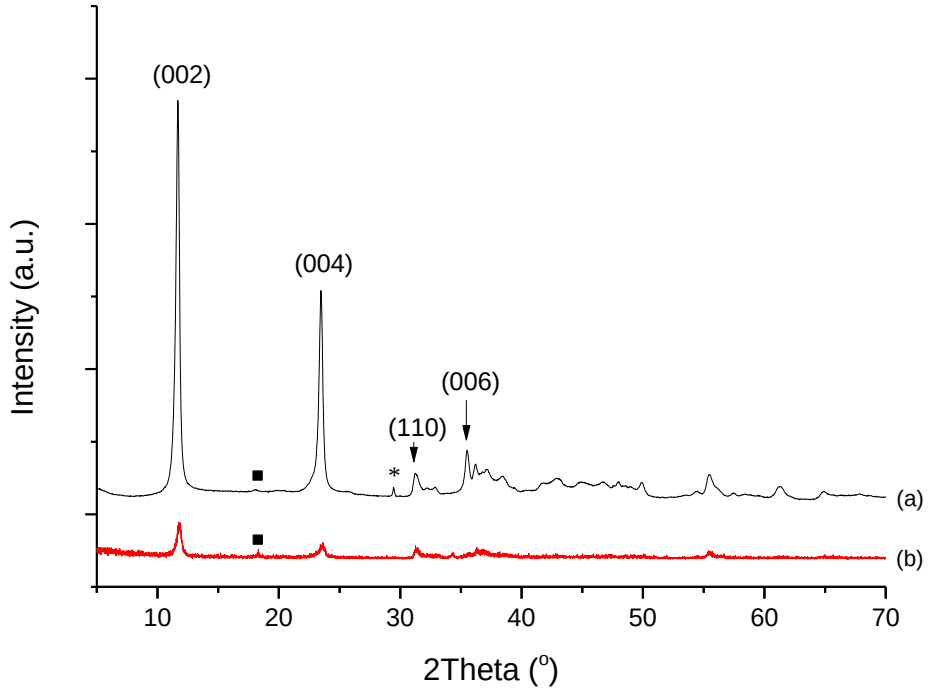

Figure 5.2. Summary of the powder XRD data for (a) $Ca_2Al\text{-}NO_2$ CP and (b) $Ca_2Al\text{-}NO_2$ BRM*10.6*. Reflections marked with ▪ correspond to $Al(OH)_3$ and reflection marked with * correspond to $CaCO_3$.

Table 5.1. A summary of the X-ray diffraction data for Ca_2Al-LDHs.

Sample	(002) Bragg Reflection			
	Position $2\theta/^o$	*d*/Å	FWHM/^{o}	Crystalline Domain Size/nm
$Ca_2Al\text{-}NO_3$ BRM 10.6	10.50	8.43	0.18	43.8
$Ca_2Al\text{-}NO_2$ BRM 10.6	11.67	7.58	0.33	23.9
$Ca_2Al\text{-}NO_2$ CP	11.69	7.57	0.26	30.4

FWHM = full width at half maximum, Scherrer equation ($CDS = K\lambda(\beta\cos\theta)^{-1}$), K = 0.89.[19]

CDS = Crystalline Domain Size, determined by Scherrer equation.

5.2.2 Infrared spectroscopy data

The FTIR spectra of the $Ca_2Al\text{-}NO_2$ BRM*10.6* and $Ca_2Al\text{-}NO_2$ CP are shown in Figure 5.3. IR absorptions represent the stretching vibrations of the hydroxyl groups in the inorganic layers and of the interlayer water between 3700-3000 cm^{-1}. The O-H bending vibration of interlayer water can be observed at 1644 cm^{-1}. The $Ca_2Al\text{-}NO_2$ samples also exhibited absorptions at 1322 and 1225 cm^{-1} which confirm the presence of intercalated NO_2^- anions corresponding to the N-O stretching of $NaNO_2$ in Figure 5.3(a).[10-12] The IR data confirm that the interlayer nitrite ions can be further oxidised to nitrate ions which the N-O stretching of nitrate appears at 1413 and 1365 cm^{-1}. The interlayer oxidation of the $Ca_2Al\text{-}NO_2$ LDHs occurred because the nitrite anion can be oxidised to nitrate under mild conditions.[12]

$$HNO_2 \rightleftharpoons H^+ + NO_2^-;\ pK_a = ca.\ 3.3 \text{ at } 18\ ^oC \qquad \textbf{Equation 5.7}$$

$$NO_3^- + 3H^+ + 2e^- \rightleftharpoons HNO_2 + H_2O;\ E^0 = +0.94\ V \qquad \textbf{Equation 5.8}$$

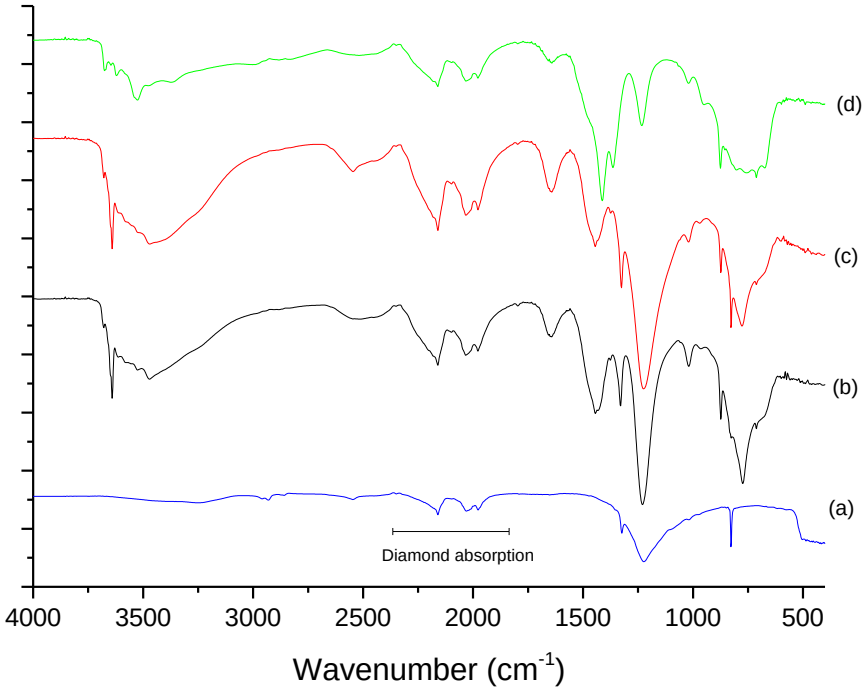

Figure 5.3. IR spectra of (a) $NaNO_2$, (b) $Ca_2Al\text{-}NO_2$ CP, (c) $Ca_2Al\text{-}NO_2$ BRM*10.6*, and $Ca_2Al\text{-}NO_2$ CP after 1 month post-synthesis.

5.2.3 Electron microscopy and energy-dispersive X-ray spectroscopy study

TEM imaging reveals that the average diameter of the $Ca_2Al\text{-}NO_2$ BRM*10.6* platelets is *ca.* 220 nm with a hexagonal-shaped platelet morphology (Figure 5.4(a) and 5.4(b)). The SEM images of $Ca_2Al\text{-}NO_2$ CP also show a platelet morphology with a much larger 15 micron particle size (Figure 5.4(c) and 5.4(d)). The results indicate that the co-precipitation method produces LDH particles of much larger size than the reverse micelle emulsion synthesis.

It was found that nitrite intercalated LDH particles formed are significantly bigger in comparison to the size of nitrate intercalated LDH formed via an equivalent reverse micro-emulsion approach. They are well-dispersed and more uniform platelets with 137.3 ± 23.8 nm size in the case of the $Ca_2Al\text{-}NO_3$ BRM*10.6*. Energy-dispersive X-ray spectroscopy has been used to analyse Ca/Al atomic ratio of LDH materials. Chemical composition of the materials was summarised in Table 5.2.

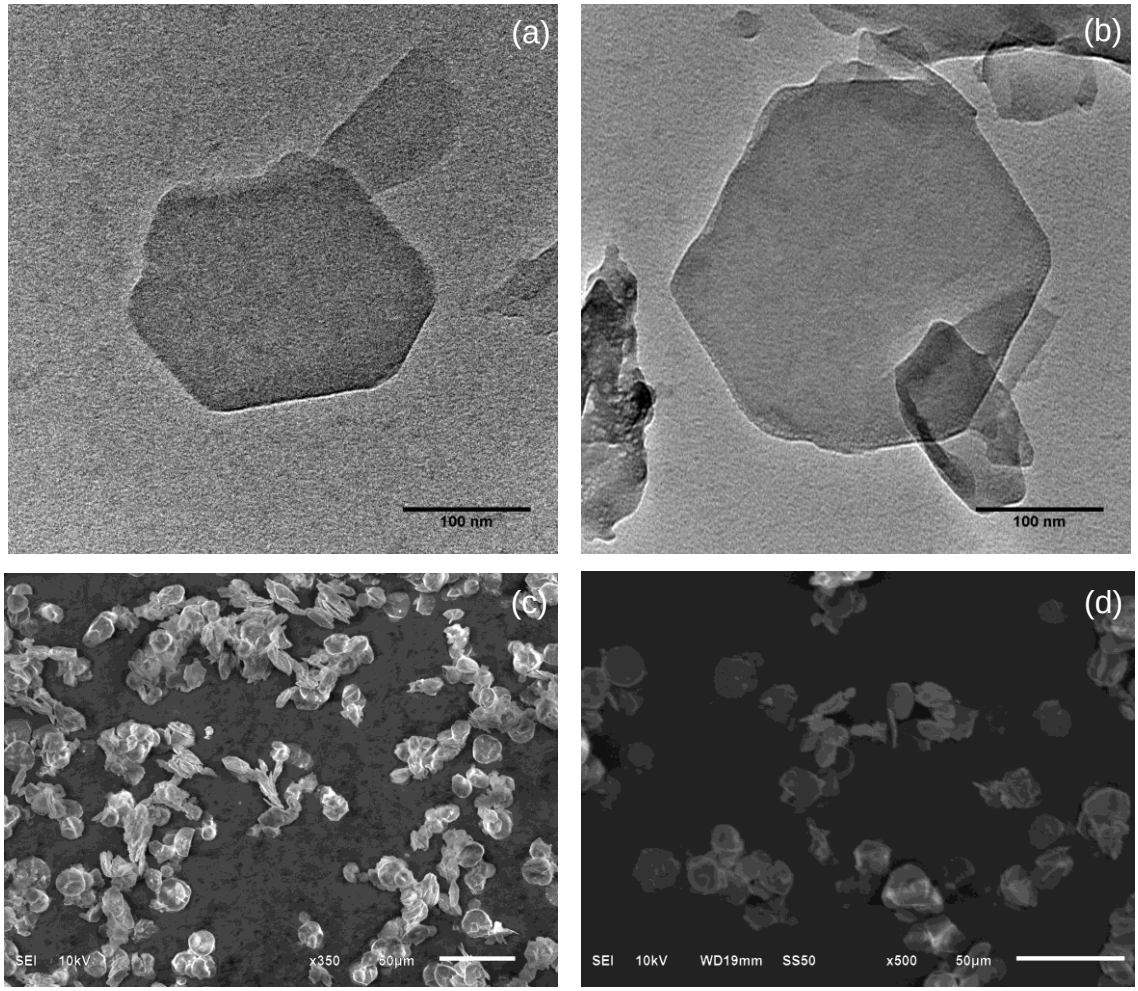

Figure 5.4. (a), and (b) TEM images of $Ca_2Al\text{-}NO_2$ BRM*10.6*; (c) and (d) SEM images of $Ca_2Al\text{-}NO_2$ CP.

5.2.4 Thermogravimetric and elemental analysis

Thermogravimetric analysis (TGA) was used to determine the thermal stability of $Ca_2Al\text{-}NO_2$ BRM*10.6* (Figure 5.5). On increasing the temperature from room temperature up to 150°C, cointercalated water is lost from LDH samples. The loss of water from dehydroxylation of the LDH layers occurs between 150 – 400°C. Nitrite starts to decompose above 400°C, giving a final product as a mixture of metal oxide, Mayenite ($Ca_{12}Al_{14}O_{33}$), and Lime (CaO).

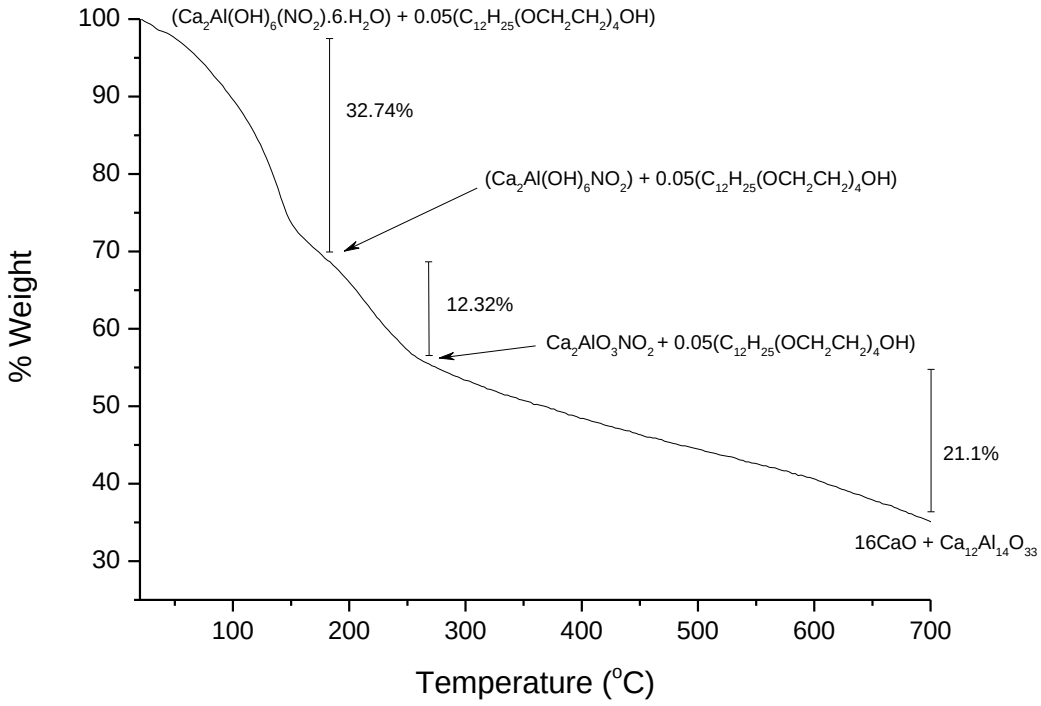

Figure 5.5. TGA plot for Ca_2Al-NO_2 BRM*10.6* from 30 to 700°C.

Table 5.2. Summary of the elemental analysis data of Ca_2Al-NO_2 BRM*10.6* and Ca_2Al-NO_2 CP.

	Chemical composition, obs. (calc.); (wt%)				
	Ca/Al mol ratio*	C	H	N	Formula
Ca_2Al-NO_2 BRM*10.6*	1.9	3.2 (3.1)	5.2 (5.3)	4.0 (3.7)	$Ca_2Al(OH)_6NO_2$•$6H_2O$ 5.0 % BRIJ30
Ca_2Al-NO_2 CP	1.95	0.0 (0.0)	4.2 (4.0)	4.7 (4.5)	$Ca_2Al(OH)_6NO_2$•$3.1H_2O$

* Determined by Energy-dispersive X-ray spectroscopy technique.

$C_{12}H_{25}(OCH_2CH_2)_4OH$ = polyethylene glycol dodecyl ether (BRIJ30) used as a surfactant to control micelles in reverse emulsion.

5.3 Effects of nitrite intercalated Ca_2Al-LDHs on cement hydration

To study the effect of adding nitrite intercalated Ca_2Al-LDHs on the hydration chemistry of cement, the time-dependence of the elastic modulus (G') of cement has been investigated using the ultrasound shear-wave reflection equipment (Section 7.2.2). The LDHs made using the co-precipitation technique were mixed with cement and water (at water to cement ratio as 0.4) by a high speed mixer and the resulting cements compared to cement with different amount of calcium nitrite added. For example, 16%wt of a nitrite intercalated Ca_2Al-LDH was added to give the amount of nitrite anion as 3.55%wt, which is comparable to the amount of calcium nitrite added to cement. Nitrite additives normally used in the range 1 – 4%wt.[2, 13] The storage elastic modulus of a range of cement samples was measured as a function of time (Figure 5.6). The effect of the nitrite intercalated Ca_2Al-LDHs was compared to a pristine cement sample and cement sample added calcium nitrite. From the inspection of the time-dependence of *G'*, the setting point of the cement mixture can be determined when *G'* starts to increase from zero. The setting point data are summarised in Table 5.3.

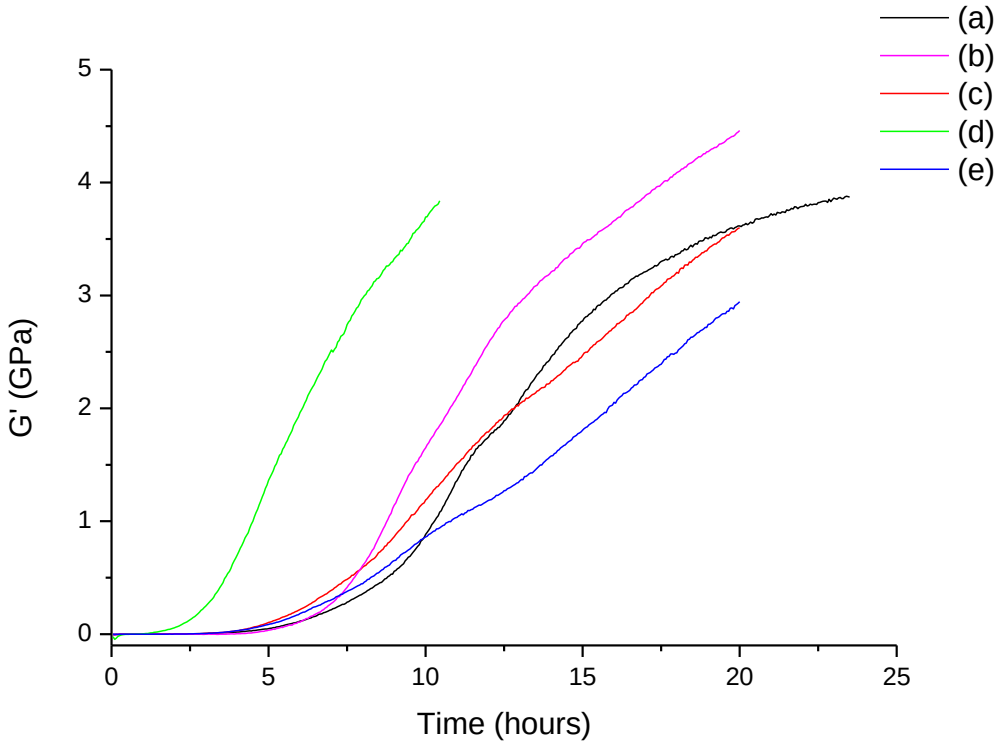

Figure 5.6. A plot of the storage elastic modulus (G') of various cement samples as a function of hydration time (a) Portland cement, (b) Portland cement with 2 %wt of Ca_2Al-NO_3, (c) Portland cement with 1 %wt $Ca(NO_2)_2$, (d) Portland cement with 4%wt $Ca(NO_2)_2$, and (e) Portland cement with 16%wt of Ca_2Al-NO_2 CP containing 3.55%wt nitrite.

Table 5.3. The setting point of cement samples determined from the storage elastic modulus data.

Cement samples	Setting point (hours)
SKK cement	3.3
SKK cement with added 2 %wt $Ca_2Al\text{-}NO_3$	2.3
SKK cement with added 1 %wt $Ca(NO_2)_2$	2.4
SKK cement with added 4 %wt $Ca(NO_2)_2$	0.9
SKK cement with added 16 %wt $Ca_2Al\text{-}NO_2$	3.3

[#]Error in the setting point measurement is thought to be *ca.* 0.1 hour.

From the elastic modulus data, it can be postulated that nitrite intercalated LDH can accelerate hydration reactions of cement compared with plain cement. However, for cement samples with the same nitrite loading (by weight), the LDH additive is obviously less efficient than calcium nitrite as an accelerator, as can be seen by the reaction time of hydration reactions at points of a given elastic modulus. Nitrite can behave as an accelerator, as nitrate (formed by oxidation of nitrite) forms a salt with the aluminate phase in cement.[14, 15] Presumably the nitrite intercalated LDH can activate the hydration reaction less effectively than calcium nitrite because of controlled release from LDH structures. In addition, the total amount of nitrite released from Ca_2Al-LDH systems is less than nitrite from calcium nitrite in cement.

Comparing with nitrite intercalcated LDHs, nitrate intercalated LDHs can increase the hydration reaction more effectively at lower loading. Calcium nitrate is normally used as an accelerator, as it can react with the calcium aluminate phase in cement to produce nitrate AFm (or called nitrate monosulfate, $Ca_3Al_2O_6.Ca(NO_3)_2.10H_2O$).[15] This structure is similar to nitrate intercalated LDH. It can be assumed that nitrate can release into solution by itself or by ion exchange with other ions in the system. Nitrate can then react directly with the calcium aluminate phase to produce more nitrate AFm into the hydration system. The original LDH layers could be seed crystals for nucleation of hydrated cement growth. It therefore takes more time for nitrite released from Ca_2Al-LDH to be oxidised to nitrate before reacting with the calcium aluminate phase.

Nitrite intercalated LDHs are now ready to be investigated for corrosion inhibition behaviour in concrete. However for corrosion inhibitor testing, the American Society for Testing and Materials (ASTM) has created a standard test method for an electrical indication of concrete's ability to resist chloride ion penetration (ASTM C1202) and a standard test method for the corrosion potentials of uncoated reinforcing steel in concrete (ASTM C876),[16, 17] These tests require very specialised equipment which is not available at present.

5.4 Conclusions

Two new nitrite intercalated Ca_2Al-LDHs have been synthesised *via* both the co-precipitation and the reverse micro-emulsion method. The XRD patterns of Ca_2Al-NO_2 BRM*10.6* and Ca_2Al-NO_2 CP have been indexed to a hexagonal cell where $a = b = 5.74$ Å and $c = 15.1$ Å. Both materials have a hexagonal-platelet morphology as observed by electron microscopy. The average diameter of Ca_2Al-NO_2 BRM*10.6* platelets is *ca.* 220 nm while Ca_2Al-NO_2 CP platelets have a much larger 15 micron particle diameter. Compared to nitrate intercalated LDH synthesised via a reverse microemulsion at the same as water to surfactant ratio, the crystalline domain size is lower for nitrite Ca_2Al-LDH, as calculated from the X-ray diffraction data. However, the average diameter of nitrite intercalated Ca_2Al-LDH particles is larger than of nitrate-intercalated Ca_2Al-LDH.

The reverse microemulsion technique using a non-ionic surfactant is a suitable way for obtaining uniform and size controllable LDH nanoparticles. Furthermore, it appears that a broad anionic selection for LDH synthesis is possible using non-ionic surfactant is used to tailor shape and size of micelles. Although, small amounts of surfactant adsorption onto the particle surface were confirmed by elemental analysis, the intercalation of surfactant into LDH framework is not observed. Use of non-ionic surfactants can reduce the adsorption and intercalation of surfactant on surface or into LDH layers compared to anionic surfactants, which can interfere the crystal growth of particles inside the microemulsion droplets. However, the amount of product formed *via* reverse microemulsion needs to be improved by scale-up in order to extend the physical testing.

The physical properties of Portland cement samples with additive nitrate- and nitrite-intercalated Ca_2Al-LDH made using co-precipitation have been studied by ultrasound shear-wave reflection. The elastic modulus data indicate that nitrite-intercalated LDH is less effective as an accelerator compared to calcium nitrite due to controlled release from LDH structures. However, nitrate-intercalated Ca_2Al-LDH can perform as accelerator more efficiently. Due to lack of equipment for corrosion resistance testing, cement samples with nitrite intercalated Ca_2Al-LDH have not yet been investigated for the concrete's ability to resist chloride ion penetration and corrosion potentials of uncoated reinforcing steel in concrete following the ASTM standard C1202 and C876, respectively.

5.5 References

1. T. A. Buerge, U. Maeder, F. Wombacher and B. Marazzani, US Patent 5,605,571, 1997.
2. K. Sideris and A. Savva, *Cement and Concrete Composites*, 2005, **27**, 277-287.
3. V. Saraswathy and H.-W. Song, *Building and Environment*, 2007, **42**, 464-472.
4. M. Collepardi, R. Fratesi, G. Moriconi, L. Coppola and C. Corradetti, *Admixtures for Concrete: Improvement of Properties*, 1990, **5**, 310.
5. J. Tritthart and P. Banfill, *Cement and Concrete Research*, 2001, **31**, 1093-1100.
6. J. P. Broomfield, *Corrosion of Steel in Concrete: Understanding, Investigation and Repair*, Spon Press, 1997.
7. M. Balonis and F. P. Glasser, *Journal of the American Ceramic Society*, 2011, **94**, 2230-2241.
8. K. Sagoe-Crentsil and F. P. Glasser, *Cement and Concrete Research*, 1993, **23**, 785-791.
9. S. Xu, Z. Chen, B. Zhang, J. Yu, F. Zhang and D. G. Evans, *Chemical Engineering Journal*, 2009, **155**, 881-885.
10. P. A. Brooksby and A. J. McQuillan, *The Journal of Physical Chemistry C*, 2010, **114**, 17604-17609.
11. J. Axe, *Physical Review*, 1968, **167**, 573.
12. N. Thomas, G. Pradeep Kumar and M. Rajamathi, *Journal of Solid State Chemistry*, 2009, **182**, 592-596.
13. L. Andion, P. Garcés, F. Cases, C. Andreu and J. Vazquez, *Cement and Concrete Research*, 2001, **31**, 1263-1269.
14. H. Justnes and E. Nygaard, *Concrete*, 2010, **44**, 34.
15. H. Justnes and E. C. Nygaard, *Cement and Concrete Research*, 1995, **25**, 1766-1774.
16. A. C876-09, American Society for Testing and Materials West Conshohocken, 2009.
17. M. Ormellese, M. Berra, F. Bolzoni and T. Pastore, *Cement and Concrete Research*, 2006, **36**, 536-547.

Chapter 6: Surfactant Directed Synthesis of Calcium Aluminum Layered Double Hydroxides Nanoplatelets

6.1 Introduction

LDHs have been investigated for a number of applications such as: catalysts[1-3], scavengers of pollutant anions[4] and as additives for polymer application.[5] However, in recent years the use of LDHs in the synthesis of inorganic/organic nanocomposites has created a new emerging class of material. Synthetic LDHs offer elemental precision and chemical homogeneity for the inorganic phase and LDH/polymer nanocomposites exhibit improved mechanical, thermal, and gas barrier properties and reduced flammability. Hydrocalumite-like structures (Ca_2Al-LDHs) are by-products of cement hydration. The LDHs have been studied and modified to play several important roles in cement including reducing water requirement or accelerating cement hydration.[6-9] Therefore, it is of interest to see if hydrocalumite-like materials (Ca_2Al-LDHs) could be prepared in a suitable form in order to act as an attractive component with enhanced physical properties in polymer nanocomposites.

In order to achieve a high dispersion of the Ca_2Al-LDHs in polymer nanocomposites,[10-13] a synthesis of highly dispersed Ca_2Al-LDH with hydrophobic surfaces is required. The reverse micelles microemulsion technique is one of the effective methods for tailoring size, shape, composition and morphology of particles synthesised at the nano-scale.[14-19] There are many types of nanoparticles synthesised *via* this method such as metal nanoparticles (Pt, Rh, Pd, and Ir), metal oxide nanoparticles, and other inorganic nanoparticles (CdS and $CaCO_3$).[15, 16, 20, 21] O'Hare *et al.* reported the first synthesis of a layered double hydroxide (LDH) using this approach.[22-24] In the present study, we report the synthesis of nanosized calcium aluminium LDHs in dodecylsulfate reverse micelles.

6.2 Synthesis of calcium aluminium LDHs via reverse microemulsion

Spherical reverse micelles are formed by addition of an aqueous solution of sodium dodecylsulfate to isooctane. Butan-1-ol is added to facilitate the formation of reverse micelles (Figure 6.1). The aqueous phase confined in the micelles can then act as a "nanoreactor" for LDH synthesis. The nucleation and growth of the LDH platelets only occurs within the encapsulated water droplets. The size of the water pools can be controlled by the amount of water added and this is defined by the water to surfactant molar ratio w = $[H_2O]/[DDS]$. An aqueous solution containing $Ca(NO_3)_2 \bullet 4H_2O$ and $Al(NO_3)_3 \bullet 9H_2O$ is then added in the mixture followed by a solution of $NaNO_3$ and NaOH. The pH value of the mixture is then adjusted to around 11.5 and the mixture is heated at 75^oC under nitrogen for 5 days. Five different inverse micelle compositions were studied, with w ratios = 10, 20, 30, 40, and 50. These conditions prepared the LDHs denoted as Ca_2Al-DDS RMn (n = 10, 20, 30, 40 and 50).

The solid products were isolated by centrifugation and then washed with a mixture of ethanol and water. The fresh gel-like samples after centrifuge separation were stirred in the mixture of ethanol and water (1:1) until the gel-like structure changed to a free flowing microcrystalline powder.

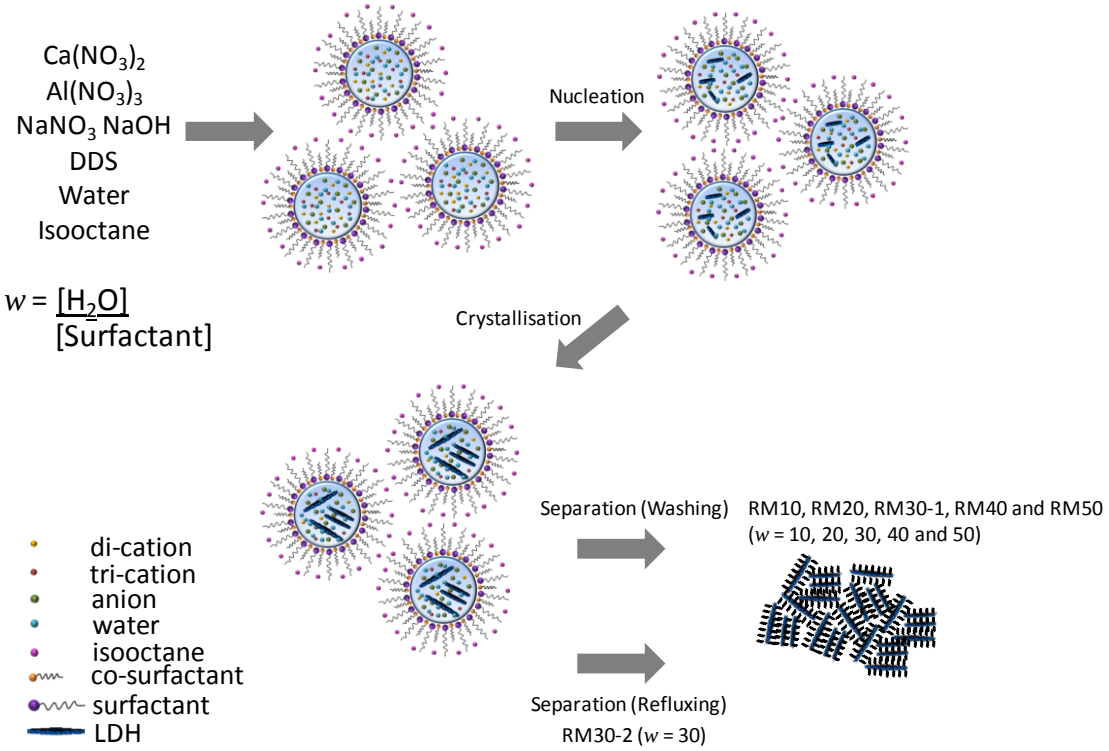

Figure 6.1. Schematic illustration of the nucleation and growth of LDHs in a reverse micelle system.

6.2.1 X-ray diffraction data

The X-ray diffraction patterns of Ca_2Al-DDS RM*n* (*n* = 10, 20, 30, 40 and 50), are shown in Figure 6.2. The XRD data for Ca_2Al-DDS RM*n* (*n* = 10, 20, 30 and 40) exhibit a low angle, broad Bragg reflection that can be indexed as the (003) Bragg reflection corresponding to a dodecylsulfate intercalated LDH. The position for the (003) reflection varies slightly from sample to sample and corresponds to a d-spacing of between 23.7 and 26.0 Å (Table 6.1). It is believed that the slight variation in the observed interlayer spacing may be due to slight variations in the amount of cointercalated water within the layers. The observed interlayer spacing is consistent with a monolayer orientation of the dodecylsulfate anions with a 69^o anti parallel angle between dodecylsulfate chain axis and the Ca_2Al-LDH layer (Figure 6.3) this packing arrangement as previously observed by Lagaly and co-workers for dodecylsulfate intercalated ZnCr-LDHs.[25] We observe a significant increase in the peak width at half maximum of the (003) Bragg reflections as the *w* value increases (Table 6.1). Application of the Scherrer equation would suggest that the crystalline domain length along the *c*-axis decreases from *ca*. 21.3 nm for Ca_2Al-DDS RM10 to *ca*. 13.8 nm for Ca_2Al-DDS RM40. The crystalline domain length derived from the *00l* reflection line widths must be related to the thickness or stacking order of these

platelet samples. Given all the assumptions in the Scherrer analysis these values are in very good agreement with the measured thickness of the samples using AFM (*vide infra*). We do not observe any (003) Bragg reflection intensity for Ca_2Al-DDS RM50 which suggests that this sample may be composed of too few layers to give sufficient coherence along the *c*-axis, AFM measurement indeed shows that these samples are on the order of a few layers thick. However, for these platelets we observe low intensity (110) and (200) Bragg reflections at $2\theta = 31.1°$ and $36.1°$ corresponding to an $a = b = 5.74$ Å which is typical for a unit cell of Ca_2Al-LDH.

In all samples, we also observed an additional series of much narrower Bragg reflections that can be indexed to the unit cell corresponding to crystalline $Ca(DDS)_2$ at $2\theta = 3.0°$ indicated in Figure 6.2. Comparison of the integrated intensity of the 00*l* reflections of $Ca(DDS)_2$ compared to the LDH phases suggests that the amount of $Ca(DDS)_2$ is relatively small in all the samples except for Ca_2Al-DDS RM10. The relative amount of $Ca(DDS)_2$ present in the sample decreases as the water to surfactant molar ratio increases. The formation of the highly insoluble $Ca(DDS)_2$ may be promoted in the smaller water pools at low *w* due to a higher dodecylsulfate anion concentration.

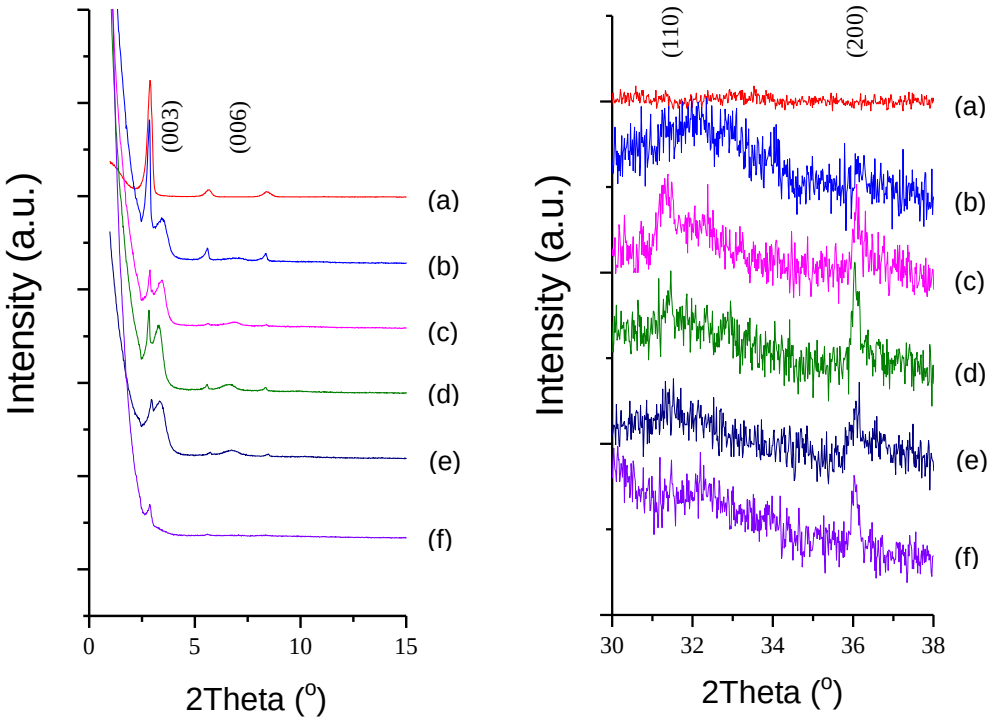

Figure 6.2. XRD data of (a) $Ca(DDS)_2$, (b) Ca_2Al-DDS RM10, (c) Ca_2Al-DDS RM20, (d) Ca_2Al-DDS RM30, (e) Ca_2Al-DDS RM40, and (f) Ca_2Al-DDS RM50.

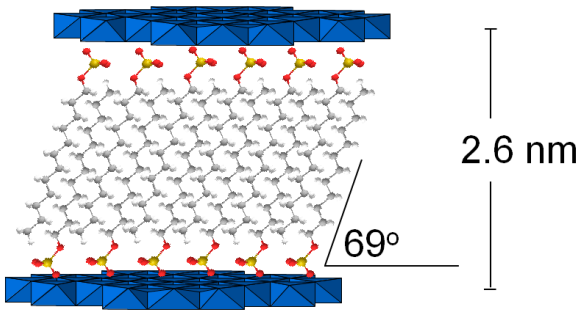

Figure 6.3. A proposed schematic representation of the dodecylsulfate anions intercalated in Ca_2Al-DDS RM*n*.

Table 6.1. A summary of the X-ray diffraction data for Ca_2Al-DDS RM*n* (*n* = 10-50).

Sample	003 Bragg Reflection			
	Position 2θ/°	*d*/Å	FWHM/°	Crystalline Domain Size (nm)
Ca_2Al-DDS RM10	3.73	23.7	0.37	21.4
Ca_2Al-DDS RM20	3.58	24.7	0.27	29.4
Ca_2Al-DDS RM30	3.40	25.9	0.36	21.7
Ca_2Al-DDS RM40	3.40	26.0	0.57	13.8
Ca_2Al-DDS RM50	NA	NA	NA	_

NA = not observed, FWHM = full width at half maximum, Scherrer equation (CDS = $K\lambda(\beta\cos\theta)^{-1}$), K = 0.89.[26] CDS = Crystalline domain size

It was found that careful control of the post synthesis processing is required in order to obtain high quality samples. The XRD data for Ca_2Al-DDS RM*n* samples change upon successive washings (Figure 6.4). For example, for Ca_2Al-DDS RM30 and RM50 no Bragg reflections associated with $Ca(DDS)_2$ are observed on first isolation of the LDHs but reflections due to this phase grow in steadily upon prolonged stirring in a water/ethanol mixture. The data is consistent with dodecylsulfate anions and Ca^{2+} leaching from the Ca_2Al-DDS RM*n* nanoplatet which then generates insoluble $Ca(DDS)_2$. The process may be driven by the very low solubility constant (K_{sp}) of $Ca(DDS)_2$ (3.72×10^{-10} mol^3l^{-3} at 25°C).[27] The water to surfactant ratio also has an influence on the rate of leaching and concomitant formation of $Ca(DDS)_2$. Similar phenomena have been reported on the exfoliation of LDHs by post-synthesis methods such as ultrasonication technique.[28-30]

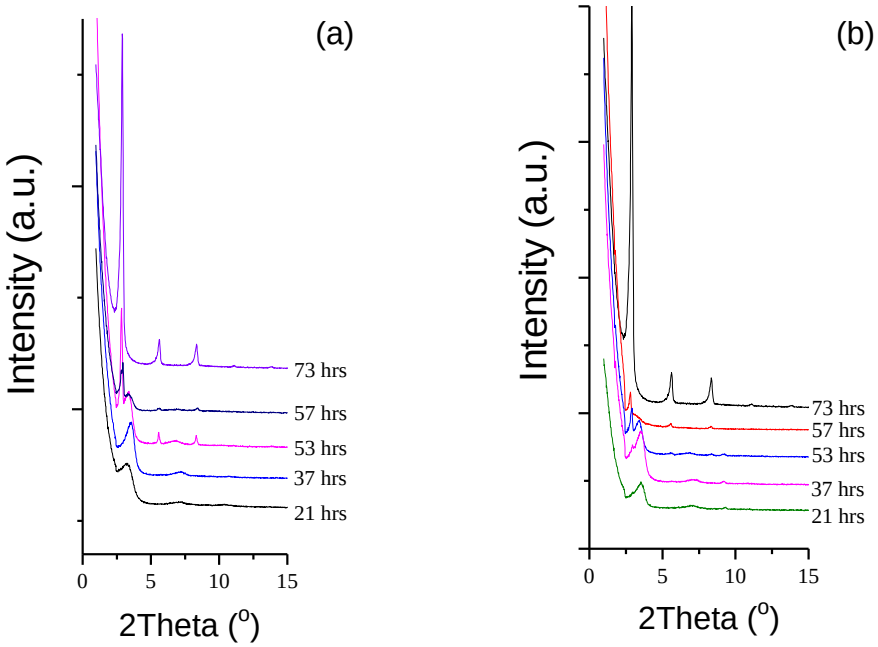

Figure 6.4. The XRD patterns of (a) the Ca_2Al-DDS RM30 and (b) Ca_2Al-DDS RM50 after washing in for 21 to 73 hrs.

6.2.2 Thermogravimetric and elemental analysis

Samples of Ca_2Al-DDS RM*n* (*n* = 10-50) were analysed by TGA in order to determine the intercalated water content, and the processes by which their decomposition occurs at elevated temperatures. A typical TGA plot is shown in Figure 6.5. Ca_2Al-DDS RM20 decomposes by the well-established route observed for most LDHs intercalated with organic molecules. In the first step, the cointercalated water is lost at temperatures up to 150°C, leaving a dehydrated LDH (calculated loss 4.1%, observed loss 4.2%). This is then followed by the loss of water from the hydroxide layers, and loss of SO_x from the intercalated DDS anion. The final steps, from around 350°C onwards, is a combination of the further decomposition of the guest and the dehydration of the hydroxide layers, resulting in a final product that is a mixture of Mayenite ($Ca_{12}Al_{14}O_{33}$, JCPDS 01-070-2144), and Lime (CaO, JCPDS 00-048-1467) (calcd. 37.0 %, obsvd. 35.0 %).

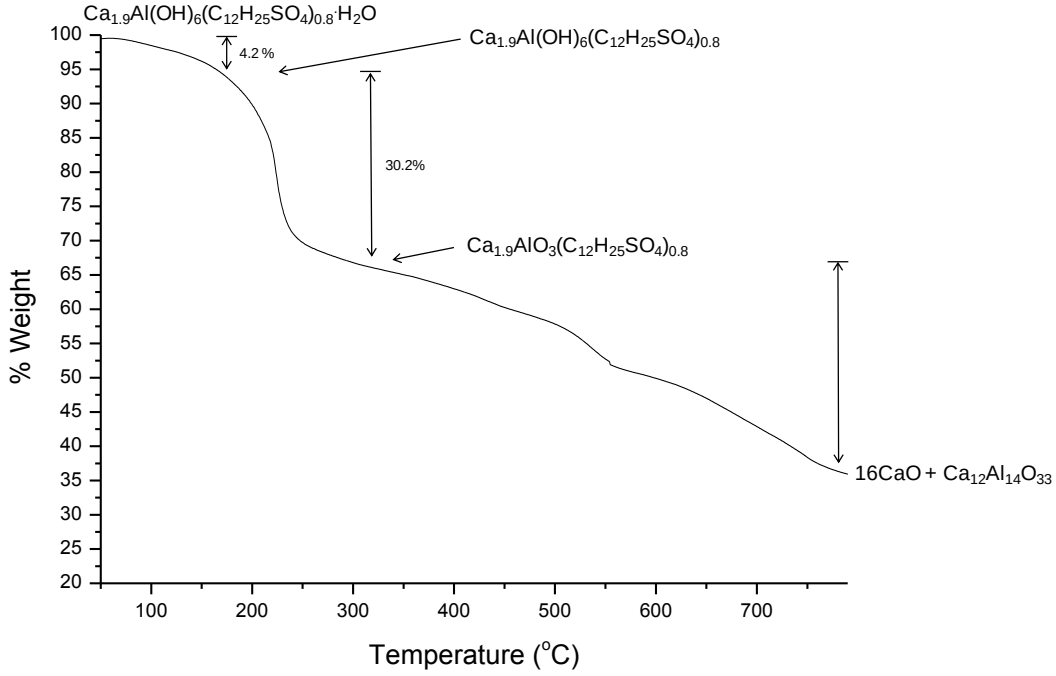

Figure 6.5. TGA plot for Ca_2Al-DDS RM20 from 20 to 800°C.

The elemental microanalysis data is shown in Table 6.2, since the XRD clearly shows that the samples contain varying amounts of $Ca(DDS)_2$ we have attempted to obtain best fits by including $Ca(DDS)_2$ as 2nd impurity phase in the calculated figures. The microanalysis data for Ca_2Al-DDS RM50 suggests that this material contains significantly less DDS than the other samples and we can only assume that the extremely small platelet size for this LDH results in being unable to retain sufficient DDS anions.

Table 6.2. Elemental composition and proposed formula of Ca_2Al-DDS RM*n* series.

	Chemical composition, obs. (calc.); (wt%)			
Ca_2Al-DDS RM*n*	C	H	N	Formula
RM10	30.0(30.7)	5.6(6.9)	0.0(0.0)	$Ca_{1.95}Al(OH)_6(C_{12}H_{25}SO_4)_{0.9}•H_2O$[a]
RM20	26.2(26.5)	4.1(6.5)	0.0(0.0)	$Ca_{1.9}Al(OH)_6(C_{12}H_{25}SO_4)_{0.8}•H_2O$
RM30	30.4(29.3)	6.3(6.7)	0.0(0.0)	$Ca_2Al(OH)_6(C_{12}H_{25}SO_4)•H_2O$
RM40	29.1(29.3)	6.7(6.7)	0.0(0.0)	$Ca_2Al(OH)_6(C_{12}H_{25}SO_4)•H_2O$
RM50	17.8(18.4)	4.2(5.2)	0.0(0.0)	$Ca_{1.69}Al(OH)_6(C_{12}H_{25}SO_4)_{0.39}$

[a] $Ca_2Al(OH)_6(C_{12}H_{25}SO_4)•H_2O$ would have calc (C%) = 29.2%. We have attributed the excess carbon to an additional 10% $Ca(C_{12}H_{25}SO_4)_2$ as a 2nd phase (which is observed in the XRD).

6.2.3 Infrared spectroscopy data

FTIR spectra of the Ca_2Al-DDS RM*n* series all exhibit broad absorptions bands over the range 3700-3000 cm^{-1} with peak maxima around 3443 cm^{-1} due to the stretching vibration of hydroxyl groups of the inorganic layers and the interlayer water (Figure 6.6). The absorption peaks of asymmetric stretching vibration of CH_3, asymmetric stretching vibration of CH_2 and symmetric stretching vibration of CH_2 of the dodecyl chain appear at 2957, 2919 and 2850 cm^{-1}, respectively. Weak absorption bands at 1637 and 965 cm^{-1} are assigned to bending vibrations of the interlayer co-intercalated water molecules. The absorption bands at 1470, 1417 and 1379 cm^{-1} are attributed to CH_2 scissoring, asymmetric bending and symmetric bending. The asymmetric ν(S=O) stretching and symmetric ν(S=O) stretching[31, 32] modes are observed at 1213 and 1060 cm^{-1} and the ν(O=S=O) bending is observed at 720 cm^{-1}. The IR spectrum of a bulk sample of Ca_2Al-NO_3 LDH exhibits absorptions at 1415 and 1348 cm^{-1} due to the presence of intercalated NO_3^- anions (Figure 6.6(g)), these absorptions are not observed in the IR spectrum of the Ca_2Al-DDS RM*n* phases.

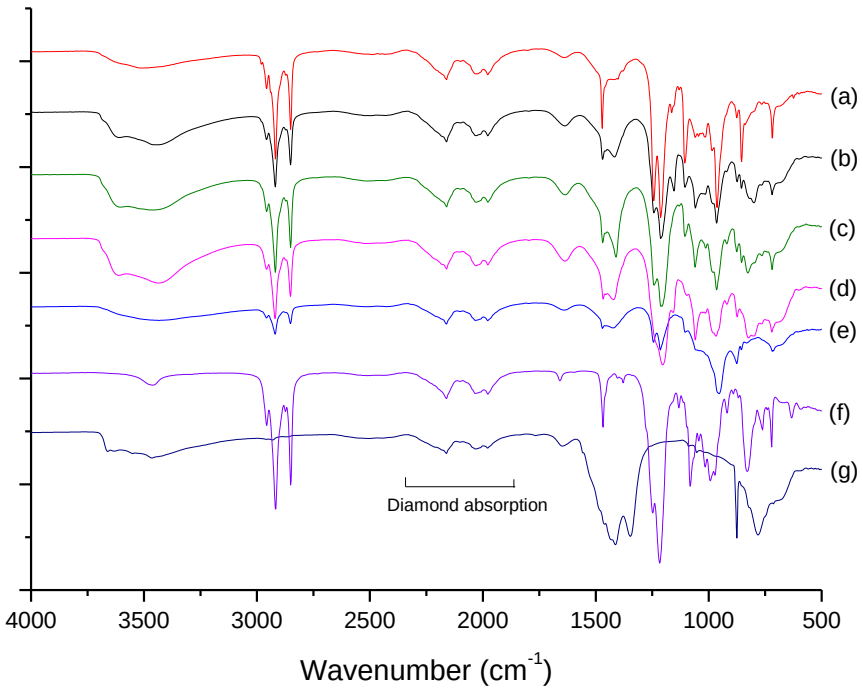

Figure 6.6. IR spectra (a) - (e) a series of Ca_2Al-DDS RM*n* (*n* = 10, 20, 30, 40 and 50), respectively, (f) Sodium dodecylsulfate, and (g) Ca_2Al-NO_3.

6.2.4 Electron microscopy study

Transmission Electron Microscopy (TEM) has been used to investigate the platelet size, size distribution and the morphology of the Ca_2Al-DDS RM*n* particles. The TEM images of a sample of Ca_2Al-DDS RM10 (Figure 6.7(a)) show aggregates of platelet morphology particles with a size distribution around 18.7 ± 2.7 nm. The TEM images of Ca_2Al-DDS RM20 (Figure 6.7(b)) revealed a well-dispersed platelet sample. By measuring the sizes of approx. 50 particles we determined that these dispersed platelets have a very narrow size distribution with an average diameter of 51.9 ± 3.2 nm. The average diameter of Ca_2Al-DDS RM30 platelets was found to be 42.1 ± 7.1 nm. The TEM images of Ca_2Al-DDS RM50 indicate that the materials are composed of very thin platelets. However, the images cannot be used to determine the thickness of Ca_2Al-DDS RM*n* particles since no edge-on particle structure could be found during TEM observation. These data directly show that the water:DDS ratio in the reverse micelles has an influence on the platelet size.[18]

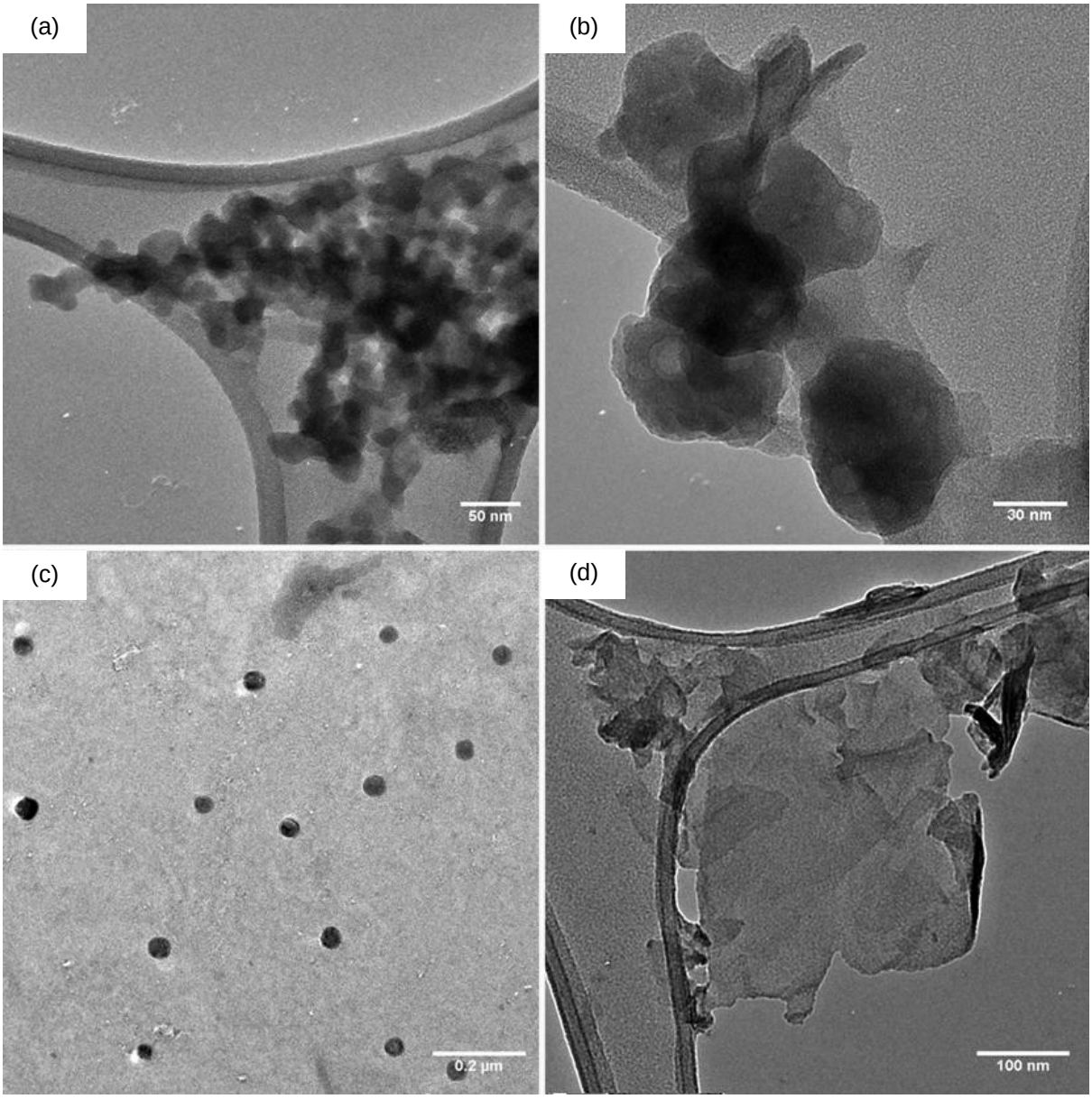

Figure 6.7. TEM images at low magnification of Ca_2Al-DDS RM samples (a) Ca_2Al-DDS RM10, (b) Ca_2Al-DDS RM20, (c) Ca_2Al-DDS RM30, and (d) Ca_2Al-DDS RM50.

6.2.5 Atomic Force Microscopy (AFM) study

AFM has been successfully employed to study the topographic morphologies of the Ca_2Al-DDS RM*n* particles. In particular, this technique is ideal for determining the thickness of platelet samples. Dilute dispersed samples of Ca_2Al-DDS RM*n* were deposited on a highly oriented pyrolytic graphite (HOPG) surface. Figure 6.8 shows examples of the AFM scans for Ca_2Al-DDS RM30 and Ca_2Al-DDS RM50. The cross-sectional scans show that Ca_2Al-DDS RM30 platelets have a thickness of 8 nm. The particles have a diameter of *ca*. 50 nm which is in good agreement with the TEM data.

An 8 nm thick platelet is consistent with a three layer model for Ca_2Al-DDS RM30 (Figure 6.8(e)). For Ca_2Al-DDS RM50, the AFM data suggests the thickness of the particles to be around 5 nm with a diameter of *ca*. 100nm. The thickness agrees well with the simulation of a two layer model for Ca_2Al-DDS RM50 (Figure 6.8(f)). Assuming a circular disk-like morphology these platelets have aspect ratios (top surface:thickness) of 330 and 2150 nm respectively.

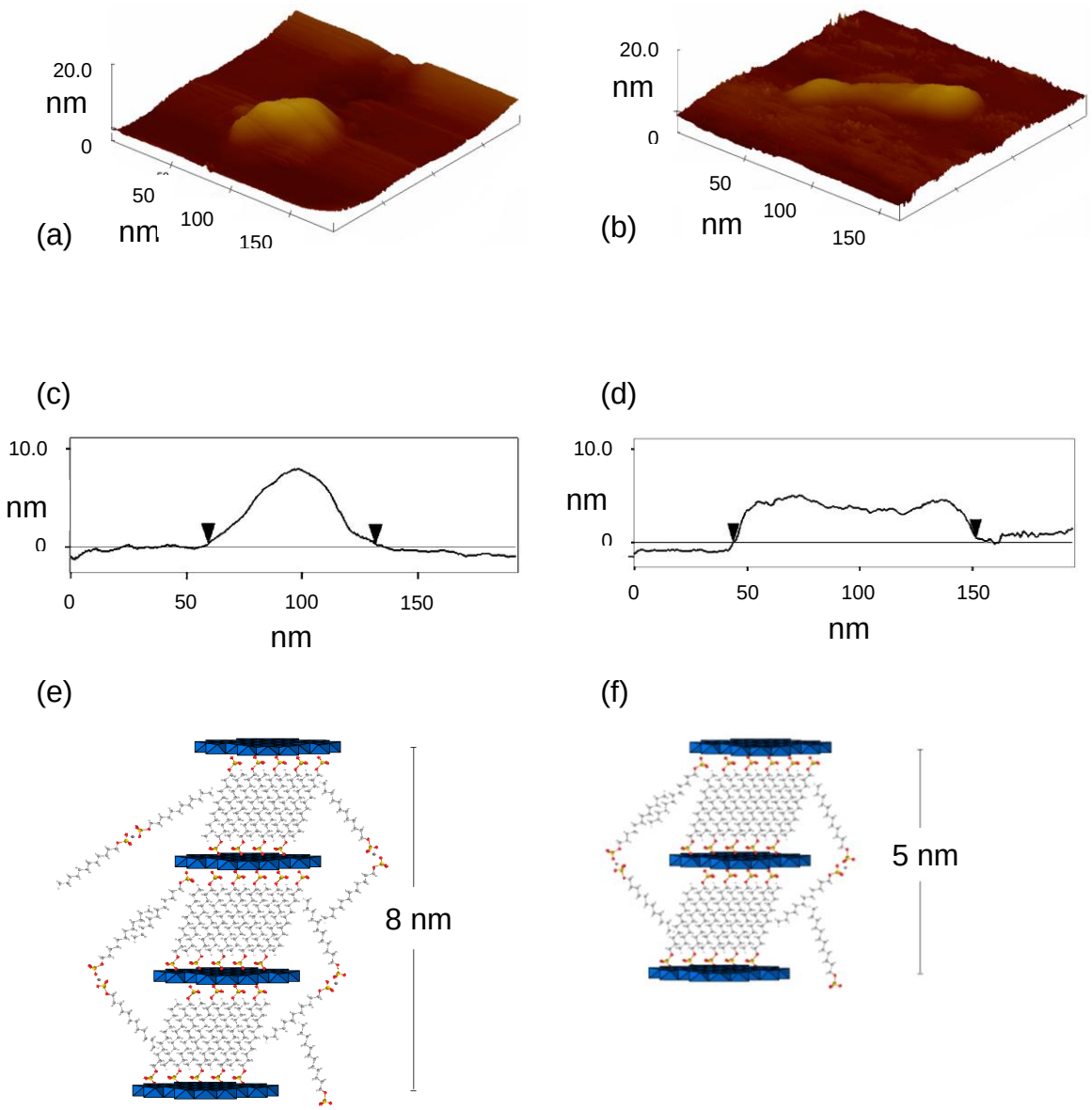

Figure 6.8. Three-dimensional AFM images of (a) Ca_2Al-DDS RM30, (b) Ca_2Al-DDS RM50; the cross-sectional image of (c) Ca_2Al-DDS RM30, (d) Ca_2Al-DDS RM50; and the structure model of schematic representations of the structures of (e) Ca_2Al-DDS RM30 and (f) Ca_2Al-DDS RM50.

6.3 A study of washing effect on the particle size and morphology

Remarkable structural difference arises from the different washing procedures required to remove the excess surfactant. Figure 6.9(a) shows an image for a Ca_2Al-DDS RM30 sample refluxed in ethanol. It is composed of hexagonal platelets with the maximum width around 50 nm. The contrast profile (Figure 6.9(c)) along the line observed the width of 6.10 Å, in close agreement with the rhombohedral unit cell parameters ($a = b = 5.74$ Å) for $Ca_2Al(OH)_6Cl{\bullet}2H_2O$.[33] By comparison, the round morphology was found for the Ca_2Al-DDS RM30 sample after stirring in a mixture of water and ethanol (Figure 6.10(b)). The difference in diameter of the Ca_2Al-DDS RM30 from the two different washing methods is negligible. The TEM results suggest that the separation method has an effect on the morphology of Ca_2Al-DDS RM*n* particles. Treatment of the products with ethanol and heat can facilitate more crystalline particles and protect dodecylsulfate leaching from the interlayers.

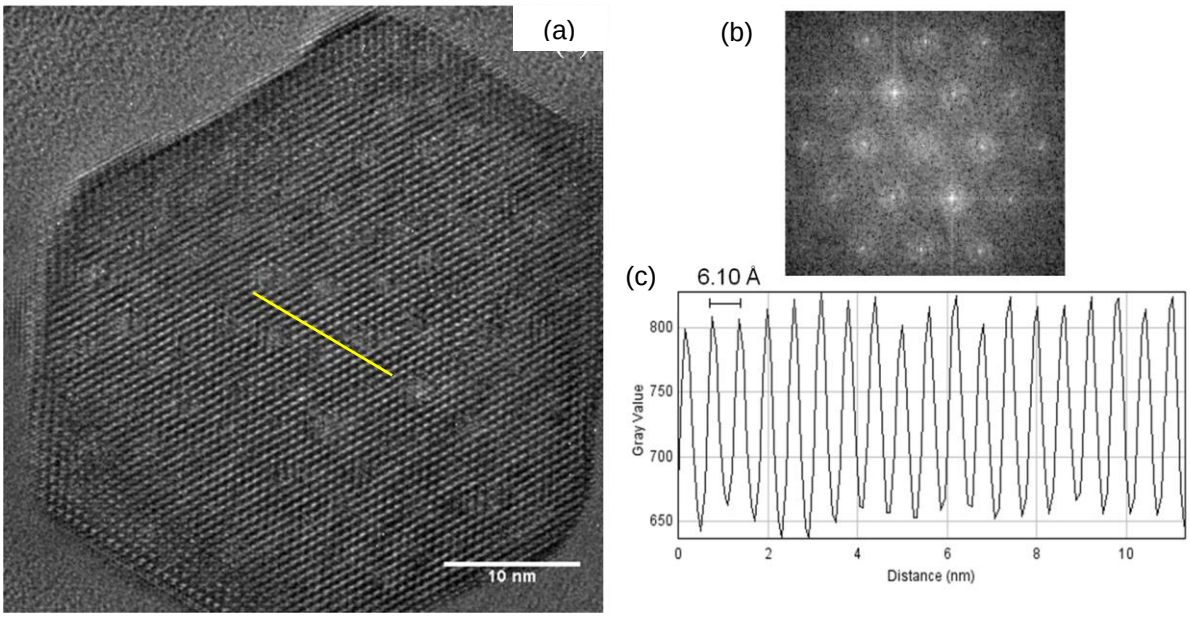

Figure 6.9. (a) TEM image of Ca_2Al-DDS RM30 refluxed in a mixture of ethanol and water, (b) Fast Fourier Transform analysis (FFT), and (c) the contrast profile of the TEM image (a).

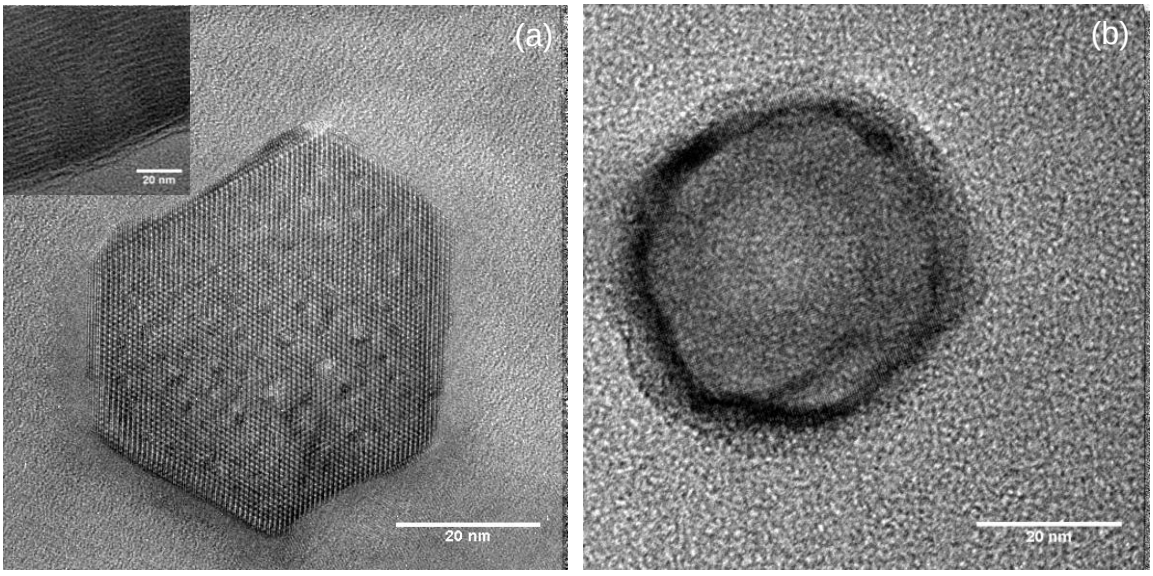

Figure 6.10. TEM images of Ca_2Al-DDS RM30 (a) refluxed in a mixture of ethanol and water, and (b) stirred in a mixture of ethanol and water.

The XRD patterns (Figure 6.11) show that there are strong reflections when Ca_2Al-DDS RM30 particles are dispersed in ethanol under reflux conditions to remove excess surfactant. It is generally acknowledged that the d-spacing (d_{003}) of a DDS-intercalated LDH sample is about 27.2 Å.[25] Similarly in the case of Ca_2Al-DDS RM30 dispersed in a mixture of water and ethanol without refluxing, the d-spacing (d_{003}) is around 25.0 Å.

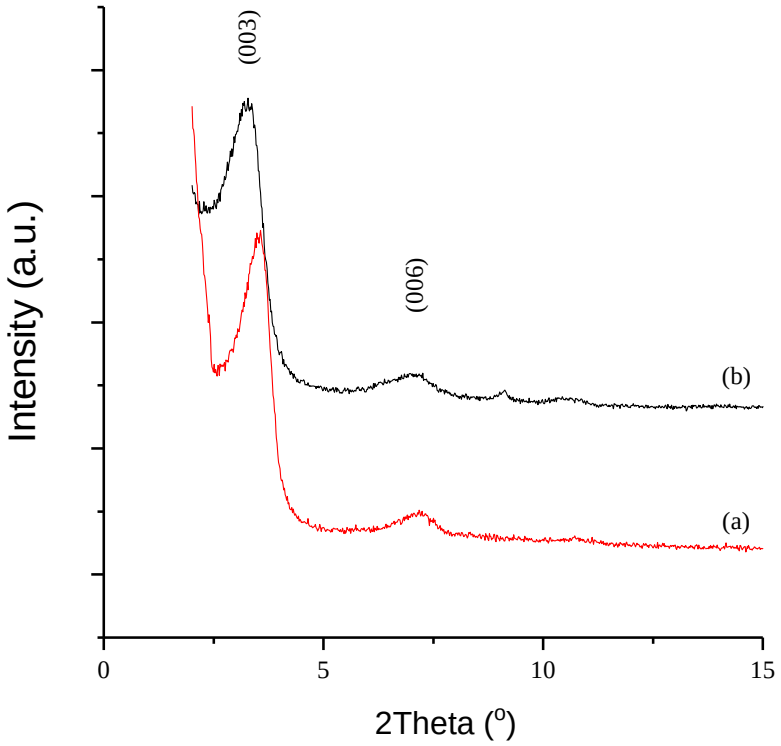

Figure 6.11. XRD patterns of the Ca_2Al-DDS RM30 samples following (a) refluxing in a mixture of ethanol and water, and (b) stirring in a mixture of ethanol and water.

6.4 Conclusions

The synthesis of dispersed, uniform nanoplatelet $[Ca_2Al(OH)_6DDS]\bullet H_2O$ LDHs is reported. The use of dodecylsulfate (DDS) derived reverse micelles allows us to control the nucleation and growth of these platelets by varying the water:DDS ratio. Nanoplatelets ranging from 18 nm to 100 nm in diameter have been isolated with an extremely narrow size distribution. These platelets are exceptionally thin and in the limiting case we have images of $[Ca_2Al(OH)_6DDS]\bullet H_2O$ with a thickness of *ca*. 5nm which correspond to 2 stacking repeats. This study is further evidence that this approach has the potential to produce homogeneous dispersions of LDH nanosheets in organic matrices in order to prepare inorganic/polymer nanocomposites.

6.5 References

1. V. Rives and M. a. Angeles Ulibarri, *Coordination Chemistry Reviews*, 1999, **181**, 61-120.
2. F. Zhang, X. Xiang, F. Li and X. Duan, *Catalysis surveys from Asia*, 2008, **12**, 253-265.
3. I. Cota, E. Ramírez, F. Medina, J. E. Sueiras, G. Layrac and D. Tichit, *Applied clay science*, 2010, **50**, 498-502.
4. Y.-H. Chuang, C.-H. Liu, Y.-M. Tzou, J.-S. Chang, P.-N. Chiang and M.-K. Wang, *Colloids and Surfaces A: Physicochemical and Engineering Aspects*, 2010, **366**, 170-177.
5. V. Realinho, M. Antunes, D. Arencón, A. Fernández and J. Velasco, *Journal of Applied Polymer Science*, 2009, **111**, 2574-2583.
6. A. N. Christensen, T. R. Jensen and J. C. Hanson, *Journal of Solid State Chemistry*, 2004, **177**, 1944-1951.
7. L. Raki, J. Beaudoin and L. Mitchell, *Cement and concrete research*, 2004, **34**, 1717-1724.
8. L. Raki, J. Beaudoin, R. Alizadeh, J. Makar and T. Sato, *Materials*, 2010, **3**, 918-942.
9. T. Matschei, B. Lothenbach and F. Glasser, *Cement and Concrete Research*, 2007, **37**, 118-130.
10. F. Leroux and J.-P. Besse, *Chemistry of Materials*, 2001, **13**, 3507-3515.
11. O. Wilson Jr, T. Olorunyolemi, A. Jaworski, L. Borum, D. Young, A. Siriwat, E. Dickens, C. Oriakhi and M. Lerner, *Applied Clay Science*, 1999, **15**, 265-279.
12. F. R. Costa, M. Abdel-Goad, U. Wagenknecht and G. Heinrich, *Polymer*, 2005, **46**, 4447-4453.
13. L. Qiu, W. Chen and B. Qu, *Polymer degradation and Stability*, 2005, **87**, 433-440.
14. I. Capek, *Advances in Colloid and Interface Science*, 2004, **110**, 49-74.
15. J. Eastoe, M. J. Hollamby and L. Hudson, *Advances in Colloid and Interface Science*, 2006, **128–130**, 5-15.
16. A. P. Herrera, O. Resto, J. G. Briano and C. Rinaldi, *Nanotechnology*, 2005, **16**, S618.
17. K. Holmberg, *Journal of Colloid and Interface Science*, 2004, **274**, 355-364.
18. M. A. Lopez-Quintela, *Current opinion in colloid & interface science*, 2003, **8**, 137-144.
19. L. Qi, *Encyclopedia of Surface and Colloid Science. Second Edition. New York: Taylor & Francis*, 2006, 6183.
20. T. Hyeon, *Chemical Communications*, 2003, 927-934.
21. Y. Lee, J. Lee, C. J. Bae, J. G. Park, H. J. Noh, J. H. Park and T. Hyeon, *Advanced Functional Materials*, 2005, **15**, 503-509.
22. G. Hu and D. O'Hare, *Journal of the American Chemical Society*, 2005, **127**, 17808-17813.
23. G. Hu, N. Wang, D. O'Hare and J. Davis, *Journal of Materials Chemistry*, 2007, **17**, 2257-2266.
24. C. J. Wang, Y. A. Wu, R. M. Jacobs, J. H. Warner, G. R. Williams and D. O'Hare, *Chemistry of Materials*, 2010, **23**, 171-180.
25. H. Kopka, K. Beneke and G. Lagaly, *Journal of Colloid and Interface Science*, 1988, **123**, 427-436.
26. V. Drits, J. Srodon and D. Eberl, *Clays and Clay Minerals*, 1997, **45**, 461-475.

27. U. Hornfeck, M. Gradzielski, K. Mortensen, C. Thunig and G. Platz, *Langmuir*, 1998, **14**, 2958-2964.
28. Q. Wu, A. Olafsen, O. B. Vistad, J. Roots and P. Norby, *Journal of Materials Chemistry*, 2005, **15**, 4695-4700.
29. M. Adachi-Pagano, C. Forano and J.-P. Besse, *Chemical Communications*, 2000, **0**, 91-92.
30. L. Li, R. Ma, Y. Ebina, N. Iyi and T. Sasaki, *Chemistry of Materials*, 2005, **17**, 4386-4391.
31. Q. Tao, J. Yuan, R. L. Frost, H. He, P. Yuan and J. Zhu, *Applied clay science*, 2009, **45**, 262-269.
32. P. Zhang, G. Qian, H. Cheng, J. Yang, H. Shi and R. L. Frost, *Spectrochimica Acta Part A: Molecular and Biomolecular Spectroscopy*, 2011, **79**, 548-553.
33. L. Vieille, I. Rousselot, F. Leroux, J.-P. Besse and C. Taviot-Guého, *Chemistry of Materials*, 2003, **15**, 4361-4368.

Chapter 7: Experimental details

7.1 Analytical techniques

7.1.1 Reflection X-ray powder diffraction

X-ray powder diffraction (XRD) patterns were investigated by using a PANalytical X'Pert Pro diffractometer, with a solid state X'Celerator detector. Cu Kα radiation ($\lambda(K\alpha_1)$ = 1.5406 Å, $\lambda(K\alpha_2)$ = 1.5444 Å; λ_{avg} = 1.5419 Å) was used and operated in reflection mode, at 40 kV and 40 mA. Stainless steel plates were used as sample holders. The divergence slit was set automatic mode. The anti-scatter slit was changed to be suitable for series of samples. A 2^o slit was used for analysing samples synthesised *via* co-precipitation method and ion-exchange reaction. 1/16, and $1/32^o$ slits were chosen for samples made by reverse microemulsion synthesis.

7.1.2 Elemental analysis

Elemental analyses were carried out by Elemental Analysis Service, School of Human Sciences, Science Centre, London Metropolitan University. C, H and N contents were calculated by quantitatively digesting the sample through oxidative combustion. Other elements were analysed using inductively coupled plasma (ICP) atomic emission spectroscopy carried out by Dr. Gareth Williams, University College London.

7.1.3 Thermogravimetric analysis

Thermogravimetric analyses were carried out on a Netzsch STA 409PC. Each sample (*ca.* 20 mg) was placed in an alumina crucible and heated at a rate of 5 ºC min^{-1} between 30 ºC and 700 ºC under a flow of nitrogen gas.

7.1.4 Scanning electron microscopy

Scanning electron microscopy (SEM) has been investigated by using a JEOL SEM JEM-6610LV microscope at Harwell research complex. The microscope is fitted with an energy dispersive X-ray spectrometer (EDX) which was used to analyse elements and

composition of elements in samples. SEM samples were prepared on aluminium SEM stubs with carbon tape before sputtering with platinum for 120 seconds.

7.1.5 Transmission electron microscopy

Transmission electron microscopy was employed using a JEOL JEM-2100 LaB6 microscope at an accelerating voltage of 120 kV at Harwell Research Complex, and a JEOL 4000EX microscope at the Department of Materials, University of Oxford, at an accelerating voltage of 80 kV for low magnification imaging and at 400kV for high resolution.

For sample preparation, approximately 20 mg of sample was suspended in 1 ml of absolute ethanol by sonication for 10 minutes. Lacey carbon and continuous carbon film coated copper grids were then dipped into the solution.

7.1.6 Atomic force microscopy

Samples were dispersed in absolute ethanol with sonication at the same concentration as for TEM sample preparation, and deposited on highly ordered pyrolytic graphite (HOPG, 10 x 10 x 3 mm from Agar) or silicon wafers (Agar) using a spin-coating technique at 3000 rpm for 30 seconds. AFM imaging was performed using a Nanoscope Multimode system (Digital Instruments, UK) with a 4909E piezoelectric scanner by a tapping mode at room temperature.

7.1.7 Infrared spectroscopy

IR spectra were recorded on a Biorad FTS 6000 FTIR spectrometer using a high performance DuraSamplIR II diamond accessing an attenuated total reflectance mode in the range of 4000 – 400 cm^{-1} with 256 scans at 4 cm^{-1} resolution. The strong absorption between 2500 – 1667 cm^{-1} is from the DuraSamplIR II diamond surface.

7.1.8 UV-VIS spectroscopy

The UV spectra for kinetics studies of anion release were recorded using a double-beam PerkinElmer Lambda 750S spectrophotometer under study in the 200 to 700 nm region with an 1 nm data interval and 266.75 nm/min scan speed. The UV-VIS source was generated by a D2 lamp and a W lamp between the ranges of 200 – 319.20 nm, and 319.20 – 700 nm, respectively. Samples were prepared in an UV quartz cuvette with a 10 mm layer thickness. For absorbance calibration, series of standard solution were prepared covering the range of the expected concentration of additive release. In addition, the absorbances of LDHs in HCl solution were used to calibrate the complete release of LDHs (100 % release).

7.2 *In situ* techniques

7.2.1 Energy dispersive X-ray diffraction

In situ time-resolved energy dispersive X-ray diffraction (EDXRD) was investigated at the Diamond Light Source using beamline I12. The ten-cell carousel was made to study the mechanism of the hydration of cement in comparison to a series of cement samples with additive-intercalated Ca_2Al-LDHs [$Ca_2Al(OH)_6X{\bullet}6H_2O$, Ca_2Al-X LDHs], and to study anion release from LDHs. The carousel was designed by Dr. Andrew Jupe, University of Oxford, and Dr. Thomas Connolley, a senior beamline scientist for beamline I12, Diamond Light Source. Each cell in the ten-cell carousel was made to fit culture tubes with a 12 mm external diameter. An image of the ten-cell carousel is shown in Figure 7.1. The carousel was rotated at a speed of 0.5 rpm and held for 20 seconds per cell to supply X-ray radiation with 4 seconds exposure time.

Figure 7.1. The ten-cell carousel on station I12.

The wavelength selected was 0.224 Å (55.35 keV), calibrated to a CeO_2 standard. The measurements were collected on a Thales Pixium detector (Pixium RF4343) which is a 2D detector with 148 x 148 μm^2 pixel size, a 2880 pixels x 2881 pixels active area with 430 x 430 mm^2 active area size. The angular range covered was 0.6 – 8.4 °2θ, taking account of the presence of a beam stop this corresponds to a *d*-spacing range of 1.53 – 21.39 Å. The raw data from the Pixium detector were analysed by using the Fit2D program. This program was further used to fit Gaussian function to the reflections observed. The peak positions and widths were recorded and an automatic Gaussian fitting routine was used to obtain peak areas of the Bragg reflections.[1] These values are subsequently converted to the extent of reaction at time t, $\alpha(t) = I_{hkl}(t)/I_{hkl}^{max}$, where $I_{hkl}(t)$ is the intensity given peak at time t, and I_{hkl}^{max} is the maximum intensity of this peak.

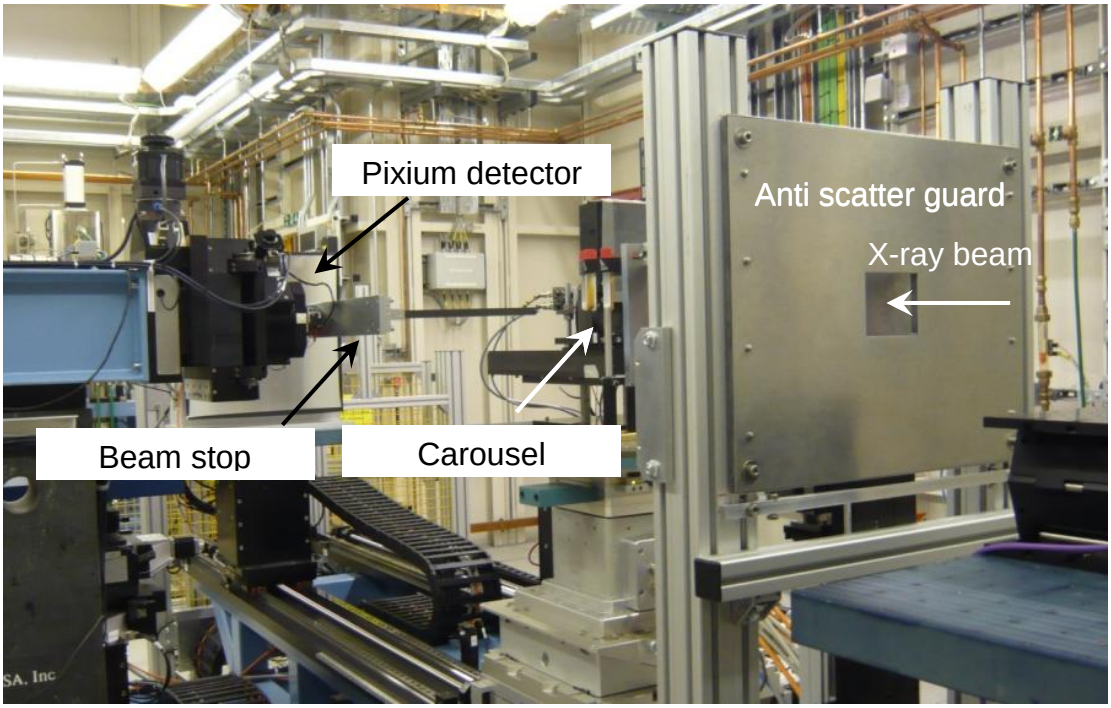

Figure 7.2. The setup on beamline I12 at Diamond Light Source.

7.2.2 Ultrasound shear-wave reflection

Ultrasound shear-wave reflection was one of techniques used to study the hydration reactions of cement in terms of reactivity by measuring changes in the physical properties of cement, such as stiffness. The change of physical properties can be inferred from the reflected wave. A digitizer generates a pulse in the ultrasound frequency range, which is transferred to a quartz sample stage (Figure 7.3(a)).[2-5] When ultrasound pulses passing through the quartz contact the cement sample, some of signals get absorbed into the cement while the rest are reflected back into the quartz (Figure 7.3(b)). The reflected pulses are collected as raw data, and used to calculate the elastic modulus. Loss of amplitude and a phase shift of the reflected waves always occur as the hydration reaction develops (Figure 7.4). They were used as parameters to calculate elastic modulus using an equation shown below:

$$G' = Z_1^2 \frac{(1-r^2)^2 - 4r^2\sin^2\phi}{\rho(1-2r\cos\phi + r^2)} \qquad \textbf{Equation 7.1}$$

Where; G' = Elastic modulus Z_1 = impedance of quartz (substrate)

r = Loss of amplitude ϕ = Phase shift

ρ = Density of liquid phase

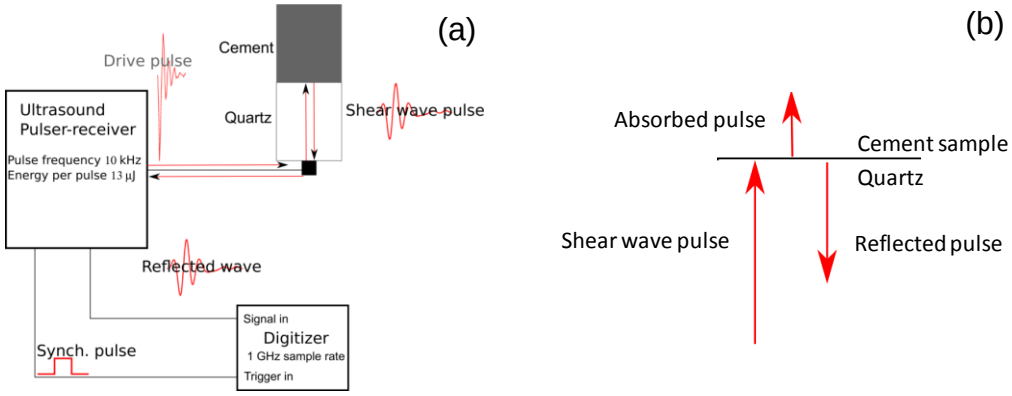

Figure 7.3. Schematic diagrams of (a) shear wave pulse contacting to sample, and (b) the ultrasound shear-wave reflection instrument.

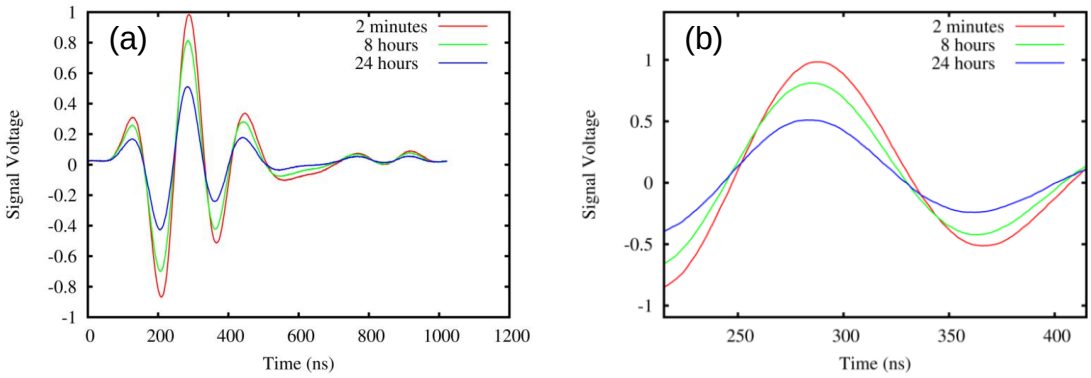

Figure 7.4. Ultrasound shear wave reflection data representing (a) loss of amplitude (*r)*, and (b) phase shift (ϕ) over time.

The Ultrasound shear-wave reflection instrument was designed and built by Dr. Andrew Jupe. Sample preparation is mentioned in Section 7.4.5.

The Ultrasound shear-wave reflection instrument was supplied X-ray radiation at station I12, Diamond Light Source to study the effect of nitrate-intercalated Ca_2Al-LDH ($Ca_2Al(OH)_6NO_3•6H_2O$, Ca_2Al-NO_3) on the elastic modulus and hydration of cement observed by the Ultrasound shear-wave reflection technique and *in situ* X-ray diffraction. SKK cement and SKK cement with 1% wt of Ca_2Al-NO_3 added were investigated at 35 ^oC for 24 hours to accelerate the hydration reactions. The image of a quartz sample stage with temperature control block exposed in the X-ray beam is shown in Figure 7.5.

Figure 7.5. An image of a quartz sample stage with temperature controlled block.

7.3 Experimental details for Chapter 2

The synthesis of novel doped variants of $[Ca_2Al(OH)_6]Cl•nH_2O$ by incorporating gallium in the LDH layers, $[Ca_2Ga_xAl_{(1-x)}(OH)_6]Cl•nH_2O$ ($Ca_2Ga_xAl_{(1-x)}$-Cl) LDH where x = 0, 0.05, 0.10, 0.15, 0.20, 0.30, 0.40, 0.50, 0.60, 0.70, 0.80, 0.90, and 1.00, were undertaken using the co-precipitation method.[6] 250 ml of a mixture of DI water and ethanol in a 2:3 ratio was prepared and adjusted to pH 4 using HCl solution, followed by 2M NaOH until pH 11.5 was reached. Separately, $CaCl_2•2H_2O$, $Al(NO_3)_3•9H_2O$, and $Ga(NO_3)_3•H_2O$ were mixed and added then to 10 ml of water. The amount of those salts was varied depending

on the amount of gallium doped into the LDHs designed (Table 7.1). After mixing, the solution was transferred into a glass Luer tip style syringe. This solution was then added into a water/ethanol mixture using a Semat A-99 syringe pump with a 1.59 $ml.hr^{-1}$ flow rate. pH was controlled to be at 11.5 ± 0.1 by adding 2M NaOH. The mixture was stirred continuously at 65 ^{o}C for 2 days. All solid products were isolated by vacuum filtration and washed extensively with deionised water to remove impurities, followed by a small amount of acetone to facilitate drying. The samples were left to dry under vacuum for *ca.* 2 hours. All products were characterised using XRD, SEM, and EDX. (with additional techniques then employed if appropriate)

Table 7.1. Experimental conditions employed to synthesise $[Ca_2Ga_xAl_{(1-x)}(OH)_6]Cl•nH_2O$.

x value in	Amount of precursors (g)		
$[Ca_2Ga_xAl_{(1-x)}(OH)_6]Cl•nH_2O$	$CaCl_2•2H_2O$	$Al(NO_3)_3•9H_2O$	$Ga(NO_3)_3•H_2O$
0	0.9703	1.2380	0
0.05	0.9703	1.1760	0.0422
0.10	0.9703	1.1141	0.0844
0.15	0.9703	1.0522	0.1266
0.20	0.9703	0.9903	0.1688
0.30	0.9703	0.8666	0.2532
0.40	0.9703	0.7428	0.3376
0.50	0.9703	0.6190	0.4220
0.60	0.9703	0.4952	0.5063
0.70	0.9703	0.3714	0.5907
0.80	0.9703	0.2476	0.6751
0.90	0.9703	0.1238	0.7595
1.00	0.9703	0	0.8439

7.4 Experimental details for Chapter 3

7.4.1 Starting materials

Nitrate intercalated Ca_2Al-LDH ($Ca_2Al(OH)_6(NO_3)•6H_2O$, Ca_2Al-NO_3 LDH) was synthesised using the co-precipitation method. 250 ml of 0.215M $NaNO_3$ was prepared and adjusted pH to 11.5 with 2M NaOH. 3.542 g of $Ca(NO_3)_2•4H_2O$ and 2.855 g of

$Al(NO_3)_3 \bullet 9H_2O$ were mixed in 20 ml of DI water. This precursor solution was transferred into the $NaNO_3$ solution dropwise. The pH of the mixture was controlled by adding 2M NaOH, and was mixed vigorously at room temperature for 16 hours. Vacuum filtration and washing extensively with deionised water was used to remove impurities. The LDHs were then washed with a small amount of acetone to facilitate drying, and left to dry under vacuum for approximately 4 hours. The samples were studied by X-ray diffraction, Infrared spectroscopy, and Thermogravimetric analysis.

7.4.2 Intercalation reactions

All ion-exchange reactions were carried out in round bottom flasks with a magnetic stirrer bar. 2.4 g of superplasticiser; sodium naphthalene sulfonate, sodium lignosulfonate, and sodium polyacrylate were added separately into deionised water. These solutions were adjusted to pH 11.5. The solutions containing the superplasticiser in each reaction was heated before adding 1.0 g of nitrate intercalated Ca_2Al-LDH ($Ca_2Al(OH)_6(NO_3) \bullet 6H_2O$, Ca_2Al-NO_3 LDH). All reactions were left at 40 ^oC for 16 hours. The superplasticiser-intercalated compounds were isolated by vacuum filtration and washed extensively with deionised water to remove impurities. They were then washed with a small amount of acetone to facilitate drying, and left to dry under vacuum for approximately 4 hours. All compounds were analysed by XRD, FTIR, SEM, EDS, NMR, TGA, and elemental analysis. Additional techniques were performed as required such as release tests employing UV and Ultrasound shear-wave reflection to study the release and the mechanical behaviours of the LDHs.

7.4.3 Release test

The series of superplasticiser-intercalated Ca_2Al-LDHs was introduced into various anionic solutions expected to appear in cement solution, and into real cement solution isolated from cement paste (water to cement ratio = 0.8) at various times. The amount of superplasticiser intercalated was controlled to match the concentration of commercial superplasticisers used in concrete applications (0.4 %wt of cement). The LDHs were added into the solutions prepared by adding a 3-fold excess of sodium carbonate, sodium sulfate, or sodium silicate to 5 ml of deionised water, separately. The release properties of the LDHs were studied and compared to the release behaviours of the LDHs in water at

pH 7 and water at pH 13.5 at different reaction times. The solutions were separated using centrifuge separation technique and analysed by UV/VIS spectroscopy at wavelengths between 200 and 700 nm. Solid samples from the separation were analysed by X-ray diffraction.

7.4.4 *In situ* X-ray diffraction studies

Superplasticiser-intercalated Ca_2Al-LDHs were prepared to study the kinetics and mechanism of the superplasticiser release from LDHs in sulfate and silicate anion solutions. 0.1 g of Ca_2Al-naphthalene sulfonate, Ca_2Al-lignosulfonate, and Ca_2Al-polyacrylate were prepared in culture tubes with a 1 mm tube thickness. Each LDH was mixed with 5 ml of silicate solution and 5 ml of sulfate solution separately. These solutions were prepared at the same concentration as used for release tests. After mixing, all samples were covered by screw caps and placed on the carousel. Each reaction was exposed to the X-ray beam and data was collected by a Pixium detector every 3 minutes with 4 seconds exposure time. All reactions were left to run for 10 hours.

A number of additive-intercalated Ca_2Al-LDHs were added to cement to study the mechanism of cement hydration using *in situ* X-ray diffraction. For sample preparation, 100 g of cement and additives were mixed with 40 g of water by a high speed mixer at 12,000 rpm for 30 seconds. The amount of additives added to each reaction is detailed in Table 7.2. Each cement paste was transferred into a culture tube with screw cap and placed on the cauorsel. All samples were exposed to X-ray radiation at room temperature for 15 hours.

Table 7.2. Experimental conditions employed to study the mechanism of cement hydration.

Additive	Amount of additives used (%wt in cement)
Ca_2Al-naphthalene sulfonate	0.4
Ca_2Al-lignosulfonate	0.4
Ca_2Al-polyacrylate	0.4
type D	0.4
PC6	0.4
Ca_2Al-OH	0.5
Ca_2Al-OH	1.0
Ca_2Al-OH	2.0

7.4.5 Ultrasound shear-wave reflection

Superplasticiser-intercalated Ca_2Al-LDHs were mixed with cement to study the mechanical properties of the cement. The amount of additives added was the same amount to that of the original superplasticisers calculated as 0.4 %wt of original superplasticisers in cement. 100 g of cement and superplasticiser was mixed with 40 g of water by a high speed mixer at 12,000 rpm for 30 seconds. The cement paste was transferred into a cylindrical tube connected to a quartz sample stage.

7.5 Experimental details for Chapter 4

A series of $Ca_2Al(OH)_6NO_3{\bullet}2H_2O$ (Ca_2Al-NO_3 LDHs) was prepared *via* reverse microemulsion method. For the Ca_2Al-NO_3 BRM*w* series (*w* = 1 – 20), 4 ml of butan-1-ol and polyethylene glycol dodecyl ether (Brij 30) was added to 200 ml of isooctane. The amount of polyethylene glycol dodecyl ether (Brij 30) was calculated to give a water to surfactant ratio in the range between 1 and 20 (denoted *w*). Reverse micelles could form upon adding 2 ml of $NaNO_3$/NaOH mixture. 3 ml aqueous mixtures containing 1.134 g of $Ca(NO_3)_2{\bullet}4H_2O$ and 0.9003g of $Al(NO_3)_3{\bullet}9H_2O$ were then introduced to the organic mixture. The mixture was mixed at room temperature overnight. All products were isolated by centrifuge separation and washed with a mixture of water and ethanol (ratio of 1:1).

For the series $Ca_2Al\text{-}NO_3$ TRM*w* (*w* = 49, 65, 98), the amount of reagents and solvent; butan-1-ol, isooctane, and the concentration of aqueous mixture of precursor solution in each reaction were controlled as employed for the series $Ca_2Al\text{-}NO_3$ BRM*w* except for the amount of octyl phenol ethoxylate (TritonX100). The amount of the surfactant was calculated to give water to surfactant molar ratios, *w* = 49, 65, and 98, which are over the range of critical micelle concentration (CMC). The procedure and condition followed were otherwise identical to the $Ca_2Al\text{-}NO_3$ BRM*w* syntheses.

The series of $Ca_2Al\text{-}NO_3$ BRM*w* and $Ca_2Al\text{-}NO_3$ TRM*w* were studied by X-ray diffraction, Infrared study, Thermogravimetric analysis, Elemental analysis, Transmission Electron Microscopy, and Atomic Force Microscopy to compare purity, crystallinity, size, and morphology of these materials with the $Ca_2Al\text{-}NO_3$ synthesised *via* co-precipitation and reverse microemulsion without surfactants.

7.6 Experimental details for Chapter 5

Nitrite intercalated Ca_2Al-LDHs have been studied to investigate whether nitrite can intercalate to LDHs which the material may be used as a smart multifunctional additive for cement applications, such as accelerator, and corrosion inhibitor. Two synthesis methods have been applied to acquire different particle size of LDHs.

$Ca_2Al\text{-}NO_2$ CP was made *via* co-precipitation. 0.6 g of NaOH and 0.1287 g of $Al(OH)_3$ were mixed in 250 ml of deionised water. 1.3662 g of $NaNO_2$ was added to the solution after the $Al(OH)_3$ had completely dissolved. 2.9062 g of 30 %wt $Ca(NO_2)_2$ solution was then added dropwise. This solution was stirred vigorously at room temperature for 3 days. The product was separated by vacuum filtration technique and then washed with a small amount of acetone to facilitate drying, and left to dry under vacuum for approximately 4 hours.

$Ca_2Al\text{-}NO_2$ BRM 10.6 was synthesised by reverse microemulsion technique. 4 ml each of butan-1-ol and polyethylene glycol dodecyl ether (Brij 30) were added to 200 ml of isooctane. Polyethylene glycol dodecyl ether with a water to surfactant ratio of 10.6 was added to organic solution. Aqueous solutions were prepared separately: 0.13 g of $Al(OH)_3$ and 1.37 g of $NaNO_2$ were mixed in 4.5 ml of 4M NaOH. The aqueous mixture was then

introduced to the organic solution dropwise followed by the addition of 2.9 g of 30 %wt of $Ca(NO_2)_2$ solution. The mixture was stirred vigorously at room temperature for 3 days. The product was separated from the mixture by centrifugation and washed with a mixture of water and ethanol (1:1).

Nitrite intercalated Ca_2Al-LDHs were fully characterised using X-ray diffraction technique, Transmission Electron Microscopy, Scanning Electron Microscopy, Energy-dispersive X-ray spectroscopy, Thermogravimetric, and elemental analysis, and physical tests of elastic modulus of additive-cement mixtures studied by Ultrasound Shear-wave reflection.

7.7 Experimental details for Chapter 6

The series of CaAl-DDS RM*n* (water to surfactant ratio, n = 10, 20, 30, 40, and 50) was synthesised *via* reverse microemulsion using sodium dodecylsulfate as emulsifier. 4 ml of butan-1-ol was added to 200 ml of isooctane. Sodium dodecylsulfate was employed into the mixture. The amount of the surfactant was calculated to give a water to surfactant ratios of w = 10, 20, 30, 40 and 50. Subsequently, 2 ml of 2.73M $NaNO_3$ and 4M NaOH mixture was then added to the organic solution and followed by the addition of 3 ml of 2.4M $Ca(NO_3)_2 \cdot 4H_2O$ and 0.8M $Al(NO_3)_3 \cdot 9H_2O$ mixture. The mixture was heated at 75 ^oC under a nitrogen atmosphere for 5 days. The solid product was isolated by centrifuge separation and then washed with a mixture of ethanol and water until the gel-like structure changed to a free flowing microcrystalline powder. All samples were fully characterised by X-ray diffraction, Thermogravimetric and elemental analysis, Infrared spectroscopy, Transmission Electron Microscopy, and Atomic Force Microscopy.

7.8 References

1. S. M. Clark, *J. App. Cryst.*, 1995, **28**, 646.
2. A. C. Jupe, A. P. Wilkinson and G. P. Funkhouser, *Cement and Concrete Research*, 2012.
3. Y. Akkaya, T. Voigt, K. V. Subramaniam and S. P. Shah, *Mat. Struct.*, 2003, **36**, 507-514.
4. T. Voigt, Z. Sun and S. P. Shah, *Cement and Concrete Composites*, 2006, **28**, 307-316.
5. T. Voigt, G. Ye, Z. Sun, S. P. Shah and K. van Breugel, *Cement and Concrete Research*, 2005, **35**, 858-866.
6. I. Rousselot, C. Taviot-Guého, F. Leroux, P. Léone, P. Palvadeau and J.-P. Besse, *Journal of Solid State Chemistry*, 2002, **167**, 137-144.

Appendix I: X-ray diffraction data for new compounds

I.i Data for Chapter 2

Table I.i: Indexing of $[Ca_2Al(OH)_6]Cl•1.1H_2O$ (Ca_2Al-Cl) and $[Ca_2Ga(OH)_6]Cl•2.7H_2O$ (Ca_2Ga-Cl) synthesised *via* a co-precipitation method.

h	***k***	***l***	**2Theta[obs]/°**	
			Ca_2Al-Cl	**Ca_2Ga-Cl**
0	*0*	*3*	11.40	11.34
0	*0*	*6*	22.80	22.76
1	*0*	*4*	23.51	23.28
1	*1*	*0*	31.85	30.69
1	*1*	*3*	33.31	32.78
0	*0*	*9*	34.40	NA
2	*0*	*2*	36.90	36.44
1	*1*	*6*	39.30	38.53
0	*2*	*4*	39.40	38.87
2	*0*	*5*	41.02	NA
1	*0*	*10*	42.58	42.55
2	*0*	*7*	45.28	44.94
1	*1*	*9*	46.94	46.80
2	*1*	*4*	50.91	50.32
0	*2*	*10*	53.60	53.40
3	*0*	*0*	55.35	54.54
3	*0*	*3*	56.65	55.87
0	*3*	*3*	56.65	55.87

NA = Not observed.

Table I.ii: Indexing of $[Ca_2Ga_xAl_{(1-x)}(OH)_6]Cl \bullet nH_2O$ ($Ca_2Ga_xAl_{(1-x)}$-Cl; $0.05 < x < 0.4$) synthesised *via* a co-precipitation method.

			$Ca_2Ga_xAl_{(1-x)}$-Cl (x) (2Theta[obs]/^{o})				
h	***k***	***l***	**0.05**	**0.1**	**0.2**	**0.3**	**0.4**
0	*0*	*3*	11.42	11.30	11.30	11.30	11.32
0	*0*	*6*	22.87	22.72	22.72	22.60	22.64
1	*0*	*4*	23.57	23.45	23.40	23.40	23.34
1	*1*	*0*	31.85	31.85	31.16	31.10	31.04
1	*1*	*3*	33.20	33.20	33.08	33.07	32.96
0	*0*	*9*	34.23	34.40	NA	NA	NA
2	*0*	*2*	36.90	36.90	36.79	36.73	36.69
1	*1*	*6*	39.28	39.30	38.85	38.73	38.71
0	*2*	*4*	39.30	39.30	39.18	39.11	39.07
2	*0*	*5*	41.02	41.01	40.90	40.89	40.80
1	*0*	*10*	42.43	42.43	42.55	42.42	42.46
2	*0*	*7*	45.28	45.28	45.26	45.12	45.18
1	*1*	*9*	46.94	46.94	46.91	46.91	46.88
2	*1*	*4*	50.91	50.91	50.91	50.80	50.78
0	*2*	*10*	53.60	53.60	53.65	53.49	53.46
3	*0*	*0*	55.35	55.35	55.27	55.16	55.08
3	*0*	*3*	56.50	56.50	56.46	56.44	56.33
0	*3*	*3*	56.50	56.50	56.46	56.44	56.33

NA = Not observed.

Table I.iii: Indexing of $[Ca_2Ga_xAl_{(1-x)}(OH)_6]Cl \bullet nH_2O$ ($Ca_2Ga_xAl_{(1-x)}$-Cl; $0.5 < x < 0.9$) synthesised *via* a co-precipitation method.

			$Ca_2Ga_xAl_{(1-x)}$-Cl (x) (2Theta[obs]/°)				
h	***k***	***l***	**0.5**	**0.6**	**0.7**	**0.8**	**0.9**
0	*0*	*3*	11.30	11.29	11.27	11.27	11.32
0	*0*	*6*	22.73	22.72	22.71	22.64	22.68
1	*0*	*4*	23.28	23.28	23.34	23.22	23.22
1	*1*	*0*	30.98	30.87	30.81	30.75	30.69
1	*1*	*3*	32.90	32.90	32.90	32.78	23.78
0	*0*	*9*	NA	NA	NA	NA	NA
2	*0*	*2*	36.60	36.55	36.50	36.46	36.44
1	*1*	*6*	38.68	38.64	38.59	38.55	38.53
0	*2*	*4*	39.00	38.96	38.90	38.87	38.87
2	*0*	*5*	40.78	40.74	40.69	40.61	NA
1	*0*	*10*	42.45	42.48	42.46	42.42	42.49
2	*0*	*7*	45.15	45.10	45.04	44.99	44.96
1	*1*	*9*	46.78	46.78	46.72	46.78	46.80
2	*1*	*4*	50.64	50.56	50.46	50.38	50.35
0	*2*	*10*	53.43	53.40	53.37	53.34	53.35
3	*0*	*0*	55.03	54.92	54.79	54.70	54.59
3	*0*	*3*	56.22	56.14	56.00	55.89	55.87
0	*3*	*3*	56.22	56.14	56.00	55.89	55.87

NA = Not observed.

I.ii Data for Chapter 3

It was found that there were not sufficient non-basal reflections to attempt a full indexing of the XRD patterns of the intercalation compounds reported in Chapter 3. However, the peaks that were visible could be indexed by hand using unit cells similar to the starting LDHs, but with an expanded *c* parameter for $Ca_2Al\text{-}NO_3$, *a* parameter ≈ 5.74 Å).

I.iii Data for Chapter 4

Table I.iv: Indexing of $Ca_2Al(OH)_6NO_3 \cdot 6H_2O$ synthesised *via* a co-precipitation method ($Ca_2Al\text{-}NO_3$ CP) and a reverse microemulsion method without surfactant.

h	***k***	***l***	**2Theta[obs]/^{o}**	
			$Ca_2Al\text{-}NO_3$ CP	**$Ca_2Al\text{-}NO_3$ WO**
0	*0*	*2*	10.32	10.28
0	*0*	*4*	20.64	20.64
0	*0*	*6*	31.13	31.11
1	*1*	*0*	31.13	31.11
1	*1*	*2*	32.86	32.51
2	*0*	*0*	36.13	36.08
2	*0*	*2*	37.64	37.59
0	*2*	*2*	37.64	37.59
2	*0*	*4*	41.85	41.84
0	*2*	*4*	41.85	41.84
1	*1*	*6*	44.58	44.46
1	*0*	*8*	45.89	45.78
0	*1*	*8*	45.89	45.78
2	*1*	*0*	48.43	48.33
2	*1*	*2*	49.58	NA
1	*2*	*2*	49.58	NA
2	*1*	*4*	53.15	NA
1	*2*	*4*	53.15	NA
3	*0*	*0*	55.41	55.30
3	*0*	*2*	56.46	56.46
0	*3*	*2*	56.46	56.46
3	*0*	*4*	59.80	NA
0	*3*	*4*	59.80	NA
3	*0*	*6*	64.86	NA
0	*3*	*6*	64.86	NA
0	*0*	*12*	65.85	65.95

NA = Not observed.

Table I.v. Indexing of $Ca_2Al(OH)_6NO_3 \cdot 6H_2O$ synthesised *via* a reverse microemulsion method at different water to Brij30 ratio ($Ca_2Al\text{-}NO_3$ BRM*w*, *3.4* < *w* < *19.6* where w is water to Brij30 ratio).

			$Ca_2Al\text{-}NO_3$ (2Theta[obs]/°)				
h	***k***	***l***	**BRM*19.6***	**BRM*13.7***	**BRM*10.6***	**BRM*4.6***	**BRM*3.4***
0	*0*	*2*	10.28	10.42	10.45	10.36	10.44
0	*0*	*4*	20.65	20.76	20.79	29.74	20.79
0	*0*	*6*	31.18	31.12	31.30	31.13	31.13
1	*1*	*0*	31.18	31.12	31.30	31.13	31.13
1	*1*	*2*	32.91	33.00	33.00	32.86	32.81
2	*0*	*0*	36.13	36.27	36.27	36.17	36.17
2	*0*	*2*	37.64	37.79	37.79	37.69	37.64
0	*2*	*2*	37.64	37.79	37.79	37.69	37.64
2	*0*	*4*	41.94	42.05	42.05	NA	NA
0	*2*	*4*	41.94	42.05	42.05	NA	NA
1	*1*	*6*	44.46	44.67	44.78	44.78	44.78
1	*0*	*8*	46.10	46.00	46.00	NA	NA
0	*1*	*8*	46.10	46.00	46.00	NA	NA
2	*1*	*0*	48.53	48.64	48.64	48.64	48.64
2	*1*	*2*	49.60	49.80	49.81	NA	NA
1	*2*	*2*	49.60	49.80	49.81	NA	NA
2	*1*	*4*	53.18	53.29	53.29	NA	NA
1	*2*	*4*	53.18	53.29	53.29	NA	NA
3	*0*	*0*	55.41	55.52	55.52	55.30	55.41
3	*0*	*2*	56.57	56.67	56.67	56.46	56.46
0	*3*	*2*	56.57	56.67	56.67	56.46	56.46
3	*0*	*4*	59.74	59.63	59.83	NA	NA
0	*3*	*4*	59.74	59.63	59.83	NA	NA
3	*0*	*6*	64.75	64.85	64.96	64.85	64.80
0	*3*	*6*	64.75	64.85	64.96	64.85	64.80
0	*0*	*12*	65.96	65.96	66.17	65.85	65.74

NA = Not observed.

Table I.vi. Indexing of $Ca_2Al(OH)_6NO_3{\cdot}6H_2O$ synthesised *via* a reverse microemulsion method at different water to Brij30 ratio ($Ca_2Al\text{-}NO_3$ BRM*w*, *1.4* < *w* < *2.7* where w is water to Brij30 ratio).

			$Ca_2Al\text{-}NO_3$ (2Theta[obs]/^{o})			
h	***k***	***l***	**BRM*2.7***	**BRM*2.3***	**BRM*1.7***	**BRM*1.4***
0	*0*	*2*	10.39	10.46	10.41	10.05
0	*0*	*4*	20.77	20.92	20.74	20.0
0	*0*	*6*	31.11	31.09	31.08	31.09
1	*1*	*0*	31.11	31.09	31.08	31.09
1	*1*	*2*	32.91	32.76	32.67	32.81
2	*0*	*0*	36.17	36.08	36.08	36.08
2	*0*	*2*	37.64	37.64	37.64	37.64
0	*2*	*2*	37.64	37.64	37.64	37.64
1	*1*	*6*	44.78	NA	NA	NA
2	*1*	*0*	48.64	NA	NA	NA
3	*0*	*0*	55.30	55.30	55.30	55.30
3	*0*	*2*	56.36	56.46	56.46	56.46
0	*3*	*2*	56.36	56.46	56.46	56.46

NA = Not observed.

I.iv Data for Chapter 5

Table I.vi. Indexing of $Ca_2Al(OH)_6NO_2 \cdot 3.1H_2O$ synthesised *via* a co-precipitation method ($Ca_2Al\text{-}NO_2$ BRM*10.6*).

h	***k***	***l***	**2Theta[obs]/^{o}**
			$Ca_2Al\text{-}NO_2$ CP
0	*0*	*2*	11.70
0	*0*	*4*	23.52
1	*1*	*0*	31.31
0	*0*	*6*	35.52
2	*0*	*0*	36.22
2	*0*	*2*	38.41
0	*2*	*2*	38.41
1	*0*	*6*	41.75
0	*1*	*6*	41.75
2	*0*	*4*	44.92
0	*2*	*4*	44.92
1	*1*	*6*	46.99
0	*0*	*8*	47.96
1	*2*	*2*	49.94
2	*1*	*2*	49.94
3	*0*	*0*	55.46
0	*0*	*10*	61.33
2	*2*	*0*	64.86

It was found that there were not sufficient non-basal reflections to attempt a full indexing of the XRD patterns of $Ca_2Al(OH)_6NO_2 \cdot 6H_2O$ synthesised by a reverse microemulsion ($Ca_2Al\text{-}NO_2$ BRM*10.6*) due to weak Bragg reflections of nano-sized $Ca_2Al\text{-}NO_2$ BRM*10.6*.

I.v Data for Chapter 6

It was found that there were not sufficient non-basal reflections to attempt a full indexing of the XRD patterns of $Ca_2Al(OH)_6(C_{12}H_{25}SO_4) \cdot nH_2O$ (Ca_2Al-DDS) reported in Chapter 6 due to weak Bragg reflections of nano-sized Ca_2Al-DDS LDHs.

Appendix II: Kinetics Models to Study the Kinetic Behaviour of Additive Releases

Kinetics models have commonly been used to calculate rate constants of reactions and determine mechanistic data. The rate-determining step of common solid state reactions can be controlled by diffusion and chemical reactions. A generalised correlation of kinetics plot between the extent of reaction (α) and reduced time is shown in Figure II.i. A is an initial reaction, sometimes related to the decomposition of unstable materials. B is the induction period, often ended by the formation of stable nuclei or products of the reaction. C is the acceleratory period of growth from the nuclei which extend to the maximum rate of reaction at D. The continued expansion of nuclei will be terminated due to consumption of reactants and the lower rate of impingement of reactants in the deceleratory or decay period (E). The rate of the reaction slows from this stage until the reaction is completed at point F.

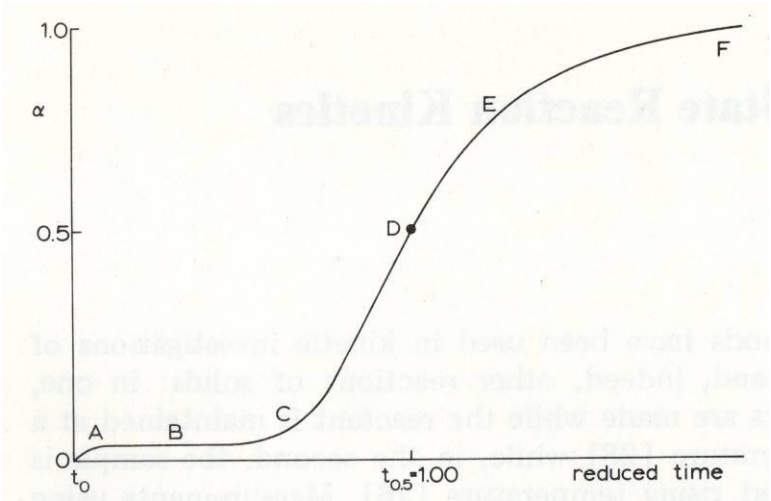

Figure II.i. Generalised correlation between the extent of reaction (α) and time, representing characteristic kinetic behaviour observed for isothermal decompositions of solids.[1]

In general, characteristic kinetic behaviour of the reactions is represented by a sigmoidal curved plot, although some stages may be negligible or absent. There are many kinetics models developed by different thought of the nucleation and the growth of nuclei.

For laws of nucleation, there are examples of equations that assume local fluctuations of energy of a crystal of reactant at preferred sites are sufficient to produce a stable particle

of product. The mathematical treatment representing this probability of the occurrence of an unimolecular process is

$$k_1 = \nu \exp(-\Delta G'_N/RT) = \nu S_1 \exp(-E_1/RT) \qquad \textbf{Equation II.i.}$$

Where ν = The frequency of lattice vibration,

S_1 = The term including entropy of activation (= $\exp(-\Delta S'_N/R)$).

For a nucleation rate,

$$\frac{dN}{dt} = k_1(N_0 - N) \qquad \textbf{Equation II.ii.}$$

Where N_0 = The total number of potential nuclei,

N = The number of nuclei present at time t.

$$N = N_0 (1 - \exp(-k_1 t)) \qquad \textbf{Equation II.iii.}$$

$$\frac{dN}{dt} = k_1 N_0 \exp(-k_1 t) \qquad \textbf{Equation II.iv.}$$

Or $$N = k_1 N_0 t \exp(-k_1 t) \qquad \textbf{Equation II.v.}$$

The equation shown above gives the Exponential law of nucleation. The exponential can be approximated to a cubic term when k is small or $\Delta G'_N$ is large:

$$\frac{dN}{dt} = k_1 N_0 (1 - k_1 t + 1/2 k_1^2 t^2 - 1/6 k_1^3 t^3) \qquad \textbf{Equation II.vi.}$$

If $k_1 t << 1$, $dN/dt = k_1 N_0$ or $N = k_1 N_0 t$ which gives the Linear law of nucleation.

If $k_1 t >> 1$, $N = N_0$ at small value of t which gives Instantaneous nucleation.

From the assumption, it is unclear whether individual interactions can cause many steps needed in the nucleation stage. These steps could be either successive processes in the region of an active site, or the interactions of several mobile reactants while the product

species are presumably blocked. This assumption has been developed by Bagdassarian, who studied the kinetics of steps of a germ nucleus locating in x atoms (ions or molecules) of product.[1] The associate is termed a group nucleus. It is assumed that the rate coefficients (k_n) of individual atoms in the group are equal below x.

$$k_0 = k_1 = k_2 = \ldots = k_{x-1} \qquad \textbf{Equation II.vii.}$$

For the individual atoms above x, k_x all are equal but of greater value.

$$k_x = k_{x+1} = k_{x+2} = \ldots = k_{x+n} > k_{x-1} \qquad \textbf{Equation II.viii.}$$

The generalised equation can be $N = k^x{}_x t^x$. **Equation II.viiii.**

Allnatt and Jacobs modified the equation by using the number of germ nuclei received in x atoms. [REF] After the integration using the Laplace transformation, the modified equation is normalised as below.

$$N_x(t) = N_0 C_0 k_0 k_1 k_2 \ldots\ldots k_{x-1} \sum_{l=0}^{l=x} \frac{\exp(-k_l t)}{\prod_{y=0, y\neq l}^{x} (k_y - k_l)} \qquad \textbf{Equation II.x.}$$

If $k_i t << 1$,

For one step: $N_1(t) = N_0 C_0 k_0 t = K_1 t$

For two steps: $N_2(t) = N_0 C_0 k_0 k_1 t^2 = K_2 t^2$

For x steps: $N_x(t) = N_0 C_0 k_0 \ldots k_x t^x = K_x t^x$ and $dN_x/dt = K t^{x-1}$

The equations above are Power laws of nucleation.

For layered double hydroxides (LDHs), kinetic study of anionic releases from the LDH structures is a method to understand chemical and physical factors relating to the release rate of additives and the stability of the additive-intercalated LDHs. There are four selected kinetics models explored for these release systems including the Avrami-Erofe'ev model, the first-order model, the modified Freundlich model and parabolic diffusion model.[2]

II.i. The Avrami-Erofe'ev model

This model has been successfully applied to study solid state kinetics of phase transformations, decompositions, and intercalation reactions for which the model was created by Melvin Avrami in 1939 from Johnson-Mehl-Avrami-Kolmogorov kinetics (JMAK).[3-5]

The Avrami-Erofe'ev model is one of the model equations determining Sigmoidal kinetic characteristics as the behaviour of common solid state reactions. The general form of the model is shown below.

$$\alpha = 1 - \exp(-kt^n) \qquad \textbf{Equation II.xi.}$$

$$-\ln (1 - \alpha) = kt^n \qquad \textbf{Equation II.xii.}$$

Taking logarithms of the equation,

$$\ln(-\ln (1 - \alpha)) = n \ln k + n \ln t \qquad \textbf{Equation II.xiii.}$$

Where α is reaction progress calculated from the ratio between the concentration of additive released at time (C_t) and the initial concentration of additive between interlayer of layered double hydroxide (C_0). The plot of $\ln(-\ln (1 - \alpha))$ against ln t allows n and k to be calculated.

The exponent, n, of the Avrami-Erofe'ev equation can be used to explain the kinetics of nucleation and growth processes of nuclei, which has been explored by Hulbert. The kinetics of nucleation and growth processes can be examined by the calculation from the equations; $n = \beta + \lambda$ for a phase boundary-controlled process, and $n = \beta + \lambda/2$ for a diffusion-controlled process. The nucleation rate of nuclei or product could be instantaneous, constant, or deceleratory depending on the value of β, whereas the dimensions of the nuclei growth can be defined from λ.[6]

For layered double hydroxides, the nucleation site would be the interactive cations surface of LDH plates. It is possible that small anionic guests could intercalate into the layers instantly to replace the additive in the interlayers of LDHs. The intercalation rate can be a

deceleratory step in cases where some different anionic guests interfere or encounter each other during the intercalation process. After the nucleation period, the growth of nuclei could be two-dimensional growth along LDH platelets during the intercalation (Figure II.ii). One-dimensional growth could happen after the intercalation process parallel c-axis of LDH structure by guests already replaced into additive-intercalated LDHs. The rate-determining step of LDHs for the Avrami-Erofe'ev model based on Hulbert's modification could be controlled by (1) the rate of expansion of the interlayer space to accommodate anionic guests, called a phase boundary-controlled step, or (2) the rate of diffusion of anionic guests within the interlayer space called diffusion-controlled step.

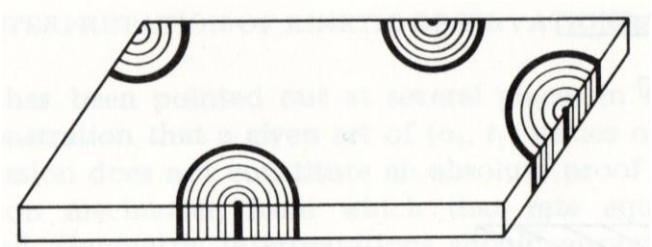

Figure II.ii. Growth of semi-circular nuclei in a thin plate of reactant.[1]

II.ii The first-order model

This kinetics model is one of the simple kinetics models series mentioned the order of a reaction studied which is the sum of the exponents of the concentrations that appear in the rate equation. The model equation is a logarithmic correlation between the reaction progress (α) and reaction time (t) as shown below.[2, 7] This equation often provides a perfect fit in numerous cases of desorption and ion-exchange kinetics.

The first-order model of substance A

$$dC_A/dt = -k'C_A \qquad \textbf{Equation II.xiii.}$$

Where C_A is concentration of substance A

$$dC_A/C_A = -k'dt \qquad \textbf{Equation II.xv.}$$

$$\ln C_A = -k't + c \qquad \textbf{Equation II.xvi.}$$

Integration c is equal to the value of $\ln C_A$; $\ln C_A$ at $t = 0$, or $\ln C_A^o$

$$\ln C_A = \ln C_A^{o} - k't \qquad \textbf{Equation II.xvii.}$$

$$\ln (C_A/C_A^{o}) = -k't \qquad \textbf{Equation II.xviii.}$$

When the reaction progress is α in case of a desorption or an ion-exchange process;

$1 - \alpha = C_A/C_A^{o}$

$$\ln (1 - \alpha) = -k't \qquad \textbf{Equation II.xix.}$$

II.iii The modified Freundlich model

The modified Freundlich model is one of the models normally selected for the study of ion-exchange kinetics in mica, zeolites, soils, clays, and layered materials such as LDHs, because it describes desorption from heterogeneous surfaces based on a diffusion-controlled process.[8] The original form of the Freundlich equation is given below. It is modeled using the empirical two-parameter Freundlich isotherm.[9]

$$\alpha = K_F C_e^{1/n} \qquad \textbf{Equation II.xx.}$$

Where K_F is the Freundlich constant, C_e is the concentration of adsorbent at equilibrium, and n is a dimensionless parameter that varies between 0 and 1.

This equation was modified by Kuo and Lotse in 1973 to study the kinetics of phosphate adsorption and desorption by hematite and gibbsite. The isotherm shown below was created with time-dependent form.[10]

$$\alpha = Kt^{n} \qquad \textbf{Equation II.xxi.}$$

For linear plotting;

$$\ln \alpha = \ln K + n \ln t \qquad \textbf{Equation II.xxii.}$$

II.iv The parabolic diffusion model

For kinetics study of ion-exchange or adsorption, the parabolic diffusion model is also used to determine the mechanism. This model assumes that diffusion-controlled phenomena are rate-limiting. The concept of thought to derive the model actually is from the rate of radial diffusion in a cylinder where diffused concentration in perpendicular directions is constant (Figure II.iii).[9, 11-13]

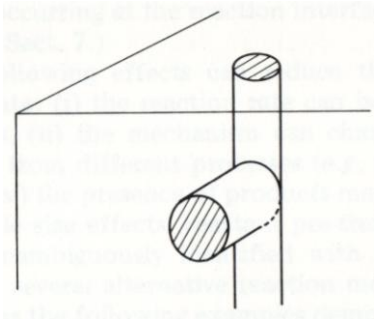

Figure II.iii. Cylindrical growth of linear internal nuclei.

$$\alpha = (4/\pi^{1/2})(Dt/r^2)^{1/2} - (Dt/r^2) - (1/3\pi^{1/2})(Dt/r^2)^{3/2} \qquad \textbf{Equation II.xxiii.}$$

Where D is diffusion coefficient and r is the radius of the cylindrical diffusion. For small values of time t, the third term may be ignored. The diffusion coefficient may be calculated from the slope of the linear correlation between α/t and $1/t^{1/2}$.[14]

$$\alpha/t = (4/\pi^{1/2})(D/r^2)^{1/2}(1/t^{1/2}) - (D/r^2) \qquad \textbf{Equation II.xxiiii.}$$

In which the slope of the plot is $(4/\pi^{1/2})(D/r^2)^{1/2}$ and the intercept is $-D/r^2$.

II.v References

1. L. Meites, *An introduction to chemical equilibrium and kinetics*, Pergamon Press Oxford (UK), 1981.
2. T. Kodama, Y. Harada, M. Ueda, K.-i. Shimizu, K. Shuto and S. Komarneni, *Langmuir*, 2001, **17**, 4881-4886.
3. D. W. Henderson, *Journal of Thermal Analysis and Calorimetry*, 1979, **15**, 325-331.
4. M. Avrami, *The Journal of Chemical Physics*, 1939, **7**, 1103.
5. M. Avrami, *The Journal of Chemical Physics*, 1940, **8**, 212.
6. X. Duan and D. G. Evans, eds., *Layered Double Hydroxides*, Springer, 2006.
7. D. L. Sparks and P. M. Jardine, *Soil Science Society of America Journal*, 1981, **45**, 1094-1099.
8. H. Freundlich, *Zeitschrift für Physikalische Chemie*, 1907, **57**, 385-471.
9. D. L. Sparks, *Environmental Soil Chemistry*, Elsevier Science (USA), 2003.
10. S. Kuo and E. G. Lotse, *Soil Science*, 1973, **116**, 400-406.
11. M. Trgo, J. Perić and N. V. Medvidović, *Journal of hazardous materials*, 2006, **136**, 938-945.
12. T. Kodama, M. Ueda, Y. Nakamuro, K.-i. Shimizu and S. Komarneni, *Langmuir*, 2004, **20**, 4920-4925.
13. X. Kong, L. Jin, M. Wei and X. Duan, *Applied Clay Science*, 2010, **49**, 324-329.
14. J. Crank, *The Mathematics of Diffusion*, Oxford University Press (Clarendon), 1976.

Appendix III: Kinetic Modelling with Superplasticiser Release Data

III.i Kinetic studies of Ca_2Al-naphthalene sulfonate

III.i.i Ca_2Al-naphthalene sulfonate in Na_2CO_3 solution

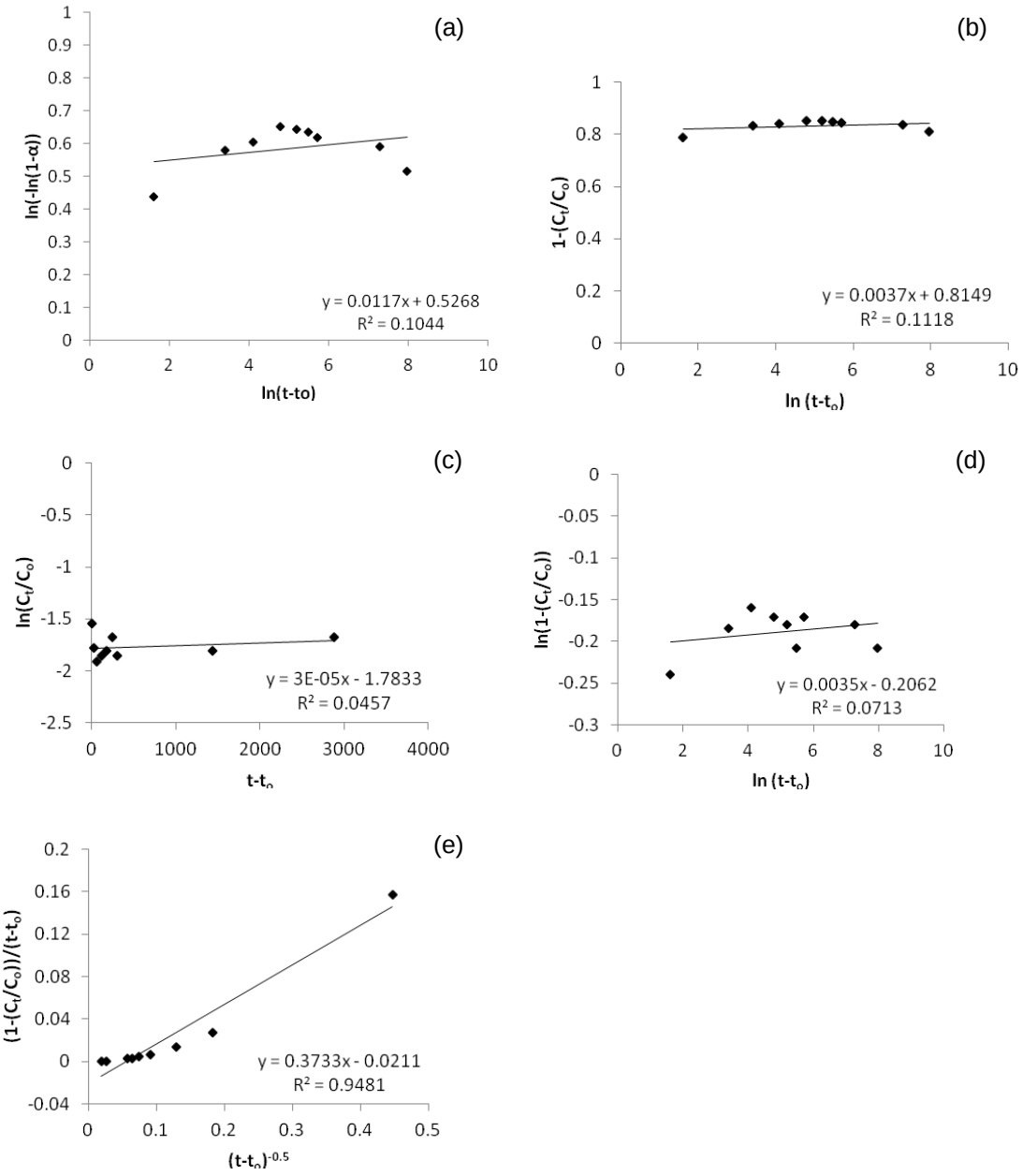

Figure III.i. Plots of (a) Avrami-Erofe'ev model, (b) Elovich model, (c) The first-order model, (d) Modified Fruendlich model, and (e) Parabolic diffusion model for the release of naphthalene sulfonate from Ca_2Al-LDH in Na_2CO_3 solution.

III.i.ii Ca_2Al-naphthalene sulfonate in Na_2SO_4 solution

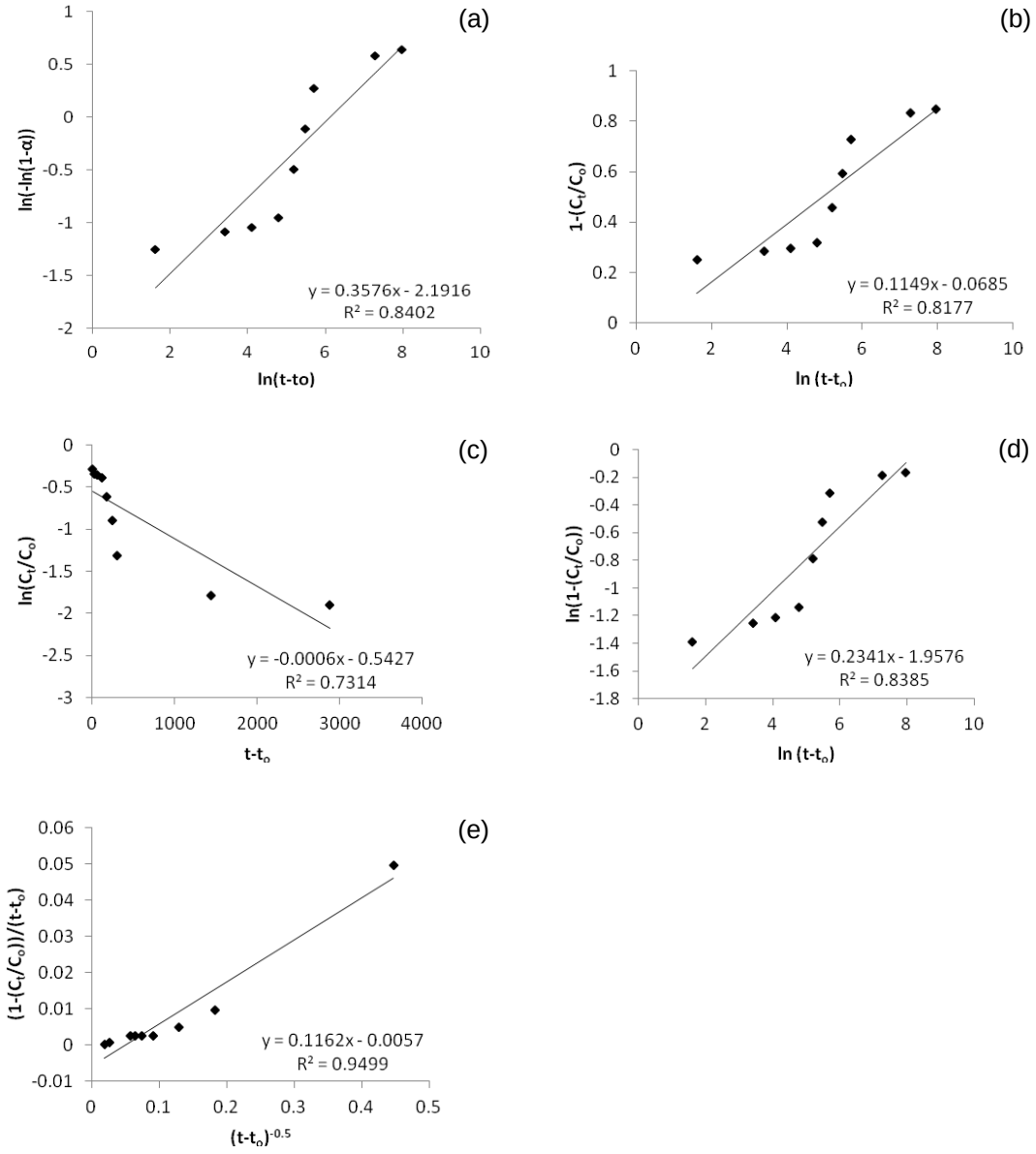

Figure III.ii. Plots of (a) Avrami-Erofe'ev model, (b) Elovich model, (c) The first-order model, (d) Modified Fruendlich model, and (e) Parabolic diffusion model for the release of naphthalene sulfonate from Ca_2Al-LDH in Na_2SO_4 solution.

III.i.iii Ca_2Al-naphthalene sulfonate in $Na_2Si_3O_7$ solution

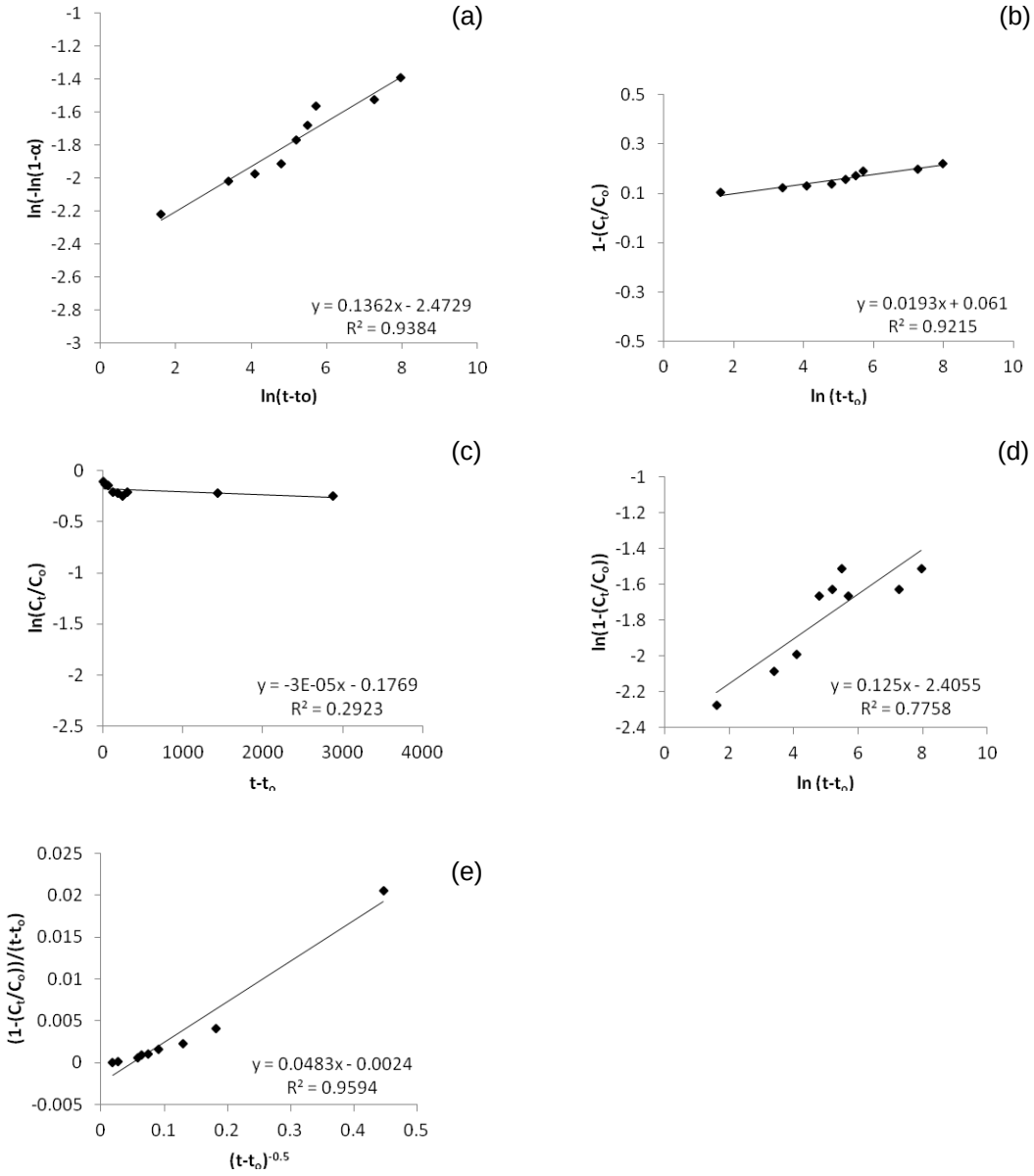

Figure III.iii. Plots of (a) Avrami-Erofe'ev model, (b) Elovich model, (c) The first-order model, (d) Modified Fruendlich model, and (e) Parabolic diffusion model for the release of naphthalene sulfonate from Ca_2Al-LDH in $Na_2Si_3O_7$ solution.

III.i.iv Ca_2Al-naphthalene sulfonate in water at pH 13.5

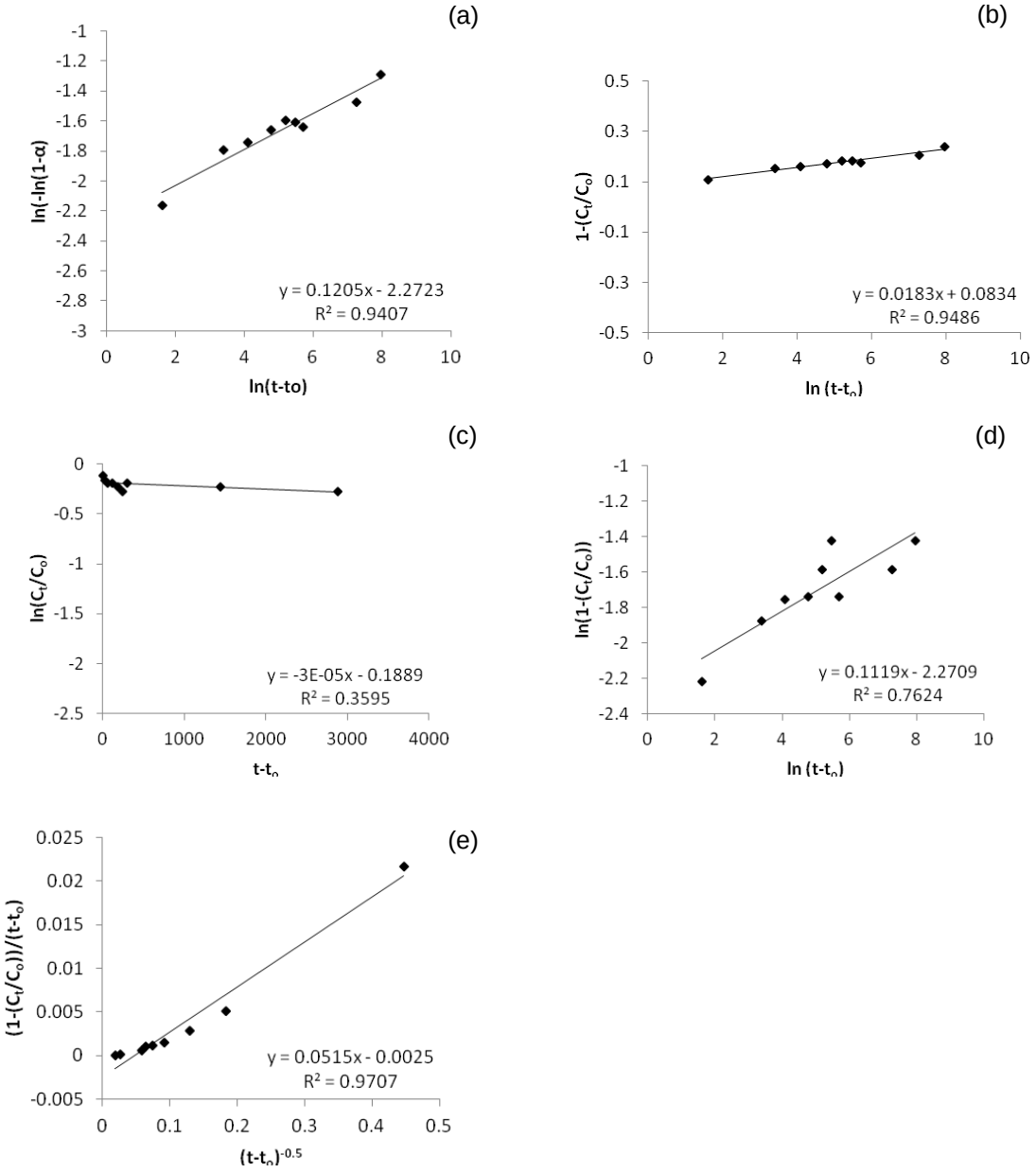

Figure III.iv. Plots of (a) Avrami-Erofe'ev model, (b) Elovich model, (c) The first-order model, (d) Modified Fruendlich model, and (e) Parabolic diffusion model for the release of naphthalene sulfonate from Ca_2Al-LDH in water at pH 13.5.

III.i.v Ca_2Al-naphthalene sulfonate in water at pH 7

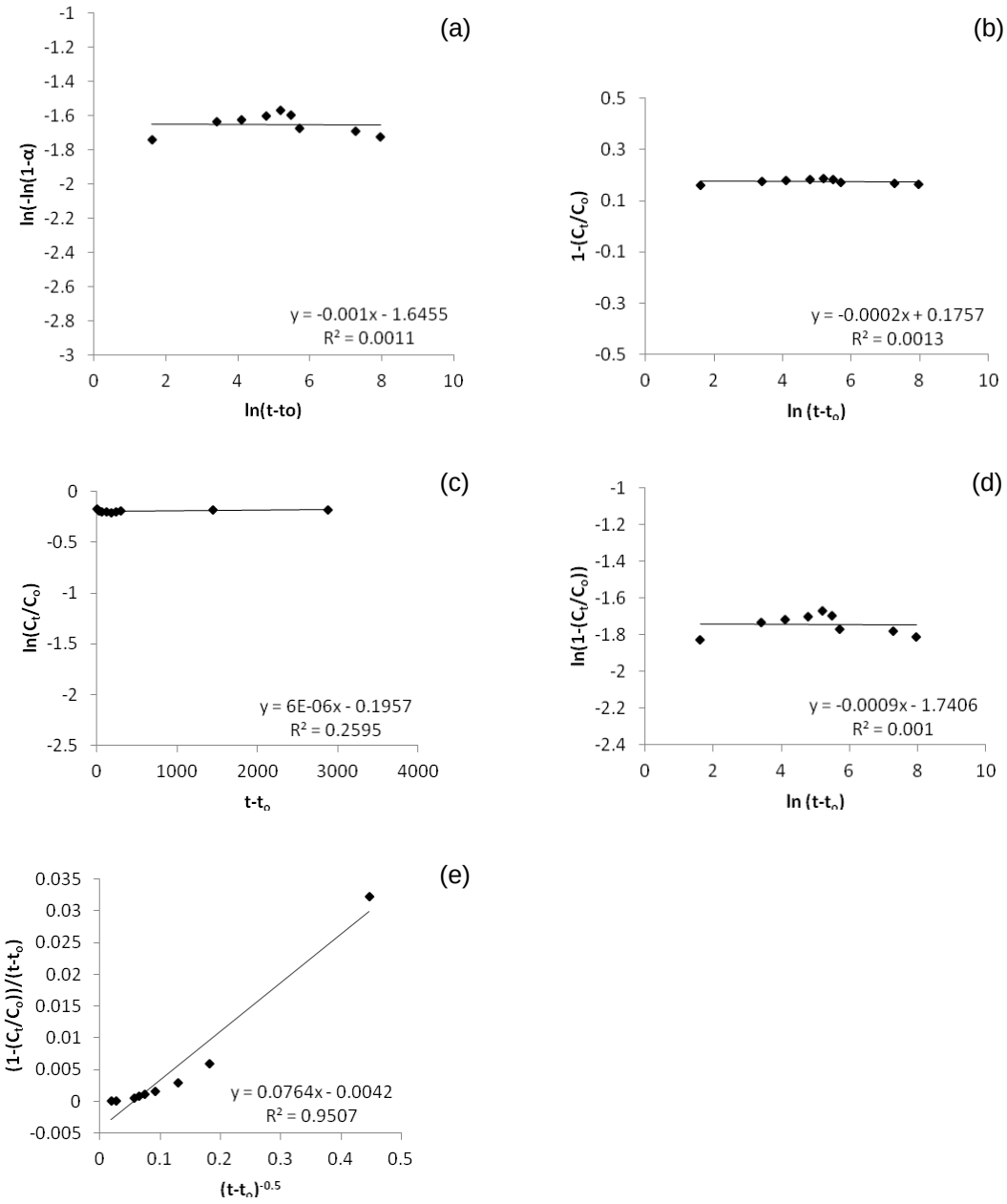

Figure III.v. Plots of (a) Avrami-Erofe'ev model, (b) Elovich model, (c) The first-order model, (d) Modified Fruendlich model, and (e) Parabolic diffusion model for the release of naphthalene sulfonate from Ca_2Al-LDH in water at pH 7.

III.i.vi Ca_2Al-naphthalene sulfonate in cement solution

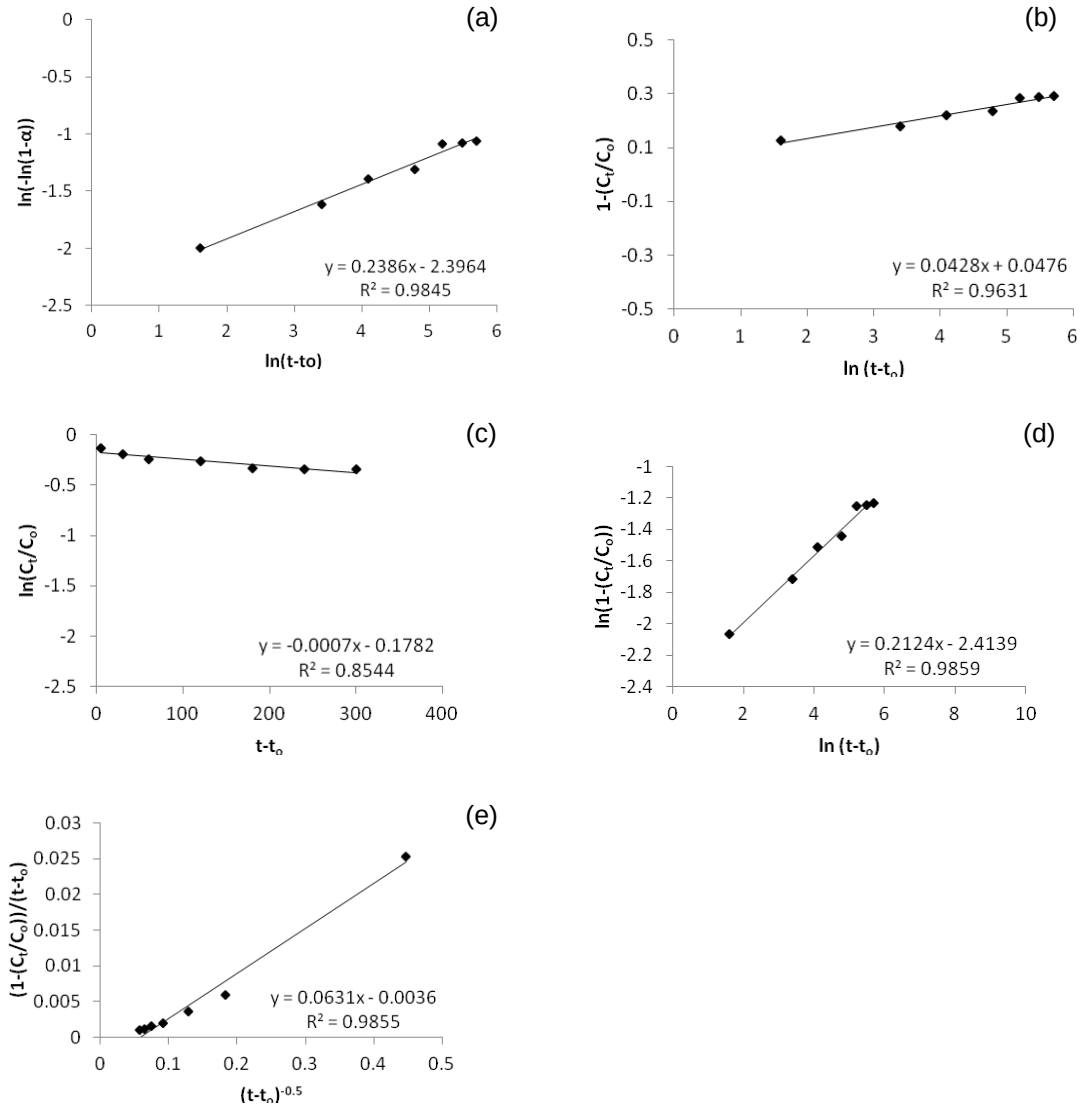

Figure III.vi. Plots of (a) Avrami-Erofe'ev model, (b) Elovich model, (c) The first-order model, (d) Modified Fruendlich model, and (e) Parabolic diffusion model for the release of naphthalene sulfonate from Ca_2Al-LDH in cement solution at water/cement ratio = 0.8.

III.ii Kinetic studies of Ca_2Al-lignosulfonate

III.ii.i Ca_2Al-lignosulfonate in Na_2CO_3 solution

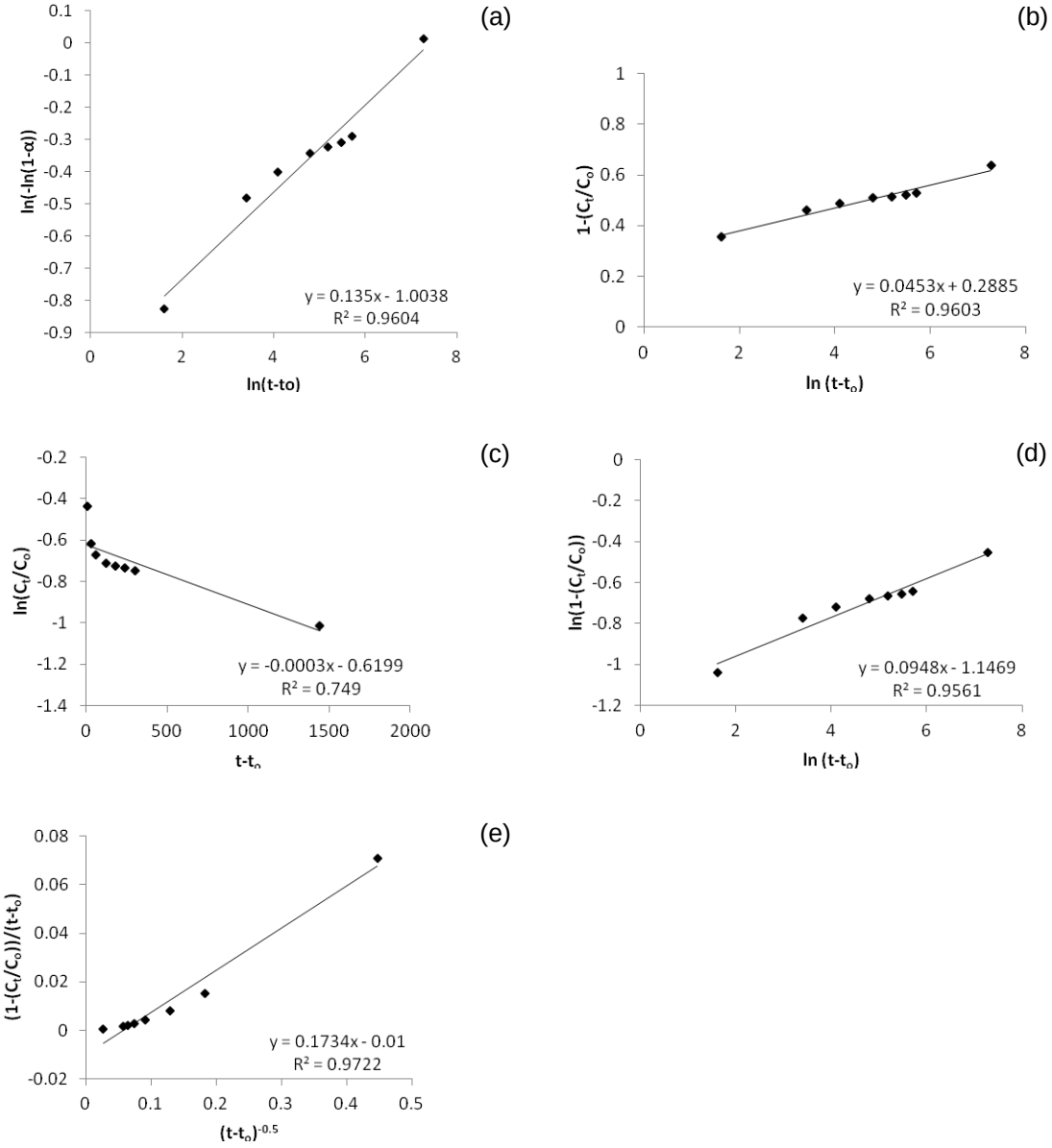

Figure III.vii. Plots of (a) Avrami-Erofe'ev model, (b) Elovich model, (c) The first-order model, (d) Modified Fruendlich model, and (e) Parabolic diffusion model for the release of lignosulfonate from Ca_2Al-LDH in Na_2CO_3 solution.

III.ii.ii Ca_2Al-naphthalene sulfonate in Na_2SO_4 solution

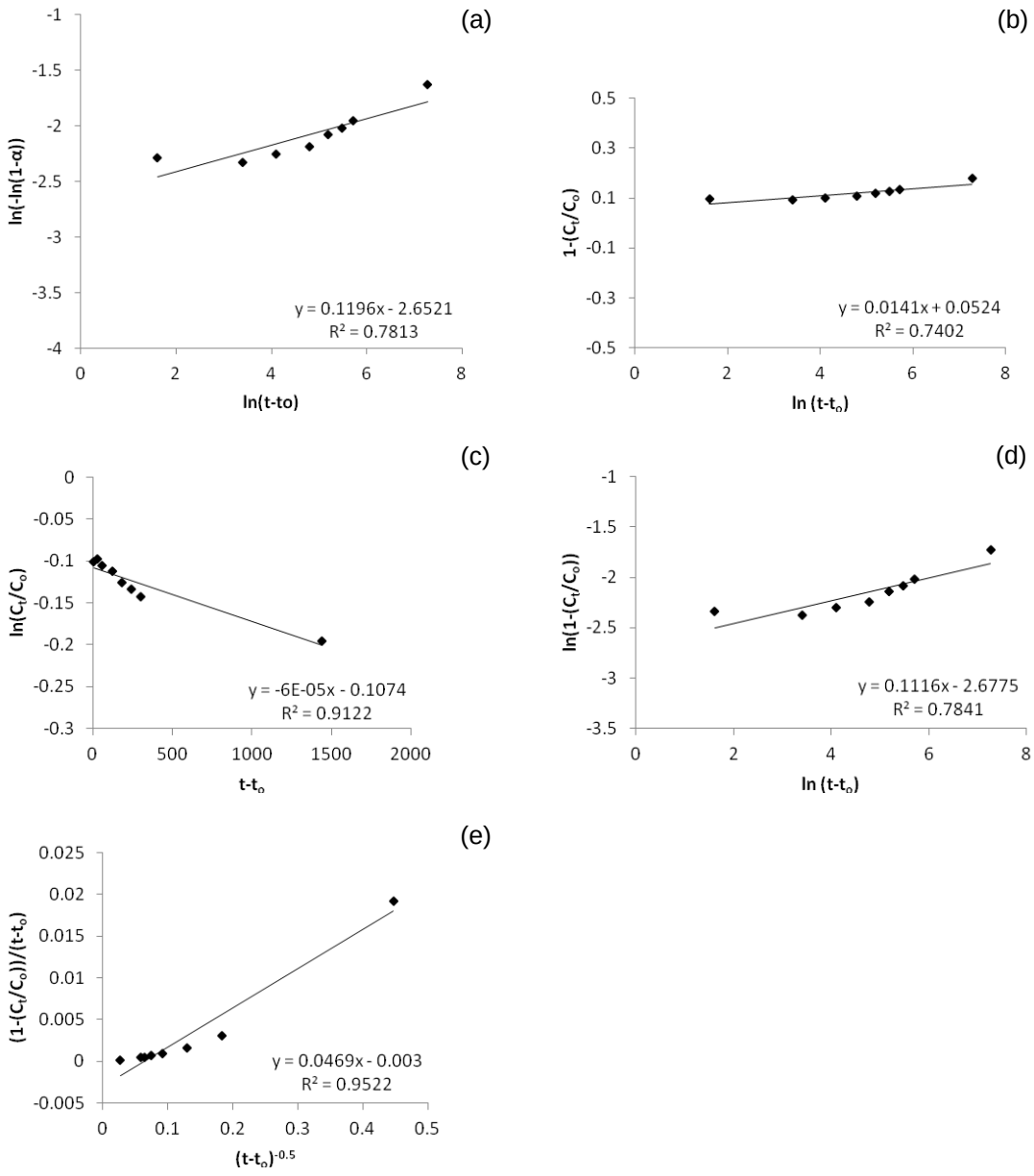

Figure III.viii. Plots of (a) Avrami-Erofe'ev model, (b) Elovich model, (c) The first-order model, (d) Modified Fruendlich model, and (e) Parabolic diffusion model for the release of lignosulfonate from Ca_2Al-LDH in Na_2SO_4 solution.

III.ii.iii Ca_2Al-naphthalene sulfonate in $Na_2Si_3O_7$ solution

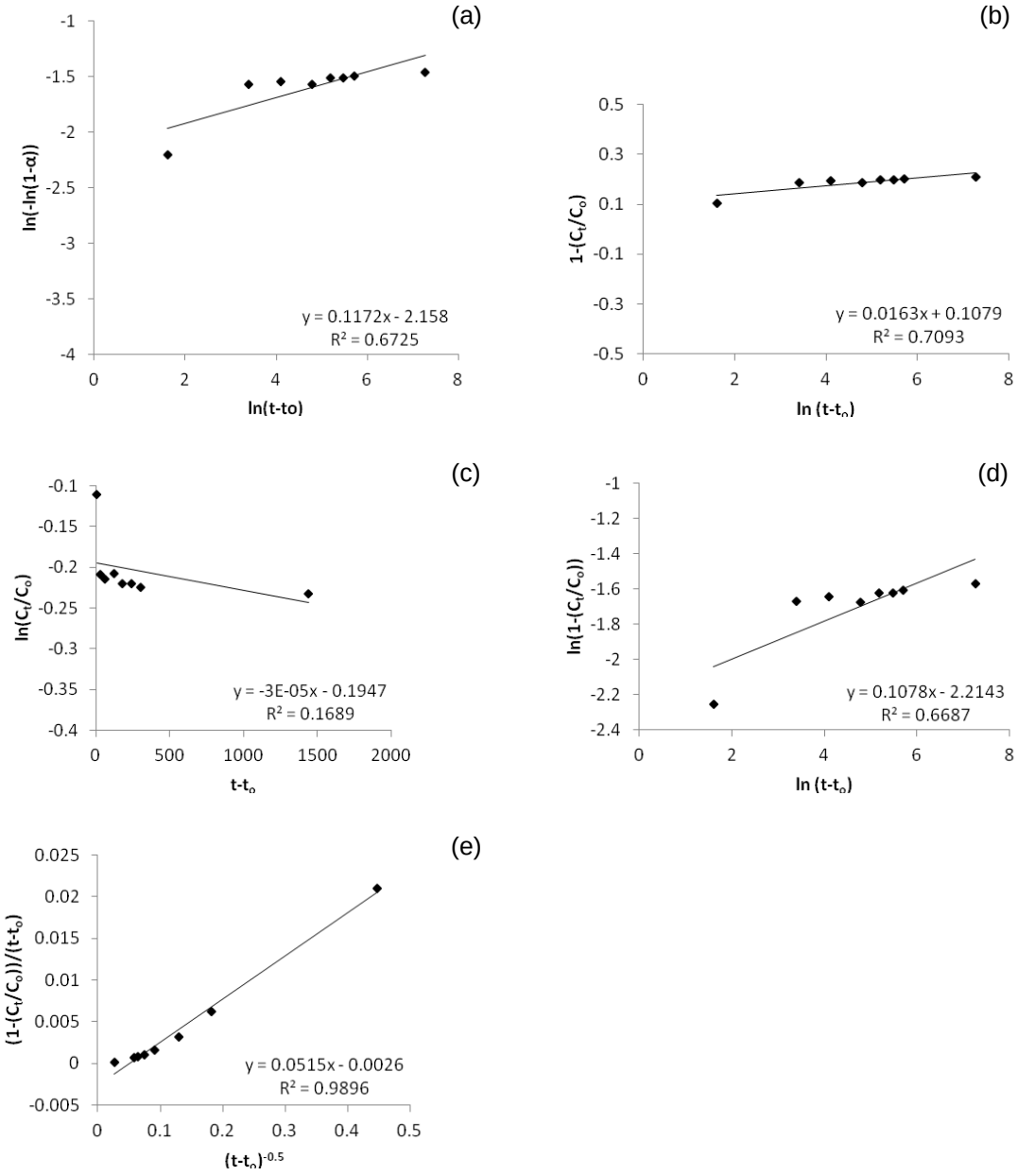

Figure III.ix. Plots of (a) Avrami-Erofe'ev model, (b) Elovich model, (c) The first-order model, (d) Modified Fruendlich model, and (e) Parabolic diffusion model for the release of lignosulfonate from Ca_2Al-LDH in $Na_2Si_3O_7$ solution.

III.ii.iv Ca_2Al-naphthalene sulfonate in water at pH 13.5

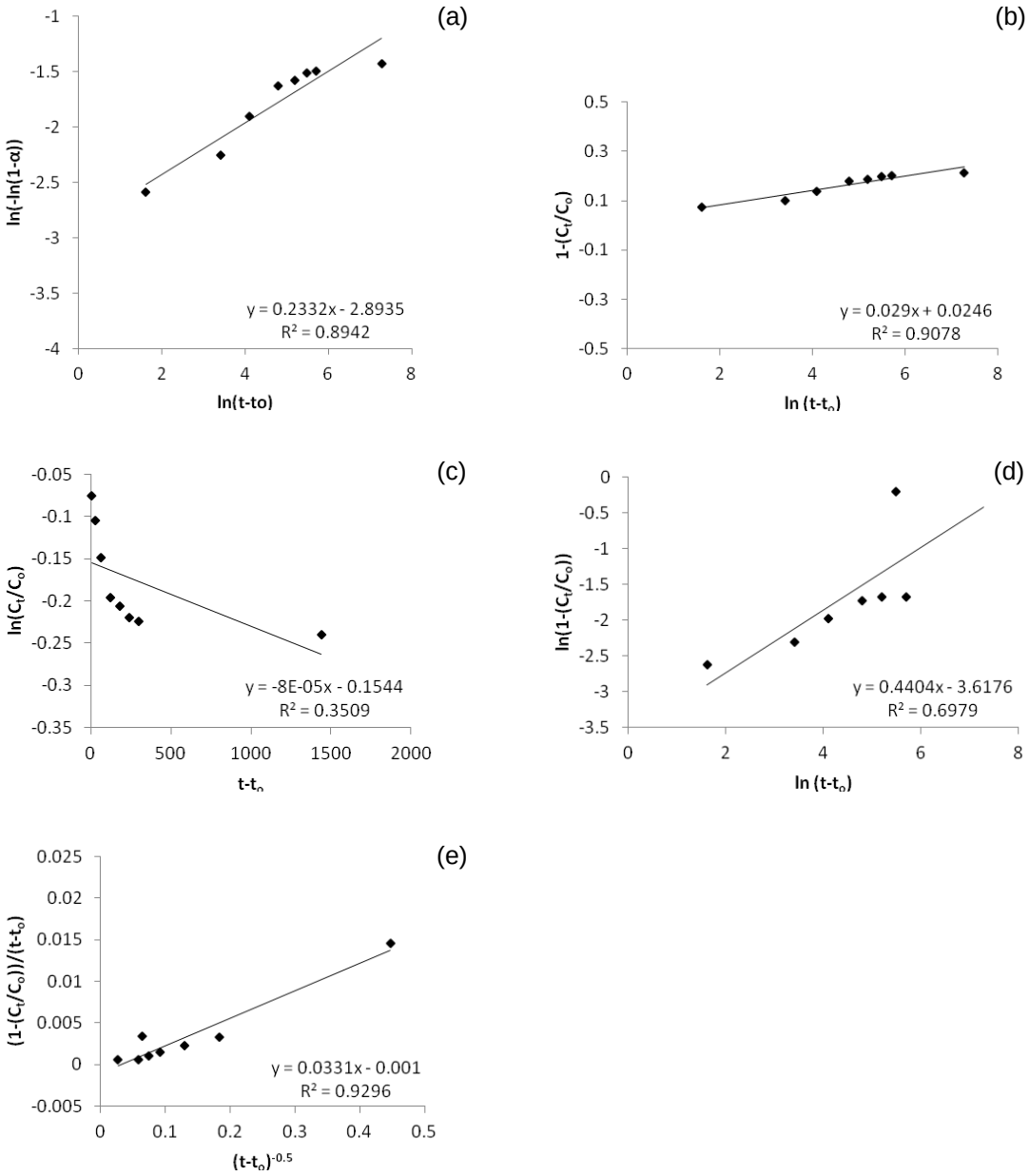

Figure III.x. Plots of (a) Avrami-Erofe'ev model, (b) Elovich model, (c) The first-order model, (d) Modified Fruendlich model, and (e) Parabolic diffusion model for the release of lignosulfonate from Ca_2Al-LDH in water at pH 13.5.

III.ii.v Ca_2Al-naphthalene sulfonate in water at pH 7

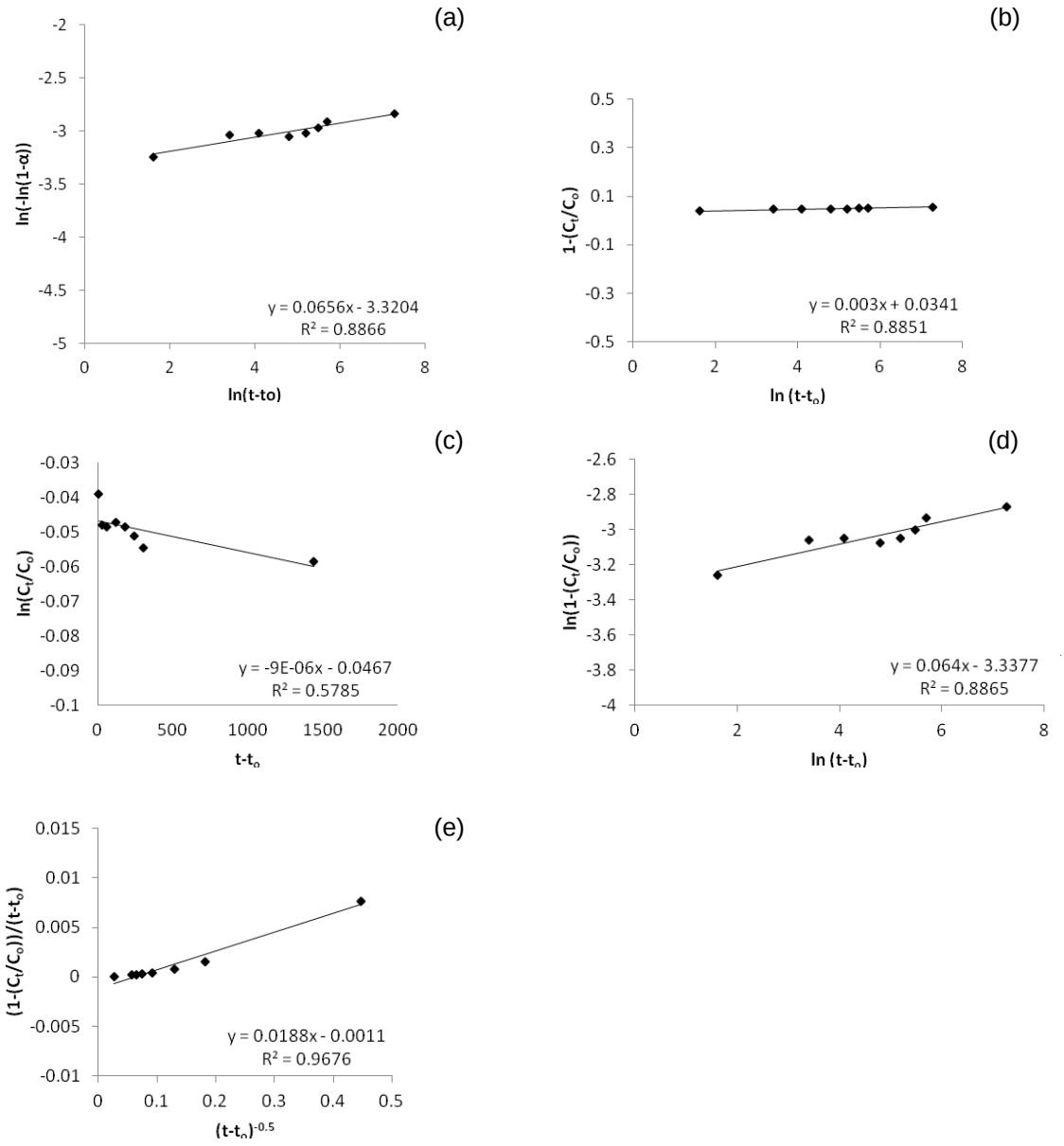

Figure III.xi. Plots of (a) Avrami-Erofe'ev model, (b) Elovich model, (c) The first-order model, (d) Modified Fruendlich model, and (e) Parabolic diffusion model for the release of lignosulfonate from Ca_2Al-LDH in water at pH 7.

III.ii.vi Ca_2Al-naphthalene sulfonate in cement solution

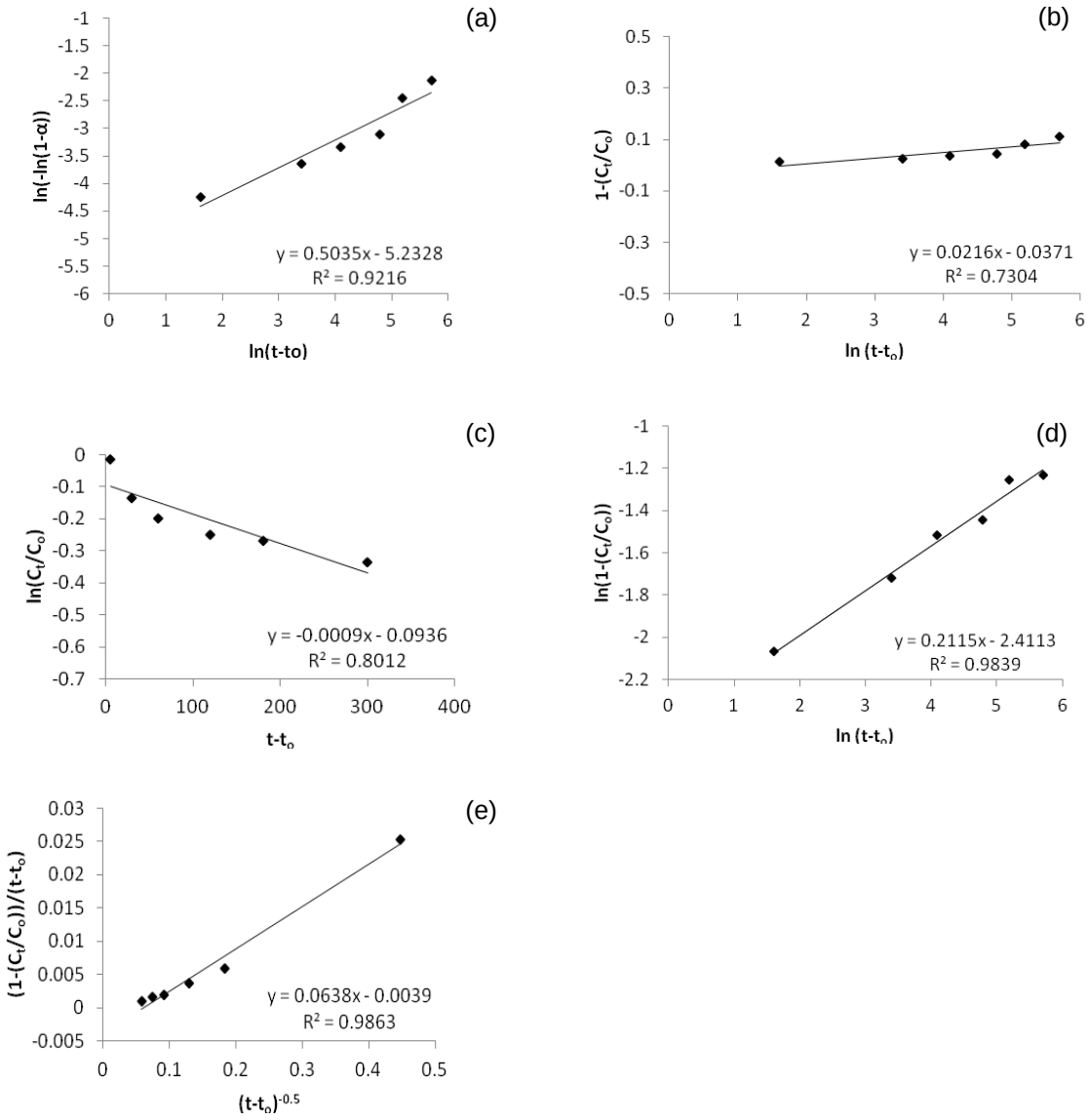

Figure III.xii. Plots of (a) Avrami-Erofe'ev model, (b) Elovich model, (c) The first-order model, (d) Modified Fruendlich model, and (e) Parabolic diffusion model for the release of lignosulfonate from Ca_2Al-LDH in cement solution at water/cement ratio = 0.8.

Appendix IV: The Storage Elastic Modulus Data using The Ultrasound Shear Wave Reflection

IV.i The Storage Elastic Modulus of cement hydration

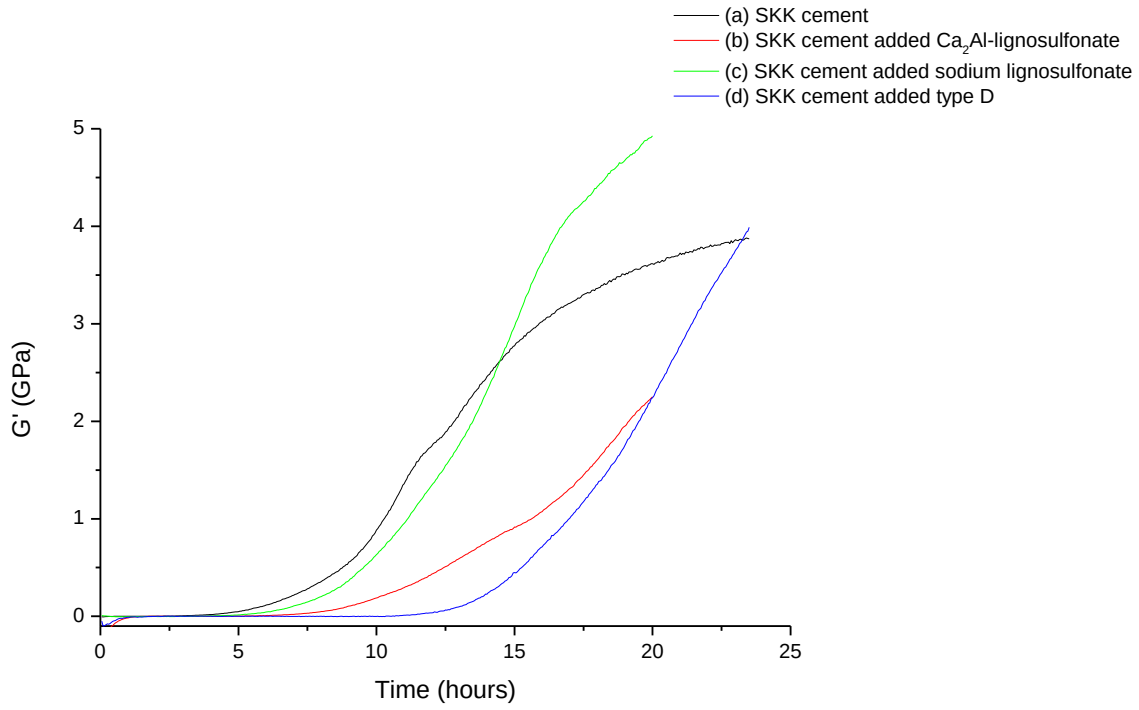

Figure IV.i. Time-dependence of the storage elastic modulus (*G'*) of cement during hydration: (a) SKK cement, and SKK cement with added; (b) Ca_2Al-lignosulfonate, (c) sodium lignosulfonate, and (d) Type D.

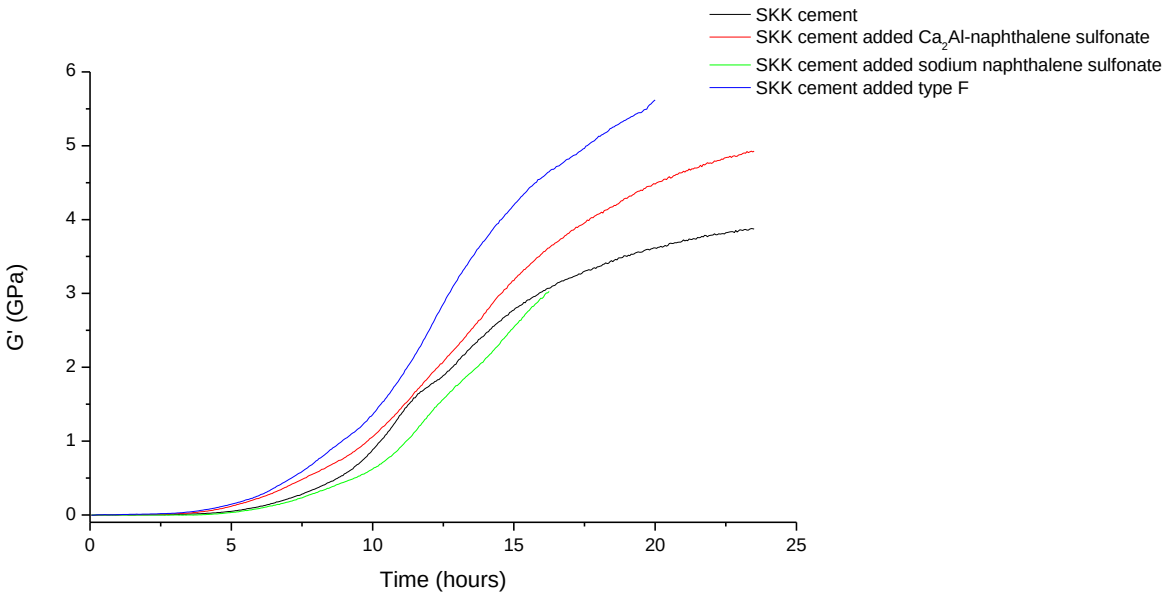

Figure IV.ii. Time-dependence of the storage elastic modulus (*G'*) of cement during hydration: (a) SKK cement, and SKK cement with added; (b) Ca_2Al-naphthalene sulfonate, (c) sodium naphthalene sulfonate, and (d) Type F.

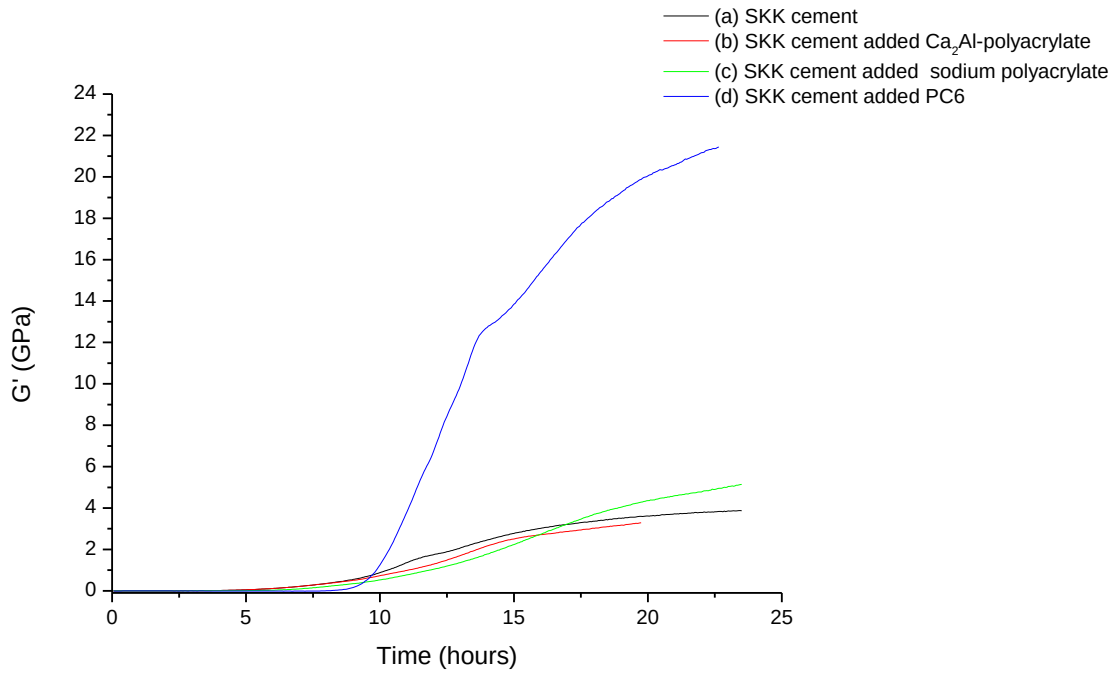

Figure IV.iii. Time-dependence of the storage elastic modulus (*G'*) of cement during hydration: (a) SKK cement, and SKK cement with added; (b) Ca_2Al-polyacrylate, (c) sodium polyacrylate, and (d) PC6.